Optical Interactions for Internal Signal Tracking in ICs - A Deeper Understanding through Numerical Simulations, Spectral Investigations and Specific Digital & Analog Test Structures

vorgelegt von
M.Sc.
Ivo Vogt
geb. in Mechernich, Deutschland

von der Fakultät IV - Elektrotechnik und Informatik
der Technischen Universität Berlin
zur Erlangung des akademischen Grades

Doktor der Naturwissenschaften
- Dr. rer. nat. -

genehmigte Dissertation

Promotionsausschuss:

Vorsitzender:	Prof. Dr. Bernd Rech, Technische Universität Berlin
Gutachter:	Prof. Dr. Christian Boit, Technische Universität Berlin
Gutachterin:	Prof. Dr. Ingrid De Wolf, Katholieke Universiteit Leuven
Gutachter:	Prof. Dr. Dean Lewis, Université Bordeaux I

Tag der wissenschaftlichen Aussprache: 4. Juni 2018

Berlin 2018

Acknowledgements

First of all I want to thank my advisor Prof Dr. Christian Boit for accepting me as a PhD student, for introducing me to the world of scientific research and electronics failure analysis and for the opportunity to work in such a nice and sympathetic group throughout the last 4 years. Many thanks go to Prof. Dr. Ingrid De Wolf from IMEC / Katholieke Universiteit Leuven for almost 3 years of successful research cooperation and her commitment in being reviewer to my PhD thesis - hartelijk dank! Last but not least I want to thank Prof. Dr. Dean Lewis from Université Bordeaux I for his agreeing and effort on reviewing my PhD thesis - merci beaucoup!

Many thanks go to my dear colleagues Orbert, Norman, Elhanne, Anham, Dr. Zohrke, and Tubi for creating such a nice work atmosphere and especially for continuously providing me with cookies and cake. Of course I'm indebted also to Dr. Uwe Kerst for sharing his office with me in the first year and also for sharing his interest in theoretical physics and mathematics in the three years after. I also want to thank Rainer Leihkauf for his extensive help in setting up the TCAD simulations and interpreting results. Arek Glowacki for his always merry mood, for introducing me into the mysteries of photon emission and electro-optical frequency mapping when I started my PhD studies and for help and collaboration in several measurements. Also Silvia Rabe for always finding simple solutions for insolvable-seeming conflicts with german bureaucracy.

Thank you Stefan Keil for a lot of help with designing test structures and bonding devices. I am also indebted to Werner Eschenberg for IT support in various situations and Rene Hartmann for bonding various test structures. Andreas Eckert for his profound knowledge and experience in preparing and packaging test devices.

I would also like to mention the important support of many project partners within the last four years: Hamamatsu Photonics KK and especially Yoshitaka Iwaki, Dr. Tomonori Nakamura, Minh Vo, Mike Fels and Mr. Ortner for a lot of help and support with and around Phemos-1000. IMEC Belgium and especially Ingrid De Wolf for providing a lot of knowledge, insights and technical advice for state-of-the-art test devices. IHP Frankfurt/Oder and especially Dr. Andreas Mai for granting free test chip space and continuous supply with new test chips. Philippe Perdu, formerly at CNES France, for several discussions and new insights on the tomography method for PEM. Last but not least Ulrike Kindereit, formerly Qualcomm Inc., for setting up the cooperation project and providing samples and answers to many questions.

Of course I want to mention my family and friends, too, who have helped and supported me in many situations throughout the last 4 years: My mother for her general support and invitations to dinner, my sister for my cute little nieces and my cousin Marcel for many exciting holidays. My friends Flo, Al, Martin, Claudia, Heide, Florian and many more, who weren't mentioned by name. I also want to mention my deer friend Mario, who died shortly before I started my Phd thesis, and whose heartily and poetic words shall not be forgotten. Also my former piano teacher Rainer, who died within the first year of my PhD studies after many, many years of piano lessons with me, which will never be forgotten.

Abstract

This work investigates and improves two common techniques of electronics failure analysis, (spectral) photon emission microscopy (PEM/SPEM) and electro-optical frequency mapping (EOFM). The scientific focus is set on the physical interaction between light and an active semiconductor device. Investigated test structures include 14-40nm FinFETs of several technology generations, as well as planar NAND-like structures, current mirrors, diodes and large area transistors.

The research on photon emission techniques in this thesis contains advances in FinFET failure analysis case studies, emission analysis of analog circuit elements (current mirrors), FinFET device parameter extraction and FinFET reliability assessment with SPEM. Furthermore a whole new 2d-tomography-like method for the enhancement of image quality and for dealing with difficult spectral emission patterns was developed including experimental, mathematical and physical considerations and numerical programming. Finally, all individual results are combined to assess the current status of photon emission techniques and forecast future application possibilities and limits with respect to shrinking device sizes, lower supply voltages and detector equipment.

Regarding electro-optical frequency mapping, the understanding and applicability of the technique towards complex analog devices (current mirrors) was expanded, thereby finding rules of thumb for EOFM signal courses. Similar analysis was performed on digital devices (NAND-like structures) investigating the influence of e.g. multiple devices in one laser spot. EOFM simulations in TCAD Sentaurus and measurements on a pn-junction deeply enlarge the physical knowledge about the laser-device interaction, influence of the spectral laser profile, bulk thickness, temperature, doping levels etc. and the evolution of electro-optical signals in general. These studies were accompanied by the development of a new method for self-heating detection of active semiconductor devices and new failure analysis case studies with EOFM.

Zusammenfassung (abstract in German)

Diese Doktorarbeit befasst sich mit der Erforschung und Weiterentwicklung von zwei physikalischen Fehleranalysemethoden für integrierte Schaltkreise und Einzelbauelemente, der (spektralen) Photon-Emissions-Mikroskopie (PEM/SPEM) und der elektro-optischen Frequenzkartografie (EOFM). Der Fokus liegt dabei auf der Vertiefung des physikalischen Verständnisses der Wechselwirkung von Laser bzw. Licht einerseits und dem aktiven Halbleiterbauelement andererseits. Zu den experimentell untersuchten Strukturen zählen 14-40nm FinFETs verschiedener Hersteller und verschiedener Technologiegenerationen, sowie planare Baulemente z.B. verschiedene Stromspiegel, NAND-ähnliche Strukturen, Dioden und großflächige Transistoren.

Im Rahmen der Untersuchungen zur (spektralen) Photon-Emissions-Mikroskopie wurden neue Fehleranalysefallstudien an modernen FinFET Strukturen durchgeführt und somit das Repertoire dieser Methode erweitert. Außerdem wurde der Anwendungsbereich von spektraler Photon-Emission auf die Parameterextraktion und Zuverlässigkeitsuntersuchung moderner FinFETs erweitert. Die Untersuchung von verschiedenen Stromspiegeln konnte erfolgreich zum Abschluss gebracht und Daumenregeln für die Anwendung von PEM in analogen oder mixed-signal Schaltkreisen gefunden werden. Einen großen Teil stellt ebenfalls die Entwicklung einer neuen 2d-tomographieähnlichen Methode zur Verbesserung des Rausch-Signal-Verhältnisses von PEM und zum besseren Umgang mit komplizierten spektralen Emissionssignalen dar. Diese Methode wurde auf mathematischer, physikalischer und experimenteller Ebene aufwändig entwickelt und anschließend in Scilab programmiert. Als Synthese aus den erwähnten Untersuchungen wurden außerdem der aktuelle Stand und die zukünftigen Anwendungsmöglichkeiten von PEM bezüglich stetig schrumpfender Technologieknotengröße, niedrigerer Betriebsspannungen und neuartiger Emissionsdetektoren analysiert.

Das Verständnis und das Anwendungsgebiet von elektro-optischen Untersuchungen an Halbleiterbauelementen konnte im Rahmen von Untersuchungen an mehreren analogen Bauelementen (Stromspiegel) deutlich erweitert werden. Es wurden zudem Daumenregeln für die in etwa zu erwartenden EOFM-Signalverläufe aufgestellt. Ähnliche Analysen an komplexeren digitalen Strukturen lieferten u.a. neue Erkenntnisse zum gleichzeitigen Einfluss mehrerer aktiver Bauelemente innerhalb des Laserspots auf das elektro-optische Signal. Mittels EOFM Simulationen in TCAD Sentaurus und experimenteller Referenzmessungen an realen pn-Übergängen konnte das physikalische Verständnis der Entstehung elektro-optischer Signale in Abhängigkeit diverser physikalischer Parameter wie spektralem Laserprofil, Substratdicke, Temperatur, Dopinglevel etc. stark erweitert werden. Außerdem konnte eine neue Methode zur Detektion von Selbstheizeffekten von aktiven Bauelementen mit Hilfe von EOFM gefunden und an Beispielen belegt werden. Darüber hinaus wurden neue Fehleranalyse-Fallstudien mittels EOFM analysiert und erfolgreich bestimmten Fehlermechanismen zugeordnet.

Contents

Scientific contributions of the author **iv**

1 Introduction **1**
1.1 Structure of this work . . . 2

2 Theoretical Basics **4**
2.1 Relevant semiconductor devices . . . 4
2.1.1 pn-junction . . . 4
2.1.2 MOSFET . . . 4
2.1.3 FinFET . . . 6
2.1.4 Inverter . . . 6
2.1.5 Ring oscillator . . . 9
2.1.6 NAND . . . 9
2.2 Relevant semiconductor optics . . . 9
2.2.1 Light emission from Silicon . . . 10
2.2.2 Complex refractive index . . . 10
2.2.3 Interference . . . 10
2.2.4 Coherence . . . 11
2.2.5 Numerical aperture . . . 11
2.2.6 Interface optics . . . 11
2.2.7 Free carrier absorption . . . 11
2.2.8 Free carrier refraction . . . 11
2.2.9 Thermo-optic effects . . . 12
2.2.10 Franz-Keldysh-effect . . . 14
2.2.11 Higher optical effects . . . 14

3 Experimental Basics **15**
3.1 Sample preparation . . . 15
3.2 Avoiding ESD damage . . . 16
3.3 Backside analysis . . . 16
3.4 Objective lenses . . . 17
3.5 Use of Solid Immersion Lenses (SILs) . . . 17
3.6 Ensuring reproducable measurement conditions . . . 18
3.7 Electro-optical frequency mapping (EOFM) . . . 20
3.8 Electro-optical probing (EOP) . . . 25
3.9 Photon emission techniques (PEM/SPEM) . . . 25
3.10 Further hints for a successful EOFM/EOP measurement . . . 26
3.11 Further hints for a successful PEM measurement . . . 27
3.12 Further hints for a successful SPEM measurement . . . 27

4 Hardware **28**
4.1 Devices under test . . . 28
4.1.1 120nm devices by Infineon Technologies AG . . . 28
4.1.2 250nm NAND-like structures and current mirrors by IHP Frankfurt/Oder . . . 28

4.1.3 24-40nm FinFETs . . . 28
4.1.4 16/14nm FinFETs by Qualcomm Inc. . . . 28
4.2 Measurement equipment . . . 29

5 Photon Emission Microscopy 30
5.1 General PEM signal observations . . . 30
5.2 InGaAs camera calibration . . . 35
5.3 Extraction of device parameters with SPEM . . . 40
5.3.1 Derivation of most important formulas . . . 41
5.3.2 Device Parameters of 16/14nm FinFETs . . . 43
5.4 Failure analysis with PEM+SPEM . . . 52
5.4.1 40nm n-FinFET . . . 53
5.4.2 24-30nm FinFETs . . . 57
5.4.3 Large 16/14nm n-FinFET from Qualcomm Inc. . . . 65
5.4.4 FA result summary . . . 68
5.5 New tomographical method for SPEM . . . 69
5.5.1 Motivation and idea . . . 69
5.5.2 Theoretical background . . . 74
5.5.3 Experimental background . . . 82
5.5.4 Numerical background . . . 88
5.5.5 Results for C11 ring oscillator . . . 91
5.6 PEM on analog devices . . . 94
5.7 Future of PEM and SPEM . . . 99

6 Electro-Optical Frequency Mapping 105
6.1 General EOFM signal observations . . . 105
6.1.1 EOFM failure analysis examples . . . 110
6.2 EOFM temperature investigations . . . 112
6.2.1 Device self-heating detection . . . 112
6.3 EOFM on analog devices . . . 115
6.4 EOFM on complex digital devices/NANDs . . . 118
6.4.1 big NAND-like structure . . . 119
6.4.2 small NAND-like structure . . . 123
6.5 EOFM on a diode . . . 129
6.5.1 EOFM simulations using TCAD Sentaurus . . . 129
6.5.2 EOFM measurements . . . 145

7 Conclusion and Outlook 147

Appendix 149

A Commented Scilab scripts for tomography 149

B TCAD Diode scripts for EOFM simulations 158

C TCAD MOSFET scripts for EOFM simulations 165

D Acronyms **174**

E Physical constants **175**

References **176**

Relevant scientific publications of the author

1. **I. Vogt**, T. Nakamura and C. Boit: *Optical probing on digital circuit elements (NANDs)*, Proceedings of IEEE 24th International Symposium on the Physical and Failure Analysis of Integrated Circuits (IPFA), IEEE, 2017.

2. **I. Vogt**, T. Nakamura and C. Boit: *Optical interaction in active analog circuit elements*, Microelectronics Reliability 76, p. 233-237, 2017.

3. **I. Vogt**, T. Nakamura, B. Motamedi and C. Boit: *Optical Investigations of Temperature Effects in 14/16 nm FinFETs*, Proceedings of IEEE 43rd International Symposium for Testing and Failure Analysis (ISTFA), IEEE, 2017.

4. **I. Vogt**, A. Glowacki, U. Kerst, P. Perdu, T. Nakamura and C. Boit: *New Method for enhancing Photon Emission Measurements similar to 2d-Tomography*, accepted at IPFA 2018.

5. A. Beyreuther, **I. Vogt**, T. Nakamura, G. G. Fischer, B. Motamedi and C. Boit: *Characterization of bandgap engineering on operative transistor devices by spectral photon emission*, accepted at IPFA 2018.

6. **I. Vogt**, R. Leihkauf, T. Nakamura and C. Boit: *New Laser Voltage Signal Insights from EOFM Simulations and Measurements on different pn-junctions*, accepted at IPFA 2018.

7. **I. Vogt** and C. Boit: *Low Power and Fault Isolation: Spectral Aspects of Photon Emission*, invited paper, IPFA 2018.

8. **I. Vogt**, T. Nakamura, B. Motamedi and C. Boit: *Device Characterization of 16/14nm FinFETs for Reliability Assessment with Infrared Emission Spectra*, accepted at ESREF 2018.

9. **I. Vogt**, T. Nakamura, I. De Wolf and C. Boit: *Detection of Failure Mechanisms in 24-40nm FinFETs with (Spectral) Photon Emission Techniques using InGaAs Camera*, accepted at ESREF 2018.

Relevant presentations at scientific conferences and workshops

1. **I. Vogt**, A. Glowacki, H. Ray, U. Kerst, P. Perdu and C. Boit: *Spectroscopic Photon Emission*, presentation at 7th European Workshop on Photonics Failure Analysis, organized by Hamamatsu KK, Berlin (2014)

2. **I. Vogt**: *Optical interaction with functional elements in digital and analog circuits*, presentation at 8th European Workshop on Photonics Failure Analysis, organized by Hamamatsu KK, Herrsching am Ammersee (2017)

3. **I. Vogt**, T. Nakamura and C. Boit: *Optical probing on digital circuit elements (NANDs)*, IPFA 2017, Chengdu, China (2017)

4. **I. Vogt**, T. Nakamura and C. Boit: *Optical interaction in active analog circuit elements*, ESREF 2017, Bordeaux, France (2017)

5. **I. Vogt**, T. Nakamura, B. Motamedi and C. Boit: *Optical Investigations of Temperature Effects in 14/16 nm FinFETs*, ISTFA 2017, Pasadena, USA (2017)

Student theses supervised by the author at TU Berlin

1. Henning Ray: *Entwicklung eines numerischen Verfahrens zur Örtlichen Rekonstruktion eines Photonemissionsspektrums von elektronischen Bauelementen mittels Tomographie (english translation: Development of a numerical method for the spatial reconstruction of a photon emission spectrum via tomography)*, bachelor thesis, successfully finished (2014)

2. Lillian Ho: *Untersuchungen zum Verhalten der EOFM-Signale großflächiger MOSFETs in Abhängigkeit verschiedener Parameter (english translation: Investigations on the behaviour of EOFM signals of large area MOSFETs with respect to different parameters)*, bachelor thesis, successfully finished (2015)

3. Malte Schmidt: *Auswertung experimenteller Daten von Photon-Emissions-Messungen mit Hilfe eines einfachen theoretischen Modells (english translation: Evaluation of Experimental Data of Photon Emission Experiments Using a Basic Theoretical Model)*, bachelor thesis, successfully finished (2016)

4. Franz Kaiser: *Laseroptische Untersuchungen an Halbleiterbauelementen (english translation: Laser-optical investigations on semiconductor devices)*, bachelor thesis, successfully finished (2016)

5. Anita Saupe: *Analyse von EOFM-Aufnahmen in Bezug auf MOS-Feldeffekttransistoren (english translation: Analysis of EOFM signals of MOSFETs)*, bachelor thesis, successfully finished (2016)

1 Introduction

The topic of this thesis is the physical research on and further improvement of two modern integrated circuit failure analysis techniques: (Spectral) Photon Emission Microscopy (SPEM/PEM) and Electro-Optical Frequency Mapping/Probing (EOFM/EOP). The focus is set on the physical understanding of the light-matter interaction at device level from the point of view of modern semiconductor physics. The application-oriented engineering point of view is of course contained, too.

PEM as a non-invasive technique for electronics failure analysis emerged during the 1980s, when links between hot carrier-induced degradation, substrate/ gate current and the emitted light of the transistor became apparent. Early research therefore concentrated on the concrete emission mechanism and the theoretical physical description of the phenomenon. PEM soon emerged as a very good frontside and backside analysis tool for the detection of currents at high electric fields (e.g. Fowler-Nordheim currents in the gate, current at pinch-off or at resistive paths etc.). From the mid 1990s up to now the research changed more and more towards further failure analysis case studies and new applications such as time-resolved emission (TRE), self-heating detection and more. Beginning in the 2000s, PEM started to loose its pole position as common failure analysis technique due to decreasing device supply voltages and the emergence of electro-optical probing. About 10 to 15 years ago silicon CCD detectors or detectors with similar range were used for photon emission microscopy. In the meantime new deeper-infrared detectors like InGaAs cameras or even Emmi-X/MCT cameras have been developed and are offered commercially. Although spectral emission microscopes were partly available on the market, spectral analysis of devices never became a major trend in device or failure characterizations. This is definitely due to a lack of published failure analysis case studies, carrier energy distributions and device parameter analysis research.

EOFM and EOP (also known under the name LVI and LVP for similar laser techniques) emerged during the 2000s, while first steps towards backside modulated laser probing were already done in 1999 contained in a famous publication at ISTFA'99 by M. Bruce [72]. Other laser-based electronics failure analysis techniques (e.g. OBIRCH, TLS etc.) had already been in use during a ten-year period before. Commercial systems were developed within the 2000s by several companies such as Hamamatsu Photonics KK, DCG systems or Checkpoint Technologies and electro-optical analysis started to emerge as a principal FA tool, thereby slowly overtaking emission based techniques. New features such as visible light probing and constant enhancements brought the electro-optical techniques to the top. As EOFM and EOP are only applicable from the backside of the device, special inverted laser microscope systems were developed for wafer- or die-level testing with probers and needles (e.g. Hamamatsu iPhemos-MP [117]). To offer the user a wide choice of applications, common commercial systems usually contain several different laser sources with varying parameters (different center wavelengths and bandwidths, coherent/incoherent light, different laser powers, pulsed or continuous) [116]. In comparison to emission-based techniques, EOFM and EOP are invasive, which is particularly important for radically thinned substrates or high laser powers and especially for laser photon energies at/higher silicon band-gap energy ($\approx 1,12eV$). A comparison with respect to the general advantages and disadvantages of emission-based and electro-optical techniques can be found in table 1.

Table 1: Comparison main features photon emission vs. electro-optical techniques

Photon Emission Techniques	**Electro-Optical Techniques**
no interference pattern due to incoherent light	complicated interference patterns (at least for coherent light sources)
non-invasive	invasive, especially for $\lambda < 1110nm$(=silicon band-gap)
backside and frontside access (at least with low number of interconnect layers)	only backside access
approx. exponential dependence on supply voltage (challenging for low-voltage devices)	approx. linear dependence on supply voltage (good for low-voltage devices)
dynamic/time-resolved probing / waveform acquisition possible	dynamic/time-resolved probing / waveform acquisition possible

1.1 Structure of this work

This work consists of two main parts: Research related to (Spectral) Photon Emission Microscopy in part 5 and research related to Electro-Optical Frequency Modulation / Probing in part 6. Before these two main chapters information and explanations about theoretical and experimental background of modern semiconductor devices, optics, measurement techniques and equipment are given in sections 2 and 3. Also a short overview of measurement hardware and devices under test used for the experiments is presented in section 4.

The part on photon emission techniques starts with a general introduction into typical physical characteristics, signal slopes and phenomena related to the emission of photons in a MOSFET/FinFET in section 5.1. As many results presented in this thesis include spectral PEM analysis, a comprehensive description and explanation of the InGaAs camera calibration and raw data evaluation procedure is given in section 5.2. SPEM is then used to extract device parameters from modern 16/14nm FinFETs (section 5.3) and to detect failure mechanisms in 24-40nm FinFETs (section 5.4). To expand the applicability of SPEM and to generally improve resolution and signal-to-noise ratio of photon emission techniques, a new 2d-tomography-like method is presented in section 5.5. This is followed by a chapter on the application of PE to analog circuit elements (namely different kinds of current mirrors), which is a current trend (section 5.6). The part on PEM/SPEM is concluded by section 5.7, which gives a prospect on future application possiblities of photon emission techniques based on the findings presented in this thesis.

The second part concerned with electro-optical techniques starts with general explanations of EOFM signal causes and slopes including failure analysis examples (section 6.1). The second section 6.2 is devoted to EOFM signal dependence on temperature and furthermore introduces a new technique to detect self-heating effects. This is followed by a comprehensive analysis of EOFM to analog circuit elements (different current mirror types) to draw general conclusions on the applicability of electro-optical techniques to analog/mixed-signal circuits (section 6.3). To expand knowledge of electro-optical signals for complex digital structures, an analysis of different small and large NAND-like structures is presented in section 6.4. The end of the electro-optical part consists of detailed physical simulations on a pn-structure particularly investigating the effect of multi-layer-

interference, different physical device parameters and spectral laser profile (section 6.5). In order to confirm the results the simulation data is accompanied by measurements on a real diode.

A final conclusion on major new findings of this thesis, as well as a prospect on sensible future research activities and developments is presented in 7. The appendix contains all TCAD Sentaurus and Scilab scripts, which were used for the 2d-tomography method and the EOFM simulations on a diode. Scientific literature and references related to the aforementioned topics can be found at the very end of this thesis.

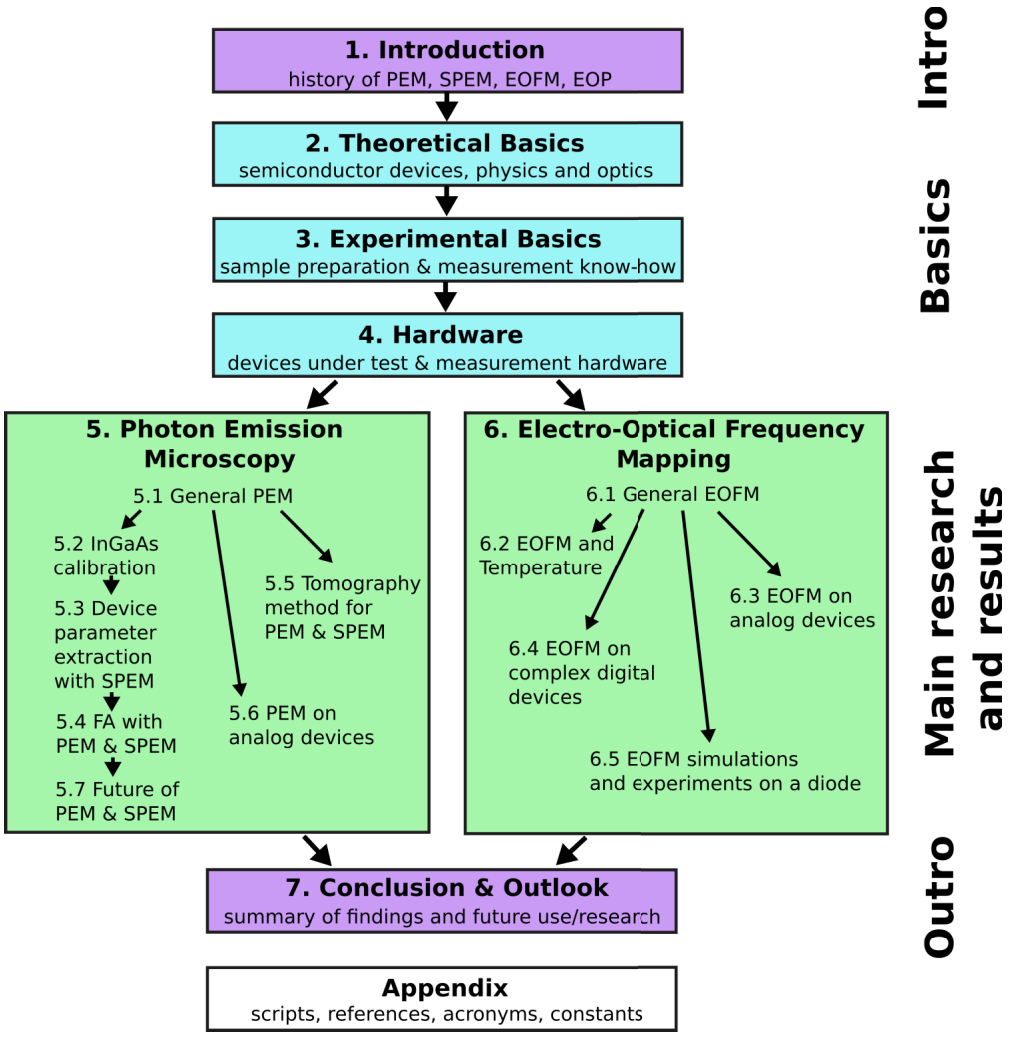

Figure 1: Structure of this PhD thesis.

For any questions arising from topics and results presented in this thesis feel invited to **contact the author** via **ivo.vogt@tu-berlin.de** or via internet research, if the email address is at that point in time no longer active.

2 Theoretical Basics

This section gives the reader an overview of the most common physical features and functionality aspects, which are important for understanding later contents of this work. It therefore consists of two parts: The first part, subsection 2.1, is about elementary semiconductor devices used as devices under test in this thesis (pn-junction, MOSFET, FinFET, inverter, ring oscillator, NAND). The second part, subsection 2.2, comprises basic knowledge about semiconductor optics and relevant physical effects (free carrier absorption, interference, refraction, coherence etc.) with respect to photon emission microscopy (PEM) and electro-optical frequency mapping (EOFM).

However, this section is not supposed to replace common semiconductor books and give analysis and explanation on every detail. These can be found in many books, lectures or scripts on semiconductor physics, semiconductor devices and optics available at every university library and also most public libraries. A very good recommendation is *Basic Semiconductor Physics* by Chihiro Hamaguchi [115], because it skillfully unites physical and engineering perspectives towards the aforementioned topics.

2.1 Relevant semiconductor devices

2.1.1 pn-junction

A pn-junction is the interface of a p-doped and a n-doped semiconductor. Due to diffusion the majority carriers of either side are drawn towards the other side of the junction (e.g. majority electrons from the n-doped side diffuse across the junction to the p-side) and recombine with a charge carrier of opposite type. The diffusion process builds up an area of space charge at either side of the junction, which is almost depleted of free charge carriers. This region is called *space-charge region* or *depletion region*. The electric field of the space charges compensates the effect of diffusion so that a stable equilibrium state is reached. The situation can be seen in figure 2. The voltage between neutral p-doped and neutral n-doped areas is called *built-in voltage*. A pn-junction with additional electrical contacts at each side is usually called *diode*, whereas originally the term diode only referred to an electric device, which is capable of transmitting current unhinderedly in one direction and isolating in the other.

If an additional voltage between both areas is supplied from the outside, two cases can be discriminated: If the outer voltage has the same polarity as the in-built voltage (*reverse bias*), the space charge region width is increased until breakthrough. If the outer voltage has the opposite polarity as the in-built voltage (*forward bias*), the space charge region width is decreased until disappearance. Even higher forward bias causes a flooding of charge carriers into the opposite side with high recombination (*high injection*). Forward bias is used in *light-emitting diodes* (LED) or *laser diodes* (LD).

2.1.2 MOSFET

A planar *metal-oxide-semiconductor field-effect transistor* (MOSFET) is the most common semiconductor device of integrated circuits (ICs). Examples of logic gates of modern ICs, which are built of (multiple) MOSFETs (or FinFETs), can be seen in sections 2.1.4 and 2.1.6. A MOSFET basically consists of three different contacts: source, gate and drain. Source and drain are realized

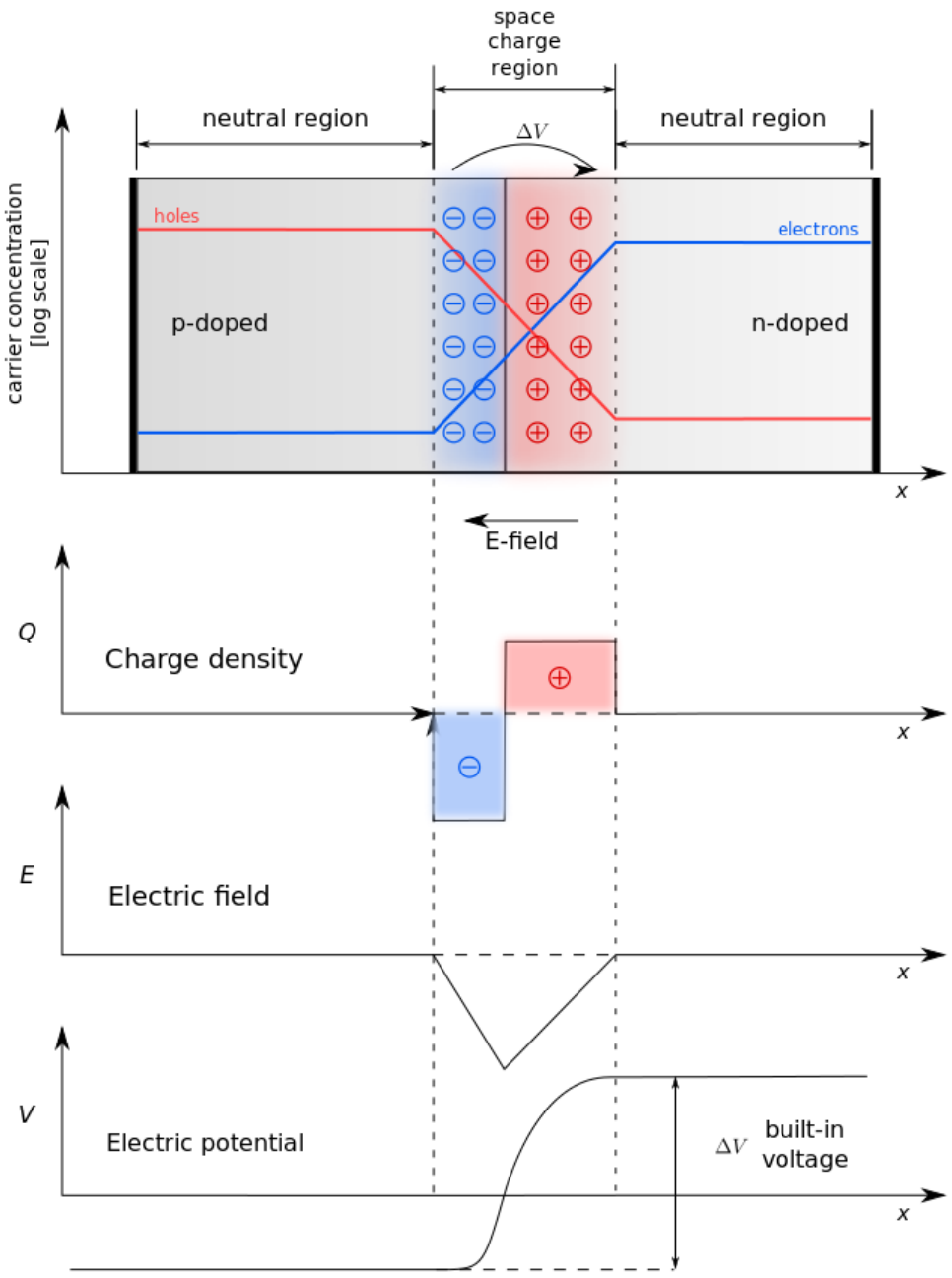

Figure 2: Carrier distribution, electric field, voltage and space charge illustrated for a simple pn-junction. Image taken from [119].

via diffusions and represent the beginning (source) and the end (drain) of the transistors' current path. The crucial feature of a MOSFET is the ability to enable or disable current flow between source and drain only with gate voltage. In integrated circuits only two voltage states are allowed: low level (V_{ss}) and high level (V_{dd}). The switching of a transistor is thus realized by a change of drain voltage from V_{ss} to V_{dd} or vice versa. To load/unload the capacity associated with drain a current flow from source to drain is necessary. The basic principle of the MOSFET/FinFET switching process made visible in the FETs' output characteristics can be found in figure 23 of section 3.7.

The current flow from source to drain is realized by a channel below the gate area, which can be build up with gate voltage. For a n-MOSFET the substrate is p-doped, so that a positive gate voltage collects electrons (minority carriers) from the substrate. Once strong inversion is reached, a few-nanometers-wide channel of electrons has built up directly below the gate, separated from the substrate via a space charge region / depletion region. In this situation the current path (channel) between source and drain is open and protected from the substrate via the depletion region. The minimum gate voltage needed to reach strong inversion and build up the channel is called *threshold voltage* V_{th}. Depending on the exact voltage conditions of a MOSFET, three different operating modes can be discriminated (also see figures 3 and 4):

Off-state. In off-state, the gate voltage is not high enough to build up a channel between source and drain ($V_g < V_{th}$). The current path between source and drain is closed.

Linear operating region (also: Ohmic mode). In ohmic mode gate voltage is high enough to build up a channel ($V_g > V_{th}$), but the drain voltage is relatively low ($V_d < V_g - V_{th}$). The source-to-drain current increases rapidly, initially with an almost linear, ohmic I-V-curve.

Saturation mode. In saturation mode gate voltage is high enough to build up a channel ($V_g > V_{th}$) and the drain voltage V_d is higher than ($V_g - V_{th}$). This leads to a pinch-off of the channel at some specific point under the gate. The source-to-drain current saturates to an almost constant value over drain voltage, which is a typical characteristic of a MOSFET/FinFET in saturation.

2.1.3 FinFET

A FinFET is very similar to a MOSFET except for a different design (three-dimensional fin/gate contact) of the gate area, which can be seen in figure 5. This design allows for faster switching processes as the channel can be built up from multiple sides at the same time. The 3d-FinFET technology, also in combination with *silicon on insulator* (SOI)-design, decreases switching times noticeably in state-of-the-art integrated circuits.

2.1.4 Inverter

An inverter is a common logic gate within integrated circuits, which gives the inverted input value as its output. The respective truth table can be seen in table 2. A possible inverter design in CMOS technology can be seen in figure 6.

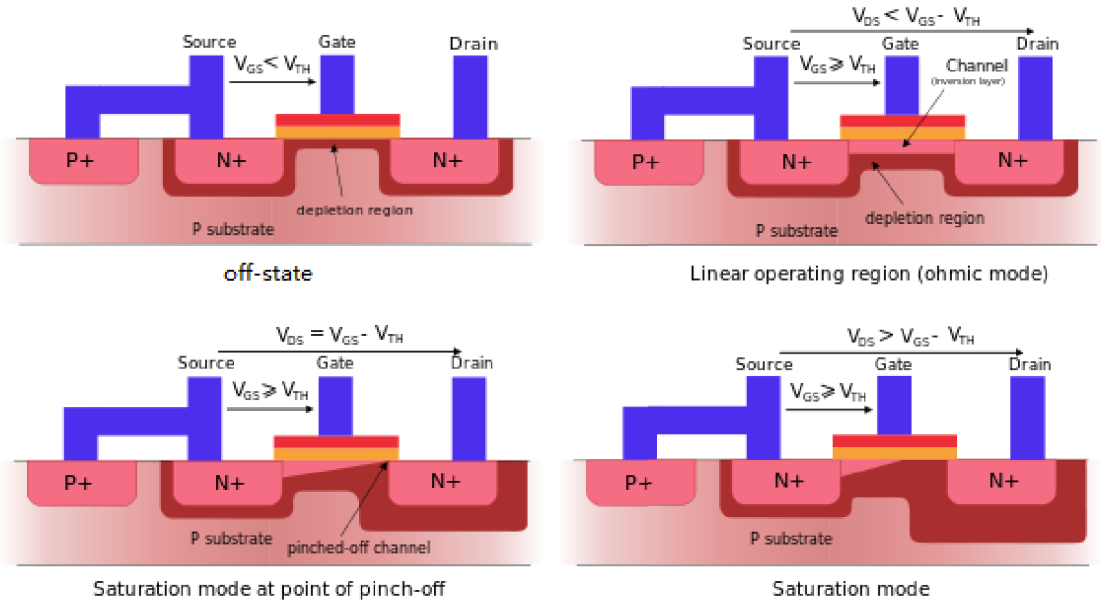

Figure 3: Different operating conditions of a planar n-MOSFET. Image taken from [120].

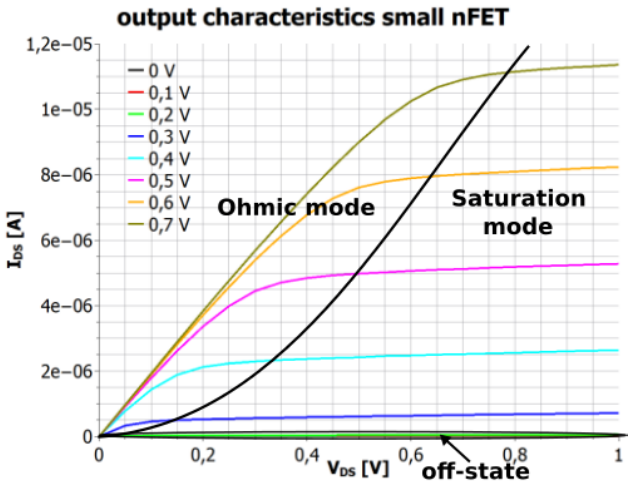

Figure 4: Typical output characteristics of a modern n-MOSFET / FinFET for different gate voltages between 0 and 0.7V with the three different operating modes indicated in black.

Table 2: Inverter truth table

input A	output Q
0	1
1	0

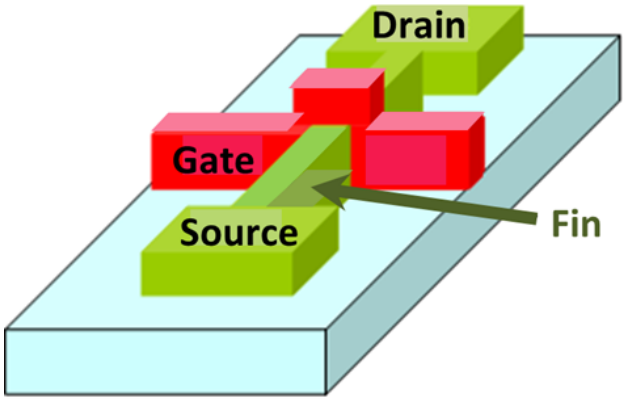

Figure 5: Picture illustrating the 3d fin-architecture of a FinFET. The fin connects source and drain and is surrounded by gate from multiple sides. Image taken from [121].

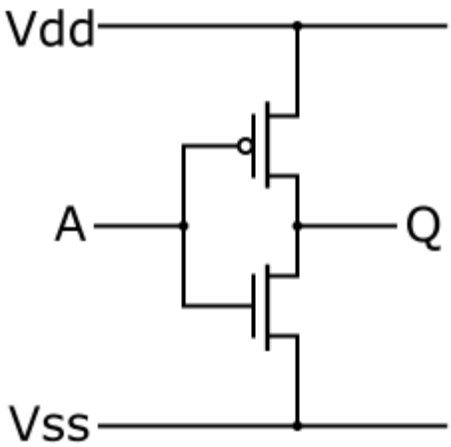

Figure 6: Schematic of a logic inverter in CMOS technology. Image taken from [122].

2.1.5 Ring oscillator

A ring oscillator consists of a chain of inverters, where the output of the previous inverter is connected to the input of the next inverter. The output of the last inverter of the chain is again connected to the input of inverter one, which leads to a closed loop. Due to this fact only uneven numbers of inverters in the chain are possible. The ring oscillator then has an output frequency f of

$$f = \frac{1}{2 \cdot \text{individual inverter delay} \cdot \text{number of inverters}} \quad . \tag{2.1}$$

As plain ring oscillators are running spontaneously / uncontrolled once the power supply is on, ring oscillators in integrated circuits usually contain a start/stop switch e.g. realized by a NAND-gate or similar. The oscillation frequency can be divided by respective additional stages until the needed frequency for the specific purpose is reached.

2.1.6 NAND

A NAND is a common logic gate within integrated circuits, which determines, if both inputs are on high level (V_{dd}) or not. The respective truth table can be seen in table 3. A possible NAND design in CMOS technology can be seen in figure 7.

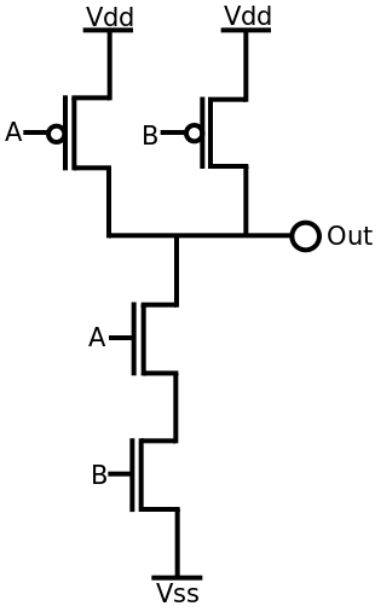

Figure 7: Schematic of a logic NAND-gate in CMOS technology. Image taken from [123].

2.2 Relevant semiconductor optics

This section is designed to give the reader a brief overview of the main optical effects and properties, which are relevant for later contents of this thesis. Very good summaries with similar focus can also be found in [101, 103].

Table 3: NAND truth table

input A	input B	output Out
0	0	1
0	1	1
1	0	1
1	1	0

2.2.1 Light emission from Silicon

Light emission from conventional silicon as an indirect semiconductor is very weak, because of the low probability of inter-band processes due to the mismatch of valence band maximum and conduction band minimum in the first Brillouin zone. Therefore, plain silicon is not used as a material for light-emitting diodes (LEDs). However, LEDs with silicon material exist, but with specific other materials as dopants, which act as scattering centers for the emission of light.

The light emission processes discussed in this thesis (photon emission / PE) are not due to statistical thermal generation and later recombination of electron-hole pairs within the silicon as above. The photon emission processes of this thesis are induced by carrier acceleration in external electric fields and occur, when accelerated charge carriers loose their energy in different scattering processes. These processes happen at the channel-to-drain junction and close to the gate dielectric of a MOSFET/FinFET or at parasitic current paths through the substrate or other high-ohmic paths. The regular photon emission of FETs under normal operating conditions forms the basis of later sections 5.1 to 5.6. Photon emission from parasitic current sources can be found in section 5.4.1.

2.2.2 Complex refractive index

Both first-order effects (absorption and refraction) of the light-matter interaction in materials can be modeled mathematically using the complex refractive index

$$\tilde{n} = n + i\kappa \qquad . \tag{2.2}$$

The real part n is also called "refractive index" and is used to describe the change of the speed of light when light enters into the medium. It can also be used to describe the angle of refraction at interfaces of different media (e.g. *Sneel's law*, *Fresnel equations*). The imaginary part κ is called "extinction coefficient" and is directly proportional to the absorption coefficient of a medium (*Beer-Lambert law*). The propagation of light within a medium can be calculated using the complex refractive index, which will be used in the transfer matrix model applied for the EOFM simulations with TCAD Sentaurus in section 6.5.

2.2.3 Interference

Optical interference refers to the (partly) destructive or constructive superposition of two or more light beams/waves. Depending on phase and amplitude of the involved individual waves, complicated interference patterns can emerge.

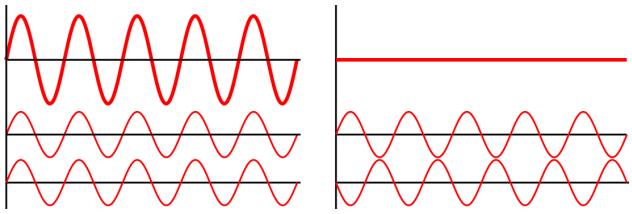

Figure 8: Constructive (left) and destructive (right) interference of two light waves. Image taken from [124].

2.2.4 Coherence

The coherence length of a bundle of light waves is defined as the spatial interval, within which two waves do not differ more than a given constant value in phase or frequency. Therefore, coherence is a crucial parameter for interference of different light waves, which have partly different optical paths (e.g. via reflection at different interfaces of a device).

2.2.5 Numerical aperture

The numerical aperture (NA) is a parameter related to an optical systems ability to focus light. The NA is a dimensionless number that characterizes the range of angles under which an optical system can emit or accept light and is given via

$$NA = n \cdot \sin(\theta) \tag{2.3}$$

with the opening angle θ of the objective and the refractive index n of the medium, in which the lens is working.

2.2.6 Interface optics

Optical transition between different media of different refractive indices and different angles of incidence is decribed by *Fresnels formula*, which allow for the calculation of transmission, reflection and absorption coefficients of a specific interface. The large set of formula with precise derivation and explanation can be found in every optics textbook and will therefore not be given here.

2.2.7 Free carrier absorption

Absorption changes induced by free carriers within silicon can be seen as a major signal cause for EOFM/EOP signals obtained on different structures later in this thesis. Especially the emergence and disappearance of the FET channel with pulse voltage and cycle results in vast EOFM signals, which usually dominate the voltage range above threshold voltage. The influence of free electron absorption on the absorption coefficient in silicon for various doping levels can be seen in figure 9. More information can be found in [112].

2.2.8 Free carrier refraction

Refractive index changes induced by free carriers can be seen as a major signal cause for EOFM/EOP signals obtained on different structures later in this thesis. The influence of free electron refraction

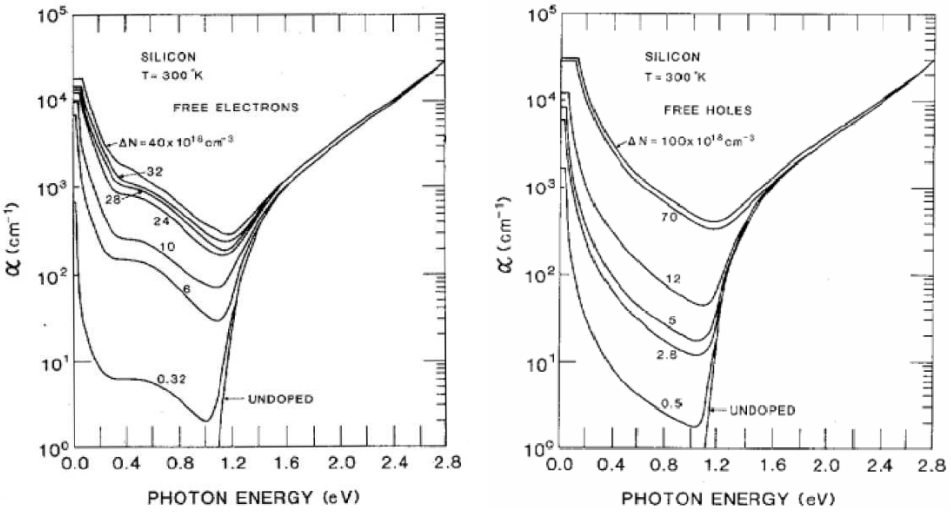

Figure 9: Absorption coefficient change induced by free electrons (left) and free holes (right) in silicon for different doping concentrations. Images taken from [112].

on the absorption coefficient in silicon for various doping levels can be seen in figures 10 and 11. More information can be found in [112].

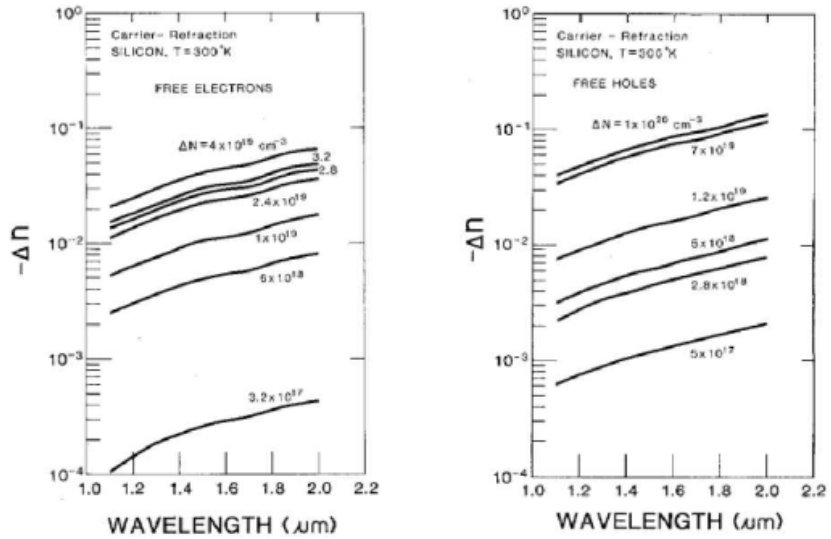

Figure 10: Refractive index change induced by free electrons (left) and free holes (right) in silicon for different doping concentrations. Images taken from [112].

2.2.9 Thermo-optic effects

Temperature has an important effect on both absorption and refraction of light within silicon. While the influence of temperature on absorption can be modeled indirectly via temperature-induced changes in the free carrier concentration, the influence of temperature on refraction is given via the

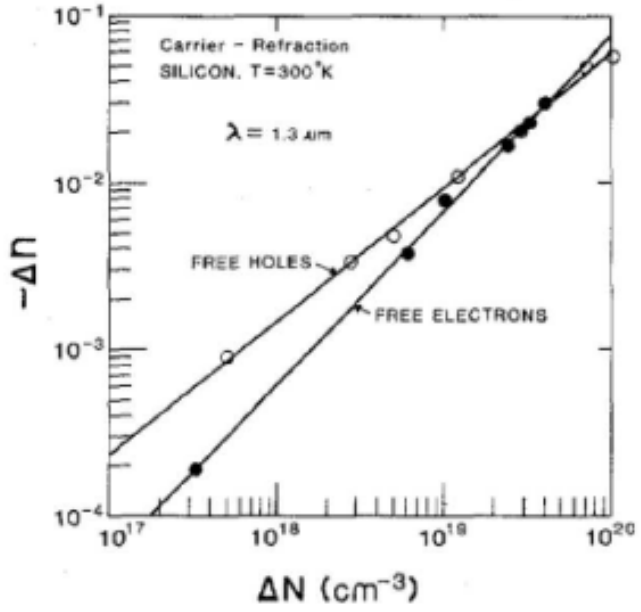

Figure 11: Refractive index change induced by free electrons and free holes in silicon over doping concentration for a wavelength of $\lambda = 1,3\mu m$. Image taken from [112].

thermo-optical coefficient $\Delta n/\Delta T$. Measurement data concerning the thermo-optical coefficient in silicon can be seen in figure 12. The EOFM signals due to global bulk temperature variations or local heating of a metal line or a single transistor can be considered as of order 10-1000 ppm.

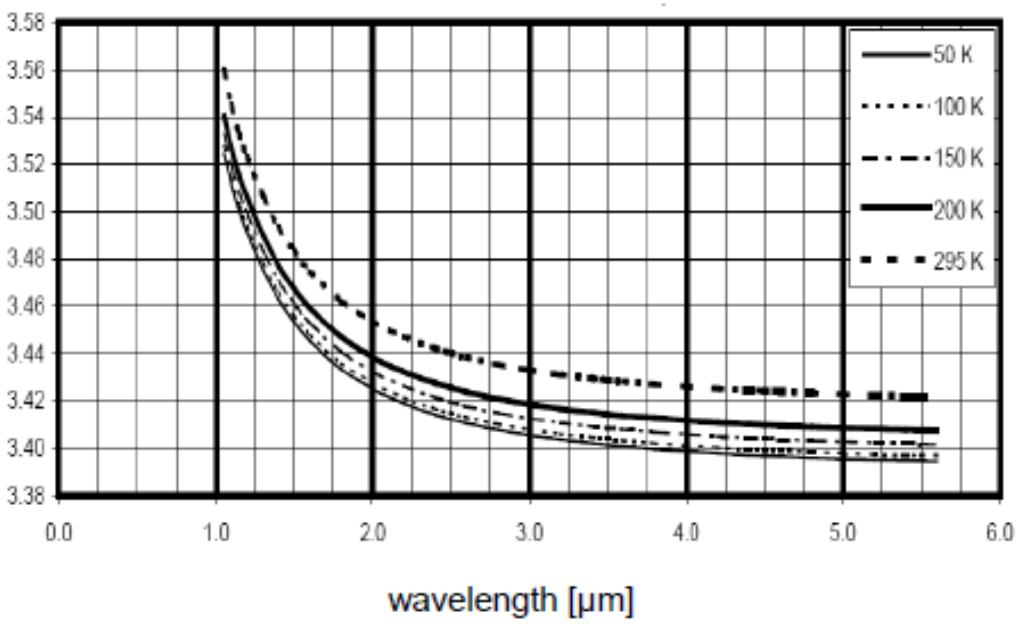

Figure 12: Refractive index of silicon over wavelength for different bulk temperatures. Image taken from [113].

2.2.10 Franz-Keldysh-effect

The Franz-Keldysh effect (FKE) refers to a light absorption phenomenon in semiconductors in the presence of high-electric fields [108, 110, 111]. The additional electric field causes slight fluctuations of the absorption coefficient near the band-gap, even leading to a small lowering of the band-gap (fig. 13). As the influence is relatively small, this effect is less relevant for photon emission results presented later in this thesis. However, for electro-optical techniques especially with light sources with center wavelengths roughly at silicon band-gap this effect can be the cause for major signal influences, as electro-optical signals usually lie in a low range of only 1-1000 ppm. As only light sources with center wavelengths above 1300nm were used for the electro-optical measurements of this thesis, the Franz-Keldysh effect was neglectable here.

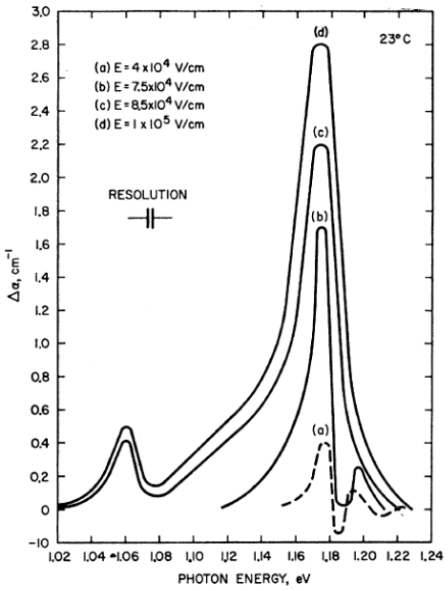

Figure 13: Electro-absorption spectrum of silicon for external electric fields ranging from $4*\cdot 10^4 V/cm$ to $1*\cdot 10^5 V/cm$. Image taken from [109].

2.2.11 Higher optical effects

Simple absorption and refraction are just first-order effects of the light-matter interaction in semiconductors or other solid-state materials. Higher orders of the relation between light intensity and optical response of the atoms within the material include effects like electro-refraction, Kerr- and Pockels-effects, two-photon absorption, self-phase-modulation, soliton formation, cross-phase modulation, four-wave-mixing and many more. Their presence in measurements cannot be excluded, but is estimated to have a much smaller effect than the changes induced by free carriers (subsection 2.2.7 above).

3 Experimental Basics

3.1 Sample preparation

Depending on the state of the test chip (wafer-level, die-level, package etc.) and intended analysis (EOFM, PEM etc.) different sample preparation procedures have to be carried out. If a simple analysis using manipulators with probing needles is planned, further steps may not be necessary. But even simple photon emission frontside measurements can suffer strongly even from very thin but non-transparent passivation layers. In this case it may be useful to remove the layer with a special focused ion beam (FIB) etching procedure.

If backside analysis is intended, several sample preparation steps have to be carried out: The wafer-level test structures have to be diced first. For most preparations of chips used in this thesis a double-sided cellotape was used to attach the chip to the package. The cellotape is usually used for the coils of electromagnetic transformers. The double-sided cellotape was thicker than normal cellotape so that enough stability for the fast ultrasonic bonding procedure was guaranteed and it was certified for temperatures up to $200°C$, which is particularly important for using a temperature hardening procedure of the moulding material below. Usually the package was opened before attaching the chip with the tape to have direct access to the chip backside after bonding and moulding.

Once the chip is glued into the package, the internal connection pads on the chip have to be bonded to the external pads of the package. Moulding the freshly bonded chip within the package with a specific filling material is compulsory to protect the thin bond-wires. The moulding material usually has to harden for a certain period of time or using a special procedure like hardening with ultraviolet light. The moulding material must be chosen individually: If the material is too rigid, it does not fill all small spaces between bond-wires and chip properly. If the material is too flexible, it is not strong enough to protect the bond-wires against vibrations and pressure especially during the backside thinning procedure. For most chip preparations within this thesis moulding materials from *Panacol-Elosol GmbH* were used. The company provides comprehensive data-sheets for all materials on their website and also specific detailed consulting for each case.

Moulding materials *Vitralit 1605* and *Vitralit 1650* are both UV-hardening within minutes with the exact time depending on thickness and shadowing of specific parts. In comparison to *Vitralit 1605*, *Vitralit 1650* has an additional filling material to give a better degree of shrinkage: It has to be taken account that the moulding material may change the cristalline structure of the underlying silicon within the chip by deflection, which may cause electric alterations especially after backside thinning (which leads to increasing deflection within the bulk silicon). If a temperature hardening procedure is used (e.g. for *Structalit 5893*, which was occasionally used for bond-wire protection and has a lower rigidity compared to the two Vitralit types) it is important to cool chip and package to avoid damage, at least when the temperature hardening takes more than some minutes. Temperature hardening was also used for UV-hardening materials when parts of the material were shaded or the moulding material thickness was too high. For backside preparation the rigidity of the moulding material is crucial: The higher the rigidity the better for the backside thinning. For complicated cases of moulding within difficult packages TU collaborated with Volker Bader from Fraunhofer IZM institute, Berlin.

Once the packaging and moulding is finished, backside thinning can start. First, the material used to glue the chip into the package (e.g. the double-sided cellotape) has to be removed at the chip backside to have free access. Then professional milling equipment can be used to slowly remove the bulk silicon until the targeted remaining thickness is reached. It is important to measure the remaining thickness from time to time during milling procedure. For standard backside laser investigations with light sources >1200nm remaining bulk thicknesses of 50-500 μm or even more are sufficient. For investigation of emitted light with wavelengths lower than $1200nm$ extensive thinning down to only few μm remaining thickness are necessary [63, 66]. The same holds true for laser investigations with visible light sources [83, 84]. After thinning, a backside polishing step is required to reduce interference effects due to varying thickness. The polishing is also essential for use of solid immersion lenses, which require direct contact to the even backside of the device.

3.2 Avoiding ESD damage

Most modern microelectronic devices are easily damageable by electrostatic discharge (ESD). For low-voltage devices with nominal voltages below 1V even relatively small voltage changes of 1-2V for some microseconds can already destroy the whole device. This holds true especially for the very thin gate dielectric and the pn-junctions / doping profiles in vicinity of source or drain diffusions. Usually commercial chips are manufactured with internal ESD protection structures like diodes. Most test chips however contain completely unprotected structures and therefore have to be treated with the utmost care.

Therefore it is essential to conform to standard ESD protection means like usage of ESD-bracelets or wearing ESD-protection shoes together with conducting floor material or special ESD-matts. The devices should be stored in special ESD-protection boxes and materials. ESD-damage can also be induced through seemingly unsuspicious sources: Switching on/off the light, relay-switching induced by opening the Phemos-1000 door or starting of cooling procedure of the cooler for CCD or InGaAs camera were all found to induce short-term ($1 - 20\mu s$) voltage fluctuations of 1-10(!)V, especially for measurements with manipulators and probing needles as the open metal of the needles is an almost perfect antenna for electro-magnetic induction. But also packaged devices inserted into socket boards are sensitive and easily destroyed. Furthermore, active measurement hardware like Phemos-1000, parameter analyzer, waveform generators etc. should never be switched on or off while the device is connected.

To ensure that no parasitic electro-magnetic fields / ESD sources are present during a measurement, an oscilloscope can be connected parallel to gate or other connections. The trigger mode can then be used to detect any unwanted voltage fluctuations above a certain level and their respective pulse length. This methodology also serves well to determine the influence of single suspected ESD sources, when switching on/off the suspected ESD source.

3.3 Backside analysis

The investigation of light emission and other FA techniques through the frontside of a chip has continuously become more and more difficult with the increase of metallization levels above the active integrated circuits and use of flip-chip packages. Reflection and absorption by these metal layers make the frontside investigation of integrated circuits in recent technologies with up to 15

metallization levels almost impossible. Furthermore, the flip-chip technology does not give direct access to the chip frontside.

Therefore, the investigation of emitted light (PEM) and modulated light (EOFM/EOP) via backside analysis has become the dominant technique over the last 10-20 years. To gain access through the backside bulk silicon of a semiconductor chip, it is often necessary to partially remove the package material. Subsequently, the thinning of the backside silicon down to thicknesses of some $100\mu m$ to even only few μm is necessary, due to absorption losses in the bulk silicon. The actual thickness required to carry out the measurement depends highly on the wavelength of the light source (EOFM/EOP) or the spectral range of the emission detector (PEM). To obtain accurate photon emission spectra the absorption coefficient for each wavelength has to be taken into account for data correction. While correction for wavelengths above 1200nm is almost unnecessary due to very weak absorption, it is absolutely essential for smaller wavelengths, especially below the silicon band-gap at roughly 1110nm. The absorption coefficient of silicon over a wide wavelength-range and the absorption-correction formula derived from Beer-Lambert law are shown in section 5.2 of this thesis.

3.4 Objective lenses

Different objective lenses were used for the optical inspection of different semiconductor devices presented in this thesis. Important parameters and comparison of the objective lenses is presented in table 4. The laser spot diameter D is given by

$$D = \frac{1,22\lambda}{2NA} \tag{3.1}$$

with numerical aperture NA of the objective lens and light wavelength λ.

Table 4: Objective lenses used with Phemos-1000

	5x lens	20x lens	50x lens	100x lens	50x lens with Nanolens (SIL)
NA	0,14	0,40	0,76	0,50	2,66
magnification	5x	20x	50x	100x	175x
laser spot diameter in focus for 1300nm wavelength	$5,7\mu m$	$2\mu m$	$1\mu m$	$1,6\mu m$	$0,3\mu m$

3.5 Use of Solid Immersion Lenses (SILs)

Solid Immersion Lenses (SILs) for optical resolution and signal improvement exist in different forms e.g. as diffractive and refractive SILs. Also liquid immersion lenses with oil immersions or similar between lens objective and device under test are in use. A comprehensive presentation and analysis

of different immersion lens types and SIL-creation with *Focused Ion Beam* (FIB) can be found in the PhD thesis of P. Scholz [114], which was published at Technical University Berlin in 2012. The Nanolens (SIL from Hamamatsu Photonics KK, Japan) used for certain experiments within this thesis is a planar, refractive solid immersion lens made of silicon and optimized for remaining bulk thicknesses between $20\mu m$ and $120\mu m$. The Nanolens' surface, which is contacting the backside of the device, has a diameter of $1,1mm$ while the optical path for light to pass through the SIL from frontside interface to backside interface is $3,5mm$, which is especially important for the absorption correction of section 5.2. The Nanolens has an additional surface coating, which causes slight alterations in optical transmission and reflection.

The basic operating principle of a SIL can be seen in figures 14 and 15: Without SIL on the backside of the device under test reflected light beams are refracted away from the optical axis due to the high difference of refractive index of air ($n_{air} \approx 1$) and silicon ($n_{silicon} \approx 3,5$). Thus a lot of light and intensity is lost due to refraction. If a SIL is applied to the backside, most light beams do not get refracted away from the optical axis but are transmitted at the SIL/air-interface without change of propagation angle and can enter the objective. Therefore, much more light from the device is collected with SIL than without SIL. A further advantage is that the coefficients of transmission and reflection at the interface are much more favorable with SIL leading to a further signal improvement. Both for PEM and EOFM signal-to-noise ratio increases of roughly a factor of 10 were confirmed within this thesis (see sections 5.1 and 6). An improvement factor for the optical resolution given by $n_{silicon}/n_{air}$ and an accordingly smaller laser spot size (see table 4) also belong to a SILs features.

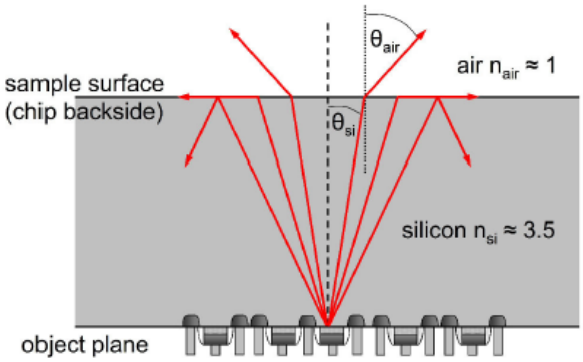

Figure 14: Refraction of light beams at the silicon-air surface without solid immersion lens (SIL). Image taken from [114].

Last but not least SILs are subject to attrition due to frequent use and have to be exchanged every few years. A laser image of TU Berlin's Nanolens after several months of usage can be seen in figure 16, showing small irregularities and scratches on the SILs' surface. Those irregularities were not of great harm to the measurements and hardly influenced image quality, but get worse with time, of course.

3.6 Ensuring reproducable measurement conditions

Before and after each optical measurement series the electrical functionality of the device under test should be controlled via checking e.g. the output/input characteristics of the transistor, the logic

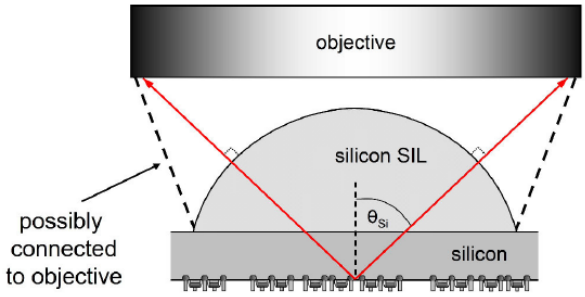

Figure 15: Transmission of light beams at the silicon-air surface due to SIL use. Image taken from [114].

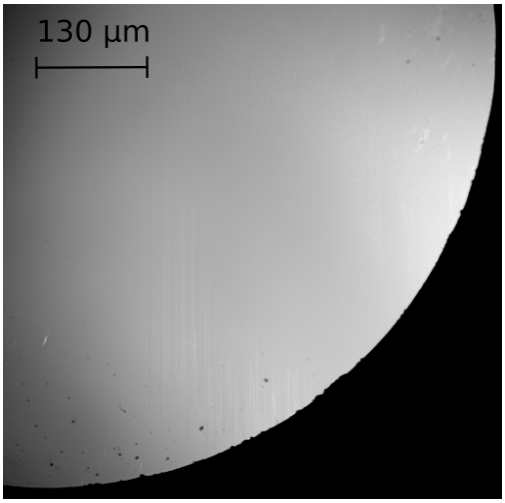

Figure 16: The image shows a quarter of the Nanolens surface used for several optical experiments within this thesis. Scratches and small irregularities at the SIL edge are due to attrition.

function of inverter or NAND or the current amplification/reproduction curve of a current mirror. It is also important to ensure that all connections in the relevant area are grounded or set to a defined voltage to avoid random behavior by floating contacts. The chuck and all measurement hardware should also be grounded to the same ground level via cable connections. With several ground connections it must be taken care too avoid ground loops. All grounds should be connected from one central ground reference and not all in a row to avoid electro-magnetic induction phenomena.

For measurements on small technologies and devices and especially when using Nanolens (SIL) any thermal drift or vibration in the building (closing a door, walking etc.) can have serious influence on measurement results. It is therefore recommended to do sensitive measurements at times, when the building is less occupied and there is no or at least less traffic or other people around. Thermal drift, which can easily make up several μm per quarter of an hour if not taken care of, can be reduced by switching on all measurement hardware a day before measurement. Air condition (temperature and humidity) should also be supplied. Great care should also be taken about air draft when opening doors, windows or under thresholds.

3.7 Electro-optical frequency mapping (EOFM)

Electro-Optical Frequency Mapping (EOFM), also known under the name of the similar Laser Voltage Imaging (LVI) technique, is a dynamic optical technique for failure analysis of integrated circuits. A periodic electrical pulse is fed into the relevant part of the circuit and at the same time a continuous laser beam is focused onto the region of interest through the backside of the device. The laser light is modulated by absorption and refraction due to light-matter interaction at device level. Relevant physical effects, which cause such light modulations in active integrated circuit elements, are free carrier absorption, free carrier refraction, thermorefraction, Franz-Keldysh-effect and several other minor effects. Details and explanation on these physical effects can be found in previous sections 2.2.7 to 2.2.11. The modulated beam mostly becomes reflected directly above the device by the first metallization layer, poly-silicon layer or similar. The reflected light propagates back to the backside of the device and through the optics onto the detector, where the reflected light intensity is measured. Common detectors are fast photo-diodes or similar with suitable detection sensitivity. A schematic image of the EOFM setup can be seen in figure 17. In order to investigate a large region with one measurement the laser beam is scanned along the image of 1024×1024 pixels.

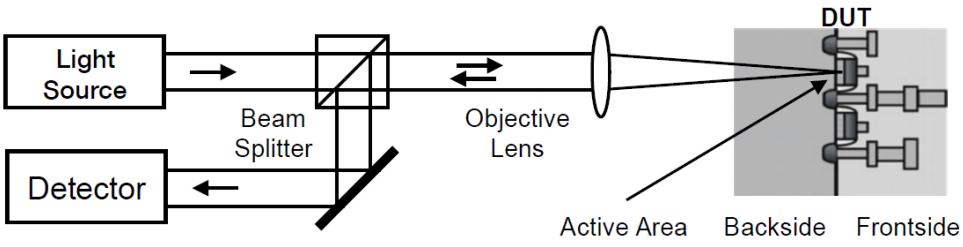

Figure 17: Basic EOFM setup. Image taken from [107].

Frontside inspection with EOFM is usually not possible because of high reflection and absorption of

the laser light within the metallization levels before reaching the device. Furthermore, the reflection interface must be as close to the laser focus as possible to avoid distortion of the reflected beam when passing the optics (objective lens, tube lens, mirrors etc.) back to the detector. This is not the case for frontside inspection: Even if light passes through all frontside layers and is focused on the active device, the reflection will mostly take place at the backside of the device, which is several μm up to $> 500\mu m$ away.

The big advantage of dynamic measurement over static measurement is that the pulse frequency can be used to separate the modulated signal from general noise using a lock-in amplifier or frequency analyzer. The amount of modulations in the reflected light beam is usually of an order of $1 - 1000ppm$, which would inevitably vanish within noise level for static measurement. The reason for dynamic photon emission measurements (TRE, PICA) is exactly the same. The extraction of the EOFM-signal from the reflected modulated laser beam will be explained in detail within the next passage.

The reflected light beam is detected by the sensor at the end of the optical path and converted into an electrical signal, which is fed into the frequency analyzer or lock-in amplifier. Here the signal parts at pulse frequency are amplified. To obtain the EOFM signal, a projection/integration of the modulated and amplified light beam part at pulse frequency f has to be carried out by the frequency analyzer or lock-in amplifier. Mathematically speaking, the projection on sine and cosine function can be expressed as an integration over a high number N of pulse periods (depending on scan time per pixel):

$$X_{EOFM} = c \cdot \frac{2}{N \cdot T} \int_0^{N \cdot T} x(t) \cdot \sin(2\pi f t + \phi) dt \tag{3.2}$$

and

$$Y_{EOFM} = c \cdot \frac{2}{N \cdot T} \int_0^{N \cdot T} x(t) \cdot \cos(2\pi f t + \phi) dt \tag{3.3}$$

with an arbitrary constant c, the modulated + amplified signal $x(t)$ and a constant phase shift ϕ. The high number of integration pulse periods is needed to improve the accuracy statistically. X_{EOFM} and Y_{EOFM} form the first order Fourier coefficients of the modulated signal. Higher harmonics can also be taken into account for signal extraction. Depending on its specific shape, the light modulation can take different positive and negative X_{EOFM}- and Y_{EOFM}-values. Even situations, where one of the components takes a high value and the other is almost zero can occur. Such a situation is illustrated in figures 18 to 20, which show two different modulated signals and their respective projections.
From the first order even and uneven Fourier coefficients of the modulated signal the EOFM amplitude R_{EOFM} can be calculated via

$$R_{EOFM} = \sqrt{X_{EOFM}^2 + Y_{EOFM}^2} \quad . \tag{3.4}$$

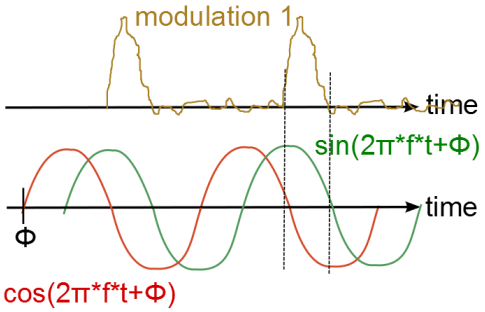

Figure 18: Image showing the periodically modulated part of an arbitrary light beam no.1 over time.

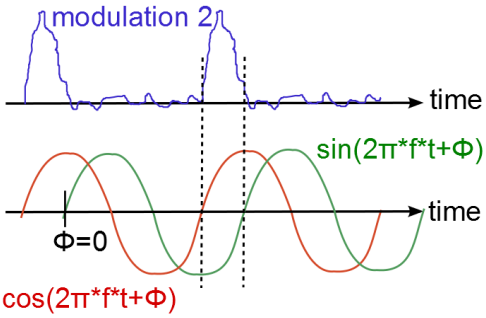

Figure 19: Image showing the periodically modulated part of an arbitrary light beam no.2 over time.

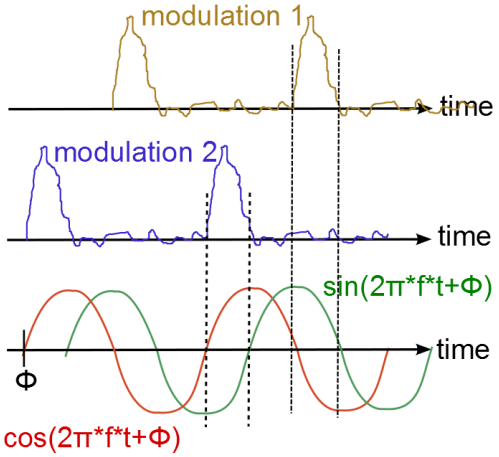

Figure 20: Projection of the periodically modulated parts of light beam no.1 and no.2 on sine and cosine function at pulse frequency.

The EOFM/EOP hardware used for all experiments presented in this thesis only gives out the R_{EOFM}-value, which will simply be referred to as "EOFM" value from now on. However, previous investigations [101, 103] used EOFM setups, which were capable of detecting and displaying X_{EOFM} and Y_{EOFM} values independently from each other.

Depending on the semiconductor device under investigation and the electrical condition at a time, the modulation of the laser light can be different. Several physical effects are contributing to the modulation. The modulation is also dependent on the focus level of the optical system applied to guide the laser beam (see figure 21), which has already been stated in [103].

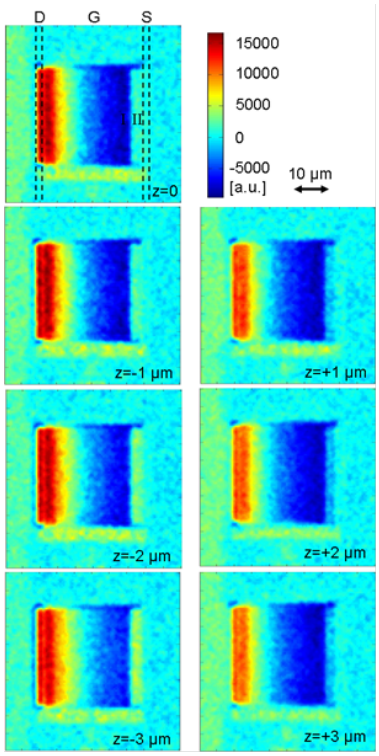

Figure 21: Dependency of EOFM investigation on the focus level. The graphic shows SLD (see table 5 below) images of a $30\mu m \times 30\mu m$-nFET for different focus heights (z). The images are taken from [103].

An overview of EOFM signals for common pulse modes for nFETs and pFETs can be seen in figure 22. The normal FET operation pulse mode is roughly a superposition of gate mode and drain mode, taking into account that the modulation of the reflected light under the gate is weaker the closer the spot is to the drain region. The reason for this is the narrowing and shortening of the channel under the gate from source to drain with positive drain bias. FET operation pulse mode (pulsing gate and drain simultaneously) is used to resemble normal FET switching behavior as illustrated in the n-FinFET output characteristic displayed in figure 23.

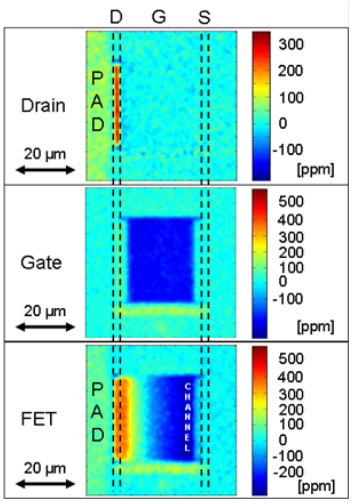

Figure 22: The graphic shows typical SLD (see table 5 below) EOFM signatures for a nFET in Gate mode (only gate pulsed), Drain mode (only Drain pulsed) and normal FET operation (Gate and Drain pulsed simultaneously). The images are taken from [103].

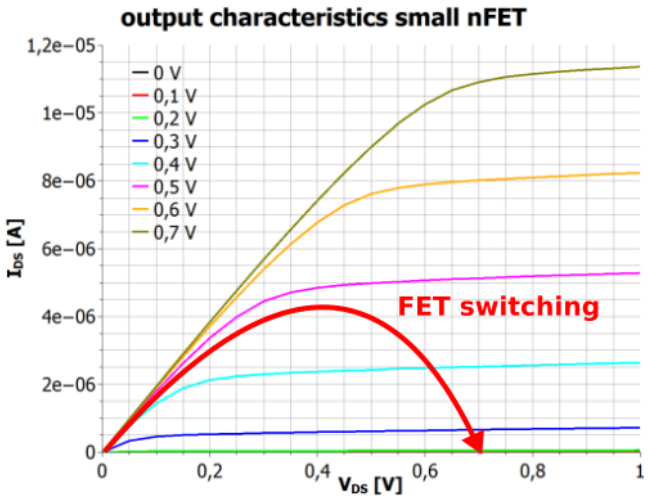

Figure 23: Illustration of the switching process of a 16/14nm n-FinFET switching from $V_D = 0$ to $V_D = V_{nom} = 0.7V$.

The electro-optical detection system for Phemos-1000 installed at TU Berlin supports pulse frequencies from $100kHz$ up to $8GHz$. Only 50x objective lens and 50x with Nanolens were used for electro-optical measurements because of higher NA, optimization of the 50x objective lens for wavelengths around $1300nm$ and higher focus depth. The standard pulse setup for EOFM/EOP was as follows: $1MHz$ Frequency, 50% duty cycle square wave, $0V$ low-level voltage and V_{nom} high-level voltage, drain and gate pulsed simultaneously, scan speed $1ms/pixel$, $1kHz$ video bandwidth (VBW), $1kHz$ radio bandwidth (RBW). All relevant contacts on the chip, which were not pulsed, were grounded to $0V$ if not mentioned differently. EOFM signals of specific regions (e.g. gate/drain/transistor, cross-section, line profile etc.) were calculated by summarizing individual pixel EOFM values over the whole region and subtracting the offset of 32.000 from each pixel. Deviation from this standard setting are mentioned in the respective passages of this work. Detailed

and precise explanation of specific parameters (e.g. RBW, VBW) can be found in [77]. Finally, an overview of the different light sources used for the experiments presented in this thesis is given in table 5. SLD refers to an incoherent super-luminescence diode, whereas HSL stands for High Stable Light source. For the HIL (High power Incoherent Light source) no further data was disclosed by the manufacturer.

Table 5: Light sources used with Phemos-1000

	SLD	**HIL**	**HSL**
center wavelength	$1320nm$	$1330nm$	$1319nm$
bandwidth	$40nm$	$20nm$	$0,563 \cdot 10^{-9}nm$
coherence length	some μm	incoherent	$> 10m$
power in spot with 50x lens at 100%	$5,8mW$	$45mW$	$71mW$

3.8 Electro-optical probing (EOP)

Electro-Optical Probing (EOP), also known under the name of the similar Laser Voltage Probing (LVP) technique, is mostly similar to EOFM. The only differences are that with EOP no frequency analysis of the modulated light beam is carried out and EOP analysis is performed at one single pixel of the image and not scanned over the entire area as with EOFM. EOP waveforms display the modulated signal in time domain with averaging over a high number of pulse periods. The EOP waveforms suffer from unwanted hardware effects like low- and high-pass behavior, which can severely distort the waveform. For inspection of physical parameters EOP therefore is less interesting and hardly used in this thesis except for the end of section 6.4.2, where waveforms are given for various spots of a small NAND-like structure. In real FA labs EOFM is usually applied first to find spots with high electro-optical signals. Then EOP analysis is carried out at the respective spots to obtain the waveform at a specific node or transistor.

3.9 Photon emission techniques (PEM/SPEM)

Photon emission (PE) techniques collect and analyze light emitted from active devices within integrated circuits. Therefore, the measurement of photon emission has been a major technique in the localization of electronic failures in integrated circuits ever since the 1980s. The technique takes advantage of high light emission intensities due to e.g. substrate/gate/source-to-drain currents in a MOSFET or leakage currents caused by bridge defects and shorts. Using a low magnification lens (e.g. 0,5x macro lens), it is mostly possible to determine the spot of an occurring failure mechanism within the chip. Using higher magnification lenses the exact area or even exact transistor causing a failure can be identified, giving valuable information for circuit re-design. For photon emission high enough to be detected high electric fields are required. The general PE signal level is directly proportional to the current across the high electric field region. Also other light emission sources like electron-hole pair recombination (spontaneous or within pn-junctions in forward bias) are possible, but the latter two are very unlikely as silicon is an indirect semiconductor and integrated circuit never have forward-biased pn-junctions under normal conditions. More information about

light emitting processes in active semiconductor devices, mostly FETs, can be found in sections 5.1 and 5.3.

In the 1980s and 1990s typical PE detectors with a spectral range of approximately $400nm$ to $1100nm$ were used (e.g. silicon CCD). Following the trend towards lower device voltage, new detectors with deeper infrared range were developed (e.g. InGaAs camera from $900nm$ to $1600nm$; also see figure 31 in section 5.2). Recent developments include the emergence of even deeper infrared detectors like MCT or Emmi-X cameras with spectral ranges going up to $2300nm$, which require excessive cooling down to 80-150 K.

Regarding this thesis, the standard setup for PEM included the use of an InGaAs camera and also a silicon CCD (only section 5.5) with a typical integration time of 80s (InGaAs) up to 300s (silicon CCD). Due to the higher noise level longer integration times for InGaAs are not possible because the detector goes into saturation. Drain and gate voltages for all (spectral) PE experiments are annotated in the respective figures. Spectral measurements were carried out by shifting a movable prism into the optical path. PE signals were summarized for a specific region by adding individual pixel PE values and subtracting noise offset, while assuming a linear detector signal relation to collected intensity. For spectral PE measurements only 3-5 pixels perpendicular to the prism's dispersion shift were added for each wavelength, whereas for simple PEM emissions of all wavelengths in the detector range were added per pixel.

3.10 Further hints for a successful EOFM/EOP measurement

As EOFM is a dynamic technique, great care must be taken of signal reflections and suitable terminal resistances at all connection endings. Usually the pulsed device connections (gate, drain) are high ohmic ($>> 1k\Omega$) and easily generate unwanted signal reflections and dangerous voltage peaks if not monitored and treated with care. Suitable terminal resistances, mostly 50Ω-terminations for respective 50Ω-coaxial cables, have to be integrated into the connecting lines at the end of cables. Where this is not possible the use of *high-z* mode at the pulse generator can prevent damage to devices by higher voltages than intended. For preventing any harm for devices under test and to ensure reproducibility of measurements careful monitoring of input and output signals is recommended with a parallel oscilloscope. A measurement should always start with lower voltages, which can then be slowly adjusted towards higher voltages.

The use of in-built frequency analysis options can be recommended to find the most appropriate center frequency to enter into the electro-optical software panel (the software for Hamamatsu Phemos-1000 is called *Semishop*). This allows for smaller video bandwidths (VBW) and thus higher signal-to-noise ratios.

In dynamic measurements capacities within the integrated circuit, the socket, the printed circuit board (PCB) or coaxial cables have to be loaded and unloaded within each pulse cycle. It is therefore important to be aware of restrictions and capabilities of internal (e.g. transistors) or external drivers (e.g. pulse generator, parameter analyzer). In some cases the use of additional external capacitors can help in dealing with such problems. A good example for limited internal driving capacity with respect to pulse frequency can be seen in figure 131 of section 6.4.2.

A common beginners mistake is to not save data in suitable raw data formats (.tiff, .tiff32, .csv), but as .png or .jpg-images, which makes quantitative analysis and comparison of data from different measurements more difficult or even impossible.

3.11 Further hints for a successful PEM measurement

For best signal-to-noise ratios the detector cooling should be adjusted to the lower limit as noise caused by temperature is a major factor for all PE signals. Attention must be paid to the presence of ESD or other structures (e.g. drivers, ring oscillators) in the area under investigation, because these structures were often seen to emit intensities of light surpassing the original FET emission. This can lead to confusion of emission sources. This is especially true, when internal chip voltage restrictions (V_{nom}) are not complied with, for example in degradation measurements or similar.

A common beginners mistake is also to not save data in suitable raw data formats (.tiff, .tiff32, .csv), but as .png or .jpg-image, which makes quantitative analysis and comparison of data from different measurements more difficult or even impossible.

3.12 Further hints for a successful SPEM measurement

For spectral PE measurements with prism or other dispersive elements the general intensity level has to be 5-10 times higher than for normal integrated PE measurements as the distribution of the emitted light along a wide dispersion tail decreases signal-to-noise ratios at individual pixels. For modern low-voltage devices a factor of 5-10 corresponds to an increase of drain / supply voltage of roughly $100mV$.

In order to be able to extract a spectrum from the raw data dispersion tail, the dispersion-over-pixel characteristic must be known and a calibration of the whole optical system with detector is necessary (section 5.2 of this thesis). For each emission image the exact position of the emission spot without dispersive element in the optical path must be known. For example, regarding InGaAs camera an integration time of 90s can be recommended: The first 10 seconds without prism and the last 80s with prism in the optical path. This ensures highest spectral evaluation accuracy for all individual image data. This procedure bears the further advantage that slight drifts or small leaps (e.g. when the SIL is not perfectly aligned with the surface or the surface is uneven) between different measurements are not relevant.

4 Hardware

4.1 Devices under test

4.1.1 120nm devices by Infineon Technologies AG

Several devices manufactured in $120nm$ technology with $V_{nom} = 1.2V$ by *Infineon Technologies AG*, Germany, are used for the investigations presented in this thesis. For basic EOFM experiments and signal understanding two large area transistor types were used: The first one with a gate width and length of $30\mu m$ and the second one with a gate width and length of $10\mu m$. Another structure included on the same test chip was a ring oscillator used for the experiments with the 2d-tomography method. Information about doping level and geometry of this technology can be found in the "Devices"-section of the tomography method (section 5.5.3.1).

4.1.2 250nm NAND-like structures and current mirrors by IHP Frankfurt/Oder

This thesis includes many experiments on small and big NAND-like structures as well as different types of current mirrors (simple, cascode, low-voltage), which were all manufactured in $250nm$ BiCMOS-technology with $V_{nom} = 2.5V$ by *IHP - Innovations for High Performance Microelectronics*, Germany. Technical process parameters can be found via the internet on the official IHP-website [118]. The design of each individual structure was done by Technical University Berlin including a re-design in 2016 after the first tape-out in 2015.

4.1.3 24-40nm FinFETs

All 24-30nm/40nm n- and p-type FinFETs presented within this thesis were produced in 28nm/40nm technology with a nominal voltage of $V_{nom} = 0.8V/0.9V$. Due to NDA restrictions no further technical data about the FinFETs or the involved manufacturing process, as well as the identity of the manufacturer and/or cooperation partner can be disclosed.

4.1.4 16/14nm FinFETs by Qualcomm Inc.

Research experiments of this thesis also include many optical investigations on modern low-voltage 16/14nm-FinFETs provided by *Qualcomm Incorporated*, United States. The FinFETs were manufactured by *TSMC*, Taiwan, in their 16/14nm process with a nominal voltage of $V_{nom} = 0.7V$ and a maximum certified voltage of $1.1V$. The small n- and p-type FinFETs had a width of 58nm with two fins, while the large n- and p-type FinFETs had a width of 922nm with 20 fins, respectively.

4.2 Measurement equipment

The main hardware used for all measurements was a roughly 20 year old Phemos-1000 by Hamamatsu Photonics KK, Japan [116]. The Phemos-1000 system at TU Berlin has been upgraded with necessary features like electro-optical probing unit, better laser scanner and control board as well as a better PE detector (InGaAs) over the past years. The electro-optical probing unit was equipped with an Advantest U3851 2-channel cross domain analyzer for spectral analysis of the reflected light beams.

Electrical device characteristics were measured with a 4-channel HP 4145-A semiconductor parameter analyzer, which also served as static voltage supply for photon emission measurements. Regarding EOFM pulsing, a Hameg HMO 2022 2-channel digital oscilloscope was used to monitor signals from input and output connections of devices under test. For the EOFM measurements with two pulses and phase shift of section 6.4 a Rigol DG 4162 2-channel function waveform generator was used.

5 Photon Emission Microscopy

5.1 General PEM signal observations

This section shall give the reader a general understanding of PEM signal behavior explaining important relations between electrical device performance and photon emission signal of a field effect transistor. Other introduction to the PEM techniques are given by C. Boit [7] and G. Shade [8] with less focus on physical parameters in an individual transistor, but more on application as FA technique and on different devices. All presented data of this introduction is new and expands previous knowledge on emission behavior of planar MOSFETs towards modern 16/14nm FinFETs. New application examples of IC / FinFET failure analysis with PEM will be given in a later section (5.4).

Generally, photon emission signals require a high electric field ($\approx 10^4 - 10^6 V/cm$) to accelerate charge carriers, as well as the existence of scattering centers in the semiconductor. Different scattering processes are relevant in different PE cases and generally have to be considered. Regarding photon emission from FETs (also named as *hot carrier emission*), electron-electron scattering is an important process parameter to consider as it strongly influences the carrier energy distribution within the channel [106]. Scattering of charge carriers at atoms of the semiconductor (e.g. *impact ionization*) is nowadays commonly regarded as the principal photon emission process in MOSFETs after a long scientific discussion in the 1980s and 1990s had taken place. Also other emission processes (e.g. bremsstrahlung) have been discussed in measurement data and theoretical deliberations (e.g. [3, 4, 12, 38, 39, 41, 51, 53]). However, all scattering processes depend strongly on physical device parameters such as free mean carrier path, doping levels or implanted materials in the channel (e.g. silicon-germanium channels). In this thesis it will be shown that many of the mentioned physical parameters can be read out from FinFET photon emission spectra and used as valuable experimental method for device characterization (section 5.3).

On the electrical side there are two main parameters, which influence the photon emission strength and spectrum of a FET: drain voltage and gate voltage. A lot of case studies and efforts to model certain features of PE with respect to voltage can be found in the literature [19, 20, 22]. As already mentioned, the electrical field distribution between source and drain of a field effect transistor highly influences the intensity (and also the spectrum) of photon emission. The exact relation between (integrated) photon emission signal and the respective voltage parameter for MOSFETs has been subject to intensive scientific study over the last decades [22]: As a rule of thumb, PE signals increase roughly exponentially with drain voltage, while PE signals are usually highest for some medium gate voltage at or slightly above threshold voltage, strongly decreasing for higher or lower values of gate voltage (typical *bell-shape* of emission). In this work, this relation could be confirmed for FinFETs, too. Figure 24 shows the previously described slopes of PE signal over gate and drain voltage for both 16/14nm n- and p-FinFET. The physical causes for these typical emission patterns as well as the derivation of an exact analytic formula are given in section 2.2.1 and will be discussed later in section 5.3. In sharp contrast to all previous measurements (e.g. [22]) on MOSFETs, the signal level for n- and p-type 16/14nm FinFET is almost equal here, clearly indicating the use of alternative channel materials like silicon-germanium. This suspicion could be confirmed in another TU Berlin PE spectra publication currently submitted to IPFA 2018 ([46]).

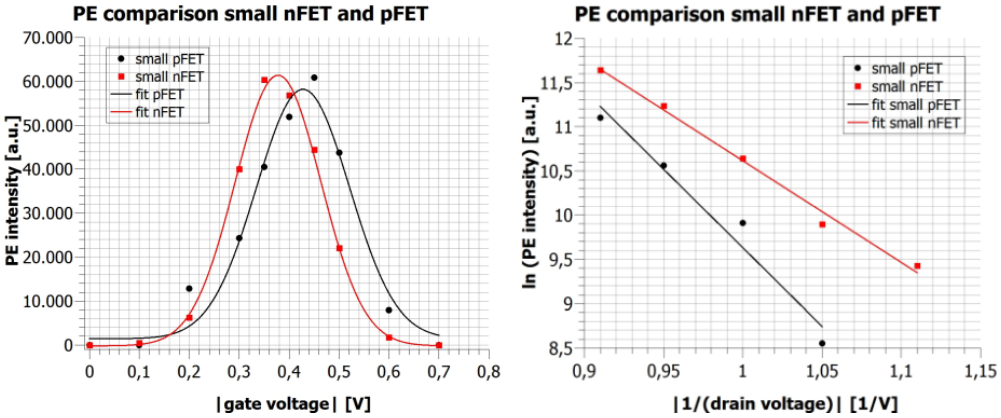

Figure 24: Integrated photon emission signal over gate voltage (left) for the small Qualcomm n-/p-FinFET at $V_D = 1,1V/-1,1V$. Integrated photon emission signal over inverse drain voltage (right) for the small Qualcomm n-/p-FinFET at $V_G = 0,4V/-0,4V$ measured with Nanolens (SIL).

The bell-shape of photon emission over gate voltage at a sufficiently high constant drain voltage can be explained by the influence of gate voltage on the electrical condition of the FinFET (figures 25 and 26): If the gate voltage is lower than threshold voltage V_{th}, the transistor remains in off-state. The gate voltage is not high enough to build up a stable channel. Therefore, the overall current leaving source towards drain is too small to generate detectable photon emission in most cases, as PE is directly proportional to this current. However, photon emission from leakage currents at high drain voltages has also been detected in the past [26, 27, 29, 32, 48]. When gate voltage is increased towards V_{th}, the channel starts to build up and the FET leaves offset operating condition to enter saturation region. This involves a rapid increase of source-to-drain current. Also the electric field at pinch-off reaches its highest values here, strongly accelerating charge carriers at the end of the channel and therefore causing high photon emission [18]. Further increase of gate voltage beyond threshold voltage region continuously shifts the field effect transistor from saturation operating condition towards linear-parabolic condition, which causes a decrease of the electric field maximum at pinch-off due to increasing channel length. This decrease of the electric field is responsible for the decline of PE intensity on the right side of the emission bell. Interestingly, the bell-shape form of emission over gate voltage usually correlates with an almost identical bell-shape form of the substrate current first observed in [50] (see figure 27), as photon emission and substrate current both originate from the same or at least similar scattering processes at the high electric field regions within the channel close to pinch-off. However it is dangerous to take this correlation for naturally granted: It was shown that substrate current and PE-slope-over-gate-voltage can take a qualitatively different course and can be influenced in different ways apart from each other even for a fully functional MOSFET (e.g. for different lattice temperatures in [28]). In general, substrate current can still be used as a good predictor for photon emission and device (dys-)functionality (see section 5.4).

The roughly exponential increase of photon emission with drain voltage can be traced back physically to the energy distribution of the charge carriers and the maximum electric field value at the end of the channel. For these deliberations it is important that the constant gate voltage takes a value between threshold and nominal voltage of the device. It will be shown later in section 5.3 that the energy distribution of the charge carriers in the channel approximately has an exponential

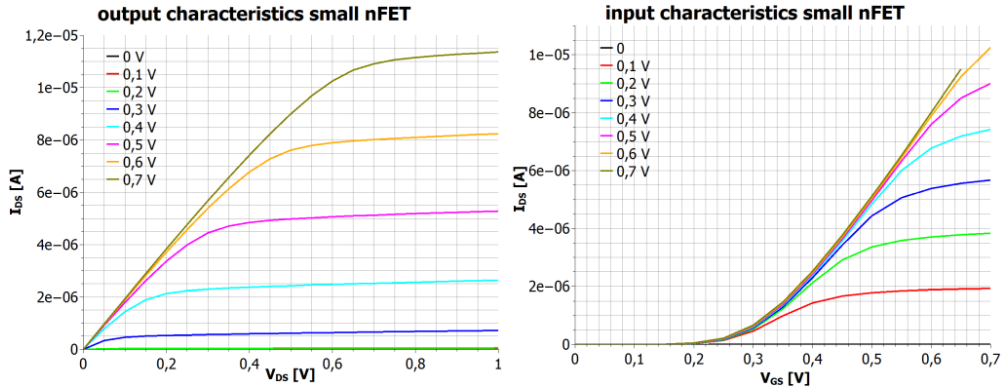

Figure 25: Output characteristics (left) of the small Qualcomm n-FinFET for various V_{GS} from $0V$ to $0,7V$. Input characteristics (right) of the small Qualcomm n-FinFET for various V_{DS} from $0V$ to $0,7V$.

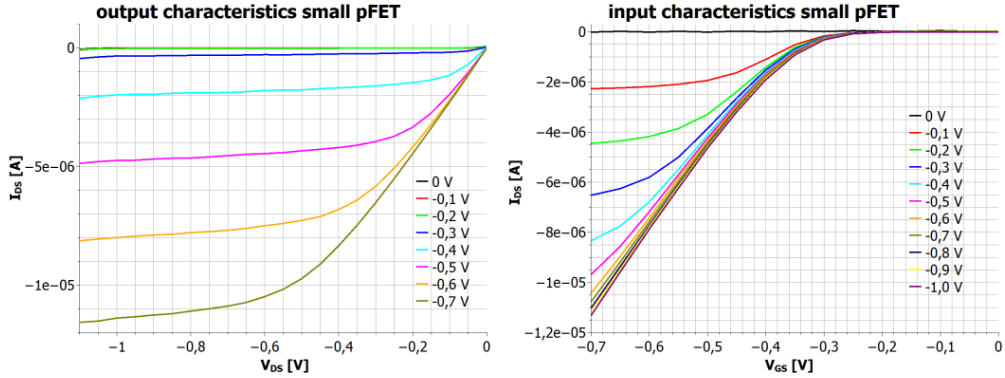

Figure 26: Output characteristics (left) of the small Qualcomm p-FinFET for various V_{GS} from $0V$ to $-0,7V$. Input characteristics (right) of the small Qualcomm p-FinFET for various V_{DS} from $0V$ to $-1V$.

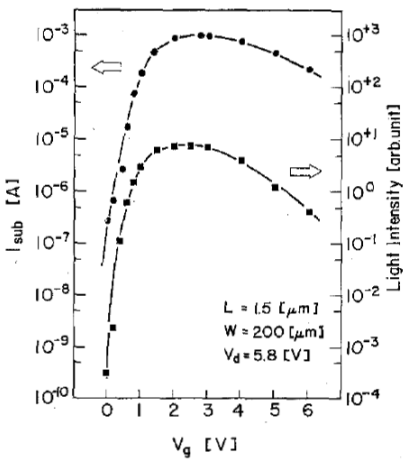

Figure 27: Correlation between substrate current and photon emission intensity over gate voltage for a $1,5\mu m$-MOSFET. Image taken from [50].

dependence on carrier gas temperature, which itself is proportional to drain voltage as will be shown later (section 5.3). Furthermore, the maximum electric field in the channel is approximately proportional to drain voltage [50]. Both effects contribute to a roughly exponential increase of PE with drain voltage. Note that the exact mathematical relation on exponential scale is roughly given by [22]

$$\text{PE intensity} \propto e^{-\frac{1}{V_D}} \quad , \tag{5.1}$$

which was experimentally confirmed in figure 24. The experimental data for various different FinFET test structures shows that the detection limit for PE signals with respect to drain voltage lies around $0.9V$ for cooled silicon CCD ($-50K$) and $0.6V$ for cooled InGaAs detectors ($-70K$) together with use of solid immersion lenses. Measurements at lower supply voltages require high-end infrared detectors (e.G. MCT, Emmi-X) with deeper and more complicated cooling. Even more valuable is the correlation between carrier gas temperature in the device and detection limit for various detector setups, which was also achieved in this thesis (see section 5.7). Talking about general signal levels, it is also important to study the intensity improvement due to the use of SILs. This was done for PE over gate and over drain voltage for both n- and p-type $16/14nm$ FinFET. While the qualitative signal-to-noise-ratio improvement with SIL can be identified directly in the emission images (figure 28), a quantitative analysis shows that the average signal improvement factor lies around $8-10$ compared to an identical measurement without SIL (figures 29 and 30). With this improvement factor it is possible to extend PE analysis to $\approx 0,15V$ lower drain / supply voltages to yield same signal level compared to an identical measurement without SIL for modern FinFETs. Whereas usually the optical resolution improvement factor ($\approx$ NA of SIL) is appreciated most, the even higher intensity improvement factor for PEM (and EOFM) plays a major role especially for low-voltage devices. The reason for the higher intensity increase factor compared to resolution factor is that regarding signal intensity not only the additional light catched by the SIL ($\approx$ NA-of-the-SIL times more than without SIL) is contributing, but also a significantly higher light transmission factor at the SIL-to-air interface (see Fresnels formula in the theory section 2.2.6) due to a more favorable angle of incidence (90°) compared to the case without SIL.

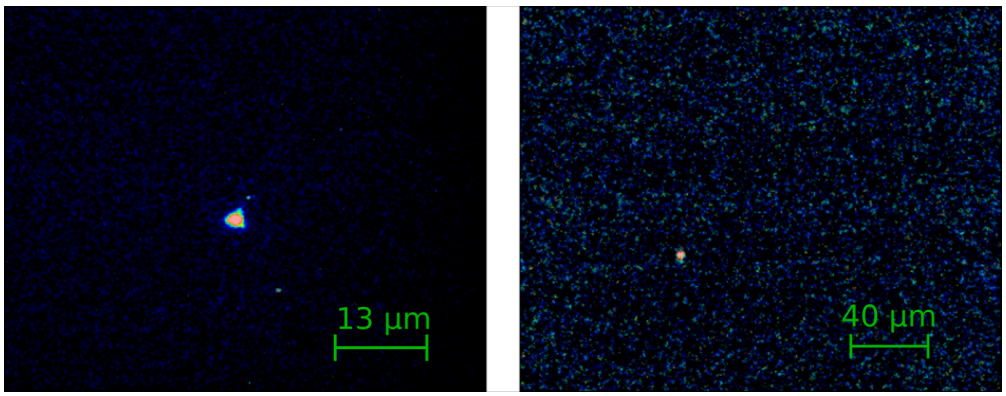

Figure 28: Emission spot for the small p-FinFET with (left) and without SIL (right). The strong improvement of signal-to-noise ratio by SIL-use is clearly visible.

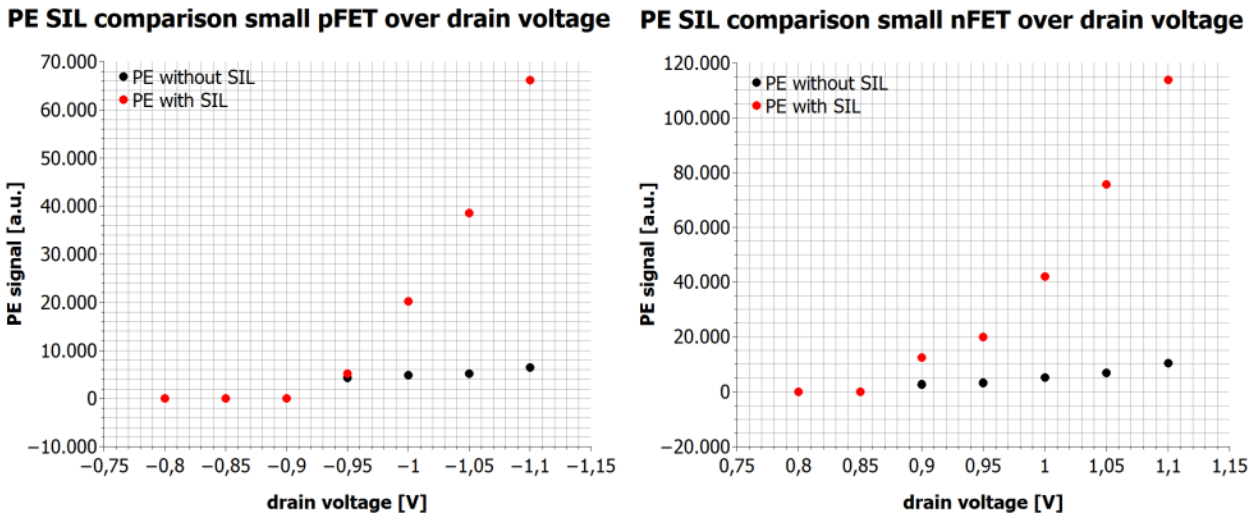

Figure 29: Comparison of integrated photon emission over drain voltage for small n-/p-FinFET at $V_G = 0,4V/-0,4V$ with and without SIL.

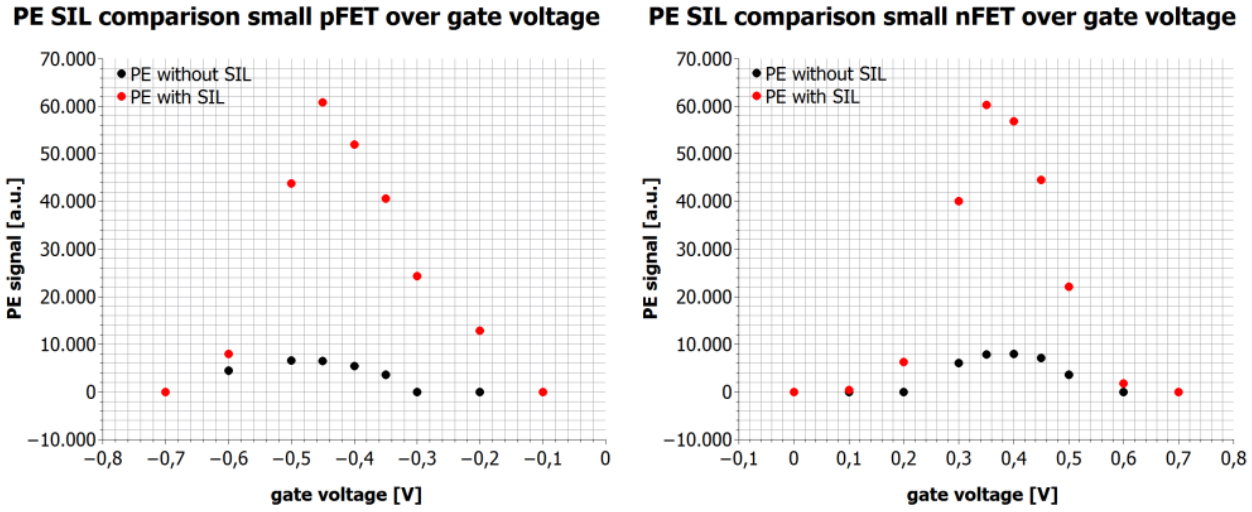

Figure 30: Comparison of integrated photon emission over gate voltage for small n-/p-FinFET at $V_D = 1,1V/-1,1V$ with and without SIL.

5.2 InGaAs camera calibration

For the accurate spectral photon emission microscopy (SPEM) results acquired with InGaAs and silicon CCD detector presented in later sections of this work, a meticulous detector calibration procedure was necessary. For the standard silicon CCD camera this calibration was carried out at TU Berlin by Arkadiusz Glowacki before 2014. The calibration data from his measurements can be seen in figures 84 and 82 of section 5.5. Regarding the InGaAs camera calibration all steps were done in collaboration with the authors' colleagues Anne Beyreuther and Norbert Herfurth at TU Berlin. The whole calibration process lasted several months as many difficult and precise measurements concerning the InGaAs prism dispersion curve, transmission characteristic of 5x, 20x, 50x, 50x + SIL objective lenses, tube lens etc. had to be carried out. In addition, a well-suited black body calibration light source (color temperature $\approx 1900K$) had to be found and prepared as very low intensity and locally concentrated light emission were needed for the calibration. Furthermore, the light dispersion curve of the individually designed prism for SPEM analysis with InGaAs had to be measured. The prism could be moved in and out of the optical path to enable / disable spectral analysis. Some contents as well as figures of this section were already published in the authors contribution to ISTFA 2017 [68].

The setup with movable prism installed at TU Berlin is not the only option for SPEM analysis. While spectral emission analysis has not become a standard feature of commercial emission microscopes offered for failure analysis of integrated circuits yet, several different SPEM setups were built at various research facilities and used for FA in the past. While early SPEM setups in the 1980s and 1990s mostly made use of bandwidth filters for spectral light characterization, the first extensive spectroscopy apparatus with a prism was built and calibrated by M. Rasras et.al. at IMEC, Belgium, in the late 1990s/early 2000s [17, 21]. The idea to integrate a prism in the optical path was later adopted by Hamamatsu Photonics KK enabling the SPEM experiments with Phemos-1000, which are presented in this thesis. Therefore, the SPEM setup from IMEC used around 1997-2001 is very similar to the setup used for this thesis, but differing in the detector sensitivity range and position of the prism in the optical path. Back then, experiments at IMEC included spectral analysis of light emission from e.g. ESD protection structures [14], Fowler-Nordheim currents [15] and different silicon device defects [16]. A very detailed description of the whole calibration procedure applied at IMEC as well as advantages and disadvantages of different spectroscopy methods (e.g. with filters, monochromator, prism etc.) can be found in the PhD thesis of M. Rasras [100].

In the evaluation stage of the calibration measurements at TU Berlin it became apparent that the correct tube lens had not been installed along with the InGaAs camera, so that the still-installed tube lens designed for use with silicon CCD had to be changed for an alternative tube lens optimized for use with InGaAs detector. All calibration measurements had to be repeated. The physical reason for the optimization of the two tube lenses for different spectral intervals can be seen in figure 31. Whereas the silicon CCD detects emission mostly from visible light range up to the silicon band-gap ($\approx 1110nm$), the InGaAs camera was designed for deeper infrared measurements in a range of 900 to $1600nm$, where much higher hot carrier photon emissions can be expected in general for modern low-voltage devices.

Regarding the actual calibration process, a $10\mu m$ pin-hole was attached to the light source to ensure high localization and intensities of photon emission low enough for the InGaAs camera. The spec-

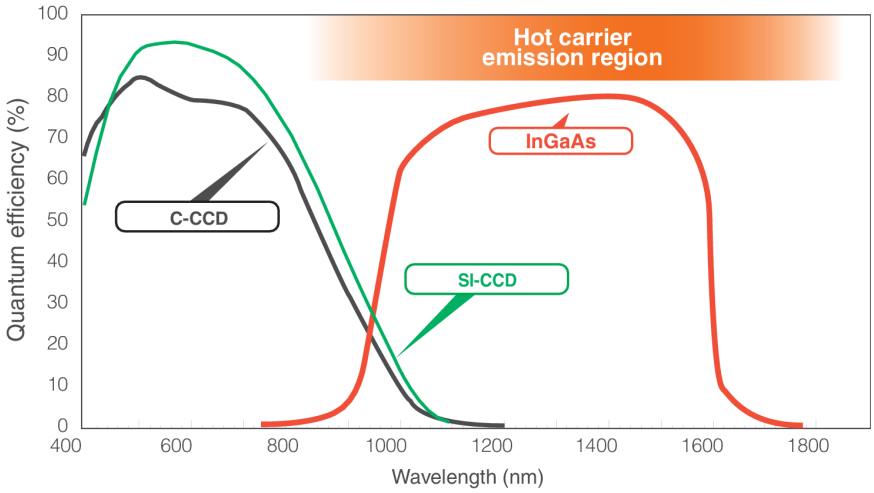

Figure 31: Quantum efficiency over wavelength for different PE detectors from Hamamatsu Photonics KK: InGaAs camera, solid intensified silicon CCD (SI-CCD) and standard silicon CCD (C-CCD). The standard silicon C-CCD was used for the tomography measurements in section 5.5. Image taken from [116].

trum of the calibration light source was then recorded at a gauged spectrometer at PVcomB, which is normally used for the characterization of solar cells (fig. 32 right). Except from small irregularities in the spectral interval from 1350 to 1450nm, which were corrected easily by a polynomial fit, the light source spectrum showed the expected black-body spectrum according to Planck's law for a color temperature of $\approx 1900K$. At Phemos-1000 the light source was measured again under identical supply voltage and current conditions with the InGaAs detector and for all different objective lenses. Before this data could be evaluated, an accurate measurement of the prisms dispersion characteristic was necessary in order to assign spectral emission points to certain wavelengths. Figure 32 (left) shows the dispersion characteristic result given in number of pixels that emission of one particular wavelengths was shifted to the right (Phemos backside mode) or left (Phemos frontside mode) by insertion of the prism into the optical path. The final correction factor (fig. 33) for each lens objective was obtained by dividing the spectral data of the reference measurement at PVcomB by the raw data measured at Phemos-1000.

For the calibration of 50x objective lens with attached Nanolens (Hamamatsu SIL), the calibration procedure described above was not possible, because the Nanolens needs direct physical contact to the DUT, which was not feasible for the calibration light source. Therefore an alternative process was used: A stable emission source (small Qualcomm n-FinFET) prepared for backside access was first measured with the already calibrated 20x and 50x without SIL. Consecutively, the measurement was repeated with 50x and attached SIL under identical electrical conditions. By comparison of already calibrated spectral data and the newly obtained Nanolens spectrum, the calibration factor for 50x with Nanolens could be obtained by division of the spectral raw data with SIL by the raw data without SIL and multiplying the result by the correction factor obtained for 20x / 50x without SIL. As the depth of focus was very small for 50x with Nanolens, a new calibration measurement had to be carried out for each measurement series and for each different position on the chip individually (fig 33 right). For 50x without Nanolens and especially for 20x lens this problem was negligible.

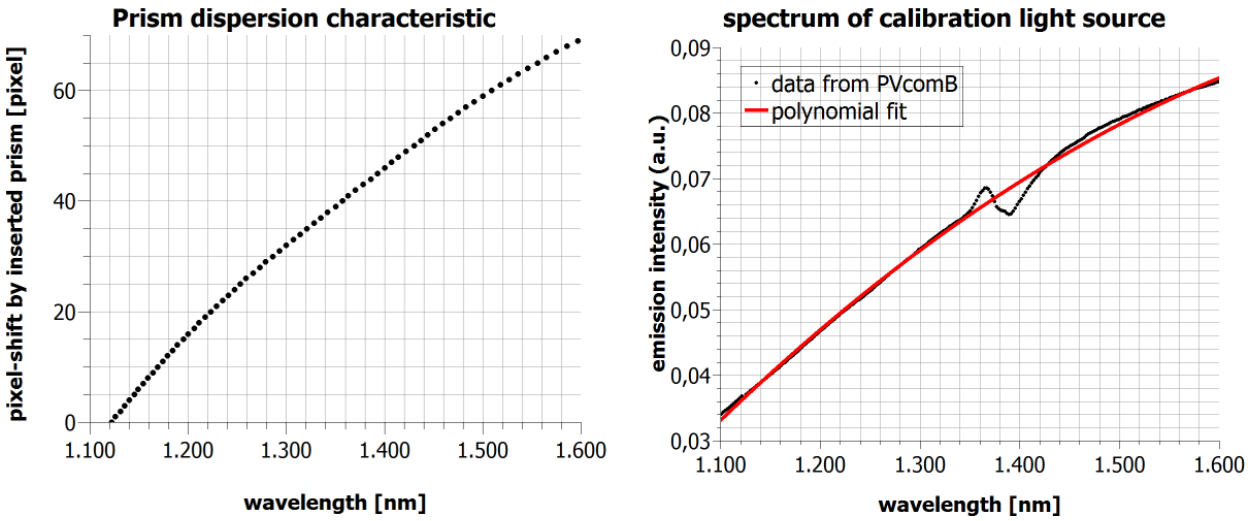

Figure 32: Dispersion curve for the prism used for InGaAs spectra acquisition (left) and black body spectrum of the light source (color temperature $\approx 1900K$) used for Phemos-1000 calibration (right) measured at PVcomB, Germany. Small measurement irregularities in the right image between 1350nm and 1450nm were corrected by fitting with a higher order polynomial.

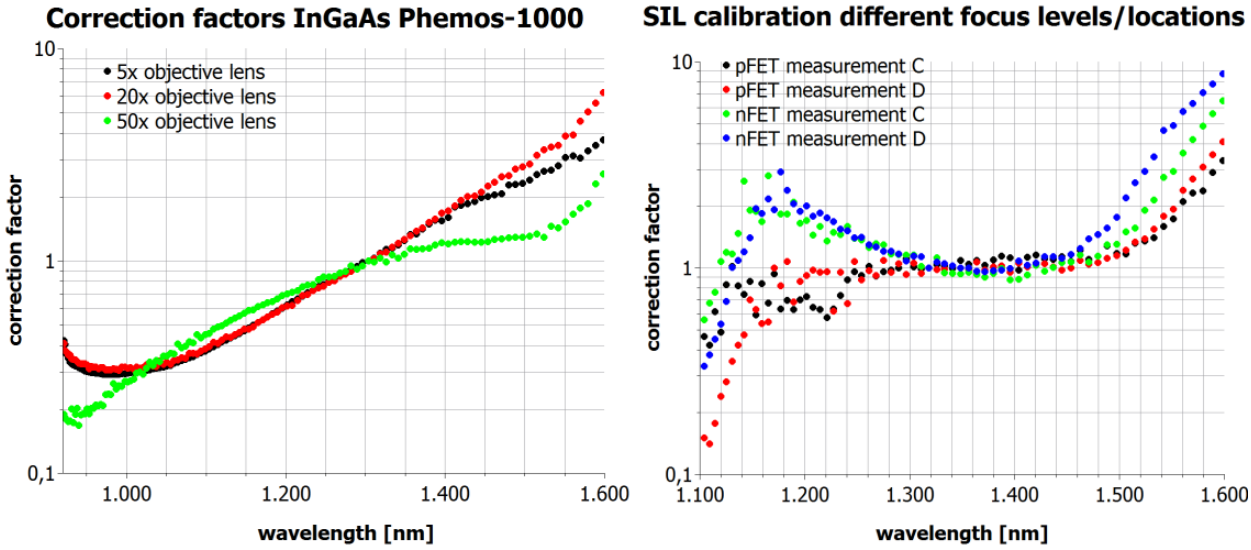

Figure 33: Correction factors acquired for 5x, 20x, and 50x lens without SIL (left). The right image shows correction factors for 50x with SIL for different positions and focus level, which were necessary due to thin focus depth of measurements with SIL.

Having finished the calibration process above, all data from spectral measurements was henceforth multiplied by the respective correction factor in a first step. For backside measurements a second step involving correction for light absorption in the bulk silicon was necessary. The correction factor in dependence of bulk thickness t is given via

$$\text{correction factor bulk absorption } (\lambda) = \frac{1}{e^{-t \cdot \alpha(\lambda)}} \tag{5.2}$$

following Beer-Lambert absorption law with the silicon absorption coefficient $\alpha(\lambda)$ for each wavelength λ taken from TCAD Sentaurus (fig. 34). The effect of substrate doping level on absorption coefficient was considered neglectable for the relevant spectral interval from $1100nm$ to $1650nm$ as long as the substrate doping concentration stayed below $10^{16} - 10^{17}/cm^3$, which is true for common substrate doping levels. This assumption is confirmed by figure 9 in the theoretical basics section 2.2.7. Both raw data correction steps can be summarized as follows:

$$\text{optics-corrected data } (\lambda) = \text{raw data } (\lambda) \cdot \text{correction factor for lens } (\lambda) \quad \text{and} \tag{5.3}$$

$$\text{corrected data } (\lambda) = \text{optics-corrected data } (\lambda) \cdot \text{correction factor bulk absorption } (\lambda)\ . \tag{5.4}$$

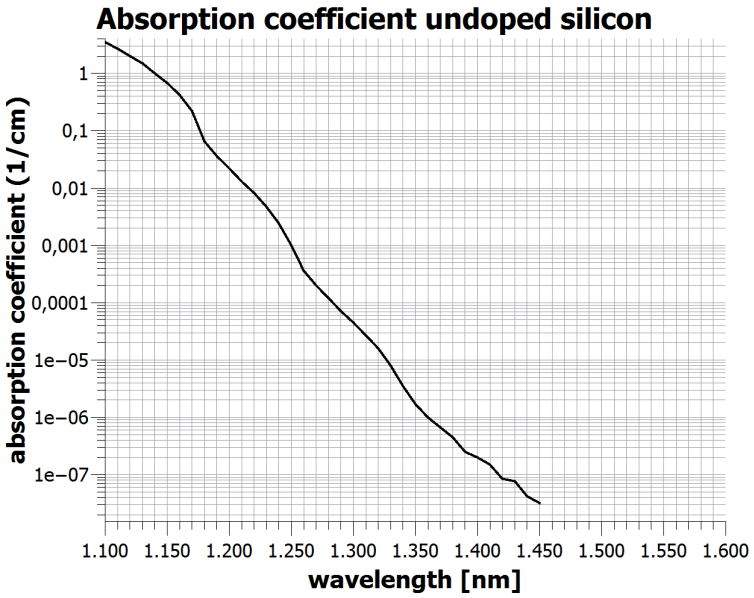

Figure 34: Absorption coefficient of undoped silicon from TCAD Sentaurus.

Due to low signal-to-noise ratios at the edges of the InGaAs detectors sensitivity interval (see figure 35), higher deviations from the ideal spectra were expected here. A similar effect was expected in backside SPEM measurements for wavelengths close to and lower than the silicon band-gap ($\leq 1200nm$) due to high absorption by the bulk silicon. In case of a Nanolens-measurement, the latter effect was even stronger due to the high radius ($3,5mm$) of the SIL and therefore vastly increased absorption in the SIL's silicon material. A special coating on the Nanolens surface was

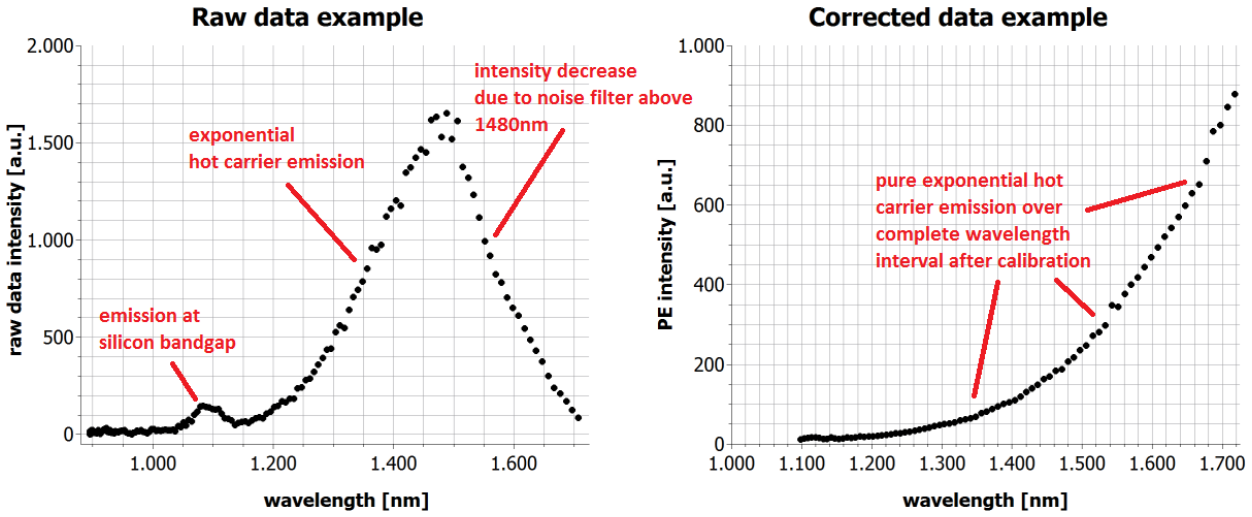

Figure 35: Photon emission raw data of a 16/14m n-FinFET at $V_d = 1.1V$ and $V_g = 0.4V$ with several different effects on intensity curve (left) and corrected intensity data (right).

also expected to have a certain effect on the signal-to-noise ratio (SNR) especially for wavelengths higher $1400nm$. The exact coating reflection / transmission data cannot be shown here due to confidentiality.

An example of raw data and fully corrected raw data (left/right in figure 35) also reveals two other effects: First, a weak emission peak at silicon band gap ($\approx 1110nm$) was sometimes visible in measurements with high supply voltages. Second, an exponential decrease of raw data intensity was detected generally above $\approx 1500nm$, which was due to a noise filter installed within the InGaAs camera. This filter was not removable, costing approximately a factor of 5 in overall collected emission intensity of each hot carrier emission measurement, as the hot carrier emission in the spectral detector region between $1500nm$ and $1650nm$ is very strong.

5.3 Extraction of device parameters with SPEM

Photon emission spectra include much more information about the emitting device than normal PE intensity-curves as introduced in section 5.1. Emission spectra of various different devices and operating conditions have been studied over the last 30 years (e.g. by C. Boit [7], J. Kölzer [56] and M. Rasras [14, 15, 16, 100]). Figure 36 gives an overview over emission spectra of typical semiconductor devices and operating conditions. Among others, spectral emissions from Fowler-Nordheim currents, gate oxide defects, latch-up and forward-bias, simple recombinaton in silicon and field accelerated carriers as in saturated MOSFETs or reverse biased pn-junctions have been studied and categorized regarding emission intensity and spectral slope.

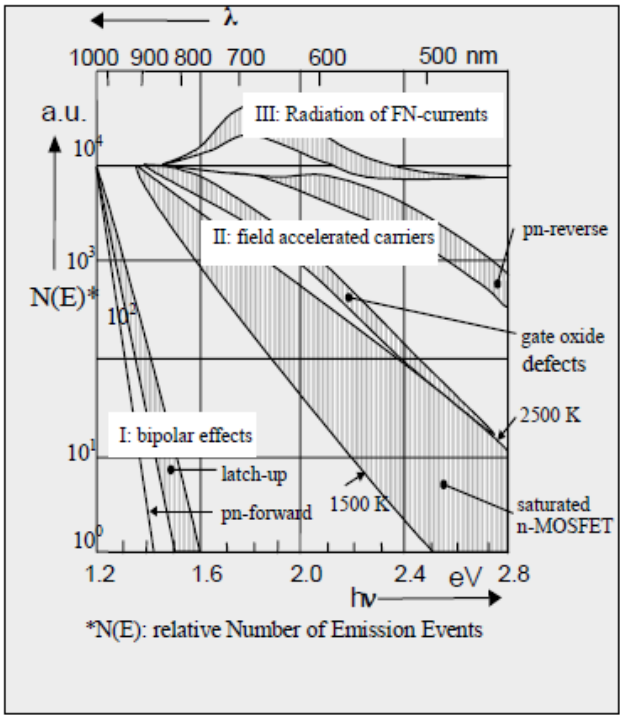

Figure 36: Different types of PE spectra for saturated MOSFETs, Fowler-Nordheim currents, reverse/forward-biased pn-junction and other. The image is taken from [7].

However, the emergence of modern low-voltage devices has led to a decline of photon emission microscopy and especially spectral photon emission intensity due to rapidly decreasing emission intensity. Therefore not much PEM and SPEM analysis is available for modern field effect transistors (e.g. FinFETs) with gate lengths smaller than $50nm$ and supply voltages around $1V$ and deeper. Seldom case studies can be found in [48], [26], [25], [27], [35], which were all carried out by one and the same research group at IBM T.J. Watson Research Center, but mostly without spectra and all without hot carrier gas temperature analysis. Publications [25] and [35] give analysis and calculations regarding device temperatures, but those temperatures are more related to self-heating of the entire device area (not restricted to the hot electron gas in the high-field region of the channel) and are strongly effected by temperature/energy dissipation mechanisms in the device. Real emission spectra as presented here contain more untainted information about the hot carrier gas

in the channel at maximum electric field, which is important for device reliability and degradation mechanisms e.g. within the gate oxide. It will be shown later that various device parameters such as charge carrier energy distribution within the channel, free mean path, energy relaxation time, maximum electric field in the channel, substrate and gate current of a functional MOSFET or FinFET are closely linked to each other via PE spectra and thus can be extracted from them. Therefore, the upcoming subsections will demonstrate a systematic and detailed analysis towards spectral photon emission behavior of FinFETs with unprecedented expansion of the spectral analysis down to hot carrier gas temperatures very close to room/test chip temperature of $300K$. In order to achieve this goal, the next subsection will introduce the reader to the most important mathematical findings about analytical treatment of photon emission spectra from the point-of-view of theoretical solid state physics.

5.3.1 Derivation of most important formulas

This subsection will give a concise overview of the most important physical relations involved in the mathematical description of the emitted carrier spectrum following the derivation of the most relevant formulas in [1] and [50]. More details than presented here can be found in these publications. From the point-of-view of theoretical physics, especially publication [1] by S. Tam and C. Hu gives a highly apt and qualitative derivation of all relevant formulas, whereas A. Toriumi 3 years later in [50] focused more on experimental confirmation and development of further applications for PE spectra. First, a formula for the spectral energy distribution of charge carriers and emitted photons will be derived, followed by several simple formula for the application towards real cases. It shall also be mentioned that other theoretic approaches partly leading to similar simulational data are available by Fischetti et. al. [2, 5, 6], Villa et. al. [4] and Bude et. al. [3].

The derivation will be done for an n-type FET with electrons as charge carriers. For p-type only the sign of the elementary charge has to be changed. The starting point of the theoretical analysis is a choice of the theoretical model to build the frame for the upcoming deliberations. Following the lucky electron concept the probability P of the hot carriers within the channel to attain an energy $U = h\nu$ can be stated as [1]

$$P(U) = e^{-\frac{U}{eE_x\lambda}} \tag{5.5}$$

with the charge carrier free mean path λ, the electrical field E_x at position x between source and drain and the elementary charge e. From this equation the number $R(U)dU$ of hot electrons within the energy interval from U to $U + dU$ can be inferred as [1]

$$R(U) = \frac{I_{DS}}{e^2 E_x \lambda} e^{-\frac{U}{eE_x\lambda}} dU \qquad . \tag{5.6}$$

As the number of carriers within a certain energy interval is now known, the missing part for the spectral emission distribution formula is the probability $Q_\nu d\nu$ of emission of a photon in the energy interval $h\nu$ to $h(\nu + d\nu)$ by a charge carrier passing through the channel length interval dx [1]

$$Q_\nu d\nu dx = DN_C \frac{d\nu dx}{m_{eff} U h\nu} \tag{5.7}$$

introducing the charge carrier effective mass m_{eff} and a constant D. The total energy W_ν emitted in the spectral interval $d\nu$ is then given as the energy $h\nu$ times the integral over the whole channel and the integral over all carrier energies higher or equal $h\nu$ over the number of carriers with relevant energy times the respective photon emission probability:

$$W_\nu d\nu = h\nu d\nu \int_0^{L_{eff}} \int_{h\nu}^{\infty} Q_\nu R(U) dU dx \qquad . \tag{5.8}$$

L_{eff} is the effective channel length. Using several reasonable approximations both integrals can be dissolved, so that Tam and Hu finally arrive at

$$W_\nu d\nu \sim \frac{1}{\nu^2} e^{-\frac{h\nu}{eE_{max}\lambda}} \tag{5.9}$$

with maximum electric field strength E_{max} in the channel. The maximum electric field as the region of highest photon emission can usually be found near pinch-off area towards drain diffusion (see figure 37). An experimental analysis and confirmation of this fact was given for MOSFETs in [18]. Simulations with respect to hot carrier gas temperature around drain [54] also argue strongly in favor of that. The exponent belongs to a Boltzmann distribution defining the hot carrier gas temperature

$$T = \frac{eE_{max}\lambda}{k_B} \qquad (k_B = \text{Boltzmann constant}). \tag{5.10}$$

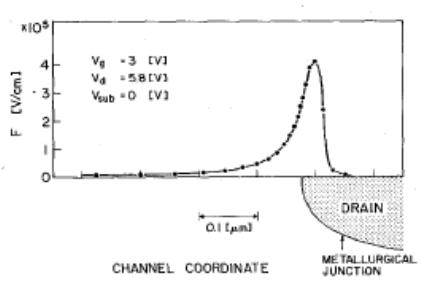

Figure 37: Distribution of electric field F along the line from source to drain for a $1,5\mu m$-MOSFET. Highest electric fields in saturation operating condition are generally observed at pinch-off close to the drain diffusion also for smaller FETs. Figure taken from [50].

Interestingly, the $1/\nu^2$-term mostly doesn't match experimental data (see [1]). Exceptions can be found in [56, 43, 65]. Most other experiments with well-calibrated spectral detectors in silicon CCD or InGaAs relate the emitted photon energy distribution to a simple Boltzmann distribution:

$$W_\nu d\nu \sim e^{-\frac{h\nu}{eE_{max}\lambda}} = e^{-\frac{h\nu}{Tk_B}} \quad . \tag{5.11}$$

An alternative derivation that leads to this formula (without the $1/\nu^2$-term) is given by Toriumi, yet with more vague physical approach. Torimui argues that transition probability in momentum space and density of states vary much slower compared to the electron distribution function and can be set constant, which eventually cancels the $1/\nu^2$-term [50]. It can be assumed that the effect/presence of the $1/\nu^2$-term in experimental data depends on the regarded spectral interval and also device characteristics. For all hot carrier gas temperature evaluations in this work formula 5.11 will be used. To extract device parameters from the hot carrier gas temperatures the equipartition theorem from statistical physics applied to an ideal gas can be used [50]:

$$T - T_0 = \frac{2}{3k_B} eE_{max}\lambda \qquad (T_0 = \text{chip/lattice temperature} \approx 300K). \tag{5.12}$$

The carriers free mean path λ is linked to energy relaxation time τ_E and carrier velocity v via

$$\lambda = \tau_E \cdot v \quad . \tag{5.13}$$

Now formulas for the extraction of the hot carrier gas temperature from experimentally obtained PE spectra (equation 5.11), the calculation of free mean path or maximum electric field in the channel (equation 5.12) and for the derivation of carrier velocity and energy relaxation time of the emitting region (equation 5.13) are available and will be used in the next section for device parameter extraction on recent technology 16/14nm FinFETs.

Toriumi even goes one step further by developing an astonishingly simple formula for the gate current I_g of a MOSFET only in dependence on hot carrier gas temperature T, channel current I_d and the energy barrier ϕ_b for carriers tunneling through the gate oxide based on Richardson's model [50]:

$$I_g \approx I_d e^{-\frac{\phi_b}{k_B T}} \tag{5.14}$$

with the reduced energy barrier $\phi_b = \phi_{Si-SiO_2} \pm e(V_d^{eff} - V_g)$ (+ for electrons, - for holes). ϕ_{Si-SiO_2} can easily be replaced with the correct value of other gate oxide materials for modern devices.

5.3.2 Device Parameters of 16/14nm FinFETs

PE emission spectra and their dependence on drain and gate voltage have not been proven to be similar to a MOSFET before. But as the general effect of drain voltages (increasing the electric field and carrier energy in the channel) and gate voltage (build up inversion channel) is the same and a FinFET also operates on basic field effect transistor functionality, it can be assumed that spectral PE dependence on both parameters stays the same. Indeed, the PEM and SPEM analysis carried out for the commercial 16/14nm FinFET from Qualcomm technologies strongly argues in

favor of that, as all emission phenomena were exactly analogous to planar MOSFETs except from generally lower electron/hole temperatures. Smaller temperatures can be explained by the general use of lower supply voltages thus reducing carrier energies and shifting the hot carrier emission spectrum deeper into the infrared wavelength regime. This topic will be taken up in section 5.7. Multiple data for older MOSFET technologies is available with respect to spectra acquired with silicon CCD or similar spectral range detectors [38, 39, 40, 41, 42, 43, 44], InGaAs detector [45] or even MCT detector [47, 48]. Several publications even include the extraction of hot carrier gas temperatures in silicon CCD range [49, 50, 51, 52, 53, 55, 56, 57, 58, 59, 60, 61], InGaAs range [62, 63, 64, 65, 66, 67, 68] and MCT range [71]. Some contents as well as figures of this section are submitted for publication at ESREF 2018 [69].

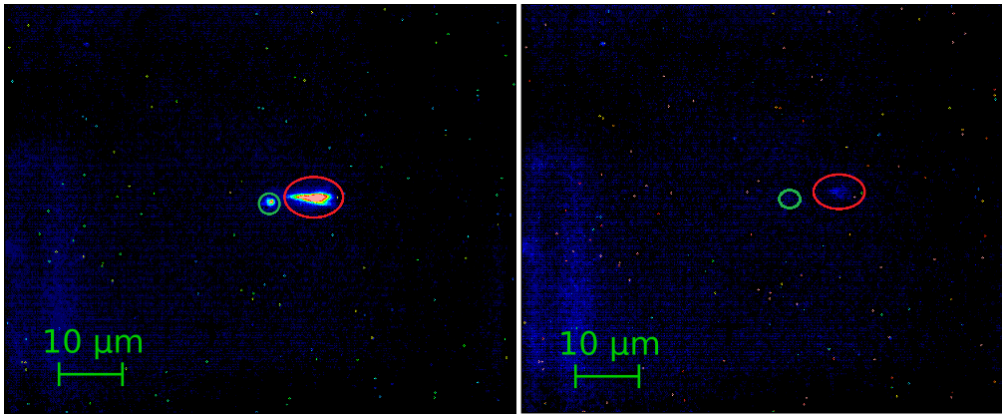

Figure 38: Example of spectral photon emission raw data for the 16/14nm n-FinFET at $V_d = 1,1V$ (left) and $V_d = 0,8V$ (right) both at a gate voltage of $0,4V$. The spectral intensity tail caused by the prism for 80s integration time is marked in red, the emission without prism is marked in green (prism was shifted into the optical path after exactly 10 seconds for each measurement). Backside measurement with SIL.

Examples of raw emission data for the n-FinFET from Qualcomm Incorporated can be seen in figure 38. The extracted photon emission spectra (fig. 39 and 40) for the small 16/14nm n-type and p-type FinFET reveal the known, strong exponential decrease of emission intensity with photon energy in the spectral region from $0,75eV$ to $1,05eV$. For photon energies larger than $0,95eV$ to $1,05eV$, the PE signal level becomes too low for good evaluation and slowly saturates into noise level especially for lower drain voltages. While the spectra over drain voltage show a clean and simple change of spectrum with voltage, the spectra over gate voltage partly intersect each other leading to a more complicated-looking spectral emission pattern. This behavior is normal and can be explained as follows: While the dependence of integrated emission intensity on drain voltage takes a simple exponential-like form, the integrated emission over gate voltage has the typical bell-shape as already introduced in section 5.1: Low and high gate voltages lead to similar, relatively low integrated emission intensities, whereas medium values of V_G correspond to much higher integrated emission. Therefore even continuous, monotonic changes of the exponential slope with voltage almost automatically lead to intersections of individual spectra.

It is interesting to compare the obtained charge carrier energy distribution to data of models from theoretical physics: Charge carrier energy distributions are known to not follow a uniform exponential course over the whole spectrum. Figure 41 shows a simulated energy distribution function

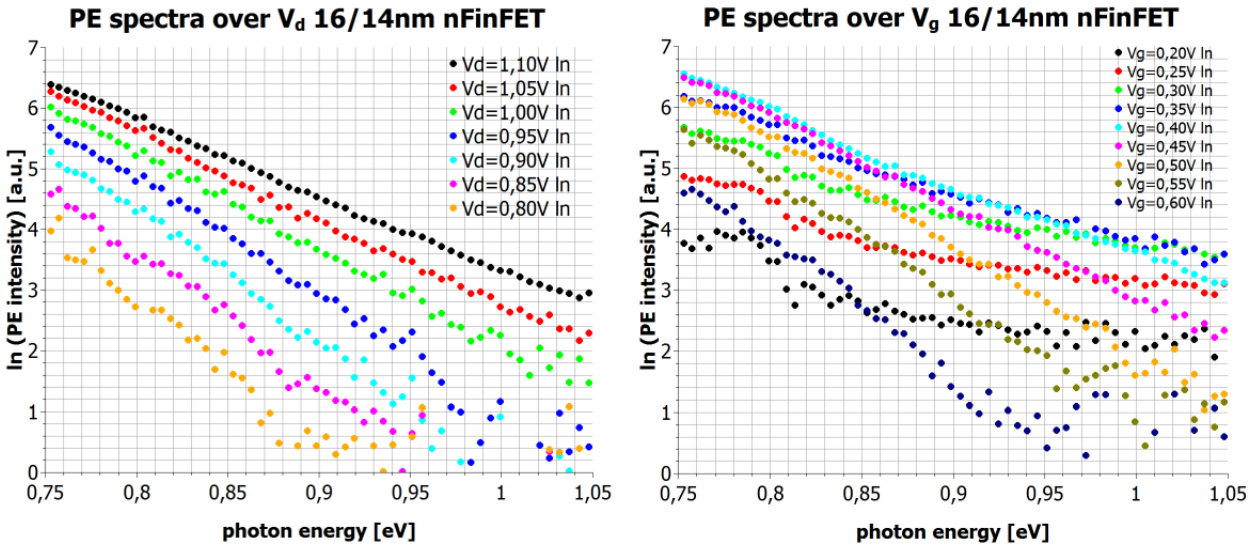

Figure 39: Photon emission spectra over drain voltage (left, at $V_G = 0,4V$) and over gate voltage (right, at $V_D = 1,1V$) for the small 16/14nm n-FinFET from Qualcomm Incorporated. Backside measurement with SIL.

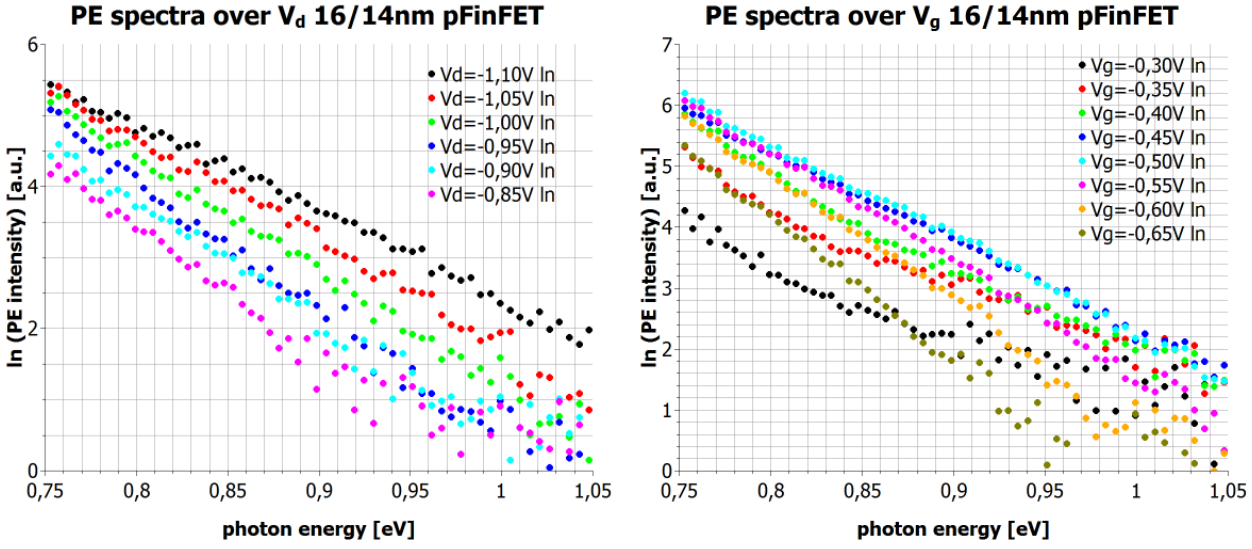

Figure 40: Photon emission spectra over drain voltage (left, at $V_G = -0,4V$) and over gate voltage (right, at $V_D = -1,1V$) for the small 16/14nm p-FinFET from Qualcomm Incorporated. Backside measurement with SIL.

(EDF) for electrons of different sized MOSFETs over a large spectral range from $0eV$ to $5eV$ published in [106]. The full InGaAs detector range ($\approx 0,75eV$ to $1,3eV$) is marked in red, bearing in mind that the interval from $1,1eV$ to $1,3eV$ is not realistically available here, due to generally lower signal levels for higher photon energies and additional high absorption in the silicon bulk for this spectral region. The figure shows different regions of the energy distribution with each region dominated by different physical phenomena (e.g. phonon-cascade, electron-electron scattering (EES) or the Boltzmann distribution of the intrinsic bulk charge carriers at $300K$ forming the strong linear rise in the most left part of each graph). For each gate length between $L_G = 65nm$ and $L_G = 150nm$ four different graphs are shown (dark red to yellow) corresponding to different positions in the channel from source to drain. Bearing in mind that the planar MOSFET data shown here is not 100% transferable to a 16/14nm FinFET, it can be stated that spectral kinks of the charge carrier energy distribution function and emission spectrum are natural and usually occur, when the physical regime changes from the dominance of one phenomenon to another.

Figure 41 also reveals another strong asset of photon emission spectroscopy on state-of-the-art structures: The obtained spectra and intensities can be used to validate simulated electron distribution functions, which are frequently used for reliability research of individual transistors. It has already occurred that simulated or theoretically derived spectra simply do not match the real data obtained in experiments. Those discrepancies can be used as indicators for parts of theoretical models, which should be reviewed again or are simply not applicable to a certain case.

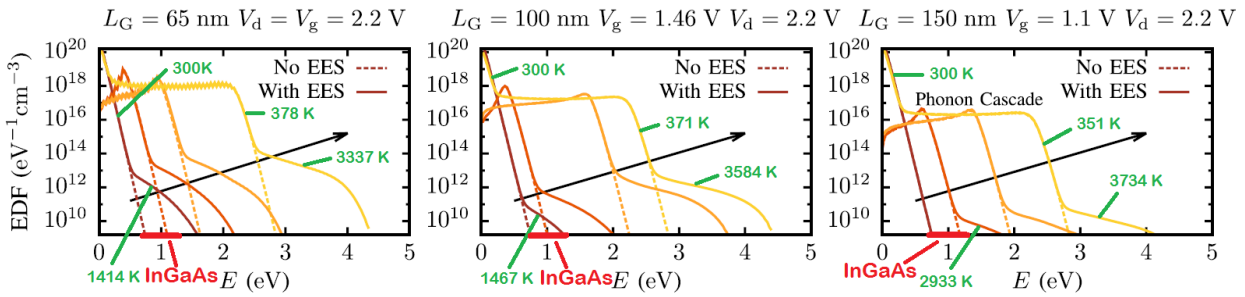

Figure 41: Energy distribution function (EDF) used for predictive modelling of hot-carriers in physics-based MOSFET degradation models from [106]. The three images show EDFs for three MOSFETs with different gate lengths and voltages. The four curves (dark red to yellow) per image refer to different position within the MOSFET channel: The evolution of the position from source to drain is indicated by the black arrows. Electron temperatures (green) and InGaAs sensitivity range ($\approx 0,75eV - 1,3eV$, red) were connoted by the author.

To examine closer the exact change in slope over drain and gate voltage for both n- and p-type 16/14nm FinFET, the electron/hole temperatures are extracted from the slope of the PE spectra following equation 5.11 above. The temperature T can be extracted easily from the slope of the logarithmic intensity graphs over photon energy above using

$$\frac{\Delta(\ln(\text{PE intensity}))}{\Delta E} = -\frac{1}{k_B T} \qquad (\text{with } \Delta E = h\Delta\nu) \quad . \tag{5.15}$$

At this stage it is important to bear in mind that absolute calibration of the emission detector

is not necessary for hot carrier gas temperature extraction: Any multiplication of the intensity spectrum by an arbitrary number (calibration factor to obtain absolute calibration) does not change the exponential slope and therefore does not change the obtained temperature. Furthermore it is necessary that the detector has an (almost) linear characteristic over raw emission intensity collected.

The course of the extracted hot carrier gas temperatures for the n- and p-type 16/14nm FinFETs (fig. 42 and 43) resembles closely the temperature trends known for planar FETs. The temperature rises almost linearly with the absolute value of drain voltage and decreases linearly with increasing absolute value of gate voltage. This makes sense: For a MOSFET or FinFET in saturation operating condition an increase of gate voltage at constant V_D leads to a decrease of electric field (thus decrease of carrier temperature), while an increase of drain voltage at constant V_G increases the electrical field below the fin (thus increase of carrier temperature). This is the first publication ever in PEM history that systematically traces the slope of the hot carrier gas temperature down to temperatures of $400-500K$. It is also the first time ever, that comprehensive spectral PE and temperature analysis is successfully performed for FinFETs. The detection of carrier gas temperatures around $400-500K$ with a simple InGaAs camera cooled to $\approx -70°C = 213K$ is also astonishing. Electron/hole temperatures below $\approx 500K$ have never been published before, allowing for a lot of room for speculations here. Furthermore it was thought before that only optimized far-infrared detectors with excessive cooling of camera and optical path (e.g. MCT detector cryogenically cooled down to $\approx 80K$ in [48]) could enter detection ranges around $500K$ and lower. This is obviously not the case, but of course such optimized detectors can be used to explore the low carrier gas temperature range between $300K$ and $500K$ even better and towards even much lower supply voltages than with InGaAs. Comprehensive analysis on this will be given in section 5.7 of this thesis.

From the physical point-of-view 300K as the lower temperature limit is fixed, as the charge carriers cannot have less energy than the average energy supplied by lattice temperature. In fact, the additional energy supplied by the electric field between source and drain increases the hot carrier gas temperature beyond lattice temperature. Obviously this additional energy increase by electric field becomes so low for modern low-voltage devices, that the carrier gas temperature remains in a small interval of $0-200K$ above lattice temperature for voltages lower than $0,8V$. The course of the hot carrier gas temperature over gate voltage has a similar behavior: Here the temperature decreases almost linearly with the absolute value of gate voltage ending in the $500K$-region. At close view a slight flattening of the temperature-over-voltage curves can be suspected around $500-650K$. This effect can be due to weaker signal-to-noise ratios caused by lower photon emission intensities, but there is also another probable reason for this: An asymptotical flattening of the linear temperature-voltage characteristic towards $300K$ is obligatory, as this temperature cannot be undercut. A further interesting observation can be made in the right image of figure 42, where by far the highest electron gas temperatures can be seen for gate voltages smaller than threshold voltage ($V_{th} \approx 0,27V$; compare to fig. 25 of section 5.1). The source-to-drain current in sub-threshold operation is very low compared to saturation mode, thus the PE intensity level is also low here. However, the electric field barrier to overcome towards drain is obviously much higher than for saturation mode, leading to very high carrier gas temperatures in sub-threshold operation.

Now that the qualitative energy distributions (fig. 39 and 40) and hot carrier gas temperatures

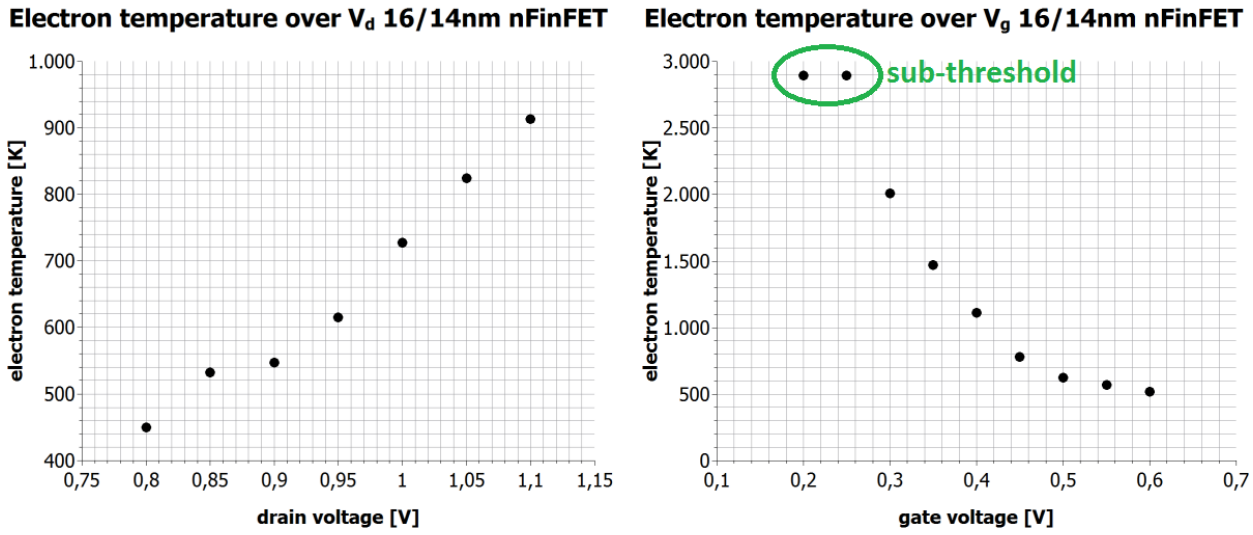

Figure 42: Electron temperature over drain voltage (left, at $V_G = 0,4V$) and over gate voltage (right, at $V_D = 1,1V$) for the small 16/14nm n-FinFET from Qualcomm Inc.

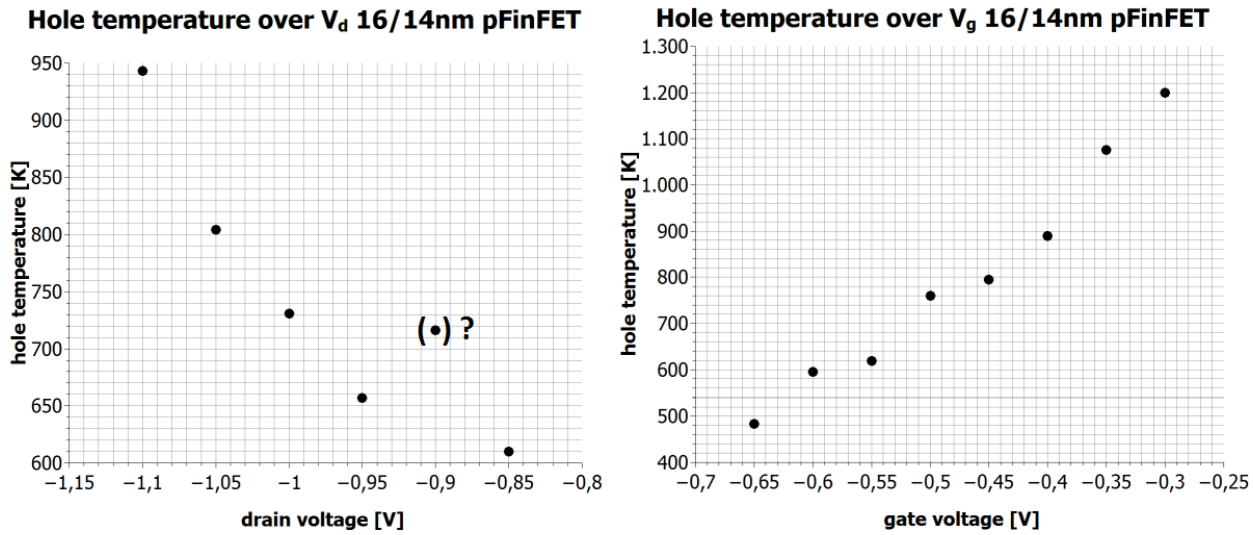

Figure 43: Electron temperature over drain voltage (left, at $V_G = -0,4V$) and over gate voltage (right, at $V_D = -1,1V$) for the small 16/14nm p-FinFET from Qualcomm Inc.

(fig. 42 and 43) have been extracted, further device parameters like maximum electric field in the channel, energy relaxation time, carrier velocity or even an estimate model for gate current over gate voltage at specific drain voltage can be derived with the formulas derived in the previous section. As an example the maximum electric field extraction will be shown here. Assuming $T_0 = 300K$ and a reasonable value of $\lambda = 4nm$ for the free mean carrier path of the FinFETs, an estimate for the maximum electric field in the channel for certain drain/gate voltage combinations follows directly from equation 5.12. The results are shown in figure 44 to 46 and can be compared to previously obtained data for planar MOSFETs (figure 44 right). The extracted maximum electric field strengths lie in a range of $0,5 \cdot 10^5 V/cm$ to $9 \cdot 10^5 V/cm$, depending on exact voltage conditions. The maximum electric field for the 16/14nm FinFETs at $V_d = 1,1V$ and $V_g = 0,4V$ is roughly a factor of 2 lower than for the $1,5\mu m$-n-MOSFET at $V_d = 5,8V$ and $V_g = 4V$ from [50]. The PE spectra, energy distributions, hot carrier gas temperatures and maximum electric fields presented in this section form a proof-of-concept for the applicability of SPEM to state-of-the-art low-voltage devices. Further device parameters like energy relaxation time, carrier velocity or substrate current are also extractable.

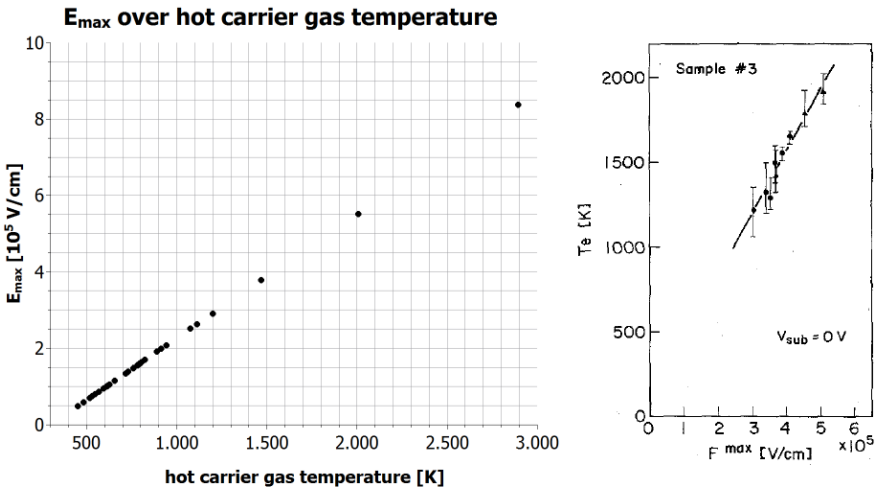

Figure 44: Correlation between maximum electrical field in the channel and hot carrier gas temperature for the 16/14 nm FinFETs (left) and a $1,5\mu m$-MOSFET (right). Right image taken from [50].

The almost linear dependence of hot carrier gas temperature on gate and drain voltage can be used to draw a final conclusion on the total integrated photon emission intensity W_{total} in dependence of the respective voltages using formula 5.11 from above:

$$W_{total} = \int_{\nu_{min}}^{\nu_{max}} W_\nu d\nu \sim \int_{\nu_{min}}^{\nu_{max}} e^{-\frac{h\nu}{Tk_B}} d\nu = -\frac{Tk_B}{h} e^{-\frac{h\nu}{Tk_B}} \quad . \tag{5.16}$$

ν_{min} is the lower photon frequency border and ν_{max} the upper photon frequency border of the PE detector. As photon emission is proportional to the number of charge carriers $|I_{DS}/e|$ flowing through the channel in a given time interval, W_{total} can be specified even more accurate as

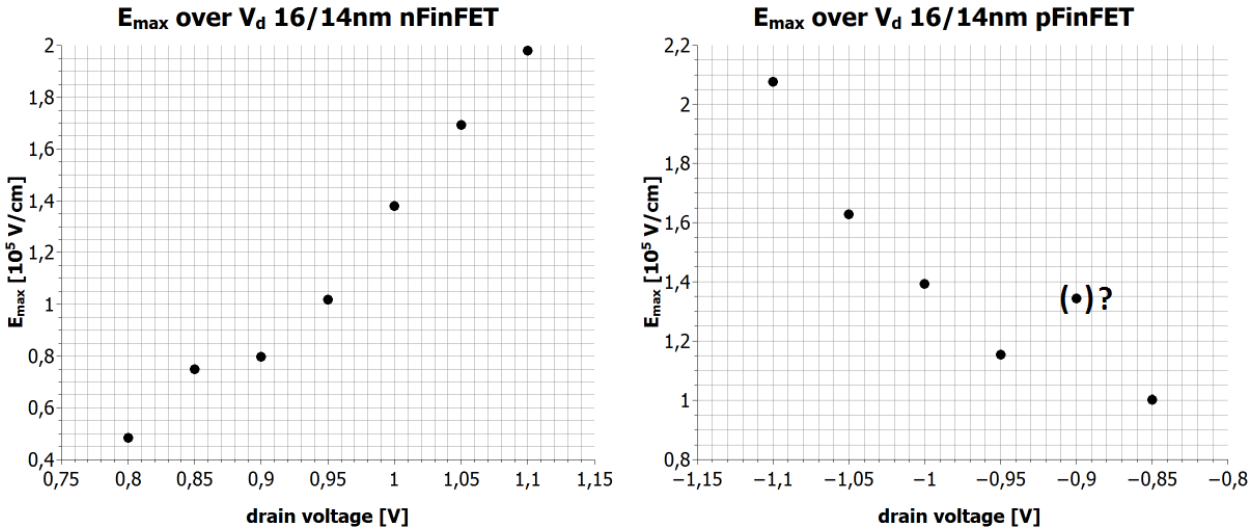

Figure 45: Maximum electric field in the channel over drain voltage for 16/14nm n-type FinFET at $V_g = 0,4V$ (left) and p-type FinFET at $V_g = -0,4V$ (right).

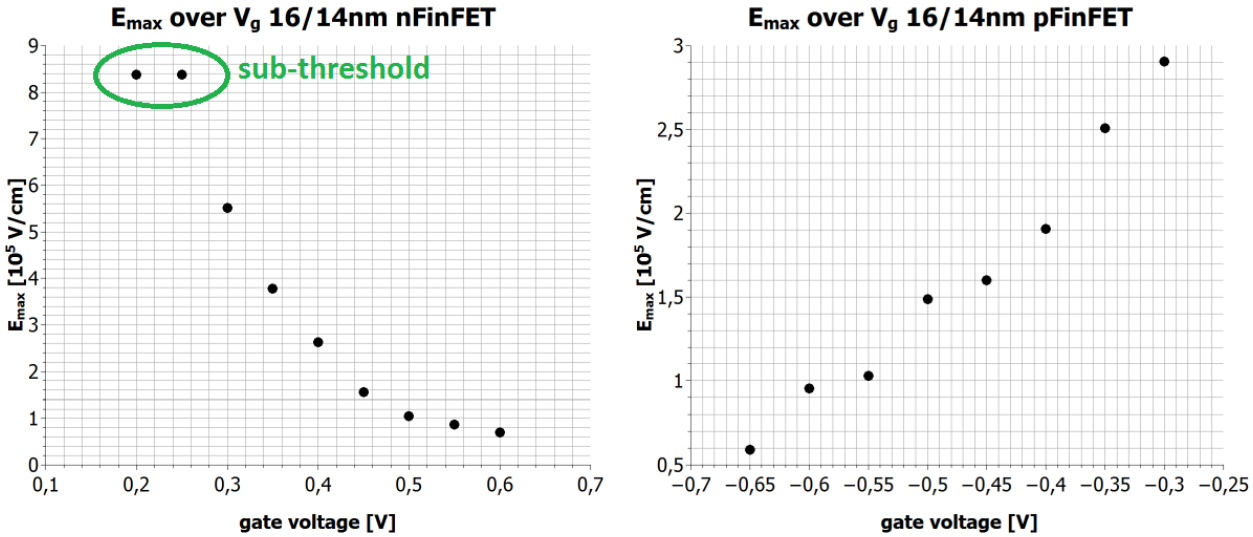

Figure 46: Maximum electric field in the channel over gate voltage for 16/14nm n-type FinFET at $V_d = 1,1V$ (left) and p-type FinFET at $V_g = -1,1V$ (right).

$$W_{total} = -\left[c_1 \cdot \left| \frac{I_{DS}}{e} \right| \cdot \frac{\left(c_2 \cdot \frac{V_{DS}}{V_{GS}} - T_0 \right) \cdot k_B}{h} e^{\left(-\frac{h\nu}{\left(c_2 \cdot \frac{V_{DS}}{V_{GS}} - T_0 \right) \cdot k_B} \right)} \right]_{\nu_{min}}^{\nu_{max}} \tag{5.17}$$

using $T - T_0 = c_2 V_{DS}/V_{GS}$ with the technology specific constants c_1 and c_2, which can be determined easily by two PE intensity measurements using a PE detector with absolute calibration. Strictly speaking, formula 5.17 is only valid for a MOSFET/FinFET in saturation, but seems to be applicable for gate voltages slightly lower than threshold voltage as long as drain voltage is high enough. It is important to bear in mind that the formula is only valid for carrier gas temperatures above $\approx 300 - 400K$, where an almost linear dependence over gate/drain voltage can be assumed. Development of a more accurate theoretical model for the this region and a new model to describe the spectral phenomena below $400 - 500K$ will have to be developed, if device parameter analysis with SPEM is intended for supply voltages approaching $0,5V$ and lower.

Formula 5.17 is also capable of describing physically the bell-shape form of integrated photon emission over gate voltage at constant V_D as well as the exponential decrease of integrated photon emission over inverse drain voltage at constant V_G, which were already shown and explained in section 5.1. A similar formula was developed/shown in [23] , [28] and [22] with a completely different theoretical approach exploiting the (risky) correlation between substrate current and photon emission over gate voltage.

Before concluding this chapter it is worth mentioning another possible application for device parameter extraction with spectral photon emission: This analysis can also be used to continuously monitor device degradation during external stress via precise observation of changes in relevant device parameters (e.g. carrier temperature, electric field, mean free carrier path). This can be very profitable for device analysis during reliability assessments.

5.4 Failure analysis with PEM+SPEM

Already over 10 years ago photon emission microscopy as a technique for the failure analysis of integrated circuits was predicted to die out soon due to the emergence of low-voltage devices [9, 10]. In the meanwhile the situation has developed quite differently: The development of deeper infrared detector equipment with high sensitivity (MCT, Emmi-X etc.) can to a certain point compensate for the PE signal drop in low-power devics. Also the predicted signal decrease rates [22] have proven to decrease not as fast with technology node size as feared. This section is supposed to give successful FA application examples of PEM and SPEM on recent 14-40nm FinFET technology as well as to give a comprehensive analysis of PE-voltage relations for up-to-date devices. Further FA applications of photon emission techniques can be found in scientific literature (e.g. [13, 29]). Some contents as well as figures of this section were already published in the authors contribution to ISTFA 2017 [68] (FA on large 16/14 nm n-FinFET). Further contents (FA on 24-40nm FinFETs) are currently submitted for publication at ESREF 2018 [70].

The PEM/SPEM setup at TU Berlin includes an InGaAs camera (fig. 31) and a Phemos-1000, which is roughly 20 years old. The measurement hardware therefore is not completely state-of-the-art as deeper infrared cameras with higher sensitivity are available on the market. It will be shown that, even with the hardware installed at TU Berlin, failure analysis with photon emission and even spectral photon emission on $14-40nm$ FinFETs is still well possible far below $1V$ supply voltage. PEM signals were detectable down to $\approx 0,6V$ for PEM and $\approx 0,75V$ for spectral analysis both with SIL. Given these parameters, it can be stated that FA with PEM and SPEM are possible even for modern $\approx 10nm$-devices and voltages $\leq 0,5V$, when optimized optics and specialized infrared detectors are used.

All emission measurements presented in the next subsections were done with an InGaAs camera cooled down to $-70°C$. No additional cooling (e.g. for optics, prism, device etc.) was needed. All measurements concerning $24-40nm$ FinFETs were carried out on wafer-level by frontside measurements. The frontside measurements had to be carried out without SIL. If the samples had been measured from the backside, one could have expected higher PE signals and an expansion of voltage range of $\approx 0,15V$ towards even lower voltages by SIL use. There was only a limited number of test structures available, which is the main reason for not cutting individual dies from the wafer and preparing them for backside access. This procedure would have carried a high risk of damaging the very small and sensitive structures e.g. in bonding, package moulding and substrate thinning process, which is the reason why it was decided to limit the measurements on all $24-40nm$ FinFETs to frontside access with manipulators and prober needles. As the wafers only contained various test structures, the number of metal levels at the frontside was not high, enabling frontside PEM/SPEM-analysis without noticeable absorption by metal layers etc. The Qualcomm 16/14nm FinFETs manufactured by TSMC were measured from the backside of the chip mounted on a customized socket board using a Hamamatsu Nanolens (SIL). For backside analysis the bulk silicon was thinned down to $\approx 70\mu m$ and polished to get a smooth backside surface. Absorption of light within the silicon substrate was taken account of in the evaluation process of the data.

When observing the analysis presented in the next subsections one has to bear in mind that electrical characteristics of individual devices are usually not available for measurement, as the structures are deeply integrated into the logic of an integrated circuit. Here, the electrical data is given for

comparison with emission results and for confirming the failure indications drawn from them. In a real commercial IC this is not possible and photon emission data is in some cases the only source to get reliable information about (dys-)functionality and operating parameters of a single transistor.

Please note that the failure mechanisms presented here are not general failures contained on all chips manufactured by a certain semiconductor company or research institute. The test structures were designed and produced for FA testing and parameter studies and therefore carry certain irregularities leading to abnormal behavior in various ways. Nonetheless all failure mechanisms detected here are typical for integrated circuits and may occur on any commercial chip.

5.4.1 40nm n-FinFET

The PE signal over voltage slopes for the 40nm n-FinFET in figure 47 are suspicious at first sight: While the logarithmic-PE-over-inverse-drain-voltage-curve on the right shows the expected linear decrease, the PE signal over gate voltage is constant throughout the whole nominal voltage range. To confirm this behavior, the emission measurements were repeated for a higher drain voltage ($1,3V$ instead of $1,1V$) and again with the same voltage conditions for a technologically identical FinFET on another die (tier 2) yielding exactly the same constant PE-over-gate-voltage result. Normally the curve should have a bell-shape (compare to ideal FET emission behavior explained in section 5.1).

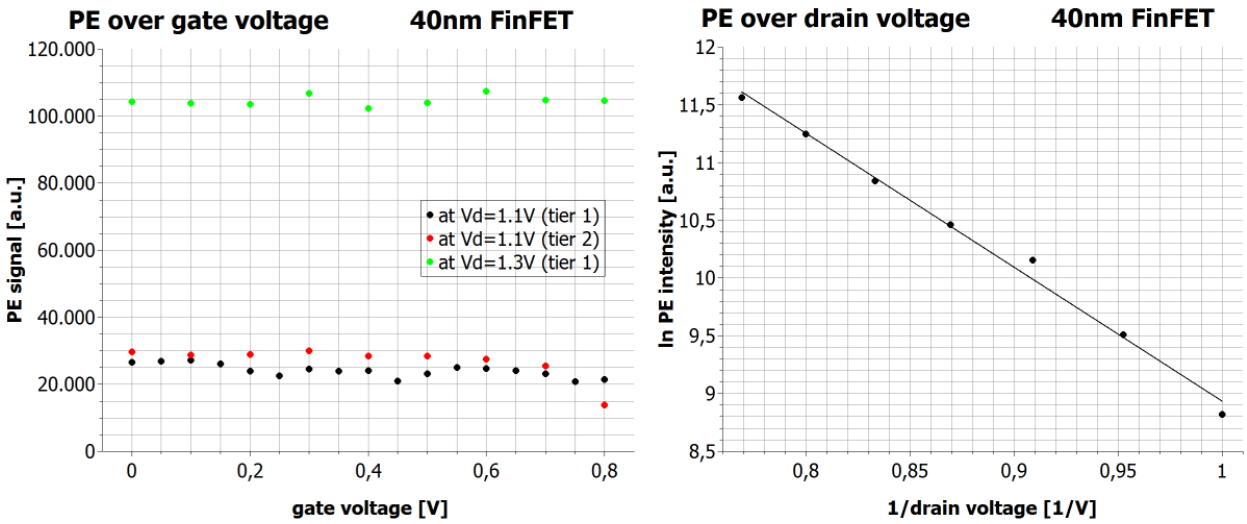

Figure 47: PE signal slope over gate voltage for various drain voltages (left) and logarithmic PE signal over inverse drain voltage (right) for the 40nm n-FinFET at a gate voltage of $0,9V$. Frontside measurement without SIL.

For further understanding of the situation the respective emission spectra for various drain and gate voltages were recorded (fig. 48). Here the aforementioned abnormality related to photon emission over gate voltage is supplemented by further proof: While the decrease of drain voltage issues the known red-shift of the spectra towards higher wavelengths and lower intensities within the spectral detector range, the spectra don't seem to be affected by gate voltage changes at all. Those spectra lie within a very narrow emission band for various gate voltages and don't change slope or total intensity noticeably. This observation is confirmed by extraction of the electron temperatures (fig.

49) for all spectra along the exponential curves as described in an earlier chapter (section 5.3). While the temperature rises linearly over drain voltage as expected, the temperature is almost independent from gate voltage. This leads to the suspicion, that the recorded emission does not originate from normal FET behavior (i.e. emission from hot electrons in the channel), but from some parasitic current path from source to drain through the substrate in between. This explains why the emission is independent of gate voltage: The parasitic path probably lies too far away from the fin/gate/channel area of the FinFET to be noticeably effected by any change of gate voltage and therefore is independent of V_G. It remains to address the question, why the current path is dependent on drain voltage in a way very similar to a completely functional transistor. The parasitic current path has to overcome the high electric field at the drain-to-substrate pn-junction to finally reach drain. The electric field at this pn-junction is increased with increasing drain voltage similar to the increase of the electric field with drain voltages in a FET channel and thus produces similar (spectral) emission patterns.

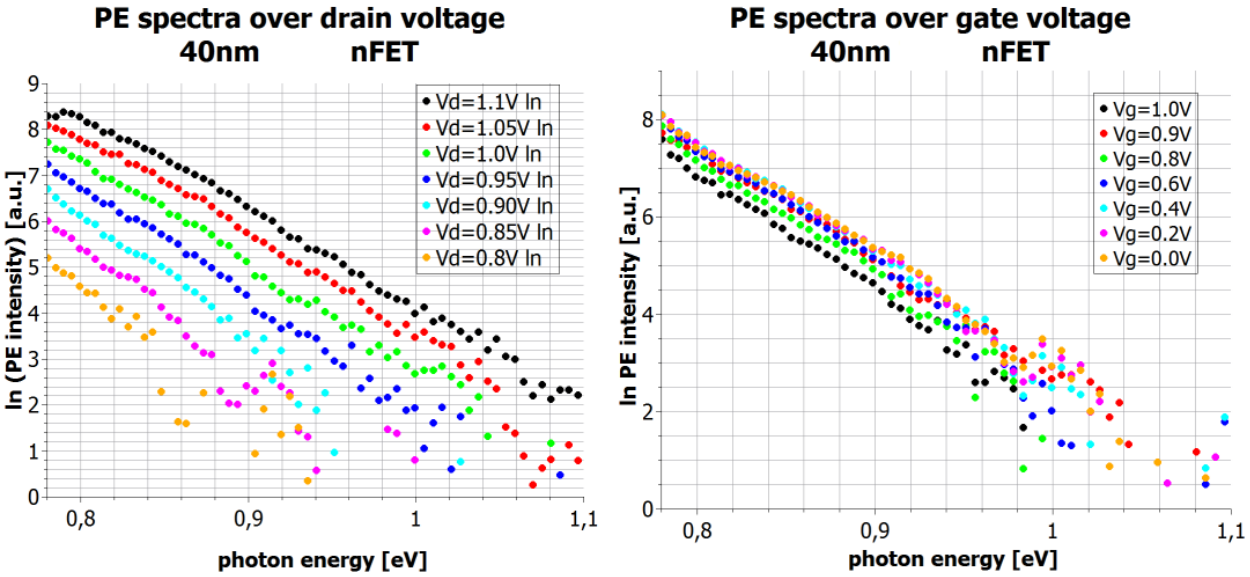

Figure 48: Photon emission spectra of the 40nm n-FinFET for various drain voltages (left, at $V_G = 0,9V$) and for various gate voltages (right, at $V_D = 1V$). Frontside measurement without SIL.

As all experiments were carried out on test structures, which were connectable individually, the analysis above can be verified or falsified by inspection of the electrical characteristics of the device: The output characteristic of the 40nm n-FinFET (fig. 50) reveals a striking abnormality: There seems to be a certain offset current for each drain voltage, which is added to the normal FET curve so that all output curves are shifted by a certain angle counter-clockwise. The offset current does not seem to interfere with normal electrical FET behavior, but is simply added to it as an offset for each value of V_D. The FET channel is functioning well, but the overall device functionality suffers from a parallel current independent of gate voltage. This parallel current has a roughly ohmic characteristic (see black $V_G = 0V$-curve) with a slight bend for lower drain voltages.

Investigating further into the situation, the n-FinFET's substrate current (fig. 51) casts light into the shadow: While photon emission is not necessarily linked to substrate current for all MOSFETs

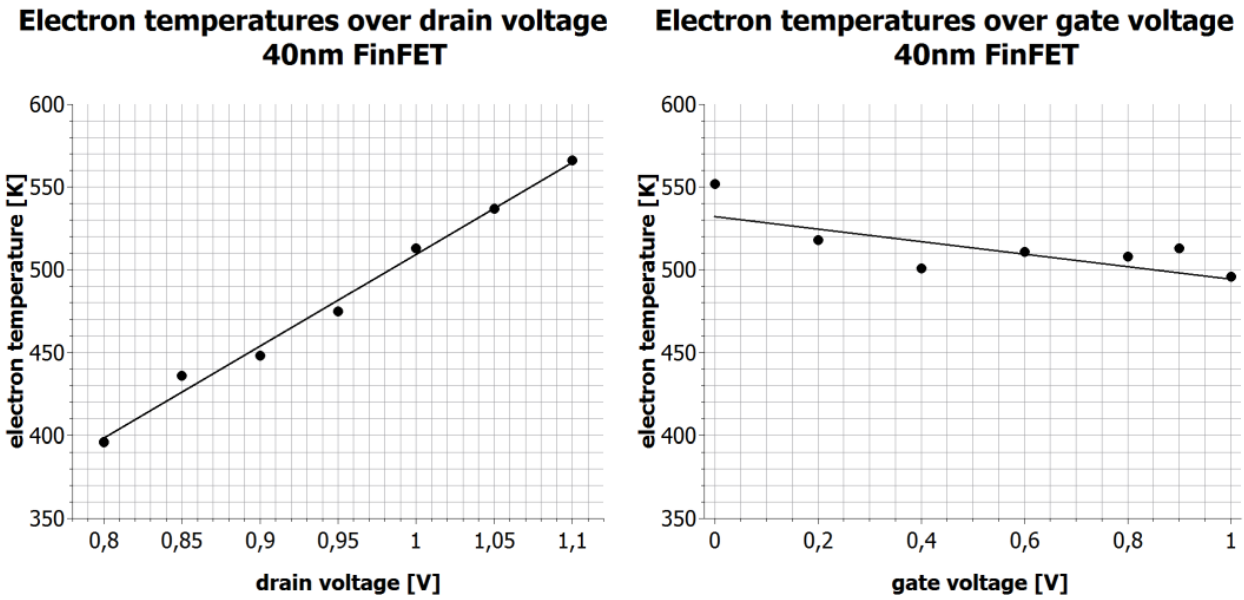

Figure 49: Electron temperature over drain voltage (left, at $V_G = 0,9V$) and gate voltage (right, at $V_D = 1V$) extracted by fit of the linear PE spectra regions of figure 48

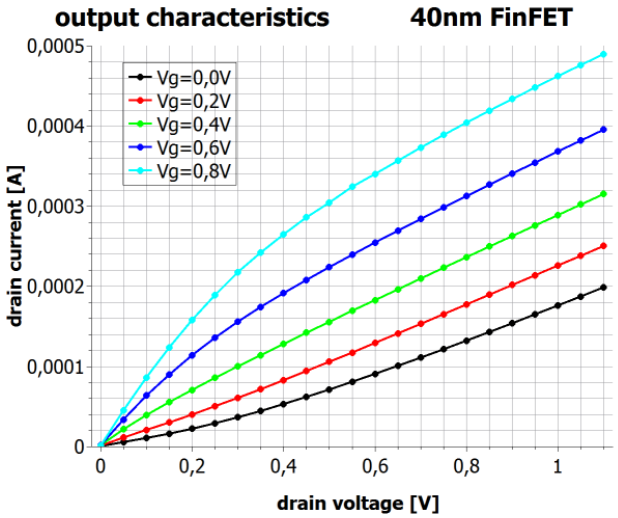

Figure 50: Output characteristics of the 40nm n-FinFET. Nominal voltage was $0.9V$.

or FinFETs as stated in an earlier section, here the link is visible: The substrate current is roughly constant over gate voltage (like photon emission, spectra and electron temperature), but at closer look a bell-shape can be identified (right image). Obviously the bulk current has a strong offset caused by the parasitic current path accompanied by a small bell-shape substrate current from normal n-FinFET operation, which only makes up less than 10% of the total substrate current. Coming back to photon emission behavior, it can be stated that PE analysis and conclusion given above are reasonable. While normal transistor current and parasitic current have similar values for gate voltages between $0,4V$ and $0,8V$, the scattering processes of both seem to be different. Obviously the scattering process leading to photon emission is roughly a factor of 10 more effective for the parasitic current path than for normal FET emission from the channel. Thus the electric field would be much higher for the parasitic light emission process. It therefore dominates standard FET emission with the latter vanishing in the noise regime ($\leq 10\%$).

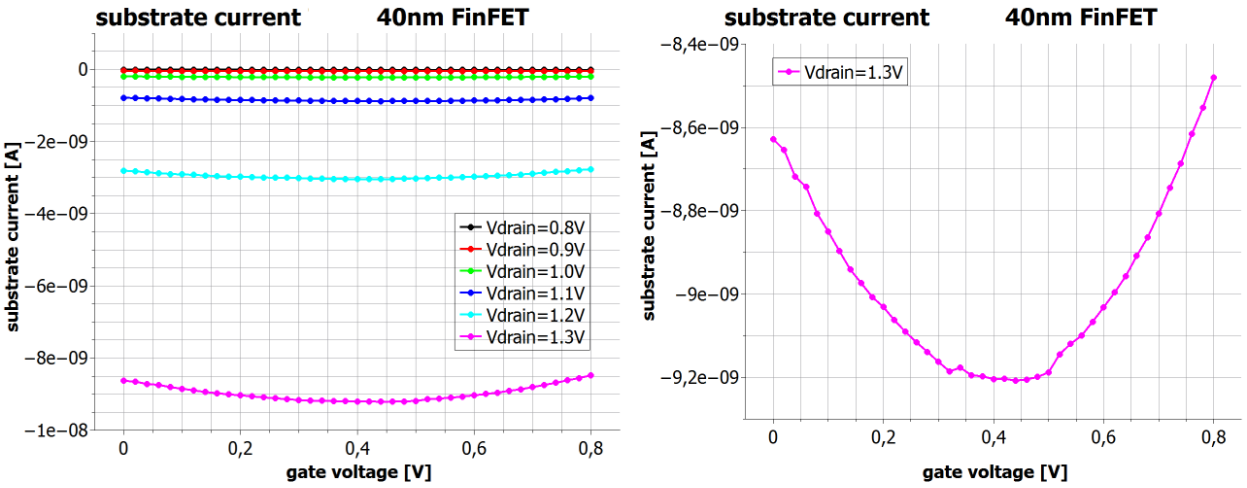

Figure 51: Substrate current measured for the 40nm n-FinFET (left) and enlarged image detail for the substrate current at $V_D = 1,3V$ (right). The bell-shape on the right can be observed for every substrate current curve for all drain voltages when the image is enlarged to the corresponding current interval.

5.4.2 24-30nm FinFETs

In this subsection photon emission of a set of 4 n-type and 1 p-type FinFET with different gate lengths will be investigated. These FETs were manufactured in a different technology compared to the 40nm n-FinFET above. Again the PE analysis starts with the simple emission-signal-over-drain/gate-voltage slopes, which are unsuspicious this time (figures 52 and 53). The normal linear decrease of logarithmic PE intensity over inverse drain voltage can be seen for all FinFETs. The PE curve over gate voltage shows the common bell-shape, but is shifted towards higher gate voltages for all n-FinFETs. This is no indicator for abnormal behavior, but is related to the presence of strong short channel effects in very small devices ($\approx\leq L_G = 50nm$) as stated and explained in [22]. For the p-FinFET the bell-shape is centered within the nominal voltage range ($V_{nom} = 0,8V/-0,8V$ for this technology) as for most other devices, especially larger planar MOSFETs. Obviously the short-channel effects are not as strong for p-type charge carriers (holes) than for n-type charge carriers (electrons), which is probably due to the higher effective mass and therefore smaller velocity of holes compared to electrons in silicon.

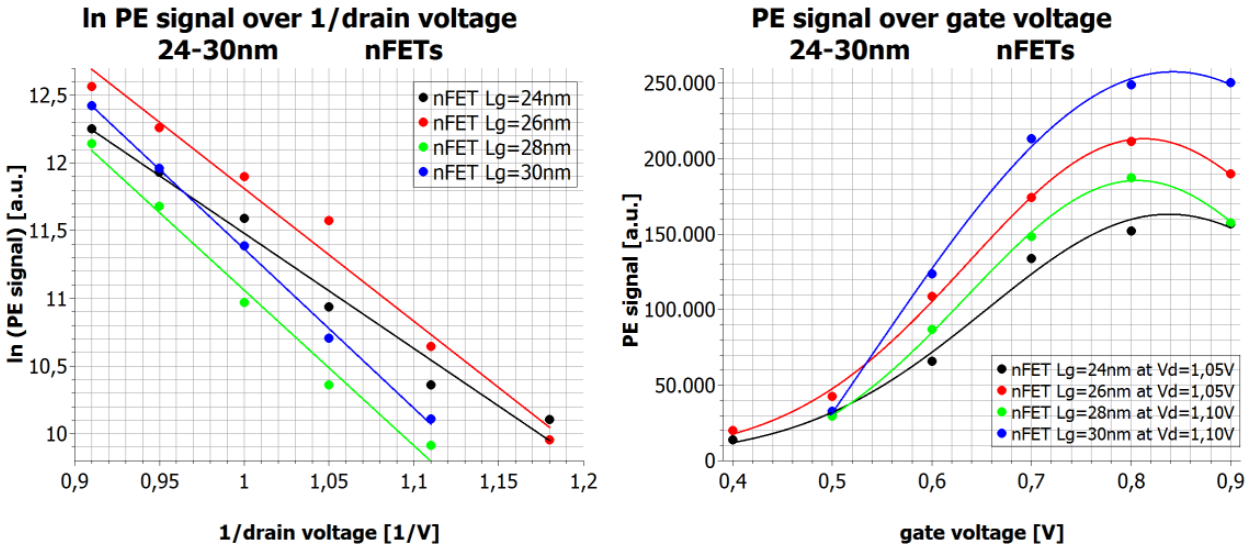

Figure 52: Logarithmic PE signal over inverse drain voltage for $V_G = 0,8V$ (left) and PE signal slope over gate voltage at different drain voltages (right) for the 24-30nm n-FinFETs. Frontside measurement without SIL.

While the PE spectra over drain voltage (left image in fig. 54 to 58) are again unsuspicious, the spectra over gate voltage are raising first questions: While the spectra occupy a larger band compared to the 40nm n-FinFET above, their slope does not seem to decrease linearly with gate voltage as it should do regarding normal FET operation.

This observation is confirmed with the extraction of electron/hole temperatures for all n-/p-FinFETs along the exponential slope of the spectra. For the n-FinFETs (figure 59) the expected normal linear rise of hot electron gas temperature with drain voltage can be seen for all different gate lengths. Interestingly, the electron temperatures take significantly higher values for the n-FinFETs with smaller gate lengths (i.e. $24nm$ and $26nm$) and have a much weaker dependence on drain voltage than for the devices with larger channel length. This adds further proof to the fact, that photon

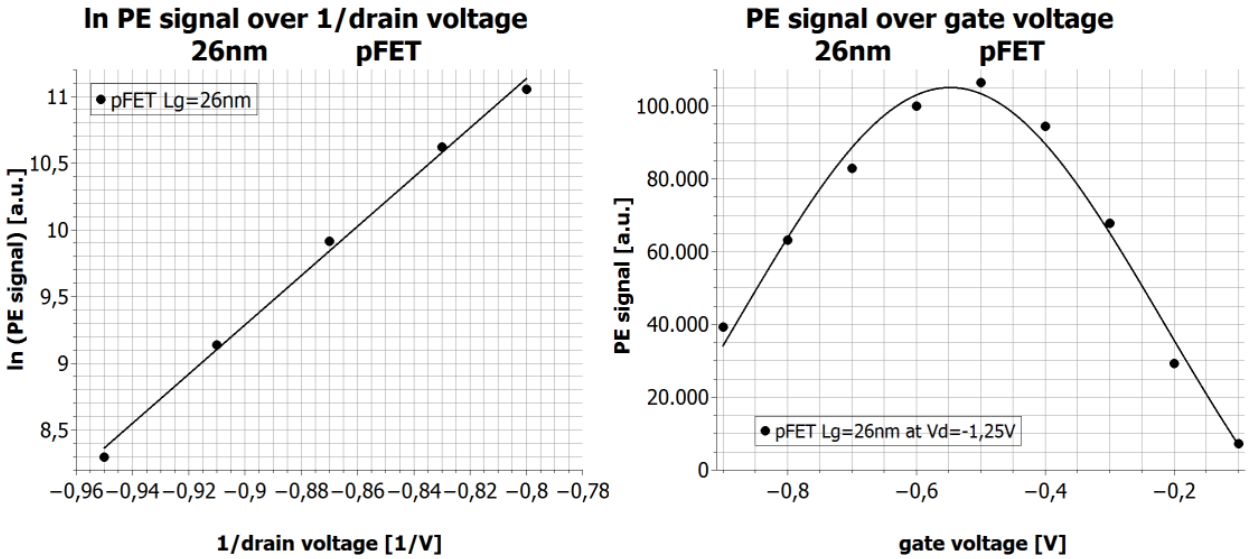

Figure 53: Logarithmic PE signal over inverse drain voltage for $V_G = -0,8V$ (left) and PE signal slope over gate voltage at $V_D = -1,25V$ (right) for the 26nm p-FinFET. Frontside measurement without SIL.

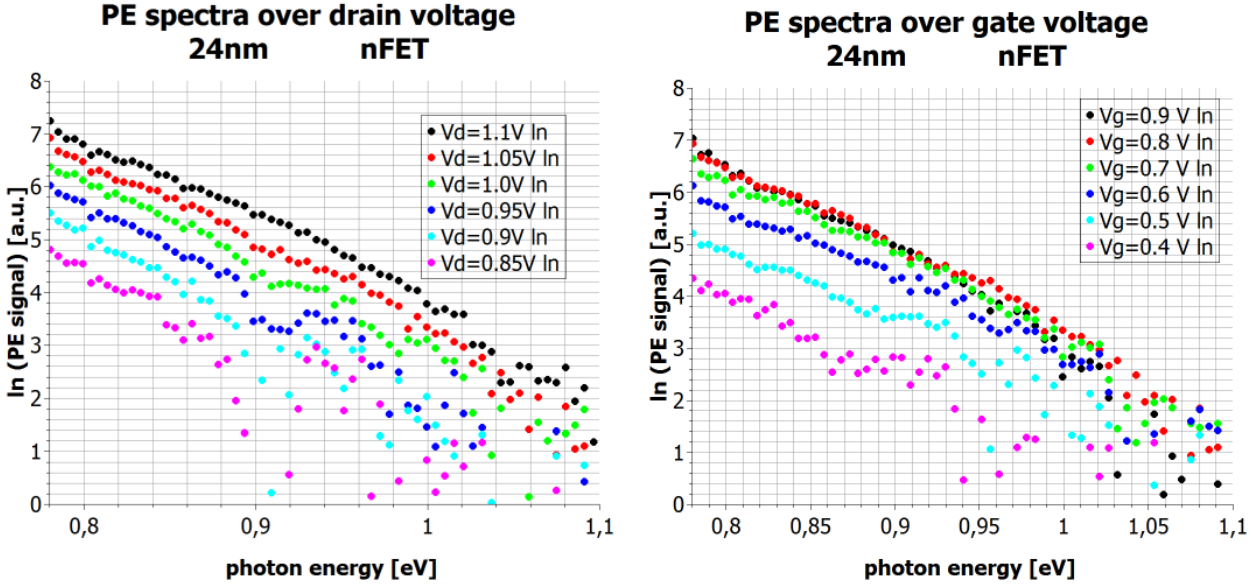

Figure 54: Photon emission spectra of the 24nm n-FinFET for various drain voltages (left, at $V_G = 0,8V$) and for various gate voltages (right, at $V_D = 1,05V$). Frontside measurement without SIL.

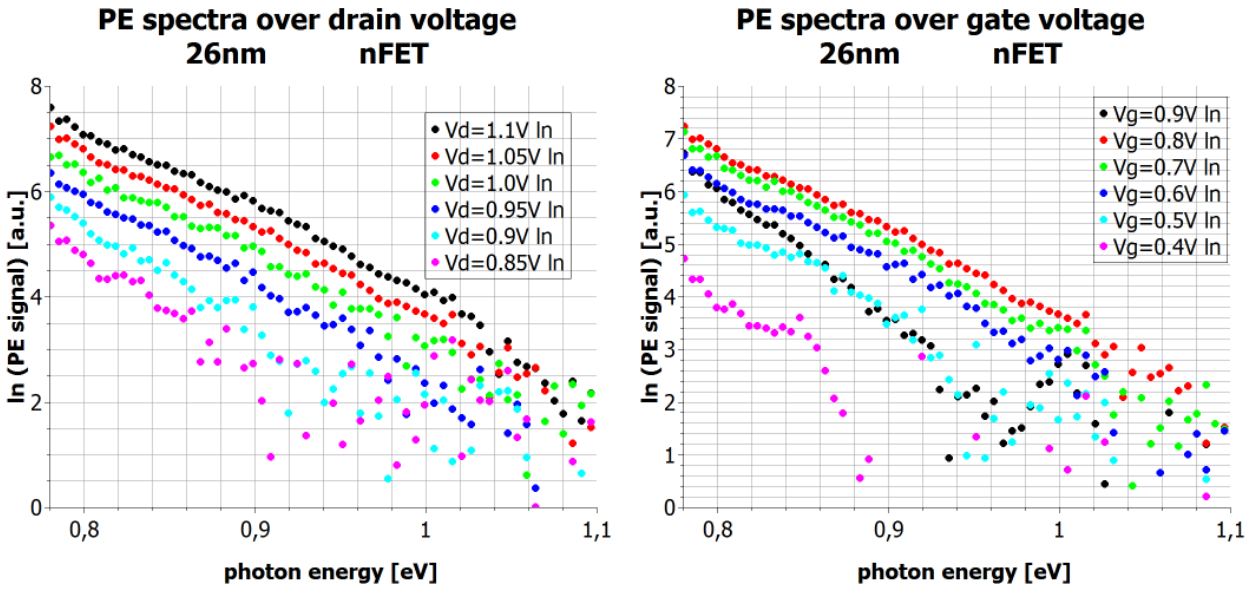

Figure 55: Photon emission spectra of the 26nm n-FinFET for various drain voltages (left, at $V_G = 0,8V$) and for various gate voltages (right, at $V_D = 1,05V$). Frontside measurement without SIL.

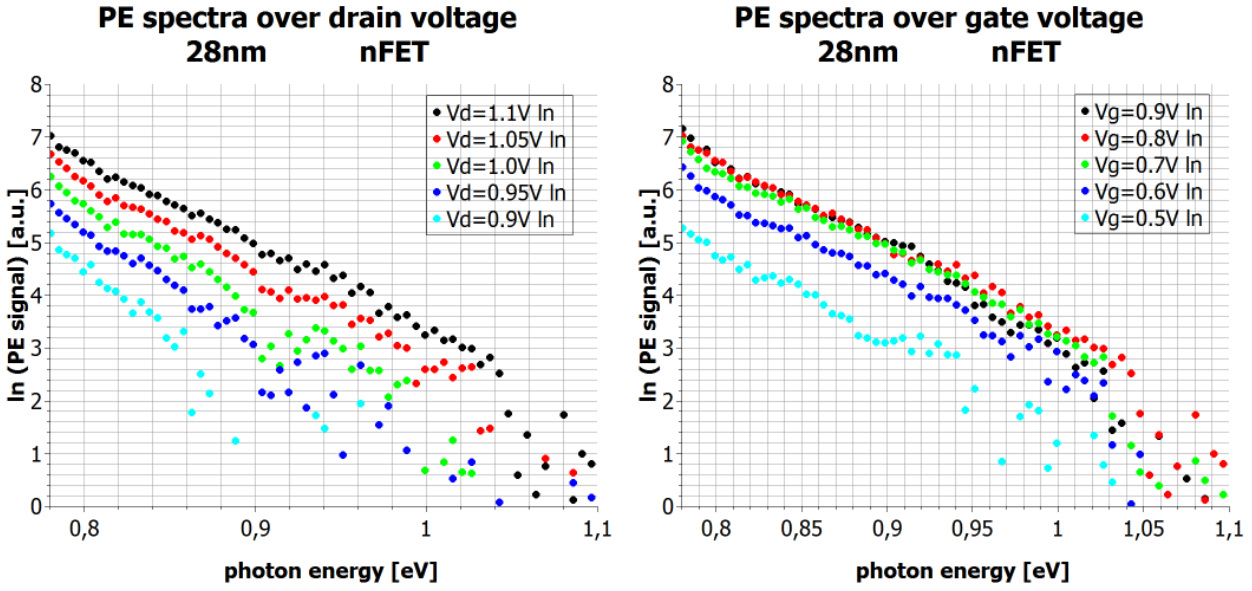

Figure 56: Photon emission spectra of the 28nm n-FinFET for various drain voltages (left, at $V_G = 0,8V$) and for various gate voltages (right, at $V_D = 1,10V$). Frontside measurement without SIL.

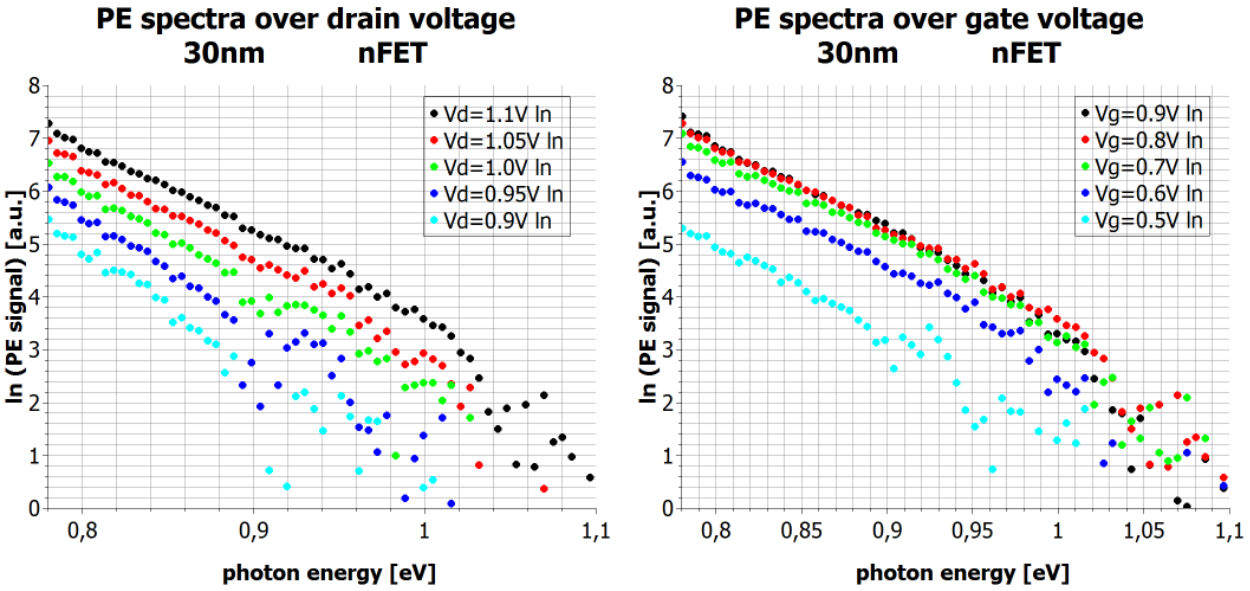

Figure 57: Photon emission spectra of the 30nm n-FinFET for various drain voltages (left, at $V_G = 0,8V$) and for various gate voltages (right, at $V_D = 1,10V$). Frontside measurement without SIL.

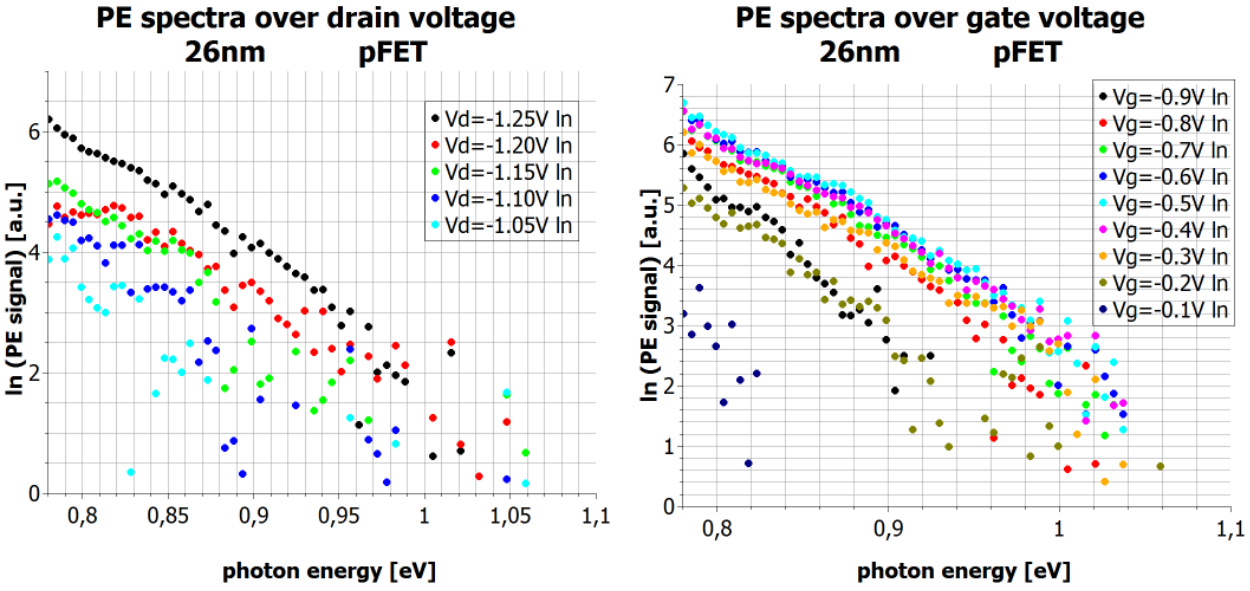

Figure 58: Photon emission spectra of the 26nm p-FinFET for various drain voltages (left, at $V_G = -0,8V$) and for various gate voltages (right, at $V_D = -1,25V$). Frontside measurement without SIL.

emission intensity in the near-infrared region ($\leq 1600nm$) decreases much less than expected with decreasing node size. Obviously the red-shift of PE spectra is not as strong as expected. A look to the image on the right of the same figure reveals a conspicuous dependence of electron temperature on gate voltage for all different n-FinFETs. While for the $28nm$ and $30nm$ n-FinFETs the elctron temperature is roughly constant here, the hot electron gas temperatures for $24nm$ and $26nm$ n-FinFET have strong deviations without a clear tendency, which does not correspond to healthy FET behavior. The same holds true for the $26nm$ p-FinFET (figure 60), where the strong hole temperature deviations occur at both ends of the nominal gate voltage range and take constant values for gate voltages in between. The hole temperatures over drain voltage (left image) don't show the expected linear rise with drain voltage either, but the temperature results for the p-FinFET have to be with caution generally, as spectral PE intensities and signal-to-noise ratios here were much lower (see figure 58) compared to the n-FinFETs and had to be acquired at significantly higher absolute drain voltages. As a summary, the PE, spectra and temperature analysis clearly indicates dysfunctional FET behaviour for all devices, but in this case it is not easy to conclude a likely physical failure cause.

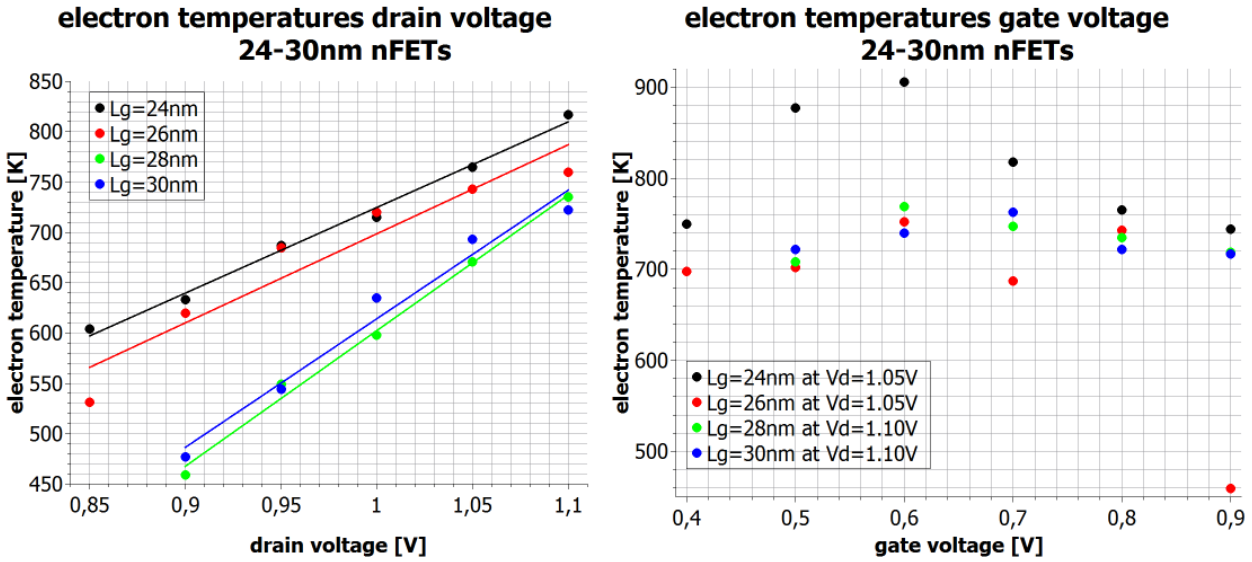

Figure 59: Electron temperature over drain voltage (left, at $V_G = 0,8V$) and gate voltage (right, at different V_D) extracted by fit of the linear PE spectra regions of figures 54 to 57.

To clear the physical cause of the failure mechanism found with PEM/SPEM analysis above, the electrical characteristics are brought in at this stage. The output characteristics (figure 61 to 63) are unsuspicious and correspond to normal FET behavior with a strong presence of short channel effects for the shorter $24nm$ and $26nm$ n-FinFETs (steeper current slope in saturation). The answer to the question about the physical failure mechanism is finally delivered by the substrate current investigations presented in figures 64 and 65. Here an abnormal, partly exponentially rising substrate current over gate voltage can be seen. Apart from the strange almost exponential rise towards higher gate voltage, the absolute values of the substrate current are by far to high, even surpassing respective transistor on-current values (!) for gate voltages close to $V_{nom} = 0,8V$. Even with given fully functional transistor output characteristic as in this case, this many orders too high

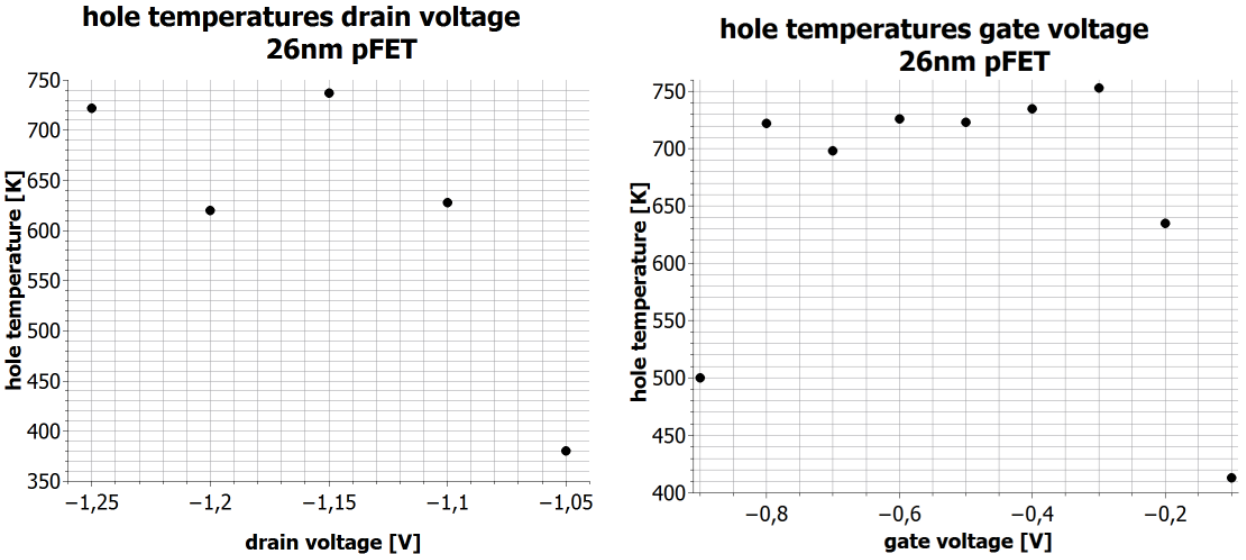

Figure 60: Hole temperature over drain voltage (left, at $V_G = -0,8V$) and gate voltage (right, at $V_D = -1,25V$) extracted by fit of the linear PE spectra regions of figure 58.

substrate current would be fatal for reliability and power consumption of any IC. Further electrical measurements proved that the high substrate current originated from the gate contact (while the gate material was obviously undamaged enabling normal FET output characteristics) and obviously effected the photon emission process at the channel in a way that PE emission was not normally influenced by gate voltage, but disturbed massively. The PE-dependence on drain voltage was left unaltered by this failure process, which indicates that the values of the high electric field in the channel were not influenced, but more the scattering mechanism leading to emission (probably by charge carriers flowing from gate area into the substrate). The root cause of this failure mechanism is probably a drain/source diffusion doping failure close to the gate/fin area somehow enabling carriers to bypass the gate dielectric and flow into the substrate or vice versa.

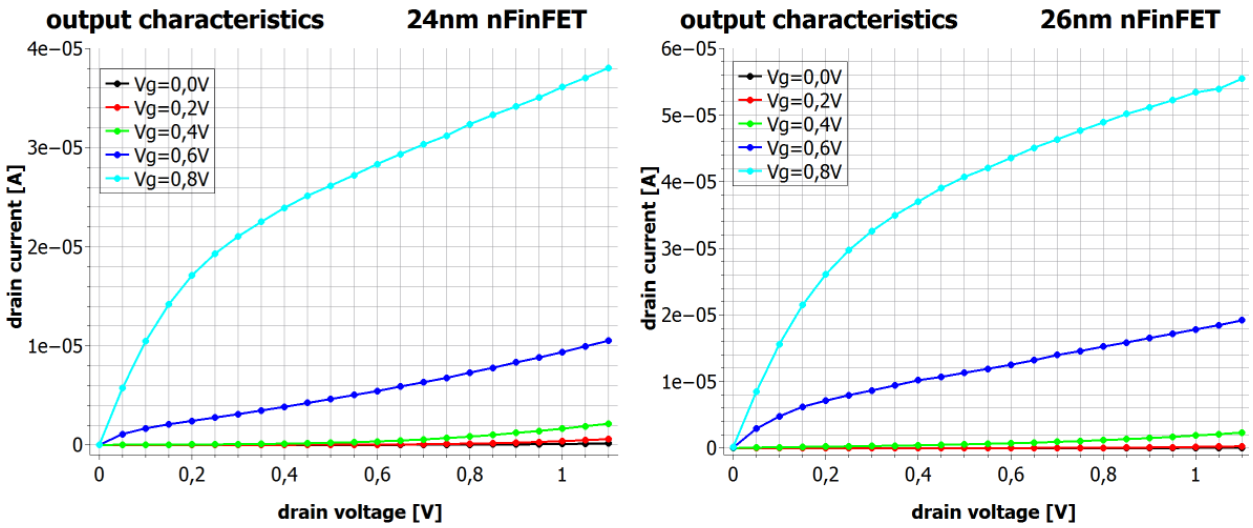

Figure 61: Output characteristics of the 24nm (left) and 26nm (right) n-FinFET. Nominal voltage was $0.8V$.

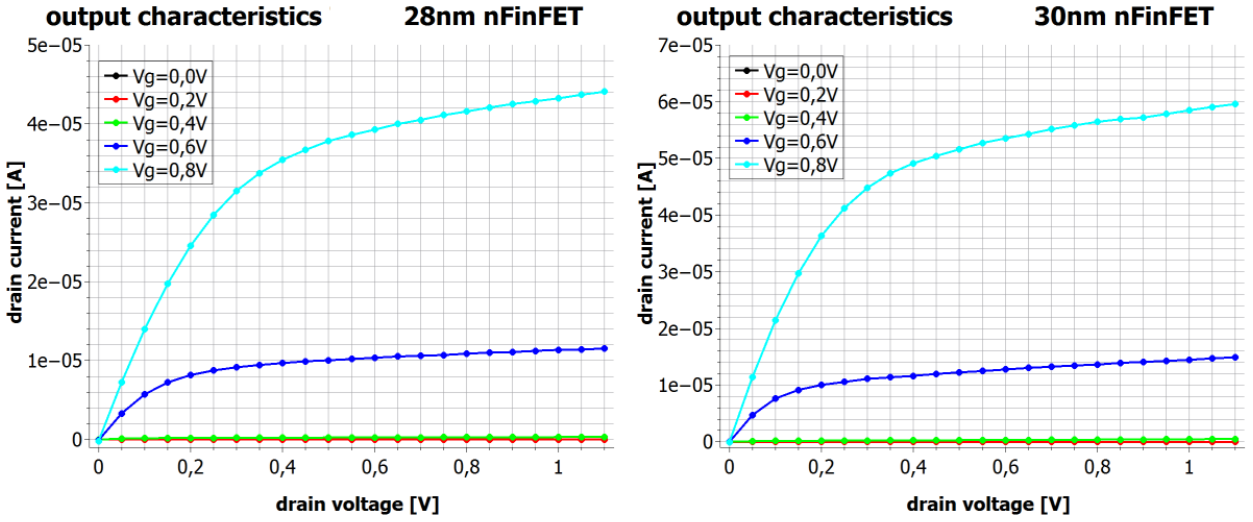

Figure 62: Output characteristics of the 28nm (left) and 30nm (right) n-FinFET. Nominal voltage was $0.8V$.

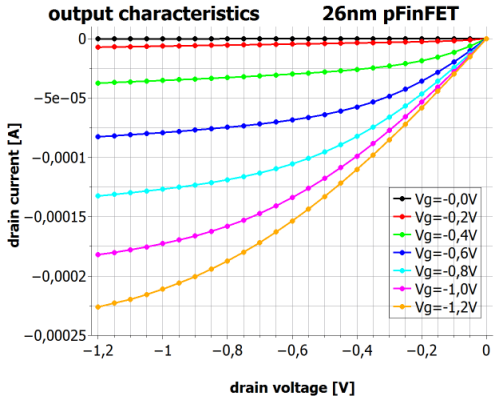

Figure 63: Output characteristics of the 26nm p-FinFET. Nominal voltage was $-0.8V$.

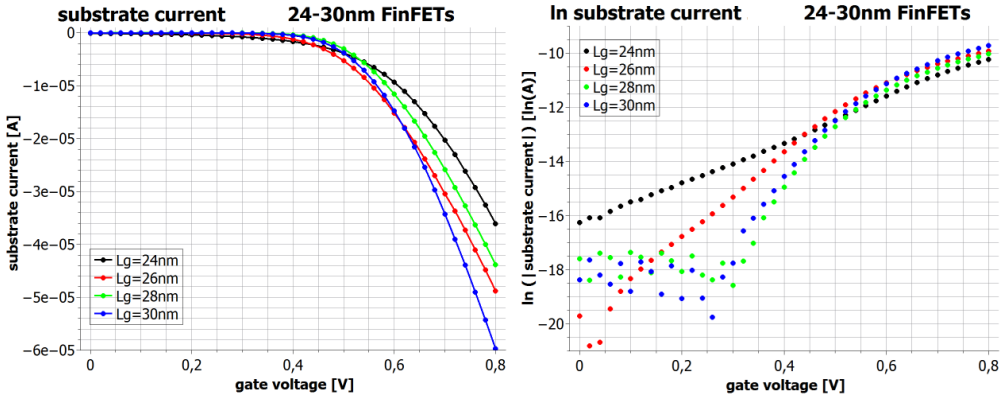

Figure 64: Substrate current measured for the 24-30nm n-FinFETs in linear (left) and logarithmic (right) scale at $V_D = 1V$.

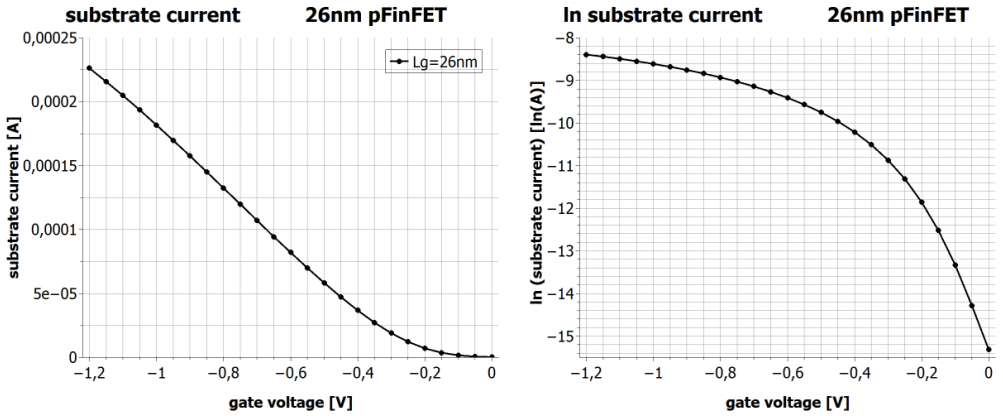

Figure 65: Substrate current measured for the 26nm p-FinFET in linear (left) and logarithmic (right) scale at $V_D = -1V$.

5.4.3 Large 16/14nm n-FinFET from Qualcomm Inc.

The PE investigations on the large n-FinFET of Qualcomm Inc. yielded a suspicious signal behavior over gate voltage when compared to the results for the small n-FinFETs (fig. 66 right). Small and large n-FinFET were technologically identical apart from a 12 times higher gate width/number of fins of the large n-FinFET. Therefore the same qualitative photon emission slope over gate voltage was expected for both n-FinFETs, which was not the case. The bell-shape emission curve for the large n-FinFET is clearly shifted to the left by almost $0,2V$(!) compared to the small n-FinFET. Also the quantitative signal strength for the large device only reached about twice the maximum value as for the small device in contrary. Due to gate width ratio, an increase factor of 12 for PE would have been expected here. Both findings clearly indicate the presence of a abnormal device functionality here. But as always it is important to be careful with seeming deviation from standard behavior: In a similar comparison for small n- and p-FinFET a similar shift (but not as large) shift of the bell-shape can be seen (fig. 66 left). This time the deviation is not a necessary indicator for abnormal behavior of both or at least one of the small FinFETs: p- and n-type FinFET are not technologically identical (e.g. different doping levels, different process technology etc.) so that slight deviations between emission behavior have to be expected consequently.

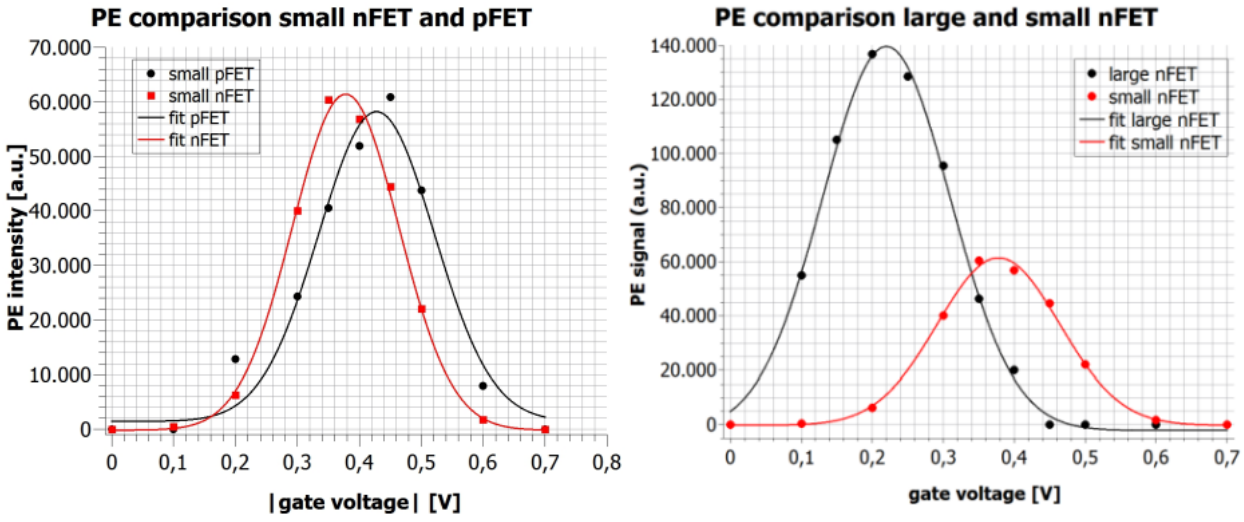

Figure 66: PE signal slope over gate voltage comparison between small n- and p-FinFET (left, at $V_D = 1,1V/-1,1V$) and between small and large n-FinFET (right, at $V_D = 1,1V$) from Qualcomm. Backside measurement with SIL.

Diving deeper into the PE analysis for the suspicious large n-FiNFET, the emission spectra over drain and gate voltage (fig. 67) do not contain any noticeable deviations (the kink at photon energies $\leq 0,85V$ is due to the Nanolens coating). On the contrary, the linear electron temperature increase with drain voltage and linear decrease with gate voltage demonstrate almost perfect agreement with the ideal theoretical model (fig. 68). Obviously the scattering / emission processes in the channel are normal and uneffected by any parasitic current / scattering mechanism as present in the $24 - 40nm$ FinFET failure analysis cases above. Given this fact, the comparably low emission over gate voltage rises the suspicion that the source-to-drain current of the n-FinFET is simply too low and somehow does not reach its planned value (12 times higher than for small n-FinFET).

Analysis of the output and input characteristics of the large n-FinFET (fig. 69) confirms this: The large n-FinFET hardly reaches saturation operating condition and carries far too low currents namely only twice as much current compared to the small n-FiNFET (compare to figure 25 of section 5.1). This confirms all PEM and SPEM findings above. The reason for the abnormal behavior of the large n-FinFET is probably a parasitic resistance in the drain and/or gate connection. As all devices were manufactured on a individually designed test chip, the connection lines layout was probably copied from small to large n-FinFET, but it was forgotten to adjust the diameter of the connection lines so that the connections are not able to carry 12 times higher currents therefore restricting the FET to a very small operating region.

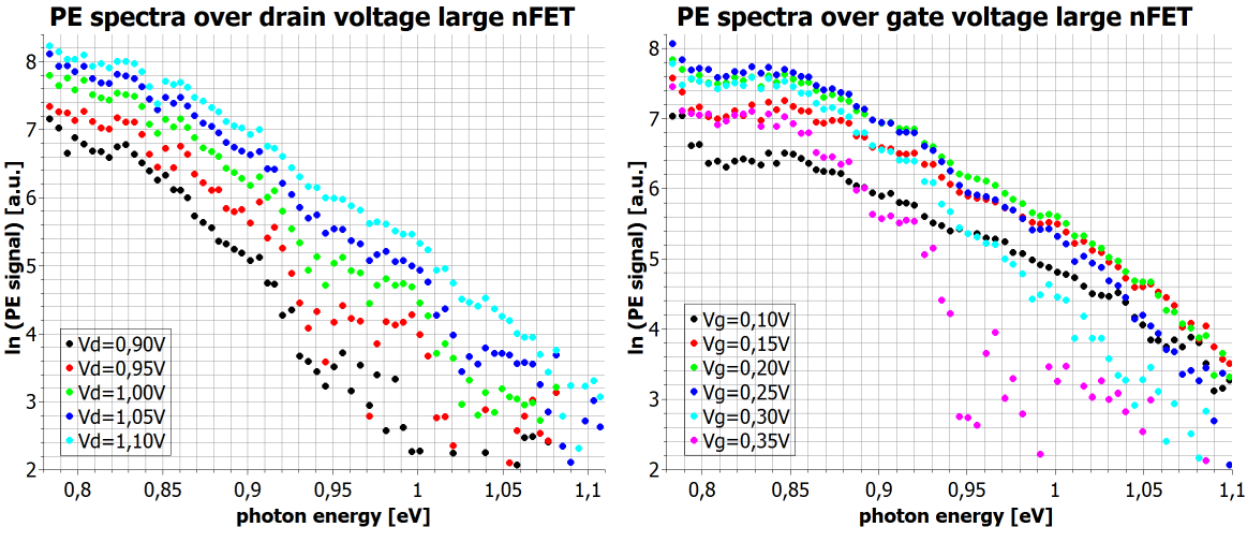

Figure 67: Photon emission spectra of the large 16/14nm n-FinFET from Qualcomm for various drain voltages (left, at $V_G = 0,4V$) and for various gate voltages (right, at $V_D = 1,10V$). Backside measurement with SIL.

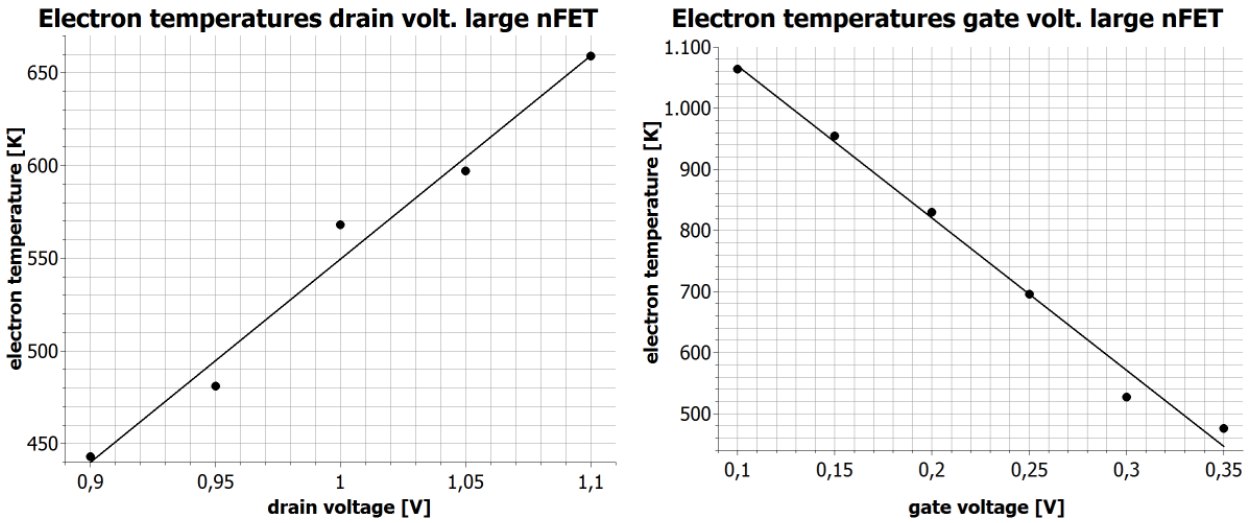

Figure 68: Electron temperature over drain voltage (left, at $V_G = 0,4V$) and gate voltage (right, at $V_D = 1.1V$) extracted by fit of the linear PE spectra regions of figure 67.

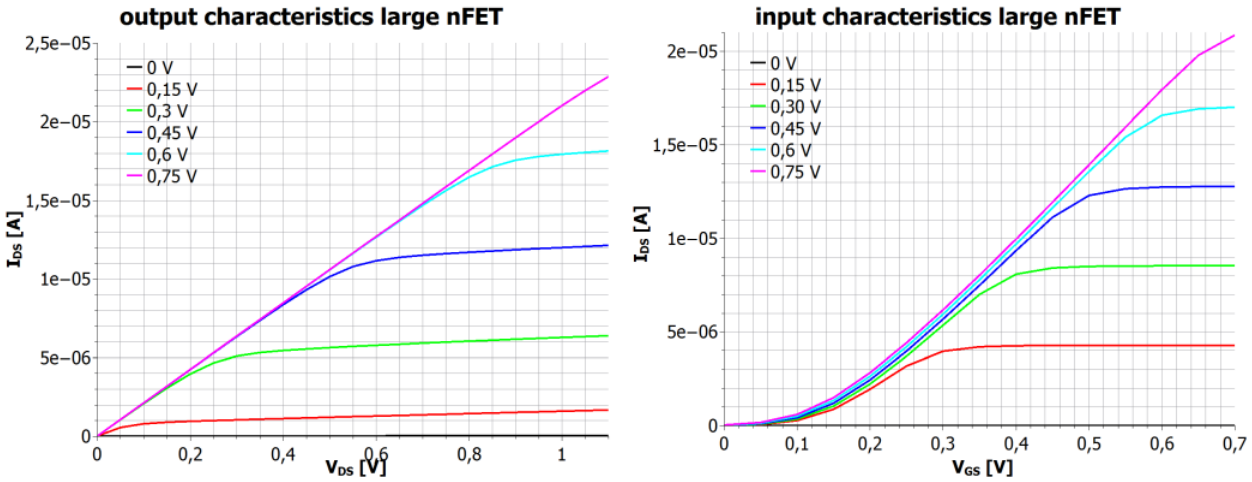

Figure 69: Output characteristics of the 16/14nm n-FinFET from Qualcomm. Nominal voltage was $0.7V$ and maximum certified voltage $1.1V$.

device	suspicious PE behavior	suspicious electrical behavior	proposed failure mechanism
40nm n-FinFET	PE, PE spectra and electron temperatures almost constant over V_G	parasitic current in output curve; normal bell-shape substrate current ($\approx 5\%$) dominated by parasitic offset ($\approx 95\%$)	parasitic current path through substrate parallel to source-to-drain
24-30nm FinFETs	electron temperatures almost constant over V_G	far too high substrate current without typical bell-shape	parasitic substrate current probably due to doping failure at source or drain diffusions
16/14nm nFinFET QCT	generally too low PE signal level; bell-shape over V_G shifted towards lower voltages	FinFET hardly reaches saturation	parasitic ohmic resistance in drain and/or gate connection probably due to design failure

Table 6: FA result summary for all FinFETs under investigation.

5.4.4 FA result summary

Table 6 gives a summary of all failure analysis findings. Interestingly, it is mostly the emission behavior over gate voltage that indicates the presence of dysfunctional or deviative behavior. This observation can be motivated: Drain voltage more or less acts as the energy supply for charge carriers flowing towards drain both for normal FET current through the channel and parasitic current paths as well. The dependence of carrier behavior, scattering and photon emission processes on drain voltage is relatively simple: The higher the drain voltage, the higher the electric field, mostly with an almost linear relation between both entities. Therefore the emission-over-drain-voltage behavior is not the best failure indicator for MOSFETs or FinFETs, but brilliantly serves for estimating general PE-signal-decreases with voltage (red-shift). PE-over-gate-voltage is more characteristic for individual FET behavior and leads to better indications towards (dys-)functionality and failure. Photon emission slopes and spectra of a functional FET may rise or fall with gate voltage, depending on what voltage region is exactly looked at. Furthermore the most important FET operation principles (i.e. emerging channel, pinch-off etc.) are more dependent on gate voltage and less on drain voltage. Gate voltage is a more intricate parameter with regard to FET operation, while drain voltage plays more the energy supply and carrier acceleration role. To conclude this section, the reader shall be reminded of the fact that all electrical information given in this section was only accessible because the transistors were test structures and therefore individually accessible. In a real integrated circuit electric characterization of single FETs (e.g. individual IV-curve etc.) is usually not possible due do deep integration of transistors. In such cases photon emission can close the gap as was shown in this section: Most information about erratic behavior of the structures and clear indications for failure could be extracted via the use of PEM and SPEM only. The electrical device data was only used to confirm the findings from previous emission experiments.

5.5 New tomographical method for SPEM

5.5.1 Motivation and idea

Photon emission microscopy (PEM) is a widely used method for the detection of failing devices in the failure analysis of *integrated circuits* (IC). Photon emission cannot only locate possible failure spots but can also give information about the specific failure mechanism or the operation mode of the device causing the PEM signal as stated for example in [7, 24]. Therefore the spectral analysis (SPEM) of photon emission patterns is a valuable and expedient method for electronics failure analysis.

The 2d-tomography method was developed at TU Berlin for two reasons:

1. The optical resolution and overall emission image quality of PEM and SPEM can be improved by taking images of a chip region from different angles and hence calculating an improved emission pattern from them. This has a similar effect as so called super-resolution techniques in biology or medicine.
2. The aforementioned procedure with images from different angles can also be used to dissolve spectral overlap occurring with closely neighboring emission sources (fig. 70). Especially with higher integration densities and continuously decreasing device sizes in ICs, the tomography technique can open access to failure analysis cases, that are not accessible by conventional SPEM measurements.

To demonstrate both advantages in one example as a proof-of-concept, different locations of a ring oscillator will be investigated later in section 5.5.5. The idea for this new 2d-tomography-like method arose within a cooperation project of TU Berlin and Centre national d'études spatiales (CNES), France. The author also wishes to thank Philippe Perdu, formerly CNES, for several inspirations and insights about the importance of the method. Some contents as well as figures of this section will also be published in the authors contribution to IPFA 2018 [37].

Regarding spectroscopy there are several methods applicable to gain spectral emission information from a device under test. Obvious choices are the use of a stepper motor monochromator, the use of a prism or a transmission grating [24] or the insertion of a slit (with additional dispersive element) in the optical path. The advantages and disadvantages of these methods can be found in table 7 .

The Phemos-1000 system installed at TU Berlin provides the opportunity to obtain information about the spectral characteristics of photon emission of semiconductor devices in integrated circuits via the use of a custom-made dispersive prism, which can be moved in and out of the optical path. Whereas the detector used for all following experiments of this section is a standard silicon CCD camera cooled down to $-50°$, all following considerations and experiments hold equally true for any other emission detector with almost linear raw data-to-signal relation. When investigating semiconductor devices with closely neighboring emission sources, a spectral intensity overlap can easily occur due to the dispersive element in the optical path (fig. 70-73). The spectral overlap prohibits an allocation of the intensity to a certain wavelength of one single emission spot by conventional methods. In this case a solution must be found in order to retrieve the fully location-resolved spectral information of the device under test.

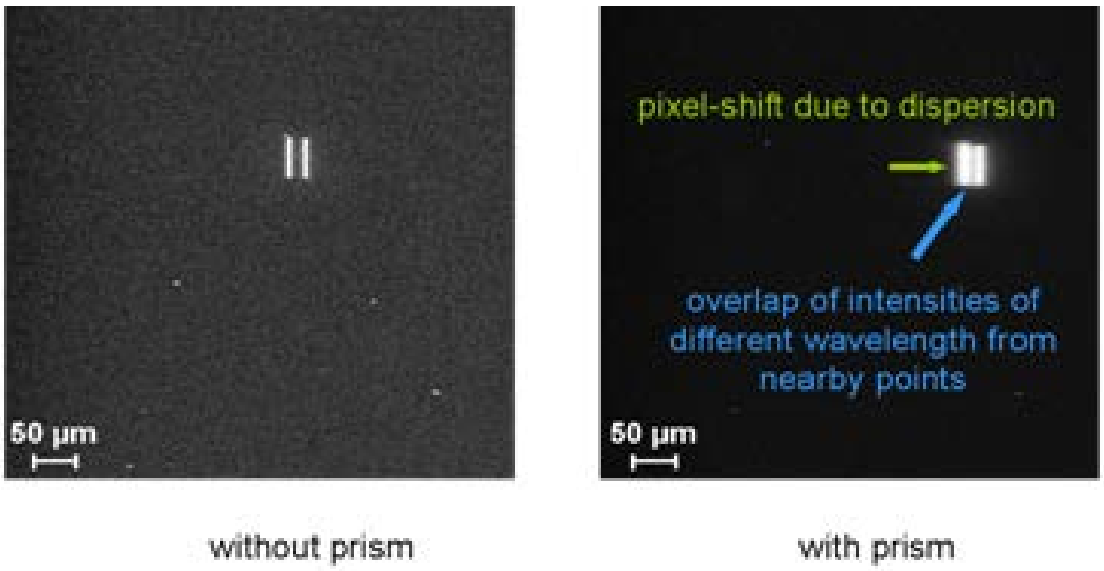

Figure 70: Photon Emission of the ring oscillator manufactured by Infineon Technologies AG without and with prism inserted into Phemos-1000. The pixel shift and intensity overlap due to the insertion of the prism are clearly visible. In this case the spectral overlap can not be circumvented by a subtle rotation; at least not for all points especially in the middle of the emission lines (case 3). Acquired with silicon CCD.

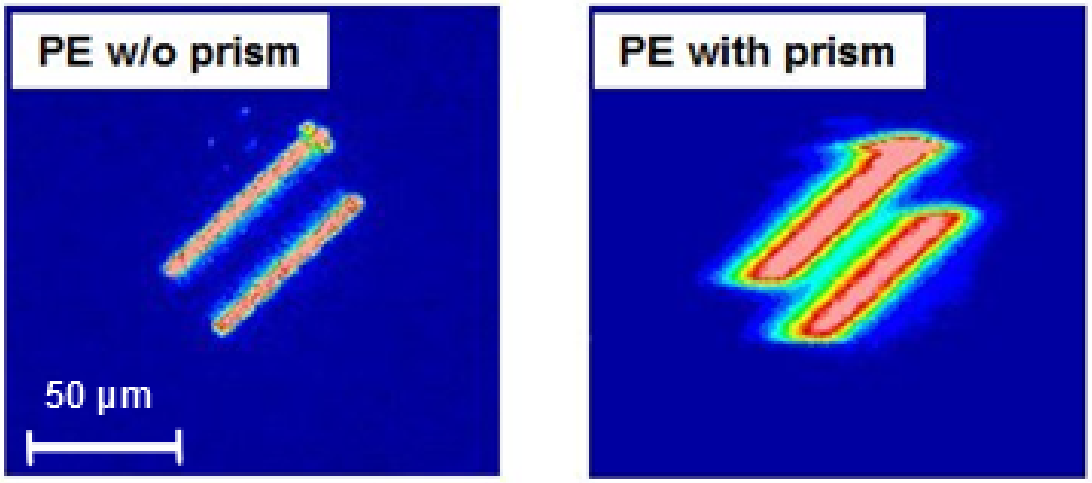

Figure 71: The same situation as above, except from an additional rotation of the device. In the case of a simple emission pattern the emission spectrum at certain points (e.g. lower right corner of the ring oscillator) can be gained via one single rotation, as no overlap for emitted light from that corner occurs [61]. Acquired with silicon CCD.

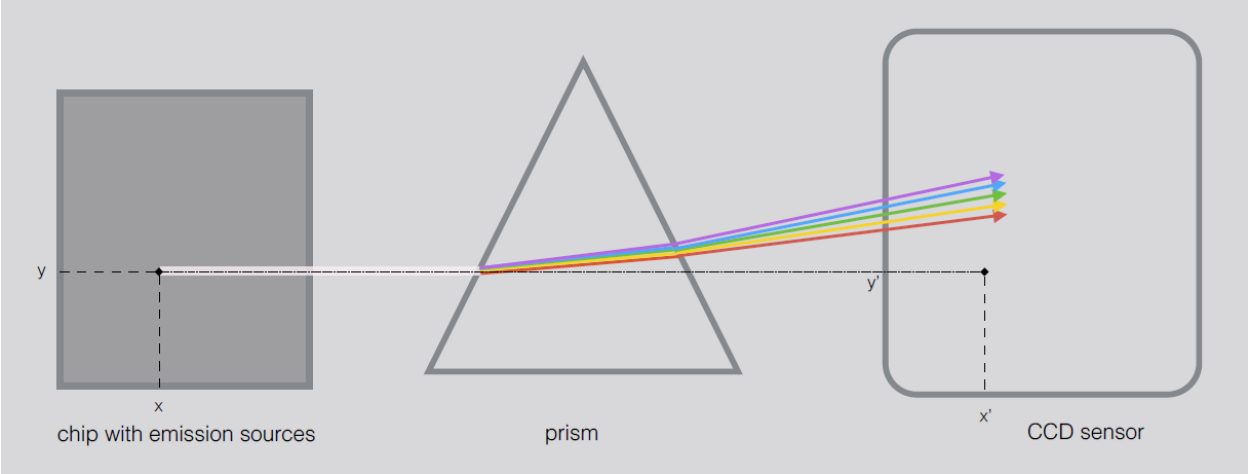

Figure 72: Dispersion of light by the prism. Image taken from [105].

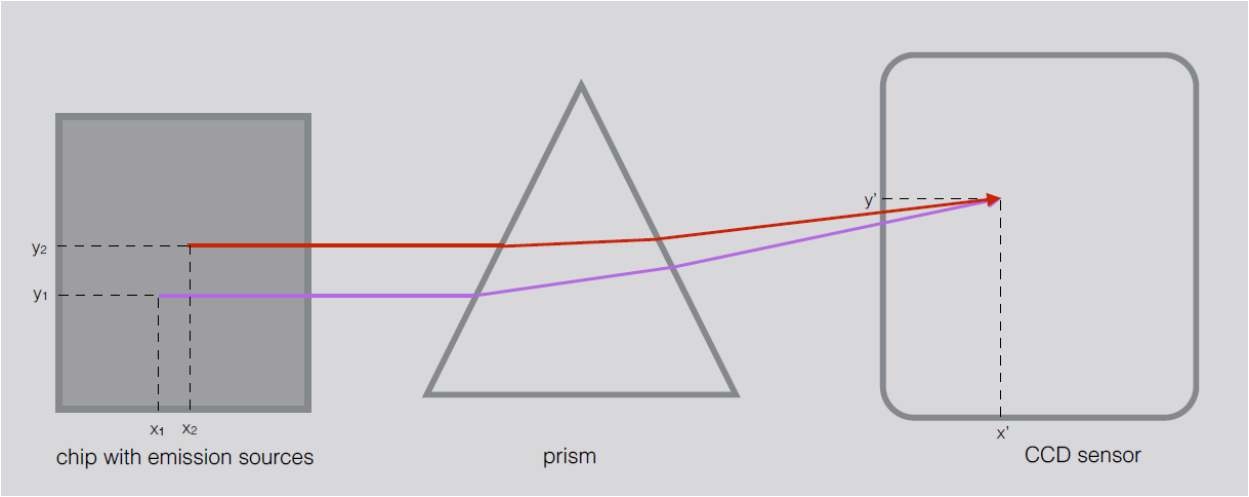

Figure 73: Overlap of intensities of different points (x_1, y_1) and (x_2, y_2) of the DUT. The spectral dependency of the dispersion may cause different wavelengths from different points on the DUT to be mapped to the same pixel on the CCD sensor. This situation is shown in the picture above for red and lilac light from to different origins on the DUT. Image taken from [105].

The situation can be categorized into three different cases:

1. Insertion of the prism causes no overlap (fig. 74).
2. Insertion of the prism causes overlap, but overlap can be circumvented by rotation (fig. 75).
3. Insertion of the prism causes overlap and overlap cannot be circumvented by rotation (fig. 70).

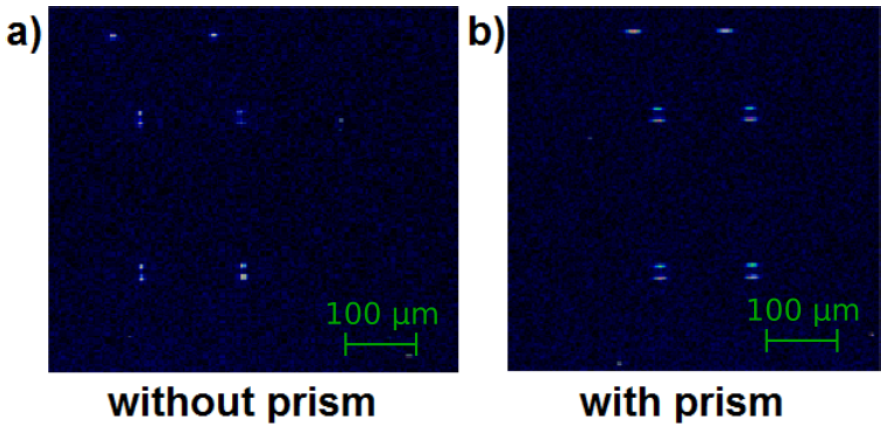

Figure 74: Photon emission image of an arbitrary test chip without (a) and with prism (b) inserted into the optical path and acquired with silicon CCD. No spectral overlap occurs here (case 1).

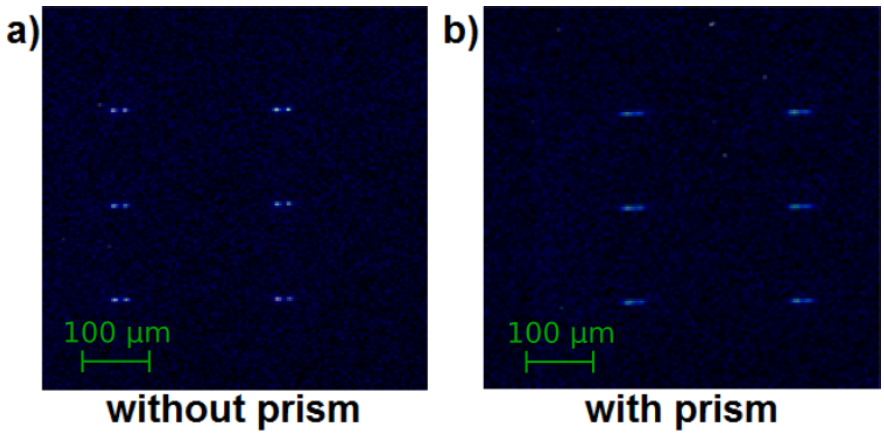

Figure 75: Photon emission image of an arbitrary test chip without (a) and with prism (b) inserted into the optical path and acquired with silicon CCD. Spectral overlap but can be circumvented by a rotation of e.g. 45° due to the relatively low complexity / geometrical density of the emission pattern (case 2).

In the first case, the fully location-resolved emission spectrum can be obtained by relatively simple back-calculation via previous measurements of the pixel shift caused by the prism, the wavelength-dependent transmission of the optical path and the bulk silicon thickness for backside analysis. The

data acquisition in the second case is similar to the first case but needs one additional rotation prior to the PEM measurement in order to orientate the DUT in a direction, which does not cause overlapping intensities (e.g. at the end points of both ring oscillator "fingers" in figure 71.

The third case is by far the most difficult one as one has to deal with overlapping intensities of different spots of the DUT. The aim of the 2d-tomography method is to retrieve the fully location-resolved spectral information lost due to the spectral overlap. This can be achieved by taking several images of the device from different angles of rotation, where every image contains slightly different information about the spectral emission of the device. The rotation is experimentally realized via rotation of the device on a custom-made rotatable table. The prism must be inserted into the optical path during all measurements and for all chosen angles. The data of all angular PEM measurements can then be compiled into a large system of equations for the unknown spectral distribution $I_{0,\lambda}(p,q)$ in each pixel (p,q) of the DUT. The system of equations not only contains the spectral measurement data for different angles, but also additional information about the pixel shift, the optical transmission of the Phemos-1000 system and the bulk silicon thickness (in the case of backside analysis). Solving the system of equations numerically can then deliver the desired spectral emission information at each point or device of the image.

Table 7: Advantages and disadvantages of different spectroscopy methods

Prism / Transmission grating	Band-pass filter	Slit (with additional prism or grating)	Stepper motor monochromator
+ high spectral resolution	+ good spatial resolution	+ high spectral resolution	+ highest spectral resolution
+ simple installation	+ simple installation	+ low cost option	+ no loss of spatial information
+ low cost option	o medium cost option	o medium installation difficulty	- more expensive option
- loss of information in 1 spatial dimension	- lower spectral resolution (Gauss shape, several transmission intervals)	o loss of 1 spatial dimension, but information for each row can be regained easily by back-calculation	- difficult installation as the light of every single pixel has to be proceeded independently
- glass or grating imperfections	- transmission dependent on filter quality and absorption characteristics	- split and prism or grating imperfections	- spectral inaccuracy due to step discretization
			- grating and mirror imperfections

5.5.2 Theoretical background

This section gives a detailed view over the situation from a mathematical point-of-view. For this part the following variables are used (taking into account that the CCD-sensor used for emission analysis in Phemos-1000 has 512×512 pixels):

$(p,q),(j,k)$	$\hat{=}$	pixel coordinates in x- and y-direction
P,Q	$\hat{=}$	discrete Fourier transformed pixel coordinates (spatial frequencies)
N_p, N_q	$\hat{=}$	absolute number of pixels in x- and y-direction
N_P, N_Q	$\hat{=}$	absolute number of the Fourier transformed pixel coordinates P and Q (note that $N_p = N_P$ and $N_q = N_Q$
$I(p,q)$	$\hat{=}$	measured intensity of pixel (p,q) on the CCD-sensor
$I_{0,\lambda}(p,q)$	$\hat{=}$	intensity of wavelength λ at pixel (p,q) on the DUT
$U_\lambda(p,q)$	$\hat{=}$	optical point spread function (mainly determined by the prism)
$\lambda_1 ... \lambda_{N_\lambda}$	$\hat{=}$	contributing wavelengths
$\tilde{I}, \tilde{I}_0, \tilde{U}$	$\hat{=}$	discrete Fourier transforms of the respective entities
N_λ	$\hat{=}$	number of different wavelengths contributing to the intensity I

For the use of the tomography method it is necessary to divide up the spectral region of interest into divisions with a certain bandwidth. For the range of visible light it would be suitable to use 20 compartments of 20nm bandwidth, starting from 400nm to about 800nm. Thus to be precise the wavelength λ_i doesn't refer to one particular wavelength but to a small wavelength strip around wavelength λ_i with a certain width.

The measured intensity on the CCD-sensor is a pixel-wise superposition of the intensities of all contributing wavelengths in the particular pixel (p,q). The transition of light from the DUT to the CCD-sensor (fig. 72 and 73) can be modeled using the point spread function $U_\lambda(p-j, q-k)$. As the diffraction of light rays within the prism is wavelength-dependent, the point spread function is so, too. The shifts $p-j$ and $q-k$ guarantee, that the matrix U_λ is centered around the point (p,q). The relation between measured intensity $I(p,q)$ on the CCD-sensor and the emitted intensity $I_{0,\lambda}(p,q)$ from the DUT can now be modeled as

$$I(p,q) = \sum_{\lambda=\lambda_1}^{\lambda_{N_\lambda}} \sum_{j,k=1}^{512} U_\lambda(p-j, q-k) I_{0,\lambda}(j,k) \quad . \tag{5.18}$$

This is a discrete two-dimensional convolution-type sum. For numerical computations, the easiest way to determine the solutions $I_{0,\lambda}(j,k)$ is to rewrite the above equation into a matrix system, which can be handled efficiently by numerical algorithms. The following pages will exhibit three possible ways to do that.

5.5.2.1 An idea to simplify the problem by Fourier transformation Analogous to the application of Radon transform for 2d-tomography in modern medical imaging (*Computer Tomography*), it will be investigated here if the application of discrete Fourier transform to equation 5.18 can provide any simplification of the solving process. In order to solve equation (5.18) for the unknown intensities $I_{0,\lambda}(p,q)$, one can apply the discrete convolution theorem in 2 dimensions (proof given in section 5.5.2.2 beneath)

$$\tilde{I}(P,Q) = \sum_{\lambda=\lambda_1}^{\lambda_{N_\lambda}} \tilde{U}_\lambda(P,Q)\tilde{I}_{0,\lambda}(P,Q) \tag{5.19}$$

using the discrete Fourier transformation (DFT) to transform the coordinates ($p \to P$) and ($q \to Q$), respectively. The above expression provides $N = N_p \cdot N_q$ equations for $N \cdot N_\lambda$ unknown components of the intensities $I_{0,\lambda}(p,q)$. Obviously it is compulsory to gain additional information to solve the equations unambiguously. The additional information is obtained by at least $N_\lambda - 1$ rotations of the DUT within the angle of 0° to 360°. For specific symmetries of the emission pattern, it can occur that certain angular ranges do not provide independent information additional to previous rotations. Using the information of additional emission images for various angles φ, we can expand the system of equations (5.19) to

$$\tilde{I}_{\varphi_0}(P,Q) = \sum_{\lambda=\lambda_1}^{\lambda_{N_\lambda}} \tilde{U}_{\lambda,\varphi_0}(P,Q)\tilde{I}_{0,\lambda}(P,Q) \tag{5.20}$$

$$\vdots$$

$$\tilde{I}_{\varphi_{N-1}}(P,Q) = \sum_{\lambda=\lambda_1}^{\lambda_{N_\lambda}} \tilde{U}_{\lambda,\varphi_{N-1}}(P,Q)\tilde{I}_{0,\lambda}(P,Q) \quad . \tag{5.21}$$

Now one has $N \cdot N_\lambda$ equations for $N \cdot N_\lambda$ variables. The obtained system can be written as

$$\tilde{\mathbf{I}} = \tilde{U} \cdot \tilde{\mathbf{I}}_0 \tag{5.22}$$

with

$$\tilde{\mathbf{I}} = \begin{pmatrix} \tilde{I}_{\varphi_0}(P_1,Q_1) & \cdots & \tilde{I}_{\varphi_0}(P_1,Q_{N_Q}) \\ \vdots & & \vdots \\ \tilde{I}_{\varphi_{N_\lambda-1}}(P_1,Q_1) & & \\ \tilde{I}_{\varphi_0}(P_2,Q_1) & & \\ \vdots & & \\ \tilde{I}_{\varphi_{N_\lambda-1}}(P_2,Q_1) & & \\ \vdots & & \\ \tilde{I}_{\varphi_0}(P_{N_P},Q_1) & & \\ \vdots & & \\ \tilde{I}_{\varphi_{N_\lambda-1}}(P_{N_P},Q_1) & & \\ \tilde{I}_{\varphi_0}(P_{N_P},Q_2) & & \\ \vdots & & \\ \tilde{I}_{\varphi_{N_\lambda-1}}(P_{N_P},Q_2) & & \\ \vdots & & \\ \tilde{I}_{\varphi_0}(P_{N_P},Q_{N_Q}) & & \\ \vdots & & \\ \tilde{I}_{\varphi_{N_\lambda-1}}(P_{N_P},Q_{N_Q}) & & \end{pmatrix}, \quad \tilde{\mathbf{I}}_0 = \begin{pmatrix} \tilde{I}_{\lambda_1}(P_1,Q_1) & \cdots & \tilde{I}_{\lambda_1}(P_1,Q_{N_Q}) \\ \tilde{I}_{\lambda_2}(P_1,Q_1) & & \\ \vdots & & \\ \tilde{I}_{\lambda_{N_\lambda}}(P_1,Q_1) & & \\ \tilde{I}_{\lambda_1}(P_2,Q_1) & & \\ \vdots & & \\ \tilde{I}_{\lambda_{N_\lambda}}(P_2,Q_1) & & \\ \vdots & & \\ \tilde{I}_{\lambda_1}(P_{N_P},Q_1) & & \\ \vdots & & \\ \tilde{I}_{\lambda_{N_\lambda}}(P_{N_P},Q_1) & & \\ \vdots & & \\ \tilde{I}_{\lambda_1}(P_{N_P},Q_{N_Q}) & & \\ \vdots & & \\ \tilde{I}_{\lambda_{N_\lambda}}(P_{N_P},Q_{N_Q}) & & \end{pmatrix} \tag{5.23}$$

and

$$\tilde{U} = \begin{pmatrix} \tilde{U}_{\lambda_1,\varphi_0}(P_1,Q_1) & \cdots & \tilde{U}_{\lambda_{N_\lambda-1},\varphi_0}(P_1,Q_1) & 0 & \cdots & 0 & \cdots & 0 & \cdots & 0 \\ \vdots & & \vdots & \vdots & & \vdots & & \vdots & & \vdots \\ \tilde{U}_{\lambda_1,\varphi_{N-1}}(P_1,Q_1) & \cdots & \tilde{U}_{\lambda_{N_\lambda-1},\varphi_{N-1}}(P_1,Q_1)) & 0 & \cdots & 0 & \cdots & 0 & \cdots & 0 \\ 0 & \cdots & 0 & \tilde{U}_{\lambda_1,\varphi_0}P_2,Q_1) & \cdots & \tilde{U}_{\lambda_{N_\lambda-1},\varphi_0}(P_2,Q_1) & & 0 & \cdots & 0 \\ \vdots & & \vdots & \vdots & & \vdots & & \vdots & & \vdots \\ 0 & \cdots & 0 & \tilde{U}_{\lambda_1,\varphi_{N-1}}(P_2,Q_1) & \cdots & \tilde{U}_{\lambda_{N_\lambda-1},\varphi_{N-1}}(P_2,Q_1) & & 0 & \cdots & 0 \\ 0 & \cdots & 0 & 0 & \cdots & 0 & \ddots & \tilde{U}_{\lambda_1,\varphi_0}(P_{N_P},Q_{N_Q}) & \cdots & \tilde{U}_{\lambda_{N_\lambda-1},\varphi_0}(P_{N_P},Q_{N_Q}) \\ \vdots & & \vdots & \vdots & & \vdots & & \vdots & & \vdots \\ 0 & \cdots & 0 & 0 & \cdots & 0 & & \tilde{U}_{\lambda_1,\varphi_{N-1}}(P_{N_P},Q_{N_Q}) & \cdots & \tilde{U}_{\lambda_{N_\lambda-1},\varphi_{N-1}}(P_{N_P},Q_{N_Q}) \end{pmatrix} \tag{5.24}$$

Equation 5.22 can be solved with respect to $\tilde{I}_0$ given the condition, that the matrix $\tilde{U}$ is invertible:

$$\tilde{\mathbf{I}}_0 = \tilde{U}^{-1} \cdot \tilde{\mathbf{I}} \quad . \tag{5.25}$$

The discrete Fourier back-transformation then yields

$$\mathbf{I}_0 = DFT_P^{-1} DFT_Q^{-1} \left[\tilde{U}^{-1} \cdot \tilde{\mathbf{I}} \right] \quad . \tag{5.26}$$

This is the desired expression for the spectral intensities on the DUT as a function of the optical response of the Phemos system with prism and the measured intensities on the CCD sensor.

The point spread function $U(p-j, q-k)$ can be generated with the knowledge of the angle of rotation and the pixel shift caused by the prism. The pixel shift (see section 5.5.3.7) can be obtained by the use of narrow bandpass filters with a sharp transmission profile and the intensity maximum (without the prism inserted) located at pixel $(p = 255, q)$. The measurements show that the emission from the DUT is simply shifted by the prism in the q-direction by a wavelength-dependent number.

There are basically two different ways to introduce pixel shift and rotation into equation 5.18, which will be elaborated in detail in the following sections. The first method has the information about pixel shift and angle of rotation both in the point spread function U, the second method consists in ascribing the pixel shift to the point spread function U and the angle of rotation to either the coordinates of the DUT or the coordinates of the CCD sensor. Including the pixel shift in the coordinates is not useful due to a complication of the Fourier transformation in this case.

First method: rotation and pixel shift in U From this data it is possible to define the point spread function for the respective wavelength. An example for $\lambda = 530nm$ corresponding to a pixel shift of 21 (here: without rotation) is given beneath. Please bear in mind that (p,q) are the coordinates of the CCD sensor and (j,k) are the coordinates on the device under test.

$$\begin{pmatrix} p \\ q \end{pmatrix} = \begin{pmatrix} j - 21 \\ k \end{pmatrix} \tag{5.27}$$

As j and k are denoted with a negative sign in front in the definition of $U(p-j, q-k)$, one gets:

$$U(p-j, q-k)_{\lambda=530\,nm} = \begin{cases} 1, & \text{if } (j,k) = (21, q) \\ 0, & \text{else} \end{cases} \quad . \tag{5.28}$$

It is important that $\sum_{j,k=1}^{512} U_\lambda(p-j, q-k)$ is normalized to 1 for each wavelength at this step of calculation, as one would otherwise loose or gain intensity within the numerical process. Now the transmittance t_λ of the system and silicon bulk have to be taken into consideration (see fig. 83). Their influence can be modeled by multiplying the point spread function for each wavelength by the referring transmittance factor. For the example above (wavelength 530nm, overall transmittance $t_{530\,nm} \approx 0,032$ for this wavelength) this would be

$$U(p-j,q-k)_{\lambda=530\,nm} = 0,032 \cdot \begin{cases} 1, & \text{if } (j,k) = (21,q) \\ 0, & \text{else} \end{cases} \quad . \tag{5.29}$$

The next problem is the rotation of the DUT by an angle of φ. This rotation can be transferred to the point spread function by $U \to U_\varphi$, as if the Phemos would be rotated and not the DUT.

$$\begin{pmatrix} p \\ q \end{pmatrix} = \begin{pmatrix} a \\ b \end{pmatrix} + \underbrace{\begin{pmatrix} cos(\varphi) & -sin(\varphi) \\ sin(\varphi) & cos(\varphi) \end{pmatrix} \cdot \begin{pmatrix} j-a \\ k-b \end{pmatrix}}_{\text{clockwise rotation from point of view of CCD-sensor}} + \begin{pmatrix} -21 \\ 0 \end{pmatrix} \quad . \tag{5.30}$$

The variables a and b represent the coordinates of the middle of the device (center of rotation) and are set to zero for the rest of this section. As j and k are denoted with a negative sign in front in the definition of $U(p-j,q-k)$, one gets:

$$\begin{aligned} &U(j,k,p-j,q-k)_{\lambda=530\,nm,\,\varphi} = \\ &0,032 \cdot \begin{cases} 1, \text{if } (p-j,q-k) = ([cos(\varphi)-1]j - sin(\varphi)k - 21, sin(\varphi)j + [cos(\varphi)-1]k) \\ 0, \text{else} \end{cases} \end{aligned} \quad . \tag{5.31}$$

As the values might not be integer, it is necessary to include a rounding at this step. The overall formula is

$$\begin{aligned} &U(j,k,p-j,q-k)_{\lambda\,\varphi} = \\ &t_\lambda \cdot \begin{cases} 1, & \text{if } (p-j,q-k) = ([cos(\varphi)-1]j - sin(\varphi)k + \Delta_\lambda, sin(\varphi)j + [cos(\varphi)-1]k) \\ 0, & \text{else} \end{cases} \end{aligned} \quad . \tag{5.32}$$

Unfortunately, it is impossible to obtain the form $U(p,q)$ of the point spread function from the above expression, as U becomes location-dependent by the rotation. Therefore the point spread matrix U cannot be discretely Fourier transformed and the presented approach is not applicable.

Second method: pixel shift in U, rotation in I or I_0 To avoid the complications occurring with the calculation of $U(p,q)$ at the end of the first method, the rotation can be shifted to either the pixel-coordinates (p,q) of the sensor or the pixel-coordinates (j,k) of the chip. Using the rotation theorem for the Fourier transform

$$\mathcal{F}\left[f(\mathbf{R}_\varphi \cdot (p,q))\right](P,Q) = \mathcal{F}\left[f(p,q)\right](\mathbf{R}_\varphi \cdot (P,Q)) \tag{5.33}$$

for an orthogonal rotation matrix $\mathbf{R}_\varphi$ and the equation (5.22) above takes the form

$$\tilde{I}_{\varphi_0}(\mathbf{R}_{\varphi_0} \cdot (P,Q)) = \sum_{\lambda=\lambda_1}^{\lambda_{N_\lambda}} \tilde{U}_\lambda(P,Q)\tilde{I}_{0,\lambda}(P,Q) \tag{5.34}$$

$$\vdots$$

$$\tilde{I}_{\varphi_{N_\varphi-1}}(\mathbf{R}_{\varphi N_\varphi-1} \cdot (P,Q)) = \sum_{\lambda=\lambda_1}^{\lambda_{N_\lambda}} \tilde{U}_\lambda(P,Q)\tilde{I}_{0,\lambda}(P,Q) \tag{5.35}$$

or

$$\tilde{I}_{\varphi_0}(P,Q) = \sum_{\lambda=\lambda_1}^{\lambda_{N_\lambda}} \tilde{U}_\lambda(P,Q)\tilde{I}_{0,\lambda}(\mathbf{R}_{\varphi 0} \cdot (P,Q)) \tag{5.36}$$

$$\vdots$$

$$\tilde{I}_{\varphi_{N_\varphi-1}}(P,Q) = \sum_{\lambda=\lambda_1}^{\lambda_{N_\lambda}} \tilde{U}_\lambda(P,Q)\tilde{I}_{0,\lambda}(\mathbf{R}_{\varphi_{N_\varphi-1}} \cdot (P,Q)) \tag{5.37}$$

respectively, defining

$$\mathbf{R}_\varphi \cdot (P,Q) := \begin{pmatrix} \cos(\varphi) & -sin(\varphi) \\ \sin(\varphi) & \cos(\varphi) \end{pmatrix} \cdot \begin{pmatrix} P \\ Q \end{pmatrix} \quad . \tag{5.38}$$

As the rotation of the CCD sensor or the DUT is different for each angle of rotation φ, the evolving system of equations contains rather complicated relations between the left and right side. Therefore the Fourier transformation does not involve any simplification in this case, but, on the contrary, a complication. Because of that, the idea of Fourier transformation for a simplification of the problem was dropped.

Third method: no Fourier transformation, straight forward calculation The most obvious choice of bringing equation 5.18 into matrix form

$$\mathbf{I} = U \cdot \mathbf{I_0} \tag{5.39}$$

is to take advantage of the δ-function characteristics of U as presented in equation 5.32. The j- and k-sums of equation (5.18) vanish due to the δ-function and the last remaining sum over the wavelength λ is the decisive parameter for the building of the matrix U, as λ has to be the summation index of the matrix multiplication $U \cdot \mathbf{I_0}$. The order of indexing for the coordinate parameters j,k,p and q can be chosen arbitrarily. These reflections lead to the form

$$\mathbf{I} = \begin{pmatrix} I_{\varphi_0}(p_1,q_1) & \cdots & I_{\varphi_0}(p_{N_P},q_{N_P}) \\ I_{\varphi_1}(p_1,q_1) & \cdots & I_{\varphi_1}(p_{N_P},q_{N_P}) \\ \vdots & & \vdots \\ I_{\varphi_{N_\phi}}(p_1,q_1) & \cdots & I_{\varphi_{N_\phi}}(p_{N_P},q_{N_P}) \end{pmatrix}, \quad \mathbf{I_0} = \begin{pmatrix} I_{\lambda_1}(p_1,q_1) & I_{\lambda_1}(p_2,q_1) & \cdots & I_{\lambda_1}(p_{N_P},q_1) \\ I_{\lambda_2}(p_1,q_1) & & & \\ \vdots & & & \\ I_{\lambda_{N_\lambda}}(p_1,q_1) & I_{\lambda_{N_\lambda}}(p_2,q_1) & \cdots & I_{\lambda_{N_\lambda}}(p_{N_P},q_1) \\ I_{\lambda_1}(p_1,q_2) & & & \\ \vdots & & & \\ I_{\lambda_{N_\lambda}}(p_1,q_{N_q}) & I_{\lambda_{N_\lambda}}(p_2,q_{N_q}) & \cdots & I_{\lambda_{N_\lambda}}(p_{N_P},q_{N_q}) \end{pmatrix} \quad \text{and} \tag{5.40}$$

$$U = \begin{pmatrix} U_{\lambda_1,\varphi_0}(p_1-j_1,q_1-k_1) & \cdots & \to \lambda_1 \text{ bis } \lambda_{N_\lambda} \text{ innerhalb des Blocks} & \cdots & U_{\lambda_{N_\lambda}-1,\varphi_0}(p_1-j_1,q_1-k_1) & \cdots & \to (j_1,k_1) \text{ bis } (j_{N_P},k_{N_P}) \text{ blockweise} & \cdots \\ \vdots & & & & \vdots & & & \\ \downarrow (p_1,q_1) \text{ bis } (p_{N_P},q_{N_P}) \text{ innerhalb des Blocks} & & \ddots & & \downarrow (p_1,q_1) \text{ bis } (p_{N_P},q_{N_P}) \text{ innerhalb des Blocks} & & & \\ \vdots & & & & \vdots & & & \\ U_{\lambda_1,\varphi_0}(p_{N_P}-j_1,q_{N_P}-k_1) & \cdots & \to \lambda_1 \text{ bis } \lambda_{N_\lambda} \text{ innerhalb des Blocks} & \cdots & U_{\lambda_{N_\lambda}-1,\varphi_0}(p_{N_P}-j_1,q_{N_P}-k_1)) \text{ blockweise} & & & \\ \vdots & & & & \vdots & & & \\ \downarrow \varphi_1 \text{ bis } \varphi_{N_\phi} \text{ blockweise} & & & & \downarrow \varphi_1 \text{ bis } \varphi_{N_\phi} \text{ blockweise} & & & \\ \vdots & & & & \vdots & & & \end{pmatrix} \tag{5.41}$$

The matrix U is filled up with entries made up of the spectral transmission for a particular wavelength, if the condition

$$(p-j, q-k) = ([cos(\varphi)-1]j - sin(\varphi)k + \Delta_\lambda, sin(\varphi)j + [cos(\varphi)-1]k) \quad , \tag{5.42}$$

with (p, q) being the CCD sensor coordinates and (j, k) the DUT coordinates, holds true for the respective matrix index. Other matrix entries, for which this condition is not true, are set to zero. The form of the matrix U and the vectors $\mathbf{I}$ and $\mathbf{I_0}$ presented in this section (third method) are selected for all further deliberations and computations.

5.5.2.2 Proof of the discrete convolution theorem for the 2d-case Starting with the definition of a 2d discrete Fourier transformation, one has:

$$\tilde{G}(P_n, Q_m) = DFT_q \left[DFT_p \left[G(p,q) := \sum_{j,k=1}^{512} f(p-j, q-k) g(j,k) \right] \right] := \tag{5.43}$$

$$\sum_{q=1}^{512} \left(\sum_{p=1}^{512} \sum_{j,k=1}^{512} f(p-j, q-k) g(j,k) e^{-2\pi i \frac{n \cdot p}{N_p}} \right) e^{-2\pi i \frac{m \cdot q}{N_q}} \quad . \tag{5.44}$$

With spatial frequencies $P_n = 2\pi n/N_p$ and $Q_m = 2\pi m/N_q$ it follows

$$\cdots = \sum_{q=1}^{512} \left(\sum_{p=1}^{512} \sum_{j,k=1}^{512} f(p-j, q-k)) g(j,k) e^{-iP_n \cdot p} \right) e^{-iQ_m q} \quad . \tag{5.45}$$

As all sums are finite, it is possible to change the order of summation to

$$\cdots = \sum_{k=1}^{512} \sum_{q=1}^{512} \left(\sum_{j=1}^{512} g(j,k) \underbrace{\sum_{p=1}^{512} f(p-j, q-k) e^{-iP_n \cdot p}}_{= \tilde{f}(P_n, q-k) e^{-iP_n j}} \right) e^{-iQ_m q} \quad . \tag{5.46}$$

The modulation theorem for the discrete Fourier transform yields

$$\cdots = \sum_{k=1}^{512} \sum_{q=1}^{512} \left(\sum_{j=1}^{512} g(j,k) \tilde{f}(P_n, q-k) e^{-iP_n j} \right) e^{-iQ_m q} \tag{5.47}$$

$$= \sum_{k=1}^{512} \sum_{q=1}^{512} \tilde{f}(P_n, q-k) \left(\sum_{j=1}^{512} g(j,k) e^{-iP_n j} \right) e^{-iQ_m q} \tag{5.48}$$

$$= \sum_{k=1}^{512} \sum_{q=1}^{512} \tilde{f}(P_n, q-k)\tilde{g}(P_n, k)e^{-iQ_m q} \tag{5.49}$$

$$= \sum_{k=1}^{512} \tilde{f}(P_n, Q_m)e^{-iQ_m k}\tilde{g}(P_n, k) \tag{5.50}$$

$$= \tilde{f}(P_n, Q_m)\tilde{g}(P_n, Q_m) \quad . \tag{5.51}$$

It follows

$$DFT_q\left[DFT_p[g * f]\right] = DFT_q\left[DFT_p[g]\right] \cdot DFT_q\left[DFT_p[f]\right] \quad \square \quad . \tag{5.52}$$

5.5.2.3 Conclusion of the theoretical background Though various mathematical attempts were made to simplify the original system of equations 5.18 by using Fourier transform, no breakthrough could be achieved. On the contrary, internal consistency problems were met when applying Fourier transform in certain cases. In other cases the difficulty of the system of equations would have been increased further so that the idea to simplify the numerical part of the 2d-tomography-like method by Fourier transform was dropped. The numerical part (section 5.5.4) will therefore only consist in a straight forward least mean square solution of equation 5.18 in real space without any transform. The idea was originally pursued on the analogy of the application of Radon transform for 2d-tomography in modern medical imaging (*Computer Tomography*).

5.5.3 Experimental background

5.5.3.1 Devices The DUT was a ring oscillator structure (RO), manufactured by Infineon Technologies AG in 120nm process technology. The nominal voltage for both, p-type and n-type MOSFETS was $\pm 1.2V$. All MOSFETs were surrounded by STI (shallow trench isolation) with additional STI and metal fills to increase the mechanical stability. The gate oxide thickness was 3nm, n-well thickness $\sim 2\mu m$ and the thickness of the n^+- and p^+-diffusions $\sim$ 100nm. The substrate doping concentration had a value of $5 \cdot 10^{15} cm^{-3}$, the well doping concentration was about $2 \cdot 10^{17} cm^{-3}$ and finally the diffusion doping concentration was $2 \cdot 10^{20} cm^{-3}$. A layout with corresponding photon emission image can be seen in figure 76.

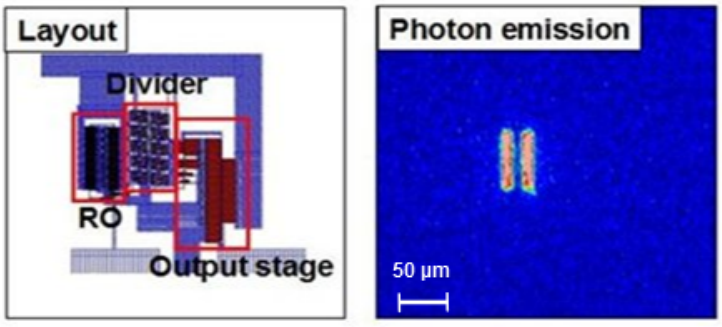

Figure 76: The left picture shows the layout of the ring oscillator structure taken for investigation. The right picture shows the corresponding photon emission [61].

5.5.3.2 Measurements The PEM measurement time for each angle was set to 100 seconds for the ring oscillator structure, while operating the device at an elevated supply voltage of 1.5 V (nominal voltage 1.2V) in order to increase the PEM signals. For the measurements the 20x-objective of the Phemos-1000 system was used. Examples of the data acquisition can be seen in figure 77 and 78. Note that the additional pixel shift causes the rotation around the center of the image to look like a rotation around a new center. This effect depends strongly on the wavelength-dependency of the pixel shift.

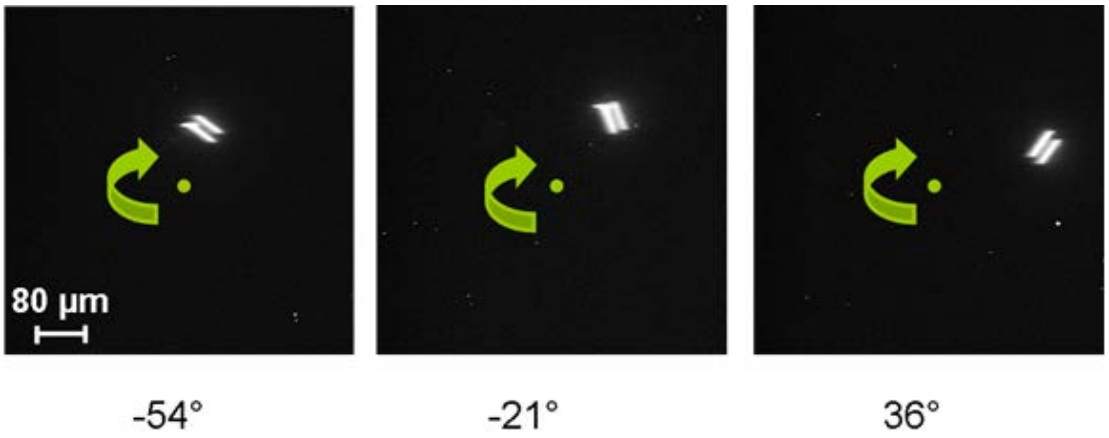

Figure 77: Examples of image acquisition for different rotations around the center of the image (green).

Figure 78: The additional pixel shift (gray) causes a similarity to a rotation around a new, shifted center (blue).

5.5.3.3 Rotating table For the rotations a rotating table was manufactured at a TU Berlin workshop with a socket for mounting the table onto the Phemos platform (see figure 79). Another socket (yellow) was positioned on top of the rotating table to be able to fix the test devices properly. The rotating table is adjustable in steps of +/- 1 degree. After each measurement the table was rotated manually. At first thought this rotation procedure may seem very difficult or even impossible to handle for needle-/manipulator-contacted devices. Bearing in mind that it is really the relative alignment of dispersive element (prism) and device that needs to be rotated by a certain angle, the rotation can also be done for the dispersive element only. In this case no extra measures compared

to a conventional PEM measurement and no rotation would have to be carried out for the device under test. This would enable broad and easy industrial use and would also enhance the accuracy of the rotation angle and time consumption for measurements because of an automated rotation procedure. For the proof-of-concept level presented in this thesis manual rotation of the device was sufficient.

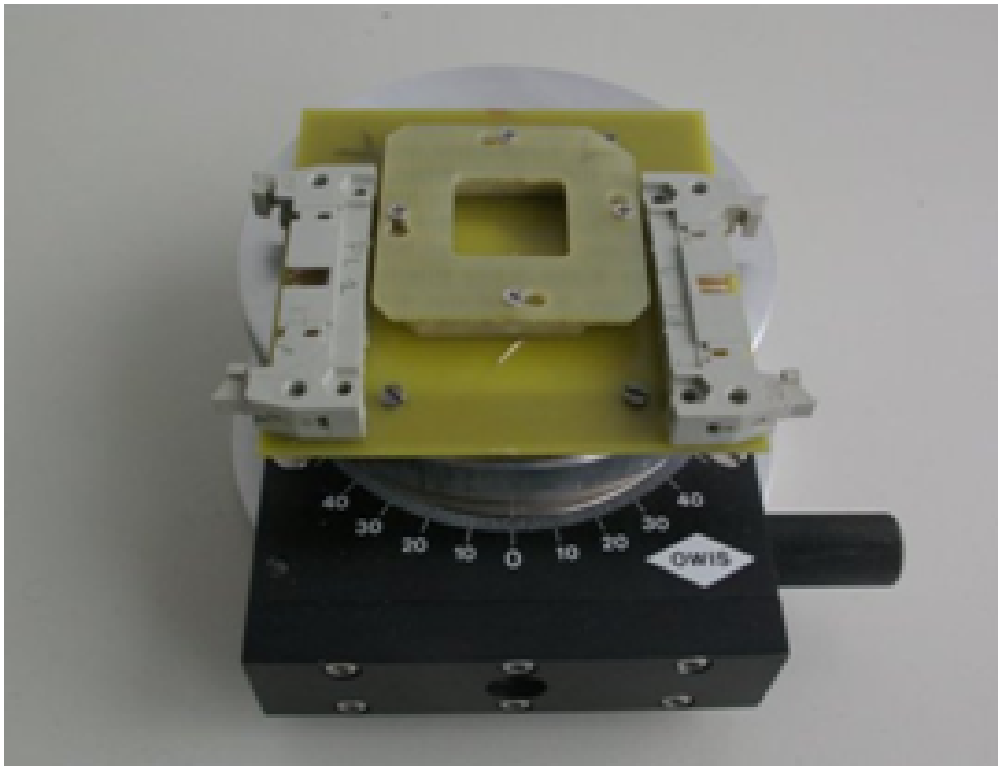

Figure 79: The rotating table for the angular adjustment of the DUT during the measurements.

5.5.3.4 Position of the image Before starting the measurements it is important to think about the appropriate positioning of the image on the device. Mainly there are two important issues to bear in mind. First, if the light emission sources are to close to the center of the image an arbitrary rotation will not give much additional information about the spectrum. This is due to the fact that a rotation affects positions close to the center much less than positions further outside. Second, the emission sources must not be to close to the edge of the image. If they are, then their intensity might be mapped outside the CCD sensor for certain rotations due to the additional pixel shift. The conclusion is that the light emission sources should be within the red-marked area in figure 80. For optimal accuracy there shouldn't be any light sources in the white area in the middle or the white area between the red circle and the edge of the image.

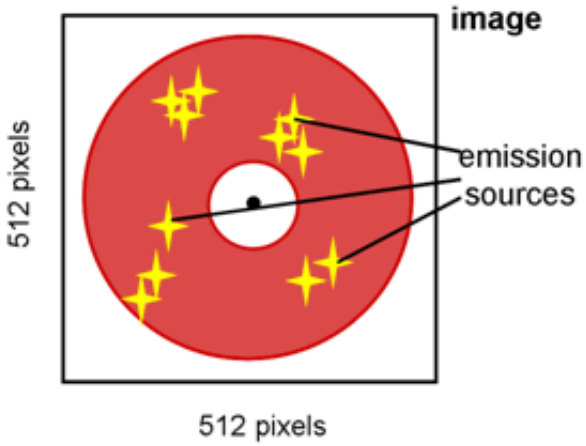

Figure 80: The best position of the DUT for the tomography method measurements is so, that all emitting light sources of interest are within the red-marked area.

5.5.3.5 Rotating the device It is not necessary to have the middle of the acquired image (turquoise) exactly in the center of rotation (red) of the rotating table (see figure 81). It will be proven below that a rotation around an arbitrary center together with re-centering the middle of the image to the same point P on the device after each rotation is equal to a rotation around the point P by the same angle. It should be emphasized that the re-centering after each rotation is absolutely crucial for this equivalency (see proof below).

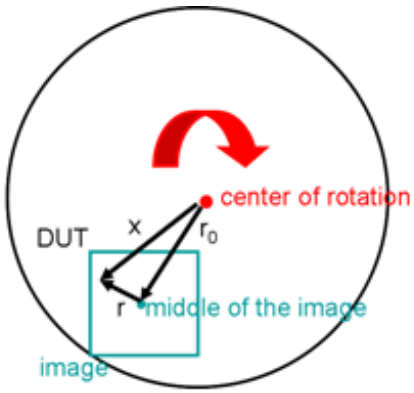

Figure 81: Sketch to discuss the question of rotation and re-centering for 2d-tomography. $\mathbf{x}$ is the position vector of an arbitrary point in the image, $\mathbf{r}_0$ gives the location of the middle of the image (turquoise) and $\mathbf{r}$ represents the distance from the middle of the image to the arbitrary point. The origin of ordinates is the center of rotation (red).

Proof: Let x be the position of an arbitrary light emission source in the acquired image for one specific angle. Now we rotate the whole device around an arbitrary point (center of rotation, red) by an arbitrary angle φ. Mathematically speaking, this rotation can be modeled by a rotation matrix R_φ . So the new position of the light emission source after the rotation will be $R_\varphi \cdot \mathbf{x}$.

Splitting up the location vector x into a vector $\mathbf{r}_0$, which represents a vector connecting the center of rotation (red) and the middle of the image (turquoise), and a vector $\mathbf{r}$ connecting the middle of

the image with the location of the light emission source within the image one has $\mathbf{x} = \mathbf{r} + \mathbf{r_0}$. It follows

$$R_\varphi \cdot \mathbf{x} = R_\varphi \cdot (\mathbf{r} + \mathbf{r_0}) = R_\varphi \cdot \mathbf{r} + R_\varphi \cdot \mathbf{r_0}. \tag{5.53}$$

Re-centering the image after the rotation means setting $R_\varphi \cdot r_0 = 0$. Hence

$$R_\varphi \cdot \mathbf{x} = R_\varphi \cdot \mathbf{r}. \tag{5.54}$$

Therefore a rotation around an arbitrary point (center of rotation, red) with additional re-centering to the center of the image (turquoise) is equal to a simple rotation around the center of the image by the same angle.

5.5.3.6 Si-Bulk and Phemos system transmission For the calculation of the unknown spectral distribution of the device it is necessary to take into account the spectral transmission of the Phemos-1000 optical system, which was measured by Arkadiusz Glowacki. As the measurements were realized through the backside of the device, the bulk silicon transmission for a thickness of $8\mu m$ has to be considered, too. Both data sets can be seen in figure 82.

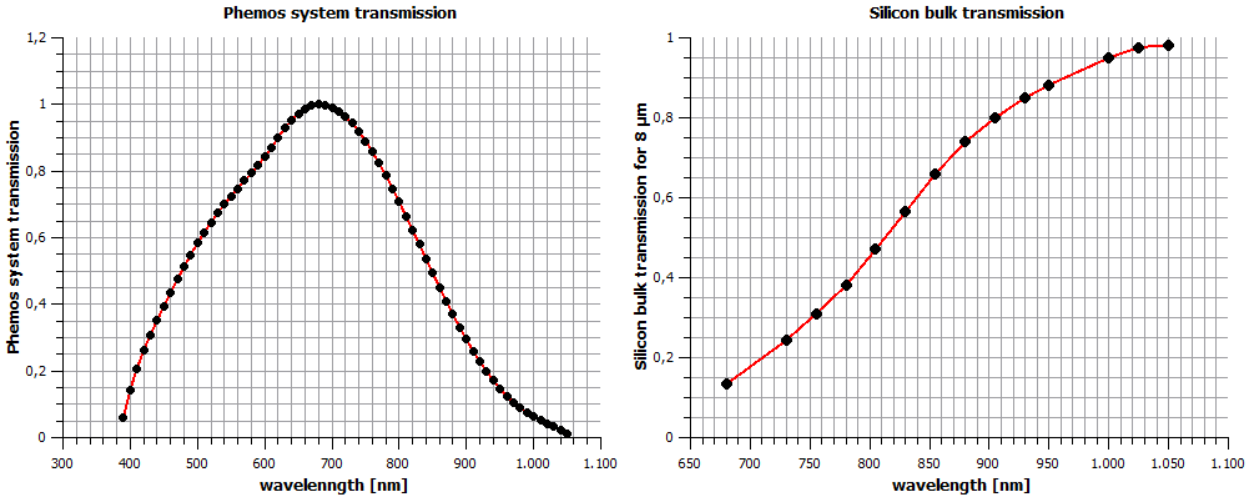

Figure 82: Spectral transmission for the Phemos-1000 system (on the left) and a Silicon bulk of $8\mu m$ thickness (on the right).

The relevant spectral interval for the measurements can be obtained by a multiplication of Phemos-1000- and Silicon bulk-transmission curves as shown in figure 83. The calibration data shows that the relevant interval for the measurements lies between about 600nm to 1000nm. For other wavelengths the overall transmission is too low.

Table 8: Measured pixel shift for Phemos-1000 with inserted prism for different wavelengths

wavelength	pixel without prism	pixel with prism	pixel shift frontside (Δ_λ)	pixel shift backside
530 nm	255	234	-21	21
580 nm	255	219	-36	36
630 nm	255	207	-49	49
680 nm	255	197	-58	58
730 nm	255	190	-66	66
780 nm	255	183	-73	73
830 nm	255	177	-79	79
880 nm	255	172	-84	84
930 nm	255	167	-89	89
950 nm	255	166	-90	90
1000 nm	255	162	-94	94
1050 nm	255	159	-97	97

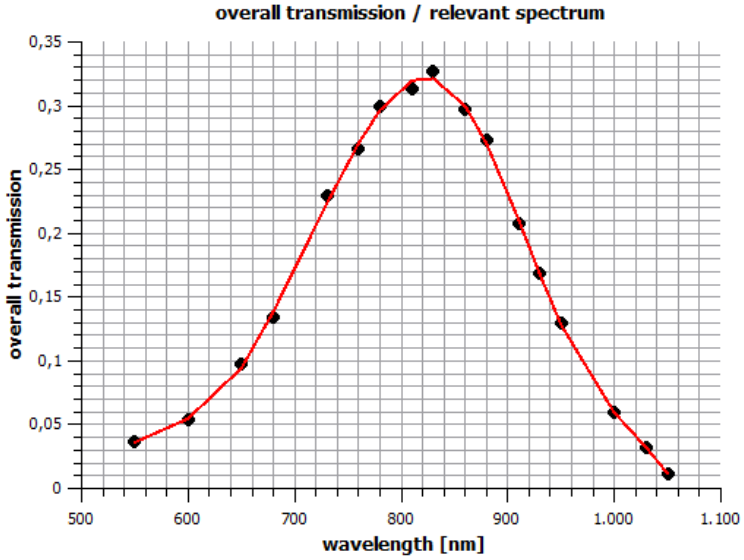

Figure 83: Overall Transmission for the measurements acquired by multiplication of Phemos-1000- and silicon bulk-transmission. The relevant spectral intervall for the measurements is the interval from 600nm to 1000nm. For all other wavelengths the transmission is too low and causes too high uncertainties.

5.5.3.7 Pixel shift The wavelength-dependent pixel shift with inserted prism can be obtained by measuring a spot-like emission source with an additional narrow bandpass filter inserted in the optical path. The filter prevents the spectral widening of the light source. Thus, the difference between the emission spots' position with and without prism can be calculated easily. Table 8 and figure 84 show the local shift of the light emission of a pixel at (p=255,q) by the number of pixels shifted. The measurements were carried out by Arkadiusz Glowacki from TU Berlin.

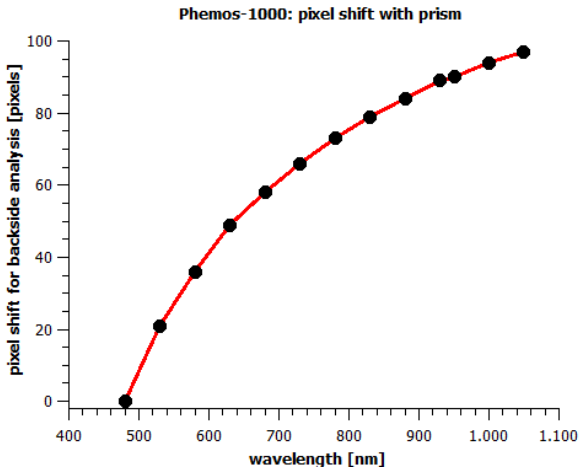

Figure 84: The graph shows the pixel shift for Phemos-1000 backside analysis with inserted prism in the optical path.

5.5.4 Numerical background

This section gives a brief overview of the main features and steps for the numerical processing of the experimental data, acquired by spectral photon emission images from different angles. The tomography program was written for use with Scilab. The whole, detailed source-code can be found in the appendix section A, where one smaller script for image data preprocessing and the main script for the solution of the system of equations (5.39) are presented with additional comments.

5.5.4.1 Pixel binning For first tests at the beginning of the methods' development the image resolution was reduced numerically by binning. Once the basic functionality of the method was confirmed, the binning procedure was excluded from the algorithm. Binning means reducing 2x2, 4x4 or 8x8 pixels to one single pixel with the average value of the 2x2, 4x4 or 8x8 pixel area. Of course, the binning procedure is not recommeded for later / professional use because it drastically reduces optical resolution, but it can be helpful at early stages to reduce computation time and complexity for basic functionality tests. The effect of binning can be seen in figure 85.

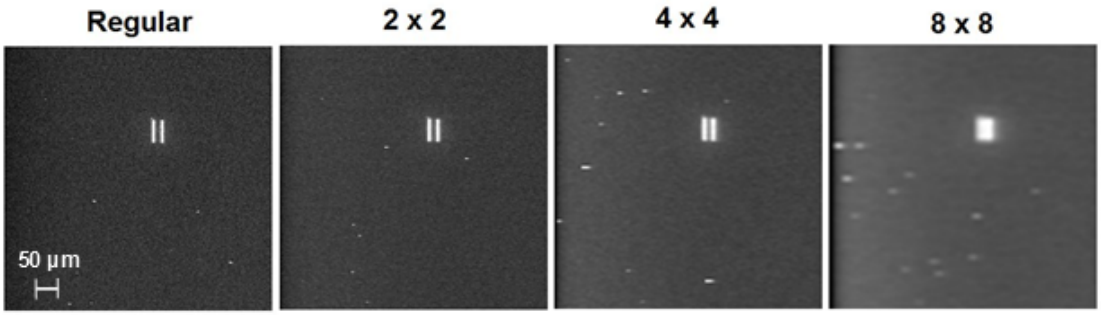

Figure 85: The image shows the effect of pixel binning for three cases. It is clearly visible that the image resolution decreases the more pixels are binned to one single pixel.

5.5.4.2 Image processing Apart from binning, it was helpful to eliminate statistical noise and obvious measurement errors like single randomly positioned spots from the images before the calculation. This elimination was realized by reading the gray-scale images into the Scilab software and setting all intensity values outside the interesting region to zero. For more complicated structures a more detailed and refined elimination algorithm has to be applied, but this is generally not a severe problem.

5.5.4.3 Solving method for system of equations Scilab offers several solution algorithms for overdetermined linear systems of equations, from which the standard b̈ackslash¨operator solution method was chosen. Here the overdetermined linear system was solved by an approximation algorithm evaluated internally with a least mean square approach.

5.5.4.4 Optimization techniques A brief overview of the overall tomography procedure with estimates on time consumption can be found in fig. 86 below. Apart from the optimization techniques presented here, there are various additional strategies and enhancement possibilities, which can be implemented. The reader should bear in mind that the whole tomography research project at TU Berlin was intended to give a proof-of-concept of the method. The aim was to demonstrate the methods applicability to real PEM/FA cases, to show its advantages and lay out a broad and detailed mathematical, numerical and experimental foundation for further development and possible industrial use. Therefore only some optimizations were included in the development for the method, leaving a lot of chances for further accuracy and speed improvement, when a professional/industrial application of the method is intended. Here only a short selection and description of strategies is presented:

1. The most promising optimization idea was to take an image of the device without inserted prism for a rotation of 0 degrees. This 0Â°-image clearly shows where emission sources exist or not. Additionally, this image gives the overall intensity (sum over all wavelengths) for each pixel on the device. This information can be used to vastly reduce the number of variables to determine in the system of equations and to add further normalization equations to guarantee that the sum of all spectral intensities in one pixel is conserved. Implementation of this technique alone reduced the computation time by a factor > 100 and also enhanced the methods accuracy by a large factor.

2. Another improvement for the numerical accuracy and time consumption can be obtained by starting the solution algorithm with a well-fitted starting value for the numerical solution algorithm. This can be realized by the use of certain preset emission profiles together with the 0Â°-image of the device (see above). Furthermore the occurrence of negative intensity values in certain pixels can be forbidden numerically, which will improve the numerical part of the method further.

3. To limit effects by degradation of the device it is possible to calculate an overall intensity sum for each image, which allows for detection of degradation accurately. If the overall intensity decreases after each rotation, it is easy to correct this effect by multiplying the pixel intensities on different images with different correction factors.

4. The deletion of lines and entries of the matrices with unnecessary information or corresponding to low intensities clearly improves numerical accuracy as well as time consumption.

5. The discretization of wavelengths will be a lesser factor for spectral inaccuracy once it is possible to include more wavelengths due to a decreased computation time. One idea to solve this problem almost completely is to preset certain emission profiles (electron temperature emission, black body radiation etc.) and to calculate the unknown spectral intensity on the device as a superposition of many different profiles.

6. Statistical noise can be subtracted from the image via statistical image processing. This has already been done with low-level statistical models, which can be enhanced for more complicated test structures.

7. All simulations were done on a standard Dell laptop from 2013. The technical advance over the last 5 years and even more so the use of multi-core parallel processing can reduce computation drastically down to some seconds/minutes even for high resolution (512×512 pixels).

8. For the proof-of-concept a prism not perfectly adjusted to the application was used due to lacking alternatives. Ideal would be a prism with more linear dispersion characteristic and generally higher dispersion per nm wavelength (see figure 84).

9. To enable broad and easy industrial use an automated rotation procedure for the dispersive element (prism) should be installed in the optical path. In this case the device under test would not have to be rotated, improving the accuracy of the rotation angle and time consumption for measurements because of the automated rotation procedure. For the proof-of-concept level presented in this thesis manual rotation of the device was sufficient.

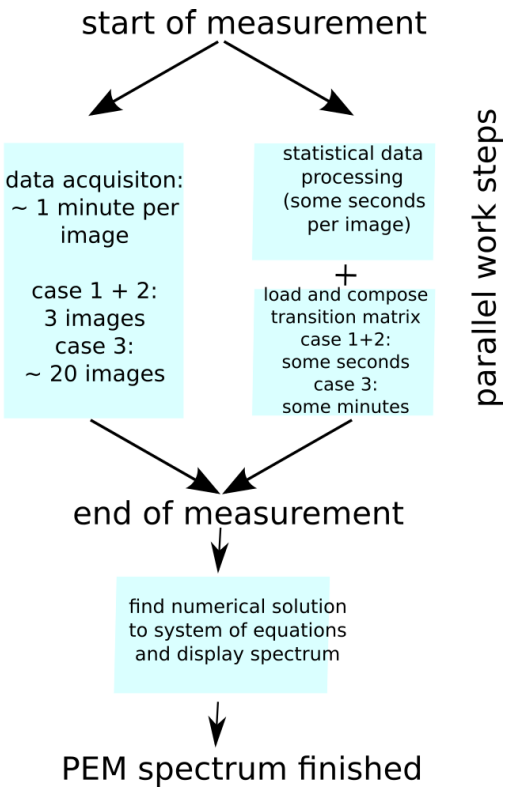

Figure 86: Brief overview of most important steps of the tomography method with rough estimates on time consumption.

5.5.5 Results for C11 ring oscillator

For the measurement and calculation presented here we chose 6/9 wavelengths with 16 rotations from -90 to 90 degrees, while the device was constantly biased with a supply voltage of $1.5V$. The resolution was reduced to $64 \times 64/256 \times 256$ pixels by binning within the numerical process. The computation time for the first case was less than 10 seconds and for the second case computation took about 2-3 minutes for 256x256 resolution on a standard Dell laptop from 2013. The first case was treated without any optimization strategy, while for the second (ïmproved¨) case strategies 1,3,4 and 6 were used (see section 5.5.4.4).

The results are presented in fig. 87 and 88. As an example fig. 87 shows an emission intensity image for $880nm$ wavelength calculated by the tomography method in simple (left) and improved setup (right). The respective spectra can be seen in fig. 88. The resulting spectrum reveals an exponential decrease of emission intensity with light energy between 600 and $1000nm$, which is the typical hot carrier emission pattern from a MOSFET channel in saturation at pinch-off region. The spectral results show that the intensity is too high at the highest and lowest wavelengths chosen for evaluation (see fig. 88 left). This is due to the effect that intensities of wavelengths higher / lower than the maximum / minimum evaluated wavelength are partly mapped into the max / min wavelength due to small spatial inaccuracies of the optical mapping on the detector and a not perfectly adjusted prism (the prism is an inherent part of our microscope that we could not exchange). This effect is much lower for wavelengths not at the edges of the chosen wavelength

interval and can thus be circumvented to a large extent by deleting the max/min wavelength data after numerical computation (fig. 88 right).

From the spectrum the electron temperature T_e of the hot electron gas in the transistor channel can be calculated via

$$I(E) = C \cdot e^{-\frac{h\nu}{k_B \cdot T_e}} \tag{5.55}$$

with the calculated intensity I at a certain photon energy $E = h\nu$, the Boltzmann constant k_B and a further integration constant C. The electron temperature is highly dependent on the strength and slope of the electrical field within the channel. In MOSFETs usually photon emission can only be detected in the channel region with the highest electrical field near to pinch-off. The conventional measurement gives an electron temperature of $2037K$ [61] in the RO's lower right corner, the tomographically obtained data for the same region indicates an electron temperature of $1837K$ (fig. 88 left). Evaluation of a bigger area (not accessible by conventional measurement) with improved numerical algorithm (fig. 88 right) gives an electron temperature of $3186K$, indicating a possible degradation and thus lower temperature at the area of the conventional measurement. The results are realistic as MOSFETs in saturation are known to have electron temperatures $1000 - 3500K$ in saturation operating condition. The statistical accuracy of the graphs slope (i.e. the electron temperature) gives a failure interval of $\pm 1.2\%$ for conventional measurements, $\pm 43\%$ for the old tomography data and $\pm 25\%$ for the improved data. As the tomographical method is only at proof-of-concept level this is no surprising. With professional optimization on experimental and numerical level, the method will reach similar accuracy intervals as conventional methods.

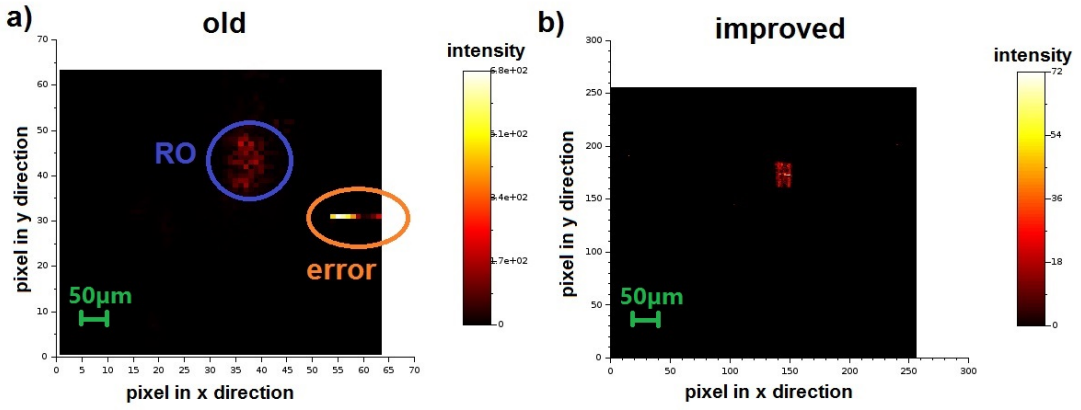

Figure 87: Intensity distribution of photon emission delivered by tomography spectra acquisition method for 880 nm at an early stage (a) and after several improvements to the numerical algorithm (b). Errors from early stages (see left) were completely patched.

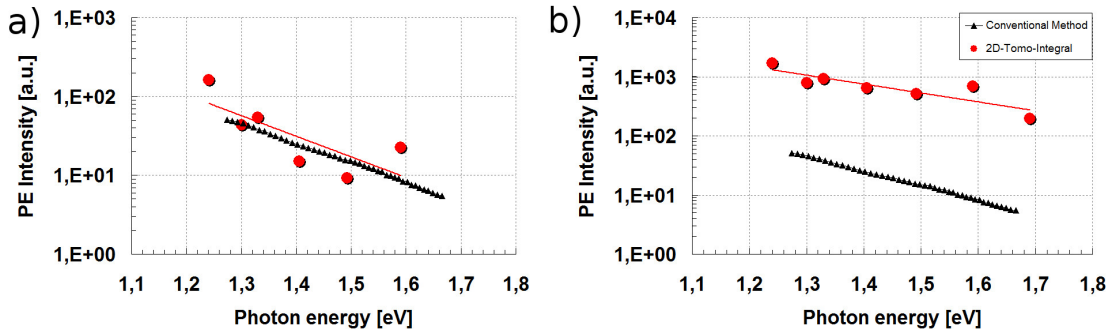

Figure 88: Resulting spectra at $1.5V$ supply voltage. The red points indicate discrete results from the tomography program fitted with the red line. The black symbols represent data from a comparison measurement with conventional methods (i.e. with prism and without tomography) on a special spot of the ring oscillator, where conventional analysis was exceptionally possible due to subtle rotation to avoid dispersion for emission for this small region of the emission pattern. Left (a): Early stage. Right (b): Improved method.

5.5.5.1 Error sources Several sources for errors during the measurement and during the numerical processing and calculation of the data exist. Measurement errors include statistical noise due to temperature effects in the CCD sensor or the electronic connections. It is also possible that small irregularities of the prism and imperfections of the optical path within the emission microscope have a certain effect on the pixel shift or the light transmission. Additionally, one has to take into account the possibility of degradation effects in the test device at higher voltages as the measurements are serial. Inaccuracies with recentering the images after rotation can also lead to loss of spatial resolution.

Considering the numerical process the most important sources for errors and inaccuracies are failures due to the discretization of wavelength. Also rounding errors occur when rotated coordinates are rounded to integers. For pixels at the very right edge of the image errors can occur due to the fact that the prisms' pixel shift partly maps emission intensities out of the image here (fig. 87 left).

5.6 PEM on analog devices

This section is supposed to enlarge the knowledge for application of photon emission-based techniques to different types of current mirrors as representatives of typical and frequently used analog circuit elements. Three different types of current mirrors will be investigated: Two different simple current mirror, two different cascode current mirrors and two different low-voltage current mirrors. A schematic of all current mirrors can be seen in figure 89. The capital letters A to F in the image refer to different size transistors on input/output side of each current mirror. The individual transistors' geometries are referenced in table 9. To expand the operation range towards higher currents, transistors A-F mostly do not consist of one single transistor but multiple FETs in parallel as indexed in the table. All transistors were n-type MOSFETs in 250nm technology with threshold voltages $V_{th} \approx 0,6V$ and a nominal voltage of $V_{nom} = 2,5V$. A pattern image of the different current mirrors can be seen in figure 90. All pattern and PE measurements of this section were done from the backside of the chip, which was individually packaged and thinned down to a backside thickness of $100\mu m$. Nanolens-use was not possible due to geometrical restrictions of the socket. Some contents as well as figures of this section were already published in the authors contribution to ESREF 2017 [67].

A current mirror is an analog circuit element built to either reproduce a given current or to increase/decrease a given current in a ratio predefined by the geometrical characteristics of the input and output side transistors of the respective current mirror. The basic operating principle will be explained on the example of a simple current mirror: As gate and drain of the input-side transistor are shorted internally, the input-side transistor is always operating in saturation once an input current I_{in} is fed in. Because the gates of the input-side and output-side transistor are also shorted internally, the output side transistor can never be in off-state, but either operates in linear-parabolic or saturation region depending on the output-side voltage V_{out}. To ensure that the output-side transistor exactly mirrors the current on the input side, the output voltage V_{out} must be high enough to ensure saturation operating condition. Usually $V_{out} = V_{dd}$ is chosen, but also smaller values for V_{out} are possible, as the drain-to-source current of a MOSFET in saturation is almost independent of drain voltage. Depending on the ratio of output-side transistor width to input-side transistor width the input current is mirrored, enhanced or increased by a stable factor. A cascode current mirror adds a second pair of transistors for input/output side to stabilize output-side behavior due to a higher output-side resistance. A low-voltage current mirror is similar to a cascode current mirror with the exception of an additional voltage V_{bias} for the upper pair of transistors (C, D), which allows for better individual adjustment of the operating point for both transistors. This expands the operating region towards lower currents and voltages.

Electrical characteristics of simple current mirror no.1 can be found in figures 91 and 92. As the output-side and input-side transistors total width was equal here (see table 9), the current amplification factor was 1. The relation between input voltage V_{in} and input current I_{in} was measured in order to be able to relate later photon emission measurements to voltage for easier comparison with other PEM data presented in this thesis. Figure 92 reflects the aforementioned internal short of the input-side and output-side gate: Thus the input current I_{in} can be used to adjust the output-side gate voltage so that the output-side current over V_{out} for different I_{in} resembles the output characteristic of an individual FET.

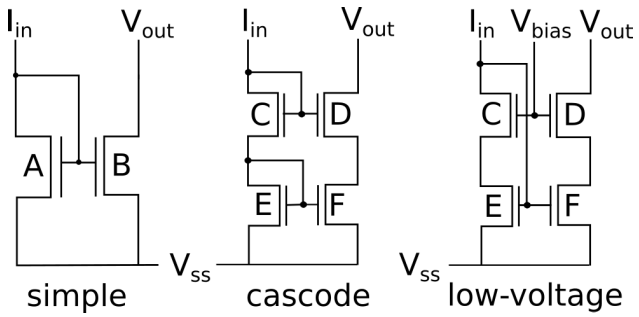

Figure 89: Schematic of the three different current mirror types. Capital letters A to F indicate different transistor geometries (see table 9).

Table 9: Current mirror types and geometrical features of individual transistors

Transistor ID	**Number of nFETs in parallel**	**Gate length x width per single transistor**
A	2	1,4 μm x 2 μm
B	2 (simple current mirror 1) 8 (simple current mirror 2)	1,4 μm x 2 μm
C, D	4	720 nm x 4,95 μm (cascode + low-voltage 1) 240 nm x 1,65 μm (cascode + low-voltage 2)
E, F	4	720 nm x 4,95 μm (cascode + low-voltage 1+2)

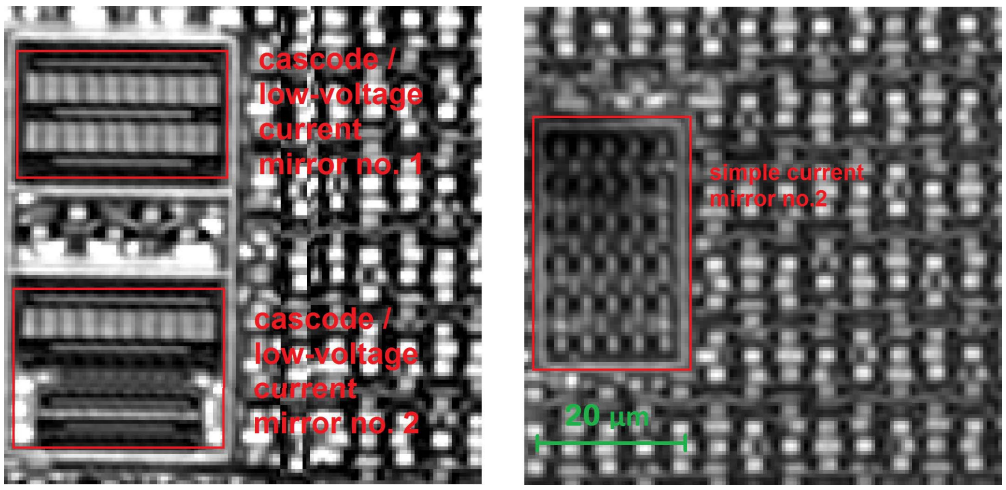

Figure 90: Pattern images of the cascode/low-voltage current mirrors (left) and simple current mirrors (right) taken with HIL light source. Different levels of metal fill can be seen in the periodic interference pattern all around the structures.

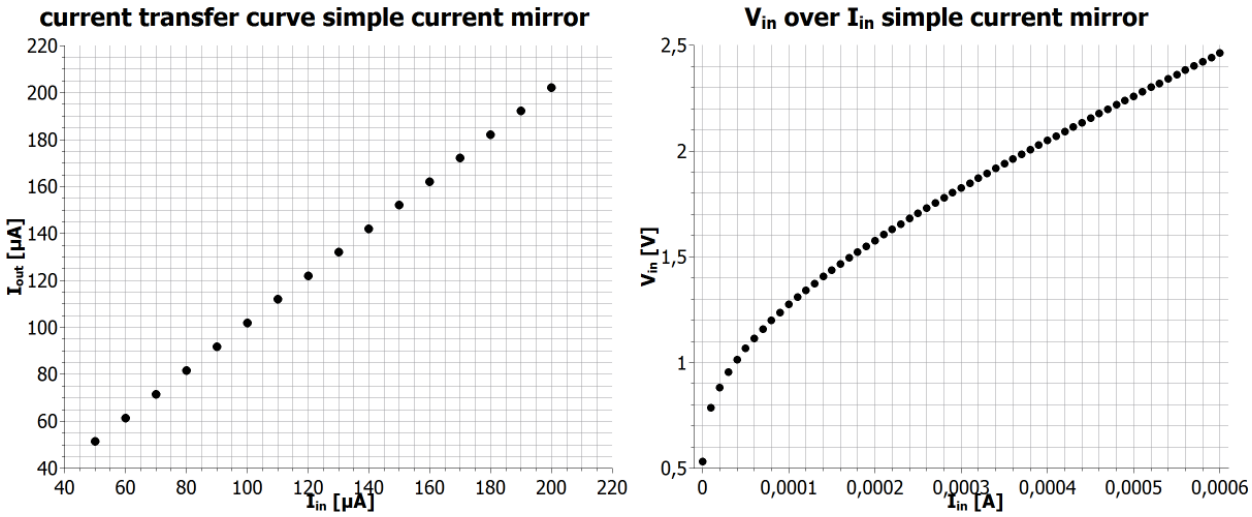

Figure 91: Transfer characteristic (left) and $V_{in} - I_{in}$-relation (right) for the simple current mirror no.1.

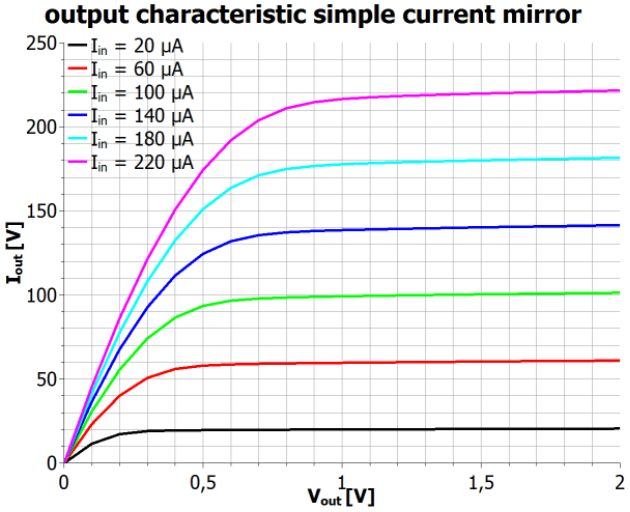

Figure 92: Output characteristics of the simple current mirror no.1 for different input currents I_{in}, which correspond to certain input voltages V_{in} as shown in figure 91.

In all PEM experiments on the simple current mirrors only the output-side transistors emitted light with detectable intensity (fig. 93). This can be motivated as follows: For PEM measurements on standard MOSFETs usually a gate voltage between V_{th} and $V_{nom}/2$ gives best signals, whereas drain voltage should be as high as possible. Due to the internal short of drain and gate of the input-side transistor, both voltages cannot be adjusted independently of each other leading to unfavorable operating conditions for photon emission. On the output side the situation is different: Here the gate voltage can be adjusted independently from drain voltage via I_{in}/V_{in}, so that optimal emission conditions can be reached. In order to find these optimal operating conditions, emission curves over inverse drain voltage and gate voltage were recorded (fig. 94). The results confirm the already known bell-shape of emission over gate voltage and the exponential decrease of emission over inverse drain voltage.

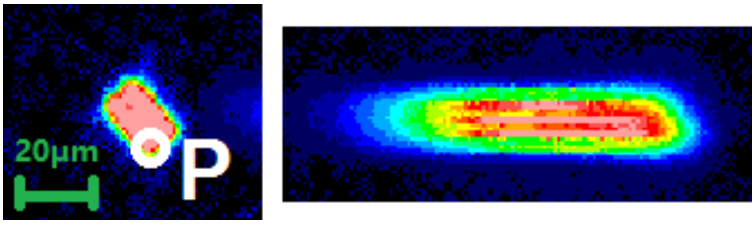

Figure 93: Photon emission image of the simple current mirror no.2 for $V_{in} = 1,5V$ and $V_{out} = 2,5V$ without (left) and with (right) prism. Only the 8 output side transistors emitted light. For extraction of spectra the whole structure was rotated by 45° so that the emission of the lower left transistor (P) could be extracted independently from the other transistors. Backside measurement without SIL.

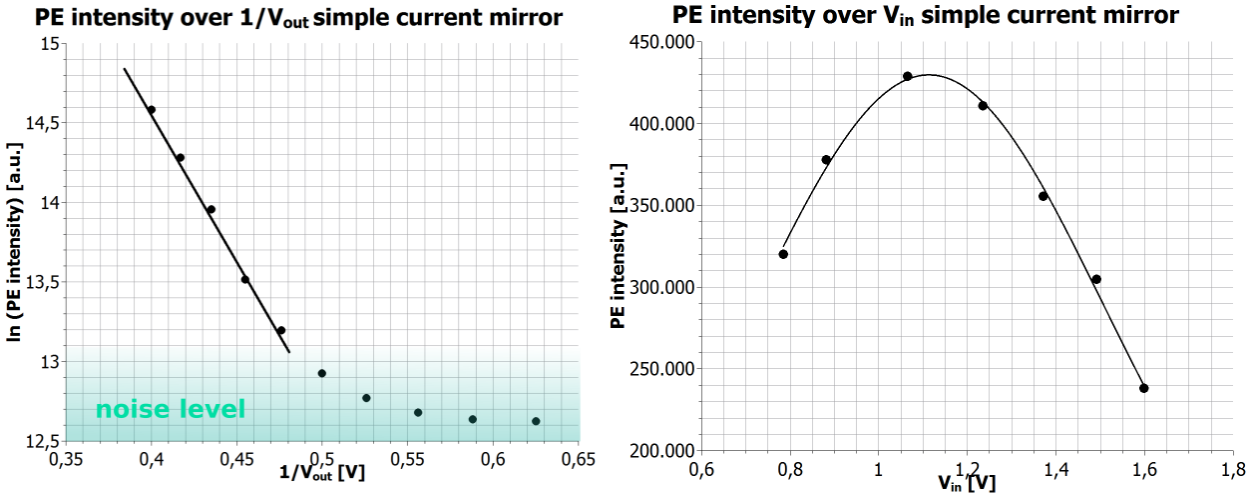

Figure 94: PE intensity slopes of the simple current mirror no.2 (only output side transistors emitting PE) over inverse output voltage at $V_{in} = 1,5V$ (left) and input voltage at $V_{out} = 2,5V$ (right). Backside measurement without SIL.

The extracted photon emission spectra of the simple current mirror no.2 showed a perfect exponential course over photon energy (fig. 95). Electron temperatures rose almost perfectly linear with drain voltage / V_{out}. In comparison to previous hot carrier gas temperatures extracted for FinFETs (sections 5.3 and 5.4), the electron temperatures lied in a range of 500 to 1000 K even for

voltages clearly lower than nominal voltage. This fact can be motivated by the larger gate length and generally higher supply voltages for the technology in this section here.

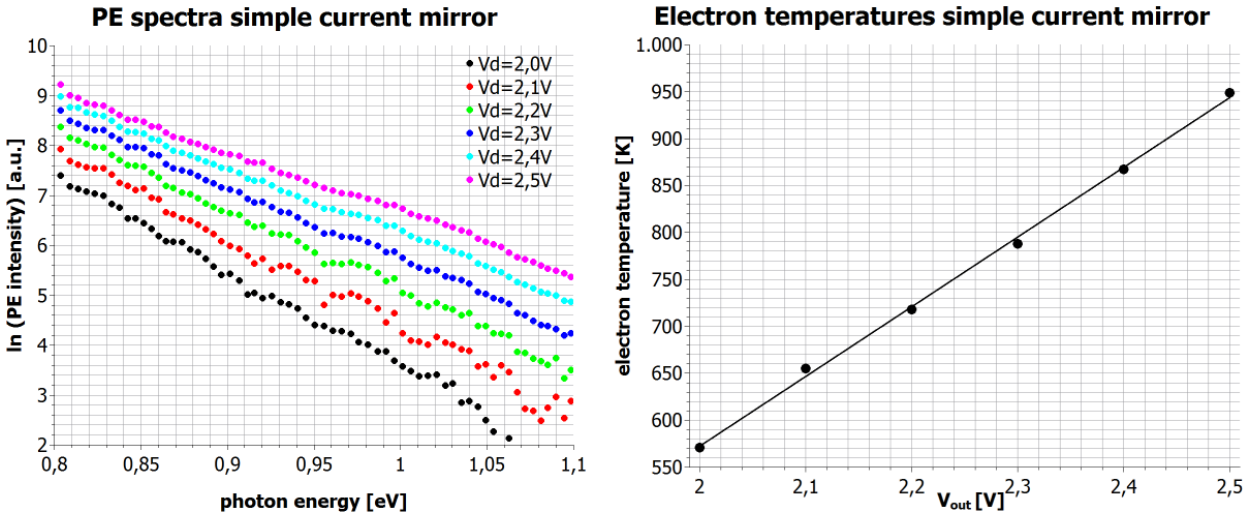

Figure 95: PE spectra (left) and electron temperatures (right) for the simple current mirror no.2 operated at $V_{in} = 1,5V$. Backside measurement without SIL.

Unfortunately, no photon emission could be detected for the cascode and low-voltage current mirrors. The reason for this is that for both current mirror types the input voltage and the output voltage are both distributed along two transistors in series (fig. 89). Therefore the drain-to-source voltage of each transistor does never leave an interval between $\approx 1V$ and $1,5V$. For detectable light emission at the simple current mirror a drain-to-source voltage of at least $1,8V$ was needed. Obviously the differences in gate length between the different current mirror types were not high enough to compensate for this. For the input-side transistor the problem is even worse, because here adjustment of individual FET voltages is even more restricted due to internal shorts of gate and drain. The hope of being able to at least see photon emission from the low-voltage current mirrors by making use of V_{bias} was dispersed, because the interval for V_{bias} was only small ($1,1V$ to $1,5V$) due to imperfect design. As a summary it can be stated that photon emission on current mirrors is possible, but becomes challenging when supply voltages are distributed along drain-to-source of several transistors in series.

5.7 Future of PEM and SPEM

This section is supposed to give an outlook on future use of photon emission techniques for low-voltage device failure analysis and device characterization / parameter extraction. Some contents as well as figures of this section will also be published in the authors contribution to IPFA 2018 [11]. First, relevant general trends regarding PE signal slopes are discussed. Figure 96 shows two main influences on the general PE signal level: The red-shift of intensities with decreasing hot carrier gas temperature in the channel leads to a stronger intensity slope over wavelength for low electron/hole temperatures, but starting at progressively higher wavelengths (lower energies). This red-shift has the advantage of strong signal levels above $1600nm$ (e.g. [48]), but requires extensive cooling of deeper-infrared detectors to avoid noise due to black-body heat radiation of surrounding areas. Another advantage is the comparably low absorption of higher wavelengths in bulk silicon (backside measurement) or in gate material / different interconnect layers (frontside measurements).

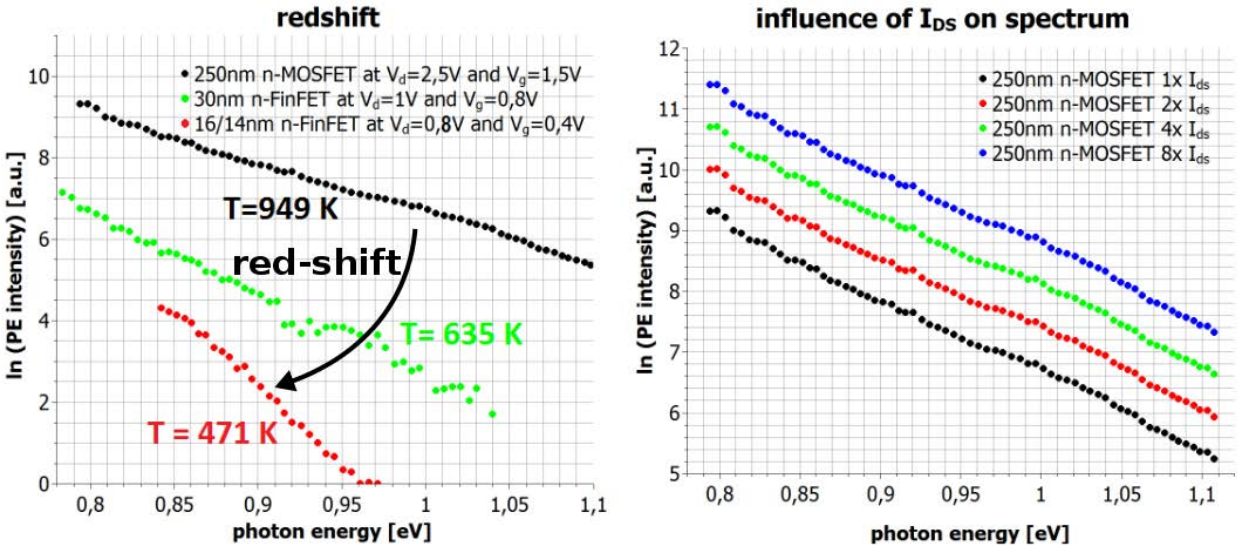

Figure 96: Illustration of the red-shift of spectral intensities with decreasing hot carrier gas temperature (left) and PE intensity dependence on source-to-drain current (right). Black curve (T=949K): backside measurement without SIL. Green curve (T=635K): frontside measurement without SIL. Red curve (T=471K): backside measurement with SIL.

An overview of spectral emission ranges of state-of the-art low-voltage devices and detector levels is presented in figure 97. Here it can be seen that detection of photon emission with silicon CCD-cameras becomes more or less impossible for hot carrier gas temperatures lower than $800 - 900K$. Analysis of hot carrier gas temperatures of older planar MOSFETs and modern FinFETs over normalized drain voltage (fig. 98) clearly shows, that temperatures for state-of-the-art devices lie (far) below $600 - 700K$.

Average PEM detection limits for silicon CCD and InGaAs detectors with respect to hot carrier gas temperatures are shown in figure 99 and 100. Even with the use of a suitable GaP-SIL the silicon CCD becomes useless for temperatures below $\approx 800K$, whereas InGaAs with silicon SIL is capable of detecting emissions from hot carriers close to $450K$. Suitable SILs roughly give a

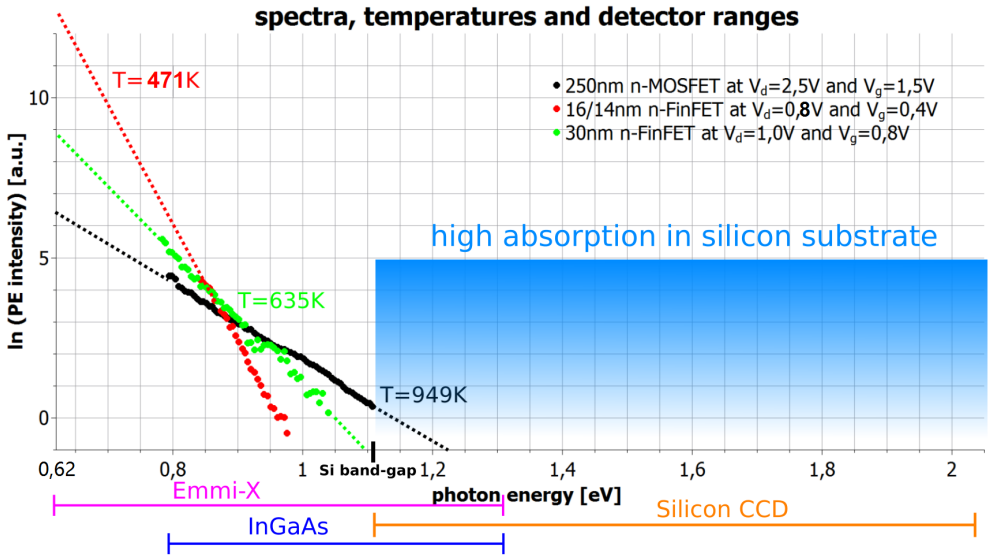

Figure 97: Comparison of detector sensitivity intervals and relevant device PE spectra for temperatures $319 - 949K$ on logarithmic scale over photon energy. For smaller temperatures the red-shift leads to high emissions below $0.8V$, requiring deeper infrared detectors (e.g. Emmi-X). I_{ds} was normalized to one and the same value of $12\mu A$ for all three devices to exclude intensity differences due to different I_{ds} here.

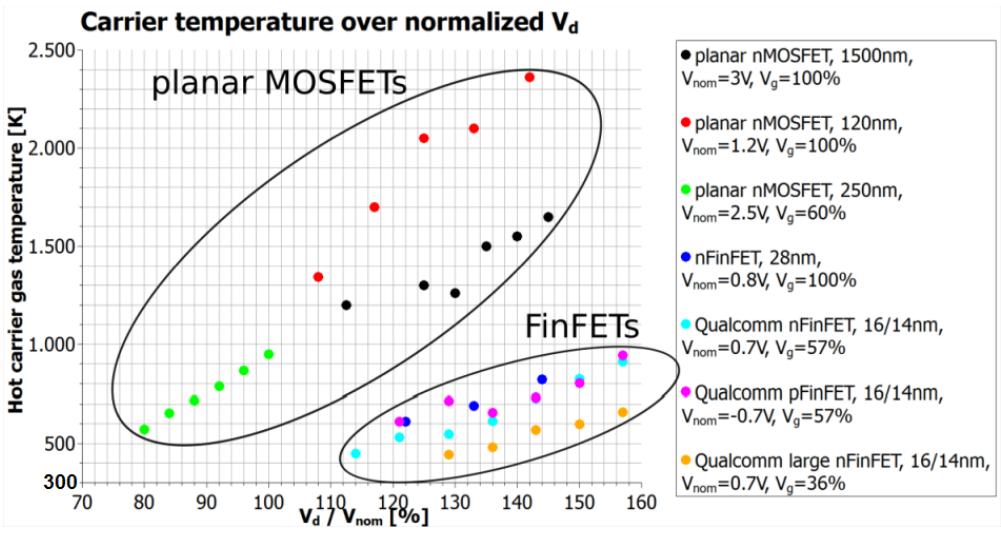

Figure 98: Comparison of hot carrier gas temperatures over relative drain voltage (V_d/V_{nom}) for several MOSFET and FinFET technologies, various gate lengths and nominal voltages. The data for the 1500nm-MOSFET (black) is taken from [50], whereas the data for the 120nm-MOSFET (red) is taken from [61].

signal increase factor of 6 to 10. In order to explore and analyze the $300K - 450K$-area of modern low-voltage devices (figure 101) with good signal-to-noise ratios and precise differentiation between small changes in operating conditions, deeper infrared detectors have to be applied necessarily as shown above.

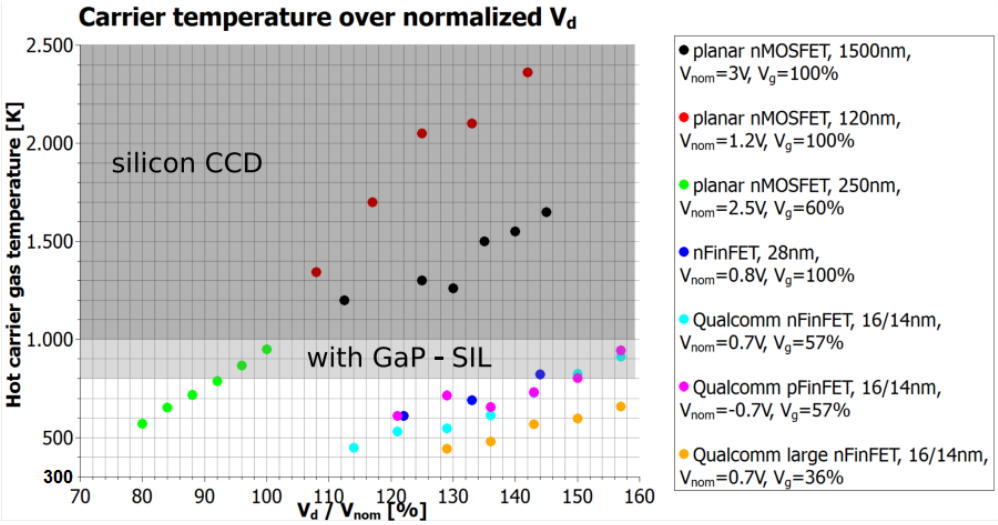

Figure 99: Same image as above in fig. 98, but with an approximation for silicon CCD detector sensitivity over hot carrier gas temperature with and without GaP-SIL. The data for the 1500nm-MOSFET (black) is taken from [50], whereas the data for the 120nm-MOSFET (red) is taken from [61].

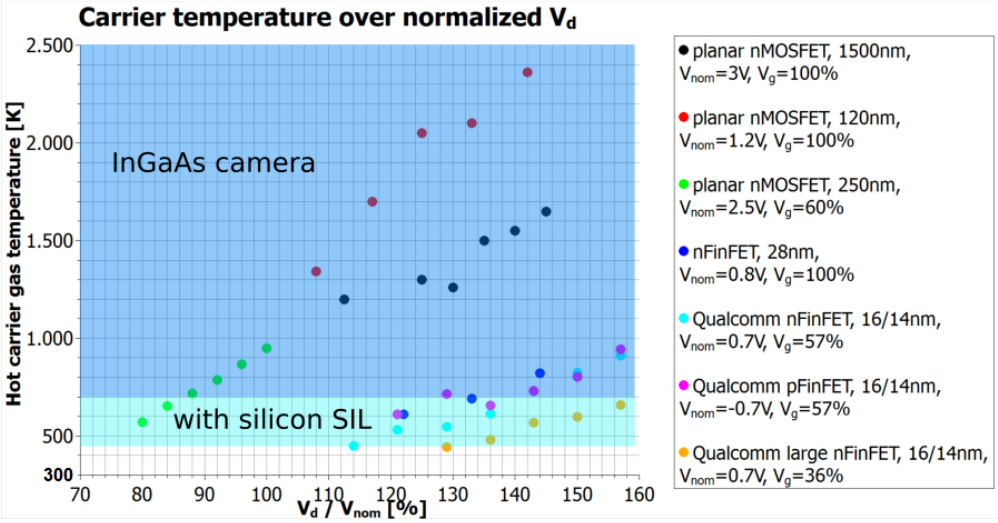

Figure 100: Same image as above in fig. 98, but with an approximation for InGaAs detector sensitivity over hot carrier gas temperature with and without Si-SIL. The data for the 1500nm-MOSFET (black) is taken from [50], whereas the data for the 120nm-MOSFET (red) is taken from [61].

A further possibility to increase signal-to-noise ratio is cooling of the chip, as this will increase the relative emission intensity difference between hot carrier gas and closely neighboring areas emitting

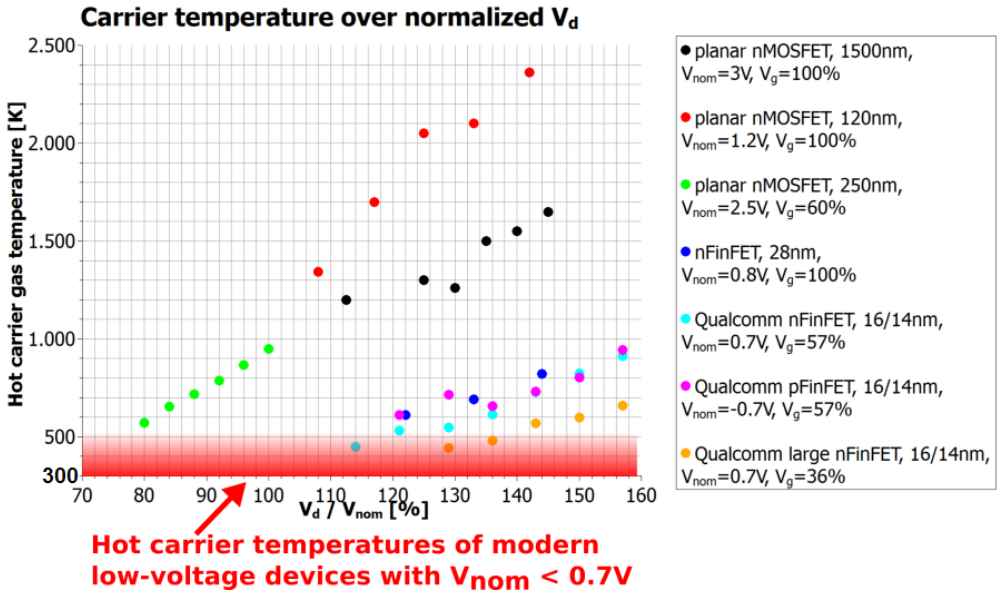

Figure 101: Same image as above in fig. 98, but with an approximation for hot carrier gas temperatures of modern low-voltage devices with $V_{nom} \leq 0,7V$. The data for the 1500nm-MOSFET (black) is taken from [50], whereas the data for the 120nm-MOSFET (red) is taken from [61].

black-body radiation at lattice temperature. Additionally, photon emission intensity change is proportional to source-to-drain current of the transistor (fig. 96). The overall development of on-current level of the transistor therefore is of considerable importance regarding PE. Regarding spectral PEM, the introduction of dynamic/time-integrated measurements to FA provides a good chance for strong signal-to-noise ratio improvement. For normal PEM this technique has already been in use within the failure analysis industry for several years under the name of time-resolved emission (TRE), also known as picosecond imaging circuit analysis (PICA).

In order to exploit the low hot carrier gas temperature regime below 400K, not only better experimental setups have to be developed, but also an expansion of the theoretical framework has to be carried out. If both improvements for the experimental and theoretical site are driven forward, the application of (spectral) PEM to even smaller devices than presented in this thesis with tech node sizes below 10nm is not a substantial problem. Even the extraction of carrier energies, free mean path, electric fields etc. will then be well possible. Further proof to that is added by results within this thesis and previous studies on PE intensity dependence on gate length: Figure 102 shows a strong exponential-like PE increase with decreasing gate length for various planar MOSFETs with L_g between $100nm$ and $350nm$ under identical electrical conditions from [22]. This trend could be confirmed for modern n-type FinFETs with gate lengths from $24 - 30nm$ within this thesis. Figure 103 shows that the hot carrier temperature decrease with drain/supply voltage is less drastic for FinFETs with smaller gate lengths than for those with higher gate lengths of the same technology. The higher the carrier temperature, the better the signal-to-noise ratio as long as a detector with suitable spectral range is used.

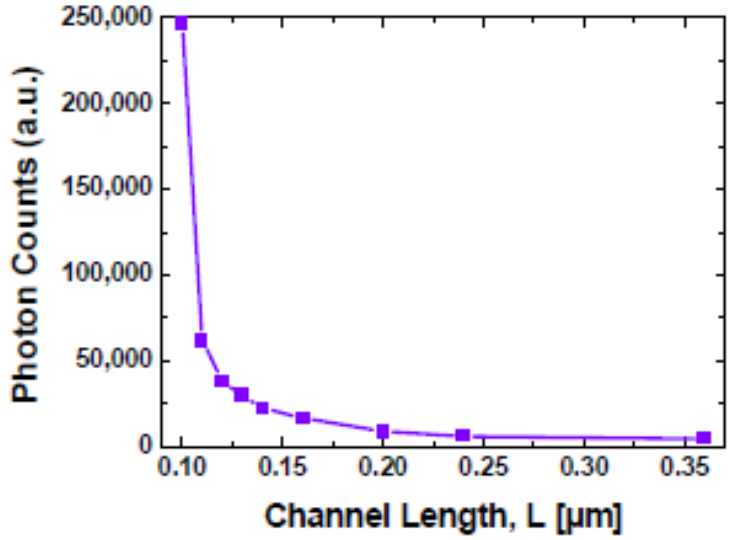

Figure 102: Photon emission over gate length at $V_{DS} = 2V$ for various MOSFETs manufactured in the same technology. Image taken from [22].

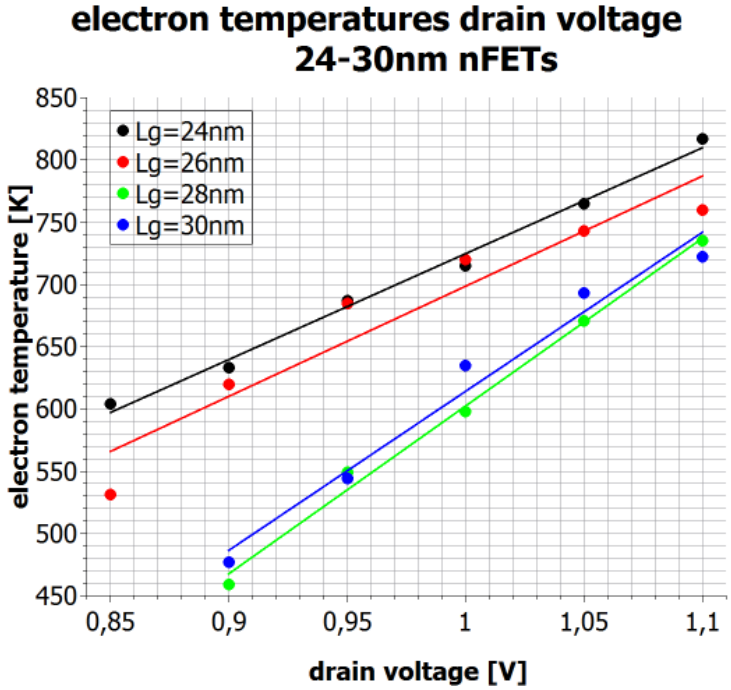

Figure 103: Electron temperature slopes over drain voltage for n-type FinFETs with various gate lengths from $24nm$ to $30nm$ for a gate voltage of $0,8V$.

Finally, a prediction of PE signal limit with respect to supply voltage is presented in table 10 taking into account mentioned improvements on the PE detection system used for this thesis. It can be seen that by combination of a deeper infrared detector with cooled optics and chip, as well as specialized SIL use and dynamic measurement, PE analysis could be carried out down to voltages of $\approx 150 - 200mV$ supply voltage. This fully covers the current range for low-voltage devices and expands the applicability of PE techniques far into the future.

Table 10: PEM and SPEM signal limit prediction for low-voltage devices

	approx. signal gain factor	approx. **PEM (SPEM) detection supply voltage limit for...**	
		16/14nm FinFET at $I_{ds} \approx 10\mu A$	**24nm FinFET** at $I_{ds} \approx 30\mu A$
InGaAs detection limit as evaluated in this thesis		0,70V (0,80V) with SIL	0,75V (0,85V) without SIL
without noise filter at 1500nm	5	0,60V (0,70V)	0,65V (0,75V)
with SIL use	6-10	already included	0,55V (0,65V)
with deeper infrared detector (1500nm to 2300nm)	100	0,35V (0,45V)	0,30V (0,40V)
dynamic measurement with Lock-In	10	0,25V (0,35V)	0,20V (0,30V)
cooling of chip and optical path	4-5	**0,20V (0,30V)**	**0,15V (0,25V)**
overall signal gain factor	120000 - 250000		

6 Electro-Optical Frequency Mapping

6.1 General EOFM signal observations

This section is supposed to give the reader a general understanding of EOFM signal behavior with the most common and important relations between electrical device performance and electro-optical signal. As the EOFM signal of individual MOSFETs has already been studied thoroughly (e.g. [101] and [103]) this section is more thought to be a preparation for new research results presented later in this thesis. Nonetheless all the presented data of this introduction is new and even expands EOFM analysis towards modern $16/14nm$ FinFETs by Qualcomm Technologies Incorporated. In order to complete this introduction, new application examples of IC failure analysis with EOFM will be given in the next subsection 6.1.1.

Before diving into physical details, a short summary of publication history with respect to various interesting fields related to electro-optical signals is given next. To get acquainted with the general topic of laser voltage probing, several short and precise introductions are available published by S. Kolachina from Texas Instruments [76] and by U. Kindereit from Qualcomm Inc. [78, 79]. The latter two are quite recent (from 2014 and 2016) and therefore are also focusing on the future of laser voltage probing with respect to shrinking device sizes/scaling. To further understand the differences between photon emission based techniques and electro-optical probing, several publications offer a detailed comparison of both techniques with focus on experimental applicability and advantages/disadvantages in certain cases [74, 92]. An excellent introduction into experimental electro-optical parameters (VBW, RBW, center frequency etc.) is given by Ng et. al. from DCG systems in [77]. Whereas electro-optical probing is usually carried out by detecting small changes in the reflected laser beam aimed at the device backside, it was also suggested in the past to use the phase [73] or polarization difference [75] between reflected beam and reference beam for better signal-to-noise ratio.

Since the emergence of standard commercial electro-optical probing systems from Hamamatsu Photonics KK, DCG systems, Checkpoint Technologies and others in the 2000s, several new features and expansions were added to the base functionality, of which some will be presented shortly in this text: Between 2011 and 2013 a new application called *Thermal Frequency Imaging* was invented by G. Celi et. al. [85, 86]. Thermal Frequency Imaging allows for the detection of resistive leakage parts exploiting the thermo-reflectance effect. Also the use of higher harmonics detection for EOFM/EOP was suggested by T. Parrassin et. al. at ISTFA 2013 [87] and K. Melendez et. al. at IRPS 2016 [96]. Further signal-to-noise ratio improvements via wavelet-transform were suggested by A. Boscaro in 2016 [97]. First steps towards application of electro-optical techniques on bipolar devices were published by M. Rebaï et. al. in [90] and on inertial MEMS by K. Melendez et. al. in [95]. Last but not least the recently emerged expansion of electro-optical probing towards the use of visible light laser sources shall be mentioned [83, 84]. Smaller laser wavelengths carry the advantage of higher optical resolution, but require extensive thinning of the device backside down to some μm or smaller and the use of solid immersion lenses made of materials with higher band-gaps to counter absorption.

An important point in the analysis of electro-optical signals is to take into account optical interference (fig. 104). The interference can be caused by many reasons including the variation of the

substrate thickness due to not perfectly even backside thinning/polishing or complex light reflection processes at the frontside of the device or within the substrate. This is the reason why a whole section (6.5) of this thesis is concerned to a huge extent with analysis of EOFM/interference-relations using simulations in TCAD. Areas of destructive interference have very low EOFM signals due to generally lower signal-to-noise ratio compared to areas of moderate or high constructive interference as can be seen in the figure. It is not only interference that might cause unexpected areas/stripes of higher electro-optical signals. Underlying metal lines (fig. 105) or metal fill can also enhance general signal-to-noise ratio due to higher frontside reflection caused by the metal. The latter can be discriminated from signal-to-noise ratio changes from interference by using incoherent light sources, which are not sensitive to optical interference.

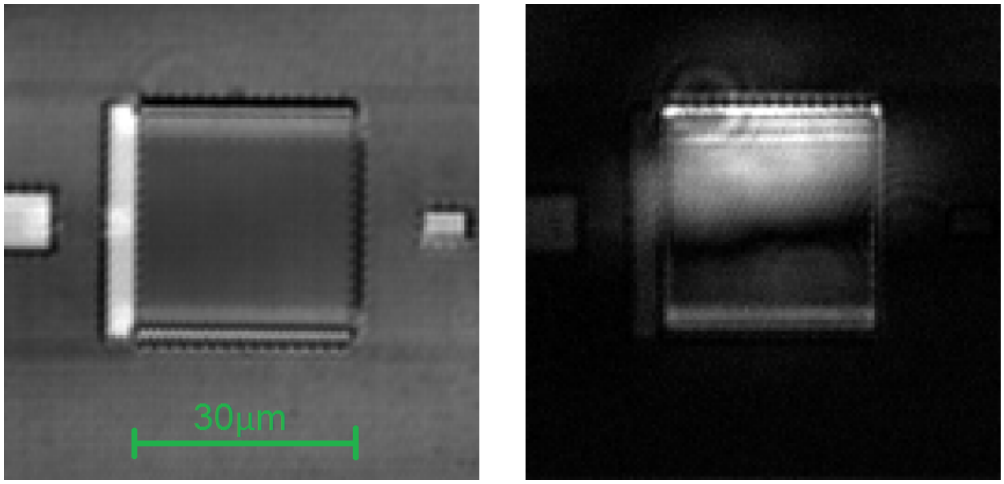

Figure 104: Pattern image of the large $30\mu m \times 30\mu m$-nFET transistor of Infineon Technologies AG (left). The light and dark stripes of the interference pattern are clearly visible in pattern image and EOFM signal (right) of the structure taken with HSL.

EOFM signals of MOSFETS and FinFETs (fig. 106) originate from modulations in the reflected light of a laser, which is incident on a device under test (section 3.7). The modulations are caused by the electro-optical interaction of laser beam and active device pulsed electrically at a certain frequency. Major signal causes for EOFM are changes in optical absorption/refraction by free carriers, space charge region changes as well as temperature. A theoretical and experimental description of the aforementioned effects along with a summary of additional minor effects, which can not be excluded completely, can be found in section 2.2.7 to section 2.2.11 of this work.

While in a MOSFET or FinFET space charge region modulations dominate voltage ranges usually lower than threshold voltage (electrical characteristics of the involved FinFETs can be seen in fig. 107 and 108), free carrier effects due to the emerging channel dominate for higher voltages than threshold voltage with a strong linear EOFM signal rise. Electro-optical signal levels are usually similar (fig. 109) for both n- and p-type MOS-/FinFETs of the same technology, contrary to PEM signals of most FETs, where especially for planar MOSFETs vast intensity differences of factors between 100 and 1000 for n- and p-type can be observed. As shown earlier in this thesis (section 5.1), this has changed partly in FinFETs due to implantation of special channel materials. But still the strong linear rise of EOFM signals above threshold voltage remains a big advantage over PEM for

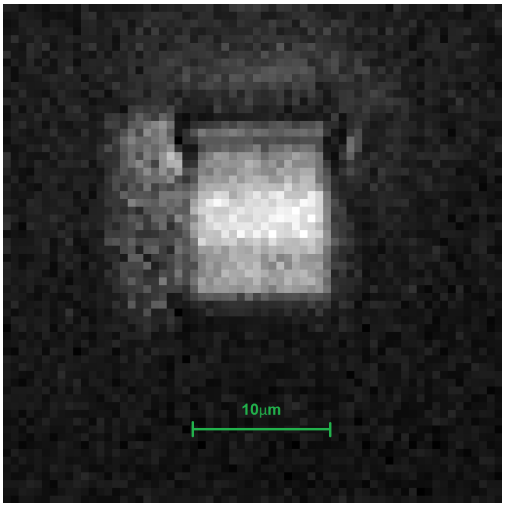

Figure 105: EOFM image of the smaller $10\mu m \times 10\mu m$-nFET transistor of Infineon Technologies AG. In the middle of the active gate area a bright stripe from left to right can be seen, which is caused by higher reflection of an underlying metal line. This increases the EOFM signal-to-noise ratio locally. The bright stripe is not due to a possible interference pattern as the EOFM image was taken with the incoherent SLD light source.

modern low voltage devices. On the other side electro-optical techniques are much more vulnerable to interference effects compared to PEM and can only be used from the backside of the device. Even for commercial state-of-the-art $16/14nm$-FinFETs clear EOFM signals can be observed down to $\approx 0,2V$ (fig. 109). The use of solid immersion lenses (SILs) with EOFM enhances signal levels by a factor of roughly 5-10 or even more similar to PEM (fig. 110).

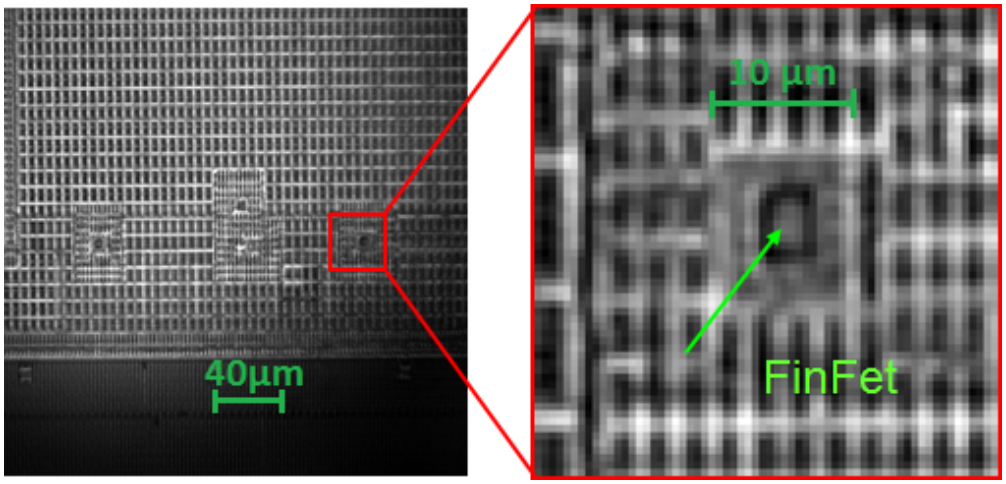

Figure 106: Pattern images of the Qualcomm FinFET test structure taken with HIL and 1x optical zoom.

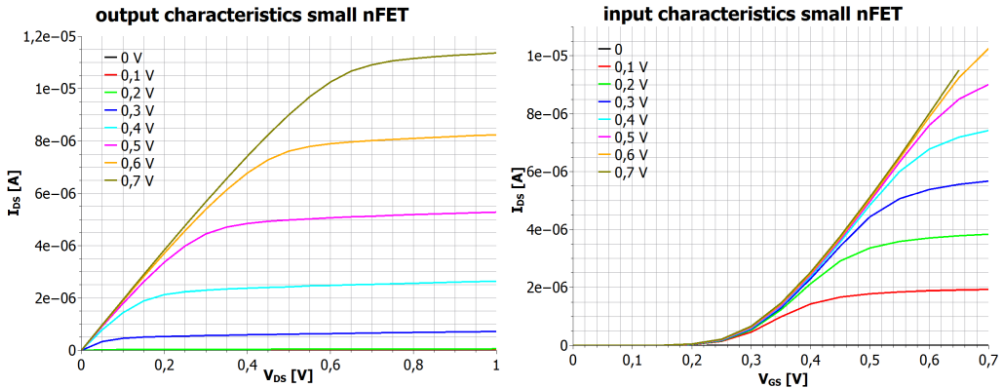

Figure 107: Output characteristics (left) of the small Qualcomm n-FinFET for various V_{GS} from $0V$ to $0,7V$. Input characteristics (right) of the small Qualcomm n-FinFET for various V_{DS} from $0V$ to $0,7V$.

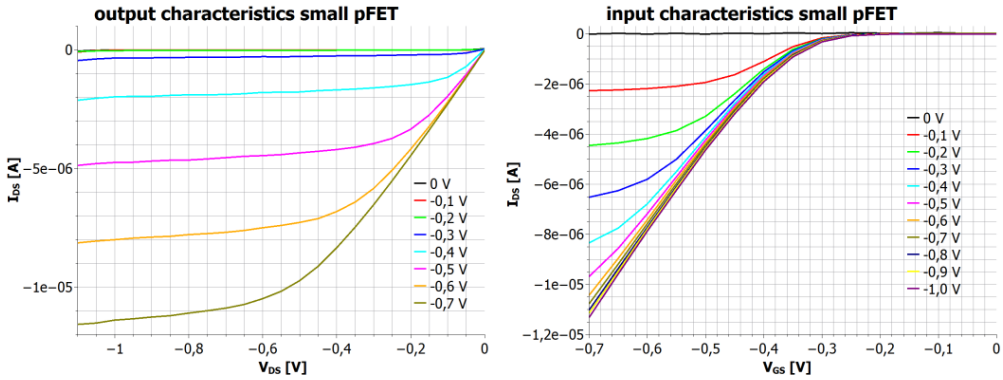

Figure 108: Output characteristics (left) of the small Qualcomm p-FinFET for various V_{GS} from $0V$ to $-0,7V$. Input characteristics (right) of the small Qualcomm p-FinFET for various V_{DS} from $0V$ to $-1V$.

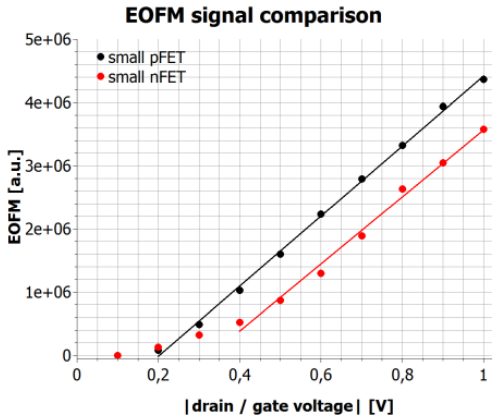

Figure 109: Integrated EOFM signal comparison for small n/p-FinFET taken with HIL light source at 100% light power. Above threshold voltage region ($\approx 0,3V$) a strong linear rise of the electro-optical signal is seen due to the linear increase of free charge carriers in the channel beneath the fin. Drain and gate pulsed simultaneously.

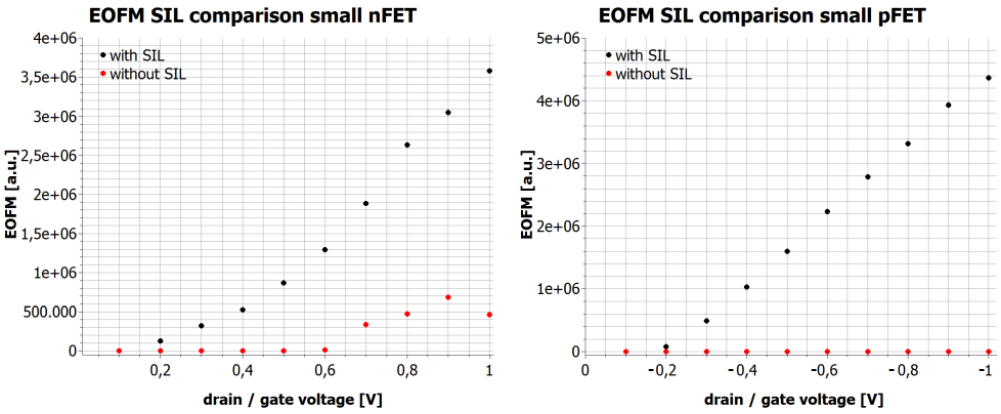

Figure 110: Comparison of EOFM signals with and without SIL for small n-FinFET (left) and small p-FinFET (right) taken with HIL light source at 100% power. Drain and gate pulsed simultaneously.

6.1.1 EOFM failure analysis examples

EOFM is used as a common technique for the failure analysis of integrated circuits and several case studies with respect to scan chain debug, passive structures and other are available [30, 81, 91, 93, 94]. Further new cases of FA using EOFM will be presented in the next paragraphs and images. In figure 111 a pattern and EOFM image of a big $30\mu m \times 30\mu m$-nFET test transistor of Infineon Technologies AG can be seen. The EOFM image doesn't show the expected equal signal distribution over gate width but a strong concentration at two spots in the upper right corner (gate close to drain) and at the right edge of the gate (in direction of polysilicon gate connection). The suspicion of locally damaged gate material was easily proven by electrical measurement of I_{GS} vs. V_{GS}, which gave an ohmic IV-curve with an ohmic resistance of some $k\Omega$. This is not surprising as the transistor had been pulsed at $2,4V$ ($V_{nom} = 1,2V$) more than 30 minutes for degradation investigations. The high EOFM signal at the two spots is suspected to be caused by high current densities through the leakages and their effect on light reflection changes caused by free carrier refraction/absorption change on the one hand and optical path variations induced to local temperature change on the other hand.

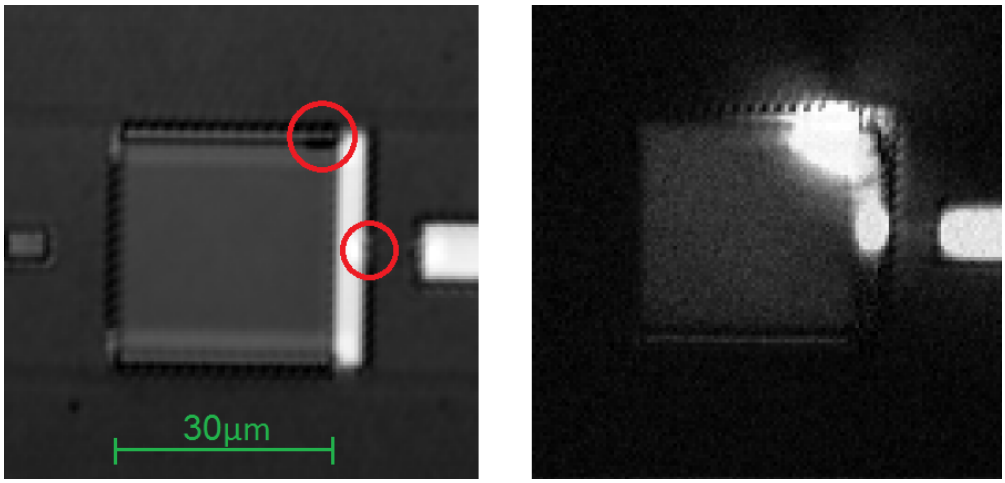

Figure 111: Pattern of a damaged $30\mu m \times 30\mu m$-nFET transistor of Infineon Technologies AG (left) and the respective EOFM image (right) with drain and gate pulsed simultaneously using SLD light source. The EOFM signal for a functional transistor should be distributed equally over the whole gate width, but here it is abnormally concentrated in two bright spots (upper right corner and right edge) indicating failure. At close look abnormalities on these locations can already be seen in the pattern image (red circles).

A more subtle failure detection case with EOFM is shown in figure 112. Due to the high dependance of electro-optical signal strength on interference patterns, a simple signal strength comparison of different devices at different locations bears risks for the verification of electrical failure. Of course, simple signal strength comparisons can be used for the identification of possible spots for further failure analysis. The figure shows the EOFM signal slope of a large n-FiNFET by Qualcomm Technologies Inc, which is technologically identical with the small n-FinFET presented earlier (fig. 109 and 107), except for a 12 times higher number of fins to increase the width of the FinFET. In general, a qualitatively identical EOFM-over-voltage slope would be expected here with the signal strength increased by a factor of ≈ 12. Both expectations don't hold true here: The linear rise of EOFM signal clearly starts below $0,2V$ for the large n-FinFET and above $0,3V$ for the small n-FinFET. Furthermore the signal strength is indeed *reduced* by a factor of > 20 for the large

n-FinFET in comparison to the small n-FinFET, which can not be ascribed only to the use of SLD instead of HIL light source (both at 100% light power). This corresponds well to previously carried out failure analysis on this structure with PEM (section 5.4.3). The reason for the large n-FinFETs erratic behavior is suspected to be a higher resistance in the connections for gate and drain, as the transistor hardly reaches saturation condition even for voltages higher than $V_{nom} = 0,7V$ (fig. 113).

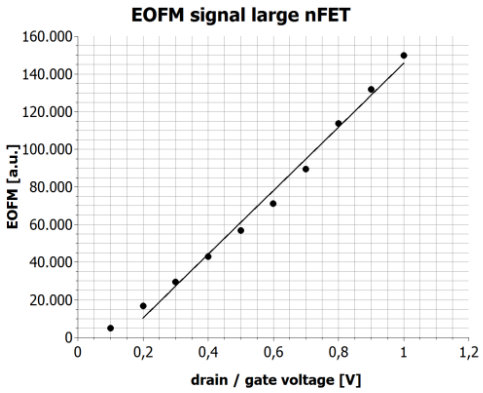

Figure 112: Integrated EOFM signal for the large n-FinFET taken with SLD light source at 100% light power. Again, a strong linear rise of the electro-optical signal can be seen, starting at a significantly lower voltage than for the small n-FinFET (fig. 109). This is a clear indicator for an electric failure as small and large n-FinFET are technically identical except for the number of fins. Drain and gate pulsed simultaneously.

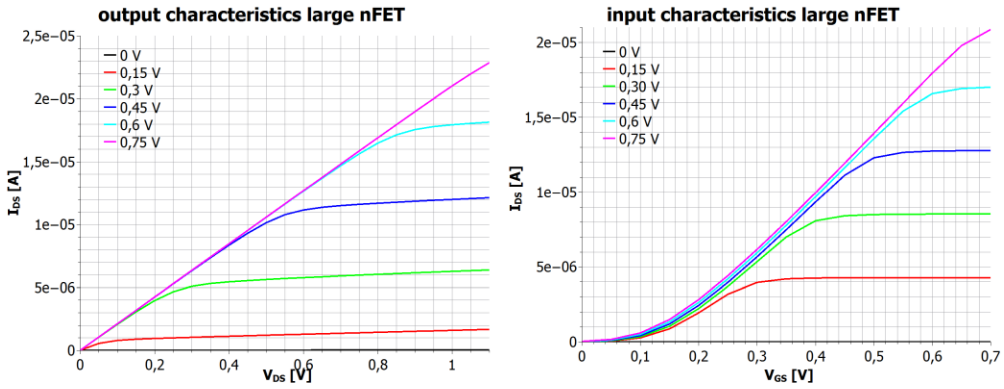

Figure 113: Output characteristics (left) of the large Qualcomm n-FinFET for various V_{GS} from $0V$ to $0,75V$. Input characteristics (right) of the large Qualcomm n-FinFET for various V_{DS} from $0V$ to $0,75V$.

6.2 EOFM temperature investigations

Device and bulk temperature is an important topic especially for device reliability. Charge carrier densities, scattering processes and light emission are directly influenced by global bulk temperature or local device temperature. Therefore a series of measurements was carried out to investigate the effect of temperature on electro-optical signals. For heating of the whole test chip a thermal chuck was installed, which could be heated in an interval between 20° and 150°. The temperature was measured with the help of a thermocouple connected to the chip backside. A custom-made heat transport channel with a copper core and heat shielding tape was manufactured for the socket board. Temperature analysis was not carried out above 80° to avoid the risk of damage to the optics / objective lenses located only millimeters above the device under test. Some contents as well as figures of this section were already published in the authors contribution to ISTFA 2017 [68].

EOFM images for two large test transistors pulsed with identical setup at different bulk temperatures can be seen in figure 114. Averaging the electro-optical signal across a line from source to drain of both transistors allowed for a comprehensive analysis of temperature effect on the signal (fig. 115). The analysis shows no strong effect of temperature on EOFM. Slight changes in intensity level $10-20\%$ are too small to be clear indicators of temperature effects, as the objective lens had to be refocused for each measurement due to chip expansion by heating, which could have had a slight effect on the signal intensity. Undoubtedly, bulk temperature has an effect on EOFM as it strongly effects especially the *minority* carrier densities, but those do not contribute enough to the major EOFM signal cause of a MOSFET (free carrier absorption mainly by free (*majority*) carriers in the channel). The other main signal cause, absorption/refraction change due to space charge region modulation, should be effected stronger by temperature. Obviously the rise in minority carriers within the SCR here is too low to cause a significant signal rise.

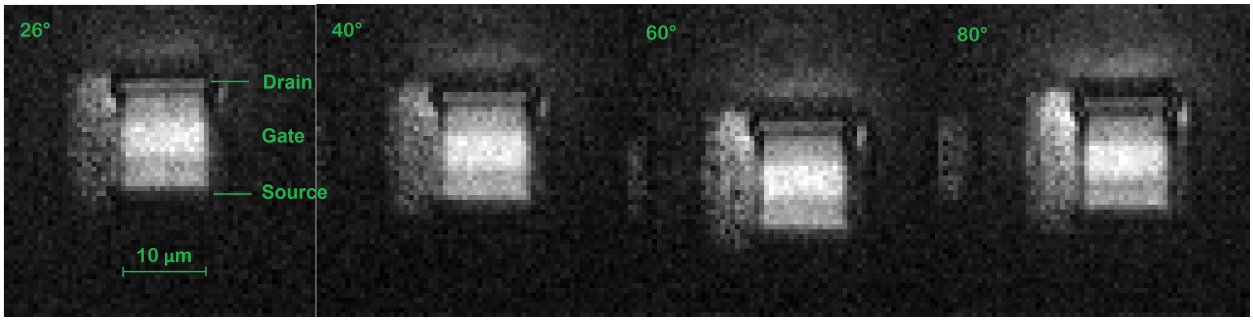

Figure 114: EOFM images of the $10\mu m \times 10\mu m$ nFET test transistor for chip temperatures 26°, 40°, 60° and 80°. The bright stripe in the middle of the gate area is caused by an underlying metal line (higher SNR because of higher reflection by metal). All images taken with SLD light source at 100% light power.

6.2.1 Device self-heating detection

A new application regarding detection of self-heating effects was found using EOFM. In comparison to the experiments involving bulk temperature above, this section is about local self-heating by the on-state of the device under test. Here the local temperature change is directly induced by the electrical pulse at the frequency used for EOFM. The frequency was chosen to be $1MHz$ to allow sufficient time for heating and dissipation of temperature [85]. The idea is to observe the EOFM

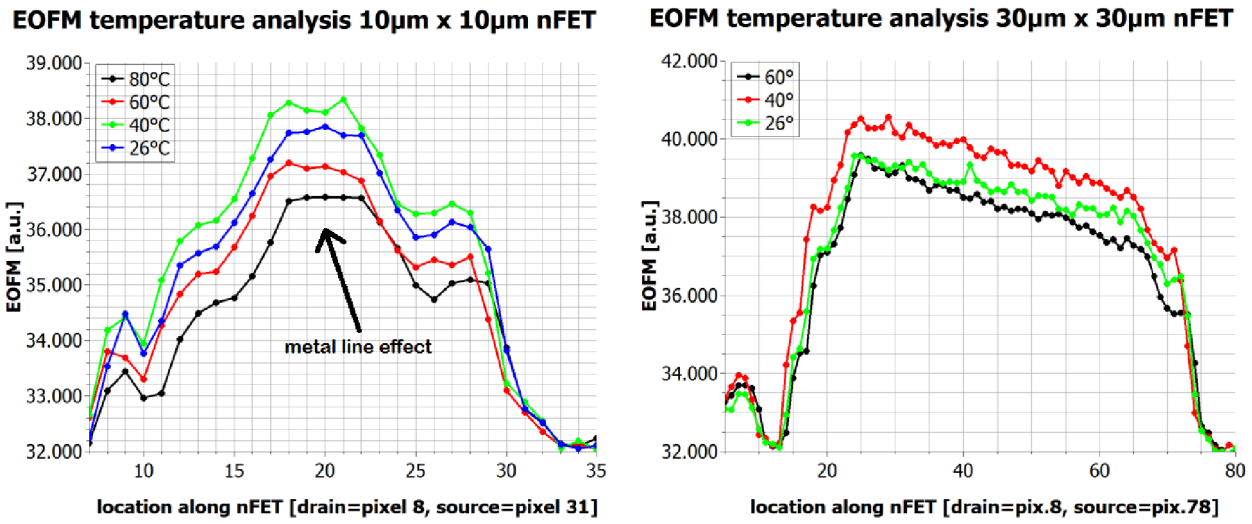

Figure 115: Averaged EOFM signal at different bulk temperatures from source to drain for a $10\mu m \times 10\mu m$ nFET test transistor (left) and a $30\mu m \times 30\mu m$ nFET test transistor (left). 32.000 is the standard signal offset generated by Phemos-1000. EOFM signals were acquired with SLD light source at 100% light power.

signal of a device under test for pulses with identical parameters except different values of the duty cycle (figure 116). Different values of the duty cycle correspond to different on-state / self-heating times of a device. By comparing the electro-optical signal slope for conjugate values (e.g. 20% and 80% or 35% and 65%) of the duty cycle self-heating can be detected. In case of strong self-heating the EOFM signal for the higher conjugate value (e.g.80%) is supposed to be higher than for the lower conjugate value (e.g. 20%). If the signal slope is symmetrical this is an indicator for low / not-detectable self-heating. An asymmetrical signal slope with higher values for the higher conjugate duty cycle values than for the lower duty cycle values is a clear indicator for detection of device self-heating (fig. 117). This method was tested on the small Qualcomm p-FinFET with a clear indication of self-heating (fig. 118).

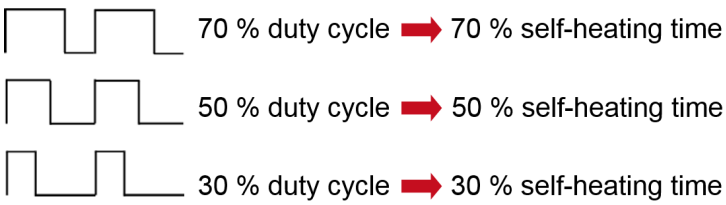

Figure 116: Pulses for different values of the duty cycle. The higher the duty cycle, the longer is the high level of the pulse within one pulse period and the more self-heating will occur in the device.

An interesting future research activity would be to compare results of the new technique with a previously existing self-heating detection method (Thermal Frequency Imaging - TFI) developed by G. Celi at Bordeaux university / CNES, France, in 2011 [85, 102]. Another promising perspective will be the quantitative analysis of EOFM self-heating effects similar to [25], [26] and [35] with PEM, where optical signals could be attributed to exact local device temperature changes.

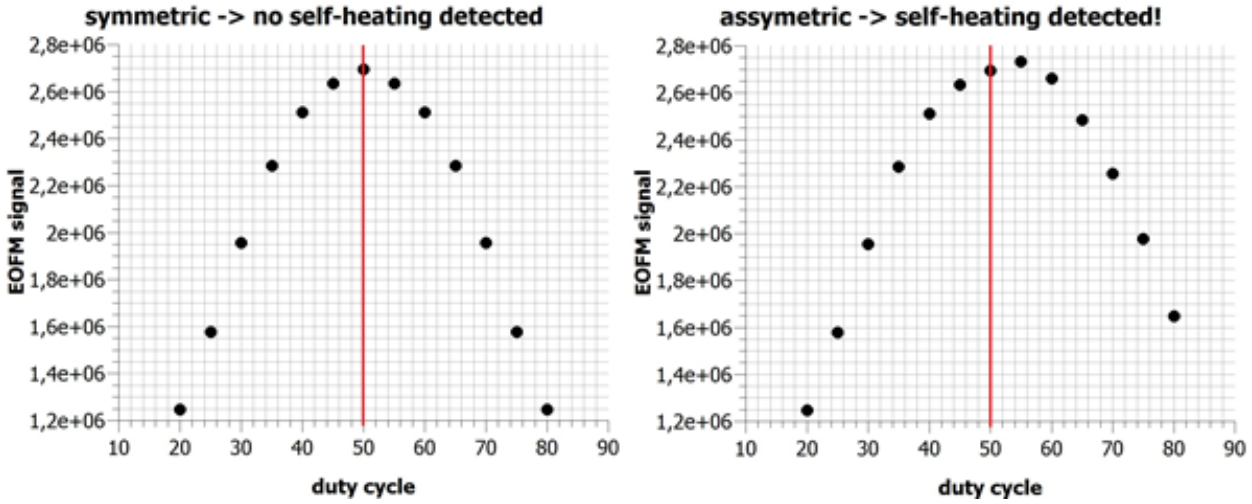

Figure 117: A symmetrical shape of the EOFM signal slope over voltage indicates no self-heating detection (left). An assymetrical shape of the EOFM signal slope over voltage with higher signals for duty cycles higher than 50% clearly indicates self-heating detection (right).

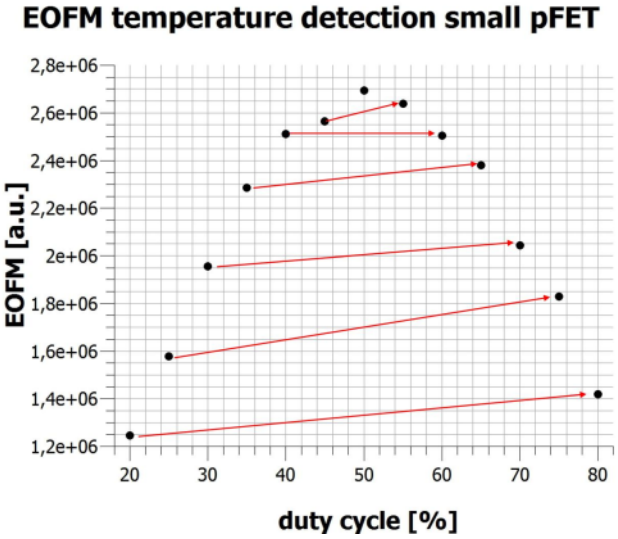

Figure 118: Affirmed self-heating detection with EOFM for the small 16/14nm Qualcomm p-FinFET using HIL light source at 100% light power.

6.3 EOFM on analog devices

This section deals with the application of electro-optical frequency mapping (EOFM) to different types of current mirrors as typical parts of analog and mixed-signal circuits. The investigations include two different simple current mirrors, two different cascode current mirrors and two different low-voltage current mirrors (fig. 119) in 250nm technology, nominal voltage of $V_{nom} = 2,5V$ and threshold voltages of $V_{th} =\approx 0,6V$. Further electrical data, pattern images, detailed explanation on the basic operating principles of current mirrors and photon emission analysis results on current mirrors can be found in section 5.6 of this thesis. Some contents as well as figures of this section were already published in the authors contribution to ESREF 2017 [67].

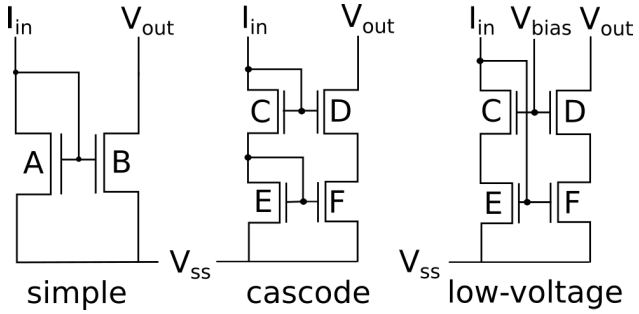

Figure 119: Schematic of the three different current mirror types. Capital letters A to F indicate different transistor geometries (see table 9) in section 5.6.

The EOFM analysis was carried out from the backside of the chip, which was packaged and mounted into an individually designed socket board. After backside thinning and polishing the silicon substrate had a remaining thickness of $\approx 100\mu m$. For EOFM investigation a square wave pulse with 50 % duty cycle and 1 MHz frequency was applied. The high level voltage took different values, which are mentioned in the respective figures. For the simple current mirror no.2 the strong linear signal rise of EOFM signals over V_{in} occurred slightly above 1V (fig. 120) with only low electro-optical signals below this value. In comparison to PEM also input-side transistors gave signals; not only the output-side transistors. The generally stronger EOFM values for output side transistors can be explained by the fact that the number of output nFETs was 4 times higher than for input-side nFETs and the signal was integrated for the whole area of all nFETs of input or output side, respectively. Pulsing V_{out} and leaving V_{in} constant, only the output side transistor signal rises, but the input side transistor signal remains almost constant (fig. 121). This makes sense because output voltage only effects the output and not the input side. The linear signal rise for the output-side transistors in this case starts already slightly above 0V. This can be explained as follows: As V_{in} takes a high constant value of 1,75V the output-side transistors area below the gate is already in strong inversion (i.e. channel has built up). Any slight increase of drain voltage above 0V will thus shift the whole inversion zone distribution towards source. When V_{in} is pulsed (as for the results mentioned first) the channel only builts up above threshold voltage so that the linear signal increase starts much later with respect to pulse high level voltage.

For the two cascode and low-voltage current mirrors the EOFM slopes over voltage looked quite similar (fig. 122). Again a strong signal rise can be seen, but this time starting around 1,5V -1,6V and not only slightly above 1V (as for the simple current mirror). This can be explained by the

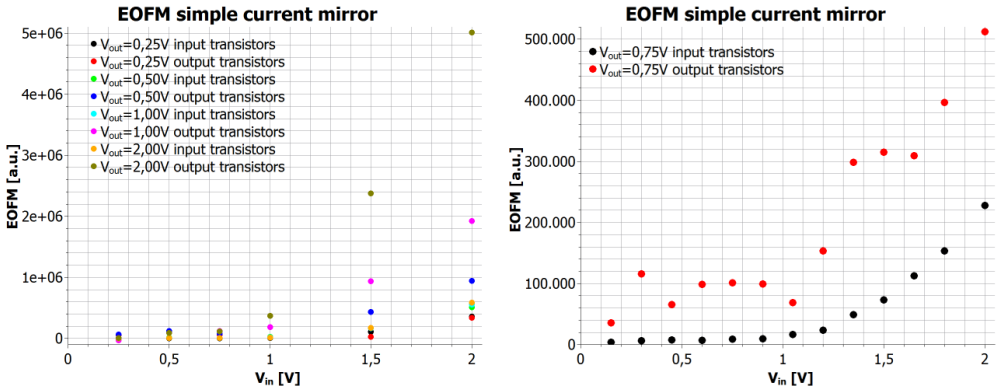

Figure 120: EOFM signal slopes over V_{in} for the simple current mirror no.2 at different output voltages V_{out}. All slopes are related to input-side and output-side transistors individually. All data acquired with HIL light source at 100 % light power.

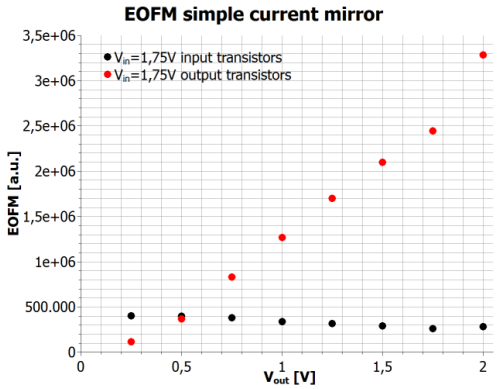

Figure 121: EOFM signal slopes over V_{out} for the simple current mirror no.2 at $V_{in} = 1,75V$. Slopes are related to input-side and output-side transistors individually. All data acquired with HIL light source at 100 % light power.

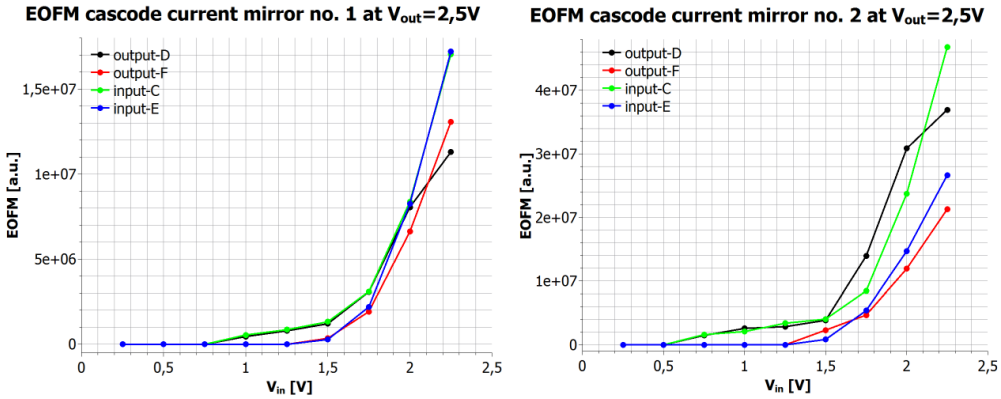

Figure 122: EOFM signal slopes over V_{in} for cascode current mirror no.1 (left) and no.2 (right) at different output voltages V_{out}. All slopes are related to different input-side and output-side transistors individually. All data acquired with HIL light source at 100 % light power.

more complex technical scheme (fig. 119) of the cascode and low-voltage current mirrors: The latter have two nFETs in series so that V_{in} and V_{out} are distributed along two drain-to-source distances. Therefore the built-up of channel and space charge regions at the individual transistors is delayed with respect to voltage similar to the analysis presented for PEM earlier. This does not effect EOFM as much as PEM, because of the weaker dependence of EOFM signals on drain-to-source voltage. EOFM seems to be the better choice for circuit elements with multiple transistors in series. Concerning the low-voltage current mirrors, EOFM curves were similar to the cascode mirrors as the additional bias voltage V_{bias} could only be adjusted within a small interval due to imperfect design.

Apart from the difficulties due to continuous voltages in analog circuits and more difficult distribution of voltages along several devices in a row, another major challenge is to feed a periodic signal, necessarily needed for EOFM/EOP, into a circuit with deep integration level without direct access to the active devices. This topic is momentarily of great importance and under discussion at several semiconductor manufacturers. In this work this topic shall not be treated further, but first reflections on this issue and a brief general analysis of electro-optical signals with respect to shrinking periodicity of the electrical signal were already published [77]. Help also comes from hardware security research: S. Tajik and H. Lohrke from TU Berlin used laser voltage probing to read out and decrypt encrypted bit streams in field programmable gate arrays (FPGAs) [107] with a tricky approach to introduce a periodic signal into the relevant part of the circuit.

6.4 EOFM on complex digital devices/NANDs

In this section a comprehensive analysis of EOFM and EOP signals from different sized NAND-like structures is given. Most contents and figures of this section were published in [99] and presented at IPFA 2017. NAND structures are frequently used elements of logical and mixed-signal circuits and are of special scientific interest due to the proximity of individual transistors within the NAND and their possible interference in terms of the optical signal. For a deeper signal understanding one big NAND-like structure and one small NAND-like structure were investigated with different pulse modes. A schematic of both structures can be seen in figure 123. Both structures are labeled N̈AND-*like*b̈ecause they are not identical with a full logic NAND (see section 2.1.6), but resemble its most relevant features. Both structures were self-designed by TU Berlin and produced in 250nm technology at IHP, Frankfurt/Oder, Germany, with a nominal voltage of 2.5V. The design of a complete NAND structure was not possible due to restricted pad number on the test chips. The test samples were bonded, thinned down to $\approx 100\mu$m and polished for backside optical analysis without SIL. The big NAND-like structure is used to understand the fundamental physical interactions in two consecutively ordered MOSFETs. The small NAND-like structure is used for optical analysis of the real and more complex situation in a commercial IC. Similar EOFM/EOP studies with respect to more complex digital structures and multiple active devices in one laser spot were carried out by W. Lua at AMD [98] and M. Rebaï at University Bordeaux [88].

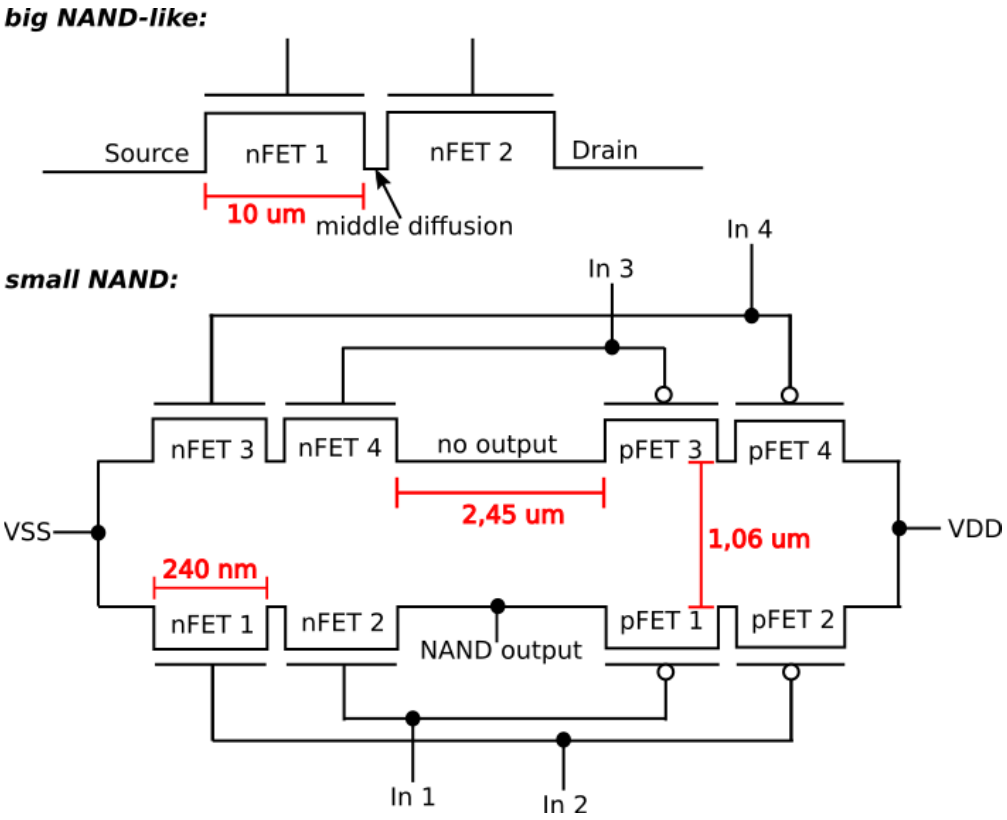

Figure 123: Schematic of both big and small NAND-like structure with relevant geometrical parameters.

6.4.1 big NAND-like structure

The big NAND-like structure is composed of two n-type MOSFETs with a gate area of $10\mu m \times 10\mu m$, with the source of the first nFET (left) internally connected to the drain of the second nFET (right) via a middle diffusion. A pattern of the structure can be found in figure 124a). For all pulsing experiments the source contact is always kept at ground level. The EOFM signal of the structure (fig. 124b) for a square wave pulse with 50% duty cycle and 2.5 V amplitude resembles the signal of a single transistor of double gate length, when drain (D), gate 1 (G1) and gate (G2) are all pulsed simultaneously. EOP analysis at different locations across the big NAND-like structure (fig. 125) roughly reproduces the shape of the electrical square wave pulse with minor deviations due to high-/low-pass characteristics and nonlinearity of the EOP Hardware. The strength of the EOP waveform at each location varies with the strength of the EOFM signal at the same location.

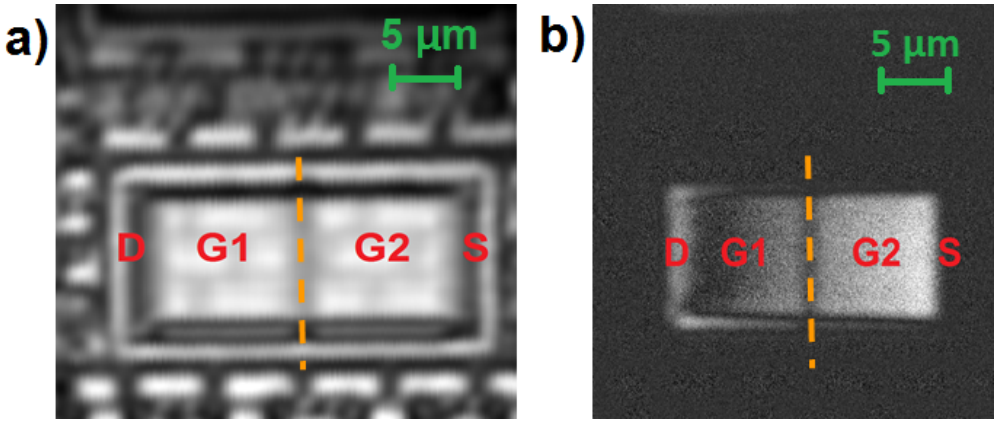

Figure 124: a) Pattern of the big NAND-like structure with drain (D), gate area of nFET 1 (G1), gate area of nFET 2 (G2) and source (S). In the middle between both gate areas a diffusion connects drain of nFET2 with source of nFET1. b) EOFM signal of the big NAND-like structure. Drain (D), gate 1 (G1) and gate 2 (G2) are pulsed simultaneously with a 2.5 V square wave pulse. EOFM image acquired with HIL light source at 100% light power.

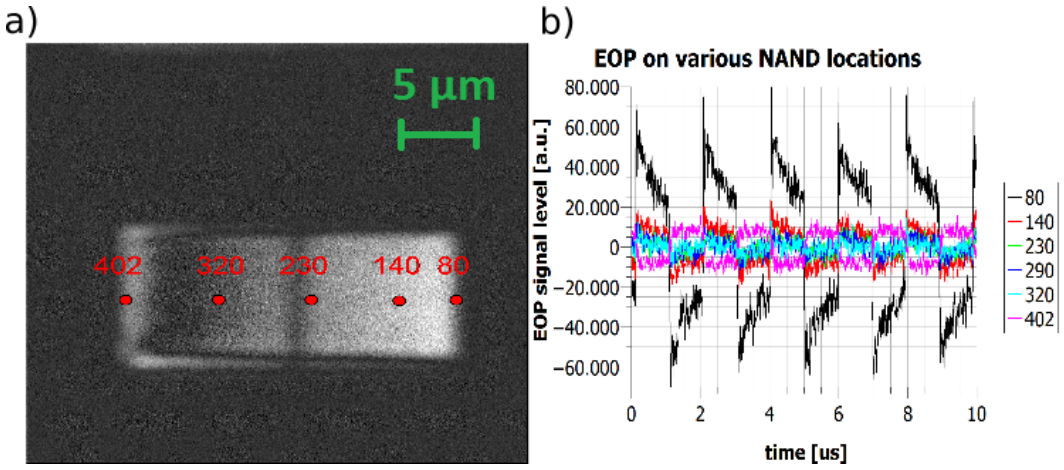

Figure 125: a) Pattern of the big NAND-like structure with locations for optical probing (EOP). b) EOP signals at different locations of the big NAND structure with drain, gate 1 and gate 2 pulsed simultaneously.

A detailed analysis of different pulse modes (figures 126 and 127) reveals information about the physical behaviour of the structure: In figure 126 the normal FET-mode pulsing of the structure (i.e. pulsing D, G1 and G2 simultaneously; green curve) indicates an EOFM signal by free carrier absorption in the channel, which is linearly decreasing from source (pixel 46) to pinch-off (pixel 18). From pinch-off towards drain the reflectance change caused by space charge modulation around drain becomes the dominant factor leading to a rise of the EOFM signal towards drain (pixel 4). Leaving both drain and source contact at ground level and pulsing only the two gates (blue curve) gives a constant optical signal at both gate areas separated by the middle diffusion. This constant signal level is mainly caused by the layer of free charge carriers directly below the gates. The small EOFM oscillations at both gate areas are due to minor interference.

In figure 127 only one of the two gates is pulsed along with drain, while the other gate contact remains at ground level with the source contact. At first view it becomes apparent that both signals are not symmetrical; thus it is important if the gate closer (gate 1) or farer away (gate 2) from drain is pulsed. When pulsing drain and gate 2 (black curve), the EOFM signal looks similar to the blue curve of figure 126 at the area of gate 2. Thus the situation here resembles the individual pulsing of gate 2. At the area of gate 1 and across the middle diffusion a signal rise towards gate 2 is noticeable, which indicates that charge carriers are drawn from drain and gate 1 areas towards gate 2, where they build up the inversion zone below the gate. At drain (pixel 4) only a small EOFM signal can be detected compared to the curves, where gate 1 is pulsed too (red and green curves). Obviously the strength of optical modulation caused by the space charge region modulation at drain is highly dependent on the fact, if the proximate gate is active or not.

A pulse at drain and gate 1 (red curve) with gate 2 and source at ground level has a different effect: The average signal level is significantly lower. Gate 1 area has a higher signal than gate 2 area, but much lower in value compared to gate 2 in the case above. Again charge carriers are drawn from gate 2 area towards gate 1 and drain across the middle diffusion. The EOFM signal at gate 1 area is higher the closer the location gets to the pulsed drain area.

It is important to mention that the 4 aforementioned EOFM pulse modes cannot only be discriminated by difference in signal slope in cases where the distance from source to drain is resolvable. Even in cases were structures are much smaller and the distance from source to drain cannot be resolved optically, discrimination of the 4 different states can be achieved by overall signal intensity: Quantitative analysis of the 4 different pulse modes by calculating the EOFM signal sum from source to drain shows that the overall EOFM signal intensity strongly varies between the pulse modes (see table 11).

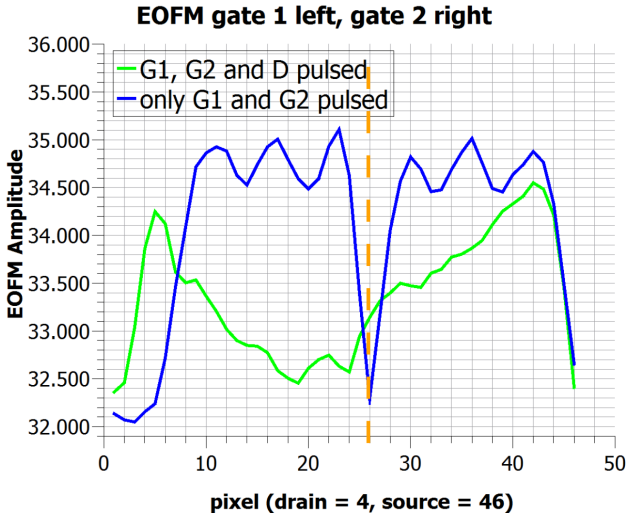

Figure 126: EOFM signals of the big NAND-like structure with different pulse combinations: Drain, gate 1 and gate 2 pulsed simultaneously (green) and gate 1 and gate 2 pulsed simultaneously (blue). Both pulses are square wave signals with 50% duty cycle and 2.5V amplitude. Data acquired with HIL light source at 100% light power.

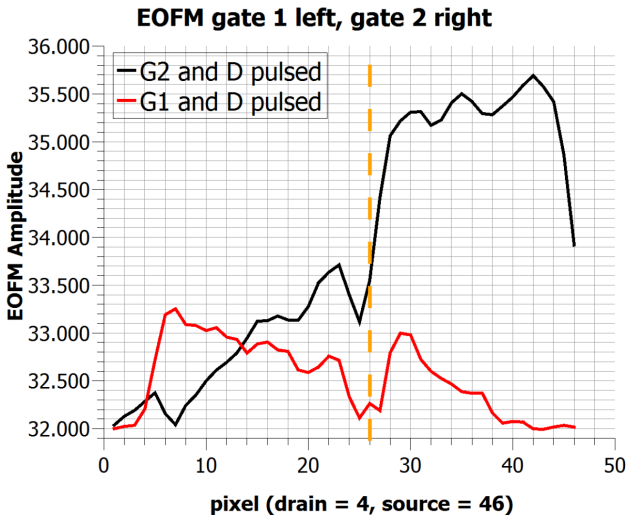

Figure 127: EOFM signals of the big NAND-like structure with different pulse combinations: Drain and gate 1 pulsed simultaneously (red) and drain and gate 1 pulsed simultaneously (black). Both pulses are square wave signals with 50% duty cycle and 2.5V amplitude. Data acquired with HIL light source at 100% light power.

Table 11: Integrated EOFM signal for different pulse modes of big NAND-like

Pulse mode	Integrated EOFM signal sum
drain + gate 1 + gate 2	62596
gate 1 + gate 2	98953
drain + gate 1	24647
drain + gate 2	85800

Another interesting investigation is the variation of the electrical pulse phase of gate 2 with a two-channel waveform generator. Drain, G1 and G2 are all pulsed in this setup with G2 getting the electrical signal with a phase shift from 0° to 360°. The EOFM signal can be categorized in two types: For phase shifts $< 90°$ (fig. 128) the EOFM signal still resembles the normal FET pulsing condition of 0°. This makes sense as the phase shift is still low enough to guarantee that most of the time the contacts (drain, G1 and G2) are all together on high level or low level respectively thus resembling the normal FET pulsing situation.

For phase shifts $> 90°$ (fig. 129) the EOFM signal corresponds to the course of pulsing only the gates individually (blue curve in fig. 126), but with a constant signal level at gate 2 area, which roughly has double the value than the constant EOFM signal at gate 1 area. The latter can be explained by the proximity of gate 1 to drain, which drains charge carriers from below gate 1 and acts out an interference on the optical signal here. The fact that the overall course of the optical signal resembles individual gate pulsing here can be explained by the fact that for phase shifts significantly higher than 90° the time where only one of the gates is on high level and the other on low level (ground) becomes dominant, which disables normal transistor-like functionality of the big NAND-like structure.

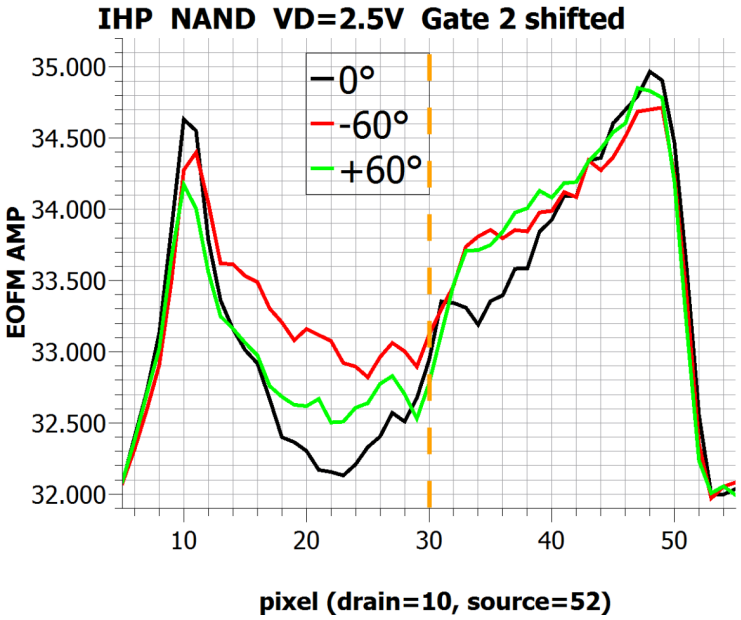

Figure 128: EOFM signals of the big NAND-like structure with different phase shifts. Drain, gate 1 and gate 2 are all pulsed at $2.5V$, but the pulse at gate 2 is shifted by a specific phase ($0°, 60°, -60°$). Data acquired with HIL light source at 100% light power.

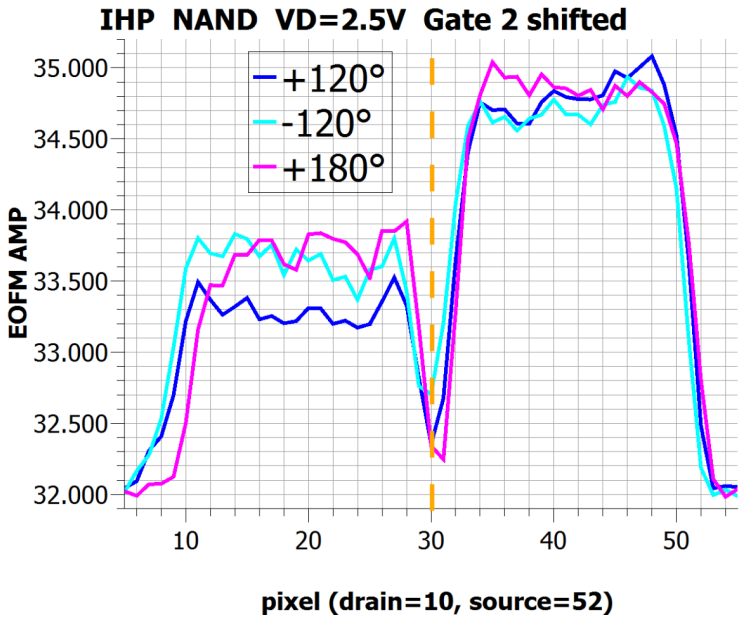

Figure 129: EOFM signals of the big NAND-like structure with different phase shifts. Drain, gate 1 and gate 2 are all pulsed at $2.5V$, but the pulse at gate 2 is shifted by a specific phase ($120°, -120°, 180°$). Data acquired with HIL light source at 100% light power.

6.4.2 small NAND-like structure

The two small NAND-like structures are each composed of two n-type and two p-type MOSFETs with a nominal gate length of $240nm$. A schematic of the structures can be seen in fig. 123. The upper structure was designed only for backup, while the lower structure with the additional *NAND output* contact was used for all experiments. The main goal of EOFM analysis on these structures was to evaluate if and how far EOFM analysis on a small structure with several different active transistors in one laser spot is possible (see layout fig. 130). The Hamamatsu HIL light source was used throughout all measurements presented here.

For all pulsing experiments the VSS contact was kept at $0V$, while the VDD contact was held at $2.5V$ constantly. The *NAND output* contact was only connected for research on the electrical behavior of the whole structure (see fig. 131) and left unconnected for all EOFM experiments. For most of those experiments the In1 and In2 contacts were pulsed simultaneously with a square wave with low level at $0V$ and high level at $2.5V$. For one experiment different pulse modes for In1 and In2 were tried. As the structure was only accessible by the use of an individually designed printed circuit board (PCB), it was important to take into account the output side capacitance of the PCB internal wire connection of the *NAND output* contact, because this capacitance was loaded/unloaded with each EOFM pulse cycle via the two nFETs or the two pFETs, respectively (fig. 123). Fig. 131 shows that the loading curve of the output contact related to the two pFETs and the unloading curve related to the two nFETs were visible from roughly 10 kHz upwards. Comparing the rise and fall times of the output slopes, the nFET-related fall and the pFET-related rise times differentiated by a factor of ≈ 3. This can be explained by the fact, that both p-type and n-type FETs were designed in the same geometrical dimensions thus leading to a ≈ 3 times smaller

on-current through the p-FET-side of the small NAND-like structure. Electro-magnetic induction could be neglected. As a result of the electrical capacitance analysis an EOFM pulse frequency of $100kHz$ as low as permitted by the Phemos EOFM hardware was chosen.

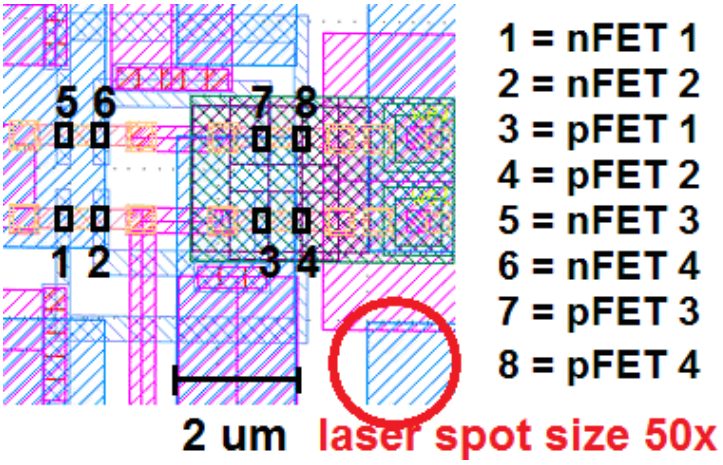

Figure 130: Layout of both (upper and lower) small NAND-like structure with relevant geometrical dimensions.

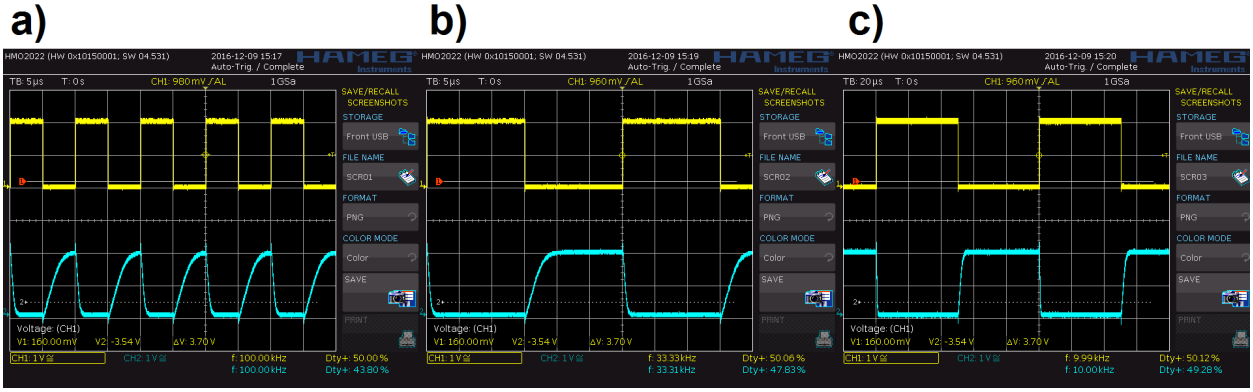

Figure 131: This figure shows the electrical behaviour of the *NAND output* contact (blue curve) investigated with a special high-ohmic probe head when pulsing In1 and In2 contacts simultaneously (yellow curve) with 2.5V square wave pulses at 100 kHz (a), 33.33 kHz (b) and 10 kHz (c).

EOFM analysis in the active region showed strong signals mainly at 4 spots (fig. 132), corresponding to regions close to the nFETs (spot 1), pFETs (spot 3), the n-well to Si substrate transition (spot 2) and the polysilicon / metal line In2-connection of nFET 1 and pFET 2 (spot 4). Spot 3 at pFET area was by far the strongest corresponding to previous observations [103] with stronger LVI signals for pFETs than for nFETs. Generally, the pure transistor signals were surpassed by optical effects in other regions close to the respective transistors. Pulsing only one input of the small NAND-like structure and leaving the other at constant voltage to simulate individual dysfunctional transistor gates within a NAND (fig. 133), a clear change in signal strength and distribution was visible (fig. 134). It was therefore possible to discriminate between different pulse conditions and identify the non-switching part of the NAND structure (e.g. compare the presence / absence of spot 4 in

the three images of fig. 134). Pulsing In1 and In2 connections simultaneously, but delaying the In2-connection by a certain phase shift, has significant influence on the EOFM signal, too (fig.135).

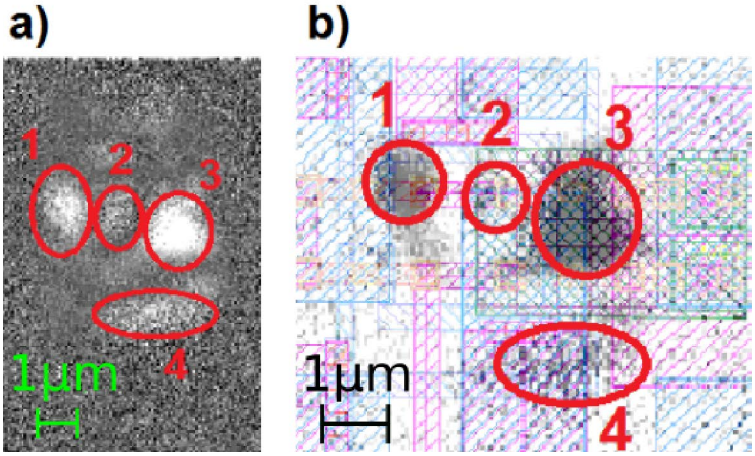

Figure 132: (a) shows the pure EOFM signal of the lower small NAND-like structure with In1 and In2 connections pulsed simultaneously. (b) shows an overlay of EOFM signal and layout. EOFM Data acquired with HIL light source at 100% light power and 50x lens with 8x optical zoom without Nanolens.

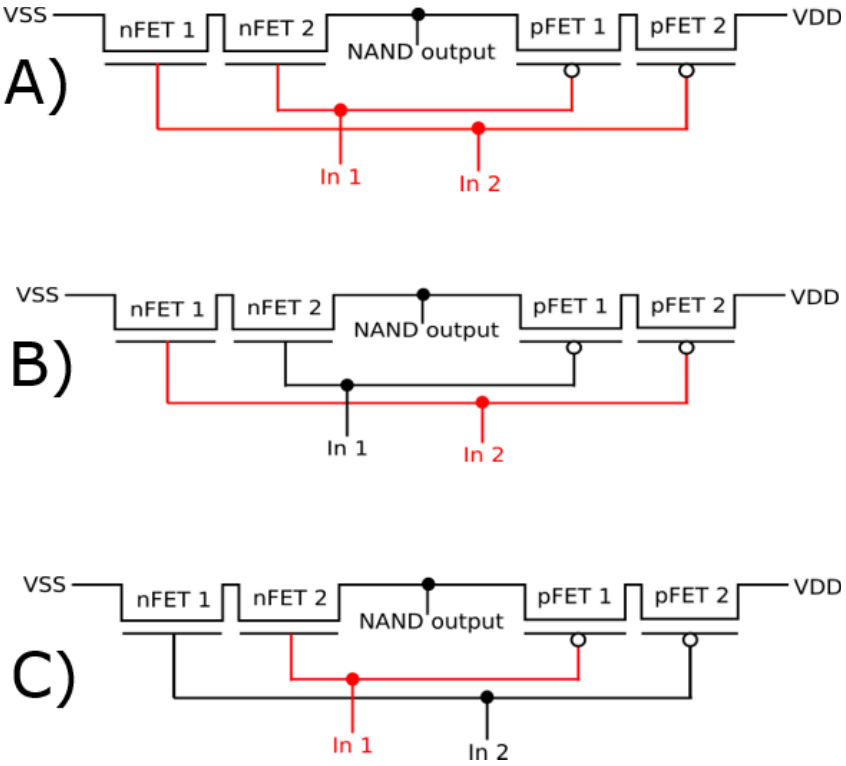

Figure 133: Different pulse combinations of the In1 and In2 connection of the small NAND-like structure. Parts of the structure, which were actively pulsed, are marked in red for each case A) to C).

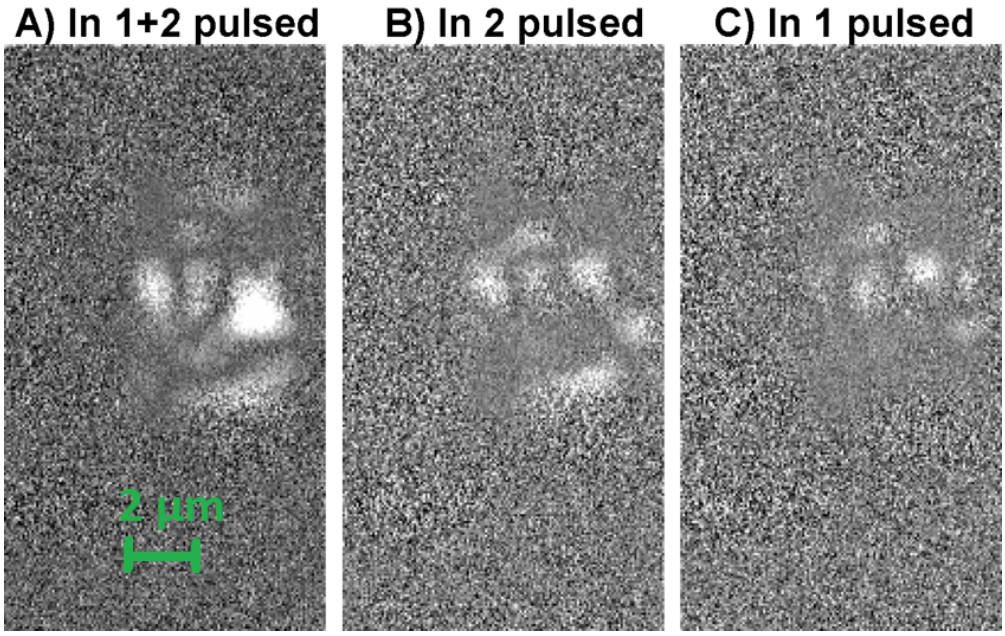

Figure 134: The image shows the EOFM signal for different pulse combinations of the In1 and In2 connection of the small NAND-like structure. The letters A) to C) correspond to the denotation of the three different pulse modes in fig. 133. EOFM Data acquired with HIL light source at 100% light power and 50x lens with 8x optical zoom without Nanolens.

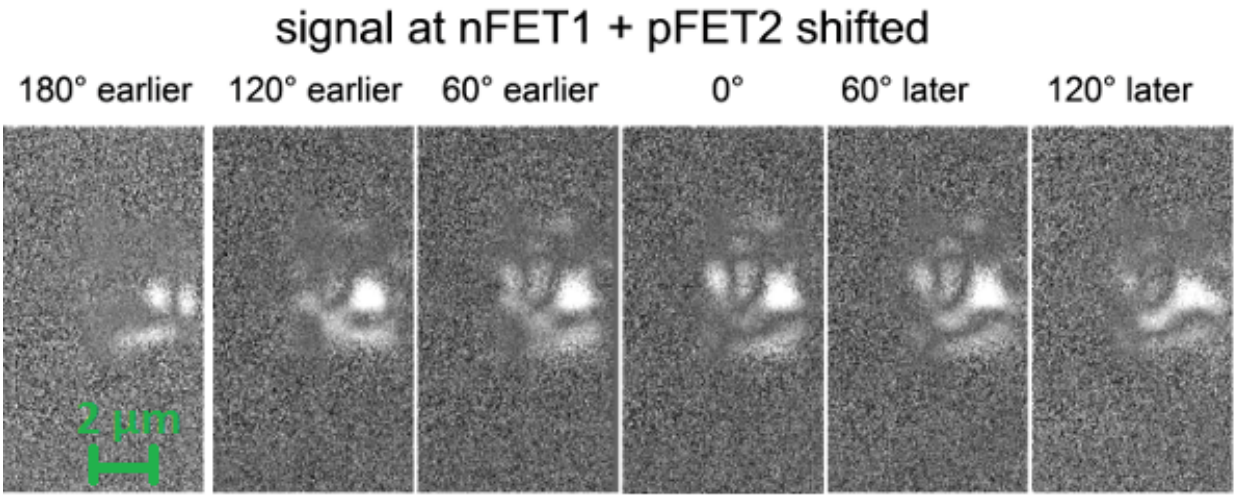

Figure 135: This figure shows the EOFM signal of the lower small NAND-like structure with both In1 and In2 connections pulsed, but with a phase shift for In2 = nFET1 + pFET2. EOFM Data acquired with HIL light source at 100% light power and 50x lens with 8x optical zoom without Nanolens.

To obtain further knowledge about signal composition at spot 1, 2 and 3 optical probing analysis (EOP) was performed on different locations within each spot (fig. 136 to 138). This investigation revealed the presence of output related signals (180° phase shift, spot 2) and input related signals (0° phase shift, spot 1 and 3) with different shapes and additional short-time spikes at some regions of the respective spots. Such spikes can occasionally be seen on EOP waveforms and can be caused by several reasons: The terminal resistance for the inputs was located not exactly at the device but some 10*cm* outside (due to PCB dimensions), which might cause short-termed higher voltage spikes at the device in switching moments. Furthermore short-circuit effects may occur within the NAND structure (pulsed as inverter in this case) and thus in the optical signal at the moment of switching, when voltages at all inputs are loaded/unloaded at switching moment. Also high-pass behaviour of the EOP hardware must be taken into account.

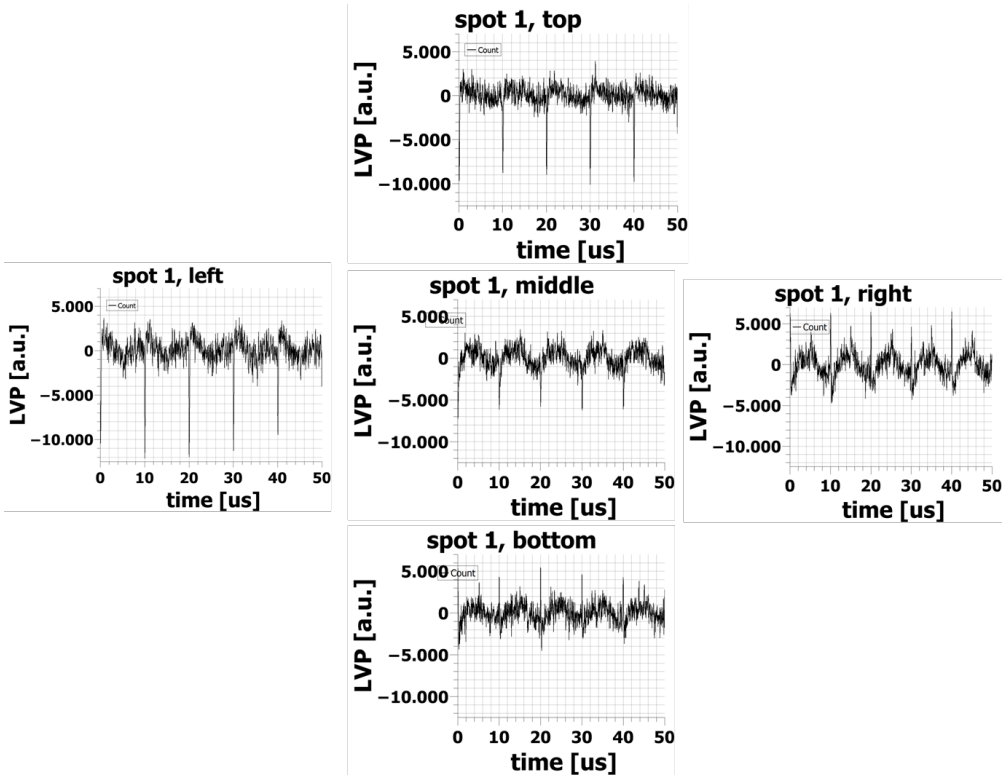

Figure 136: EOP signal for different regions within spot 1. Data acquired with HIL light source at 100% light power and 50x lens with 8x optical zoom without Nanolens.

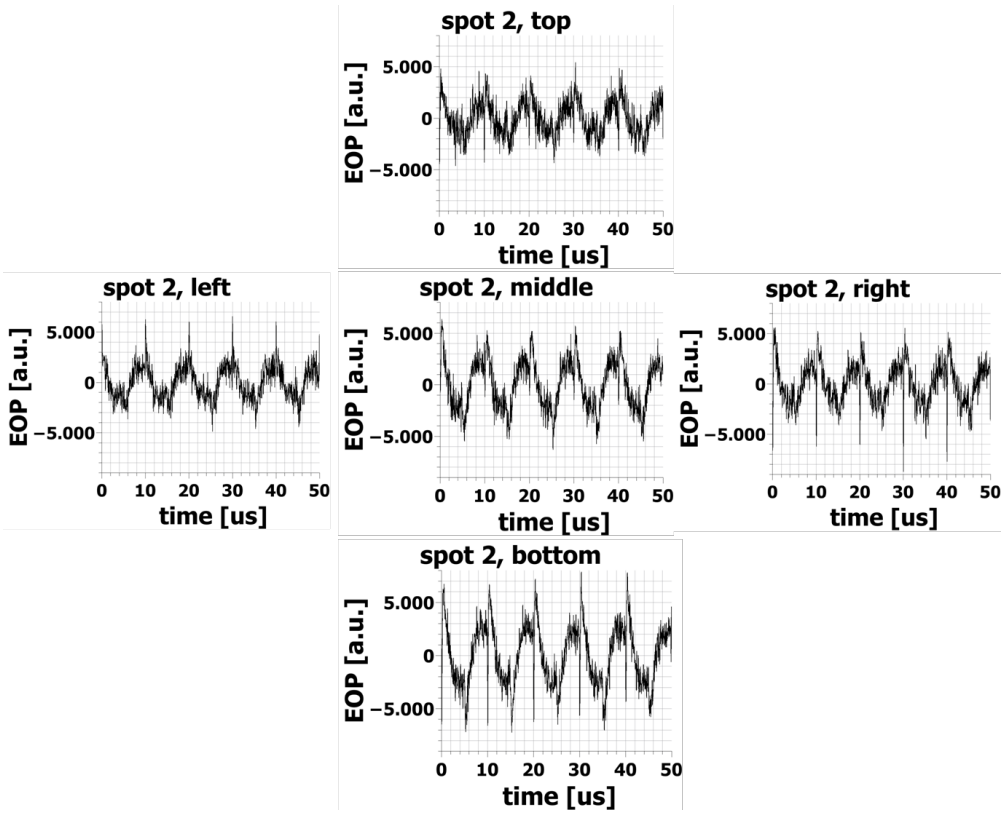

Figure 137: EOP signal for different regions within spot 2. Data acquired with HIL light source at 100% light power and 50x lens with 8x optical zoom without Nanolens.

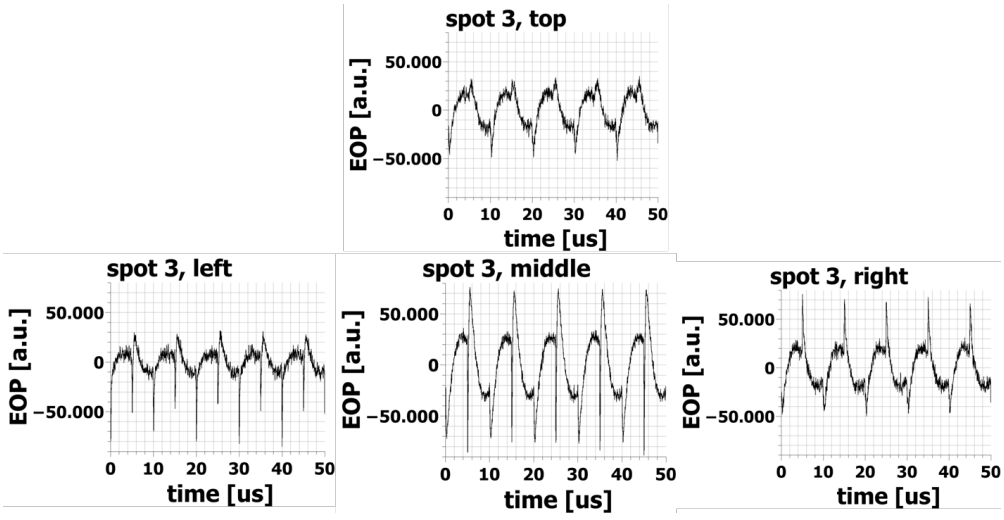

Figure 138: EOP signal for different regions within spot 3. Data acquired with HIL light source at 100% light power and 50x lens with 8x optical zoom without Nanolens.

6.5 EOFM on a diode

To extend the knowledge about the exact physical causes of electro-optical signals (EOFM + EOP), simulations and corresponding measurements were carried out on a pn-junction/diode. Some contents as well as figures of this section will also be published in the authors contribution to IPFA 2018 [80]. As space charge region modulation effects form one of two major causes for regular (e.g. section 6.4.1) and parasitic (e.g. section 6.4.2) electro-optical signals, a pn-junction is perfect for studying the effect of various physical parameters such as doping level, spectral laser profile, wavelength and temperature on electro-optical signals. In comparison to previous EOFM simulations the focus here is clearly on the influence of physical device parameters and especially interference. Whereas U. Kindereit in [101] as well as C. Pagano in [64] and [103] used a simplified transfer matrix formalism with only few material layers to roughly model a diode or MOSFET, this work uses the extensive transfer matrix model toolset of the TCAD Sentaurus program. Here, a threshold value with respect to the complex refractive index can be defined for the formation of a new layer, which is necessary to include complicated multi-layer interference and spectral laser profile effects, which is necessary for incoherent light sources. The average number of layers in each simulation was higher than 1000. Other previous EOFM simulations by M. Rebaï at Bordeaux university / CNES ([88], [89] and [104]) were focused less on physical behavior, but strongly on analysis of EOP/EOFM signals from logic devices such as inverter, inverter chain, XOR chain or bipolar devices.

The diode structure was manufactured by IHP, Frankfurt/Oder, Germany, in 250nm technology. For accurate physical, electrical and optical simulation of the structure the TCAD Sentaurus Software was used. To ensure best fit of simulational and experimental results the simulations were carried out with similar geometrical (substrate thickness, laser beam size etc.) and process parameters (doping levels etc.) compared to the diode structure used for the experiments. Detailed information about the parameters can be found below and in the TCAD script in appendix B. The author wishes to thank Rainer Leihkauf from TU Berlin for his help with setting up the simulations in TCAD, as well as for sharing many ideas and expertise during the whole simulation project.

6.5.1 EOFM simulations using TCAD Sentaurus

6.5.1.1 Information on the structure and doping of the designed and simulated pn-junction: The substrate has a thickness (Y-axis) of $100\mu m$ and a width (X-axis) of $500\mu m$ and a boron doping level of $5 * 10^{14} cm^{-3}$. The n-contact is in the upper left corner at $X = 0$ and $Y = 0$ and the p-contact is at the backside at $X = 0$ and $Y = 100\mu m$. The front side of the junction has a phosphorus doping level of $1 * 10^{20} cm^{-3}$ at $Y = 0$, decreasing with a Gaussian profile towards higher Y with a front doping depth of $0,15\mu m$ (see fig 139). Further details on the exact doping and geometrical profiles as well as all simulation parameters can be found in the simulation scripts in appendix B. For certain investigations different parameters (device temperature, front doping level and substrate doping level) were changed to different values as indicated later.

6.5.1.2 Different light sources For data evaluation two different light sources with different spectral profiles were used similar to the common Hamamatsu Phemos-1000 light sources:

1. HSL with a wavelength of $1319nm$ and $1kHz$ ($\approx 0,563 \cdot 10^{-9} nm$) bandwidth (FWHM) and

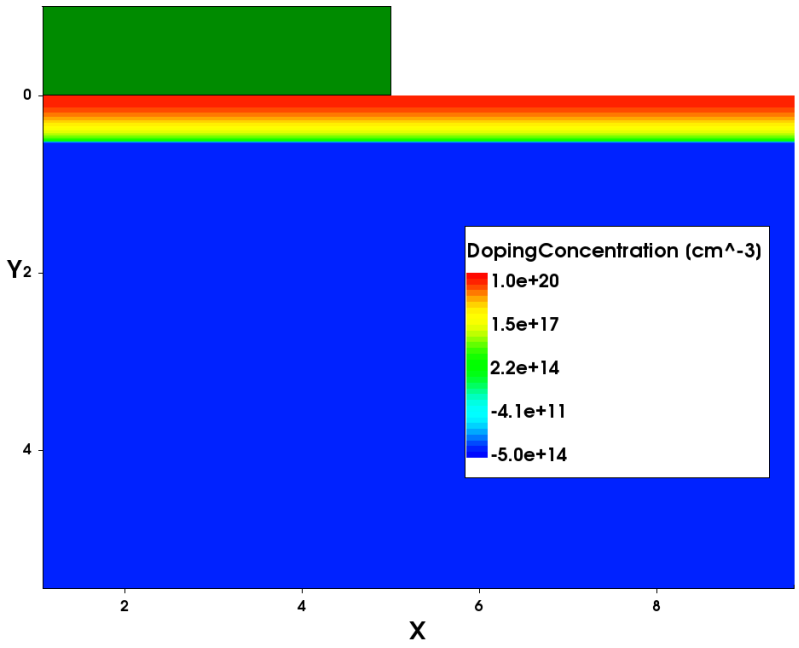

Figure 139: Doping and geometrical profile of the diode structure used for simulation with TCAD Sentaurus. The front contact (dark green) is located in the upper left corner, while the back contact (not included in figure) extends over the whole backside at $Y = 100\mu m$ from $X = 0\mu m$ to $X = 500\mu m$.

2. HIL with a wavelength of $1330nm$ and $20nm$ bandwidth (FWHM)

with FWHM referring to the Full Width Half Maximum of the Gaussian profile. Bandwidth in nm ($\Delta\lambda$) and kHz (Δf) can be transformed into each other using the mathematical relation

$$\Delta f = \frac{c \cdot \Delta\lambda}{\lambda^2} \tag{6.1}$$

with c being the light velocity in vacuum. Light power in the simulations was adjusted to match Phemos light sources with values of $45 - 71mW$ in the spot on the device with a spot diameter of $2\mu m$ for the standard 50x lens objective used for EOFM/EOP analysis.

6.5.1.3 Calculation of the reflectance/EOFM signal A full electrical simulation was carried out with the help of TCAD Sentaurus for each parameter and/or voltage combination on a simulation grid with an accuracy ensuring sufficiently smooth parameter curves. The electrical data and the grid were then used to divide the laser path from outside the structure through the backside and substrate to the front side into a layer stack using the internal Transfer Matrix Model (TMM) kit offered by Sentaurus. The single layers size was determined according to a threshold value of not more than $2,43 \cdot 10^{-7}$ change of the total reflectance within the layer. Areas outside the structure were considered with the standard physical parameters of air. The simulation algorithm repeated this calculation for wavelengths within the laser profiles spectral interval (see fig. 140) in predefined wavelength intervals of roughly $0.1 - 1nm$. The predefined wavelength interval was chosen in order to obtain a smoove reflectance curve. To obtain the final EOFM-value (=total reflectance change

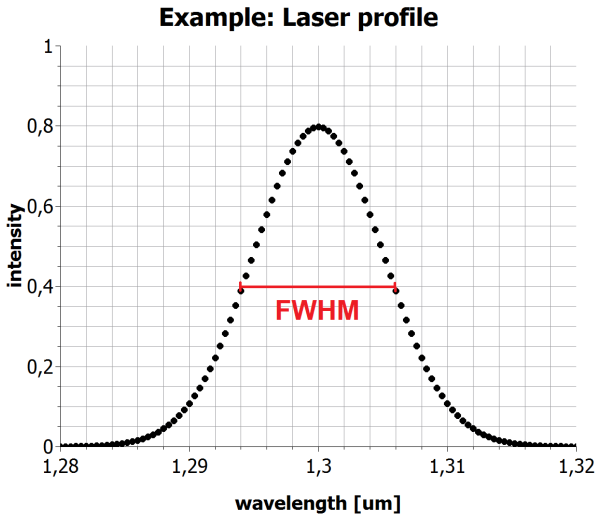

Figure 140: Example of a laser spectral profile with center wavelength $1.3\mu m$ with a normalized intensity of 1 (area under curve). The Full Width Half Maximum is indicated in red.

= dR-total), the reflectance at $0V$ was subtracted from all curves, which gave the relative change of reflectance over wavelength for each voltage. The hereby obtained reflectance-over-wavelength curve was then multiplied with one of two laser profiles and integrated along the whole interval in a final step (see figure 141).

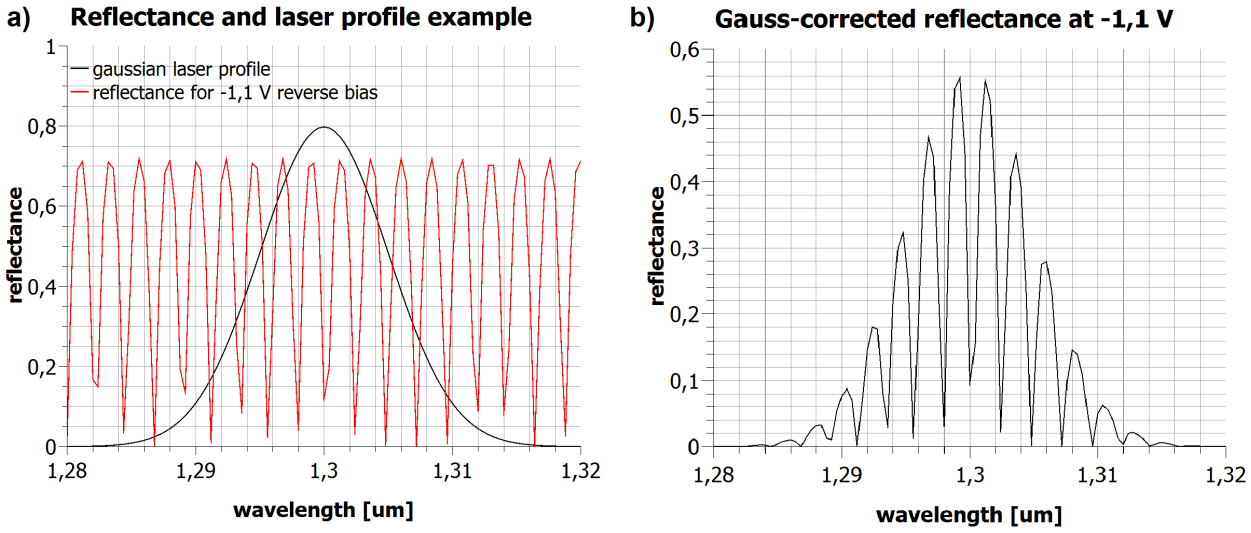

Figure 141: (a) Total reflectance from the TCAD simulation for a reverse bias of $-1.1V$ (red) and spectral profile of the laser (black). (b) Corrected reflectance profile obtained by multiplication of the two curves on the left. The corrected reflectance change profile was integrated along the spectral interval to obtain the value for EOFM signal / dR-total.

Especially for light sources with very narrow bandwidths (e.g. HSL) it is interesting to think about where in the spectral reflectance range the best condition for strong electro-optical signals exist.

This is obviously not the case for a spectral region close to destructive interference (i.e. reflectance ≈ 0), because here the amount of reflected light is too low to deliver a good signal-to-noise ratio when looking for light modulations at a certain frequency. It is neither the case at spectral regions close to constructive interference (i.e. very high reflectivity), because here a slight shift of the interference pattern as caused by modulations in the active device causes only a small variation of reflection. For best signals the laser light needs to be at a spectral point, where a slight shift of the interference pattern causes maximal variation in the reflectance at that particular wavelength. Such points can be found at the flanks between points of constructive and destructive interference. Here the amount of reflected light is still high enough to ensure good signal-to-noise ratios and the variation of reflectance due to modulations caused by the active device is maximal. For light sources with broad spectral profiles (i.e. light source spectral profile stretching over several constructive interference peaks of the reflection) these considerations are of minor importance, as for those lasers the electro-optical modulation is calculated as an average over a wide spectral interval (several peak-to-peak distances). Here the exact spectral position of the center wavelength is less relevant (fig. 141 serves as a good example for this). The influence of different bandwidth light sources on EOFM-signal can be observed also in figure 145.

The average distance between two reflectance peaks in fig. 141 was found to be a function of substrate thickness. The exact peak-distance-over-substrate-thickness correlation was investigated with a series of simulations with identical setup except for variation of substrate thickness and laser position outside the device (fig. 142). The peak-to-peak distance drastically increases for decreasing substrate thickness with a

$$y_0 + A \cdot e^{(-x/t)} \tag{6.2}$$

characteristic (x =substrate thickness, y_0 = offset, t = model parameter). This is especially relevant for use of visible light optical probing, where backside thicknesses of $\approx 1 - 10\mu m$ are required in backside thinning and polishing, because of the high visible light absorption in silicon. Peak-to-peak distances of $\approx 25 - 100nm$ in this region carry the risk of very weak electro-optical signals here. For example with a backside thickness of $5\mu m$, a peak-to-peak distance of $\approx 50\mu m$ and a light source with narrow bandwidth (e.g. FWHM$\leq 5nm$ or even smaller) it might well happen, that the laser central wavelength lies close to a point of destructive interference in the reflectance spectrum (fig. 141). In this case almost no electro-optical signal could be detected even if there is a lot of light modulation by the active device.

6.5.1.4 Simple simulations Due to the high doping level at the front (close to $Y = 0$) most interesting physical effects and analysis is concentrated in this region. Figure 143 shows that most voltage-dependent changes in the light absorption take place in this small region. The change in the absorbed photon density has very small values outside a small interval between $Y = 0,3\mu m$ and $Y = 0,9\mu m$ except for a forward bias of $0,9V$ (orange curve), where the increase of charge carriers causing absorption is very high also at deeper substrate areas due to high injection. This correlates directly to the change of both parts of the refractive index (see figure 144). A change in the real part of the refractive index indicates an alteration of the light path length in the medium, whereas a change in the imaginary part stands for absorption of light and thus decreasing beam intensity.

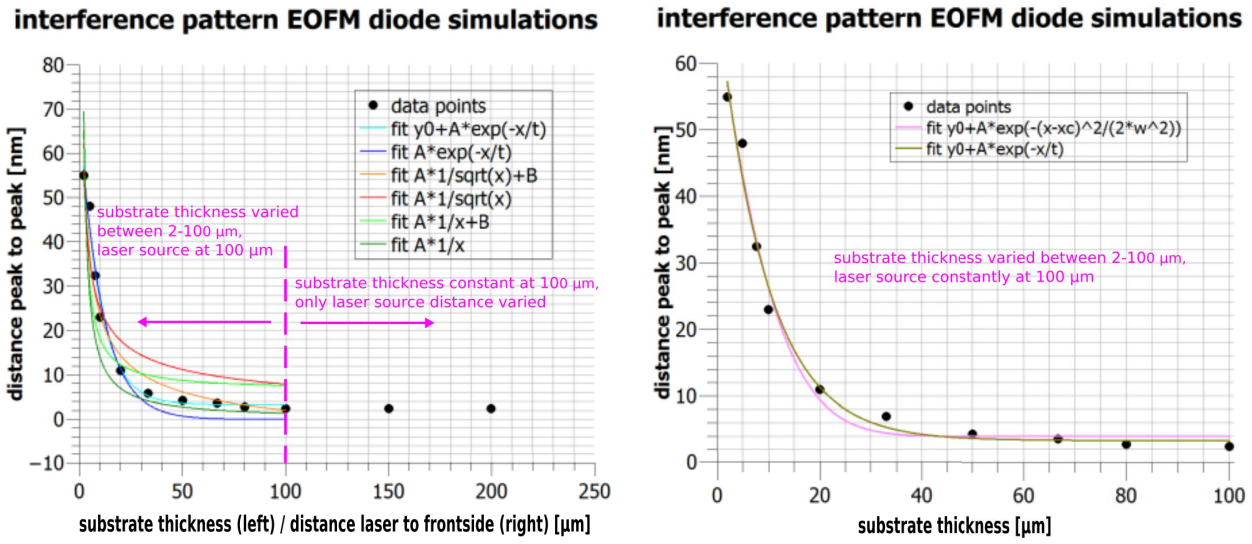

Figure 142: Correlation between peak-to-peak distance of reflectance peaks (constructive interference) and substrate thicknesses between $2\mu m$ and $100\mu m$. The two values of $150\mu m$ and $200\mu m$ refer to a substrate thickness of $100\mu m$ but with the laser source originating from a distance of $50\mu m$ and $100\mu m$, respectively, outside the device. Several fit function were tried to obtain a rule of thumb relation.

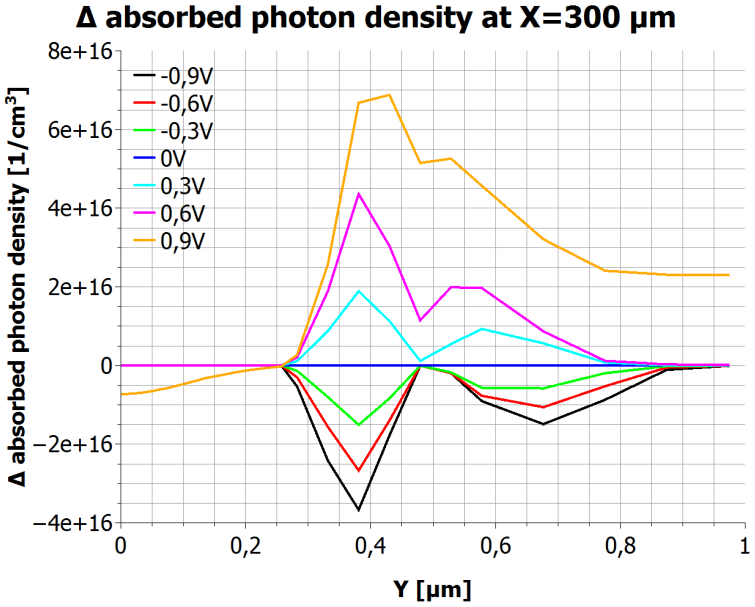

Figure 143: Graph showing the change of the density of absorbed photons relative to a voltage of 0V for various voltages (negative voltages: reverse bias; positive voltage: forward bias).

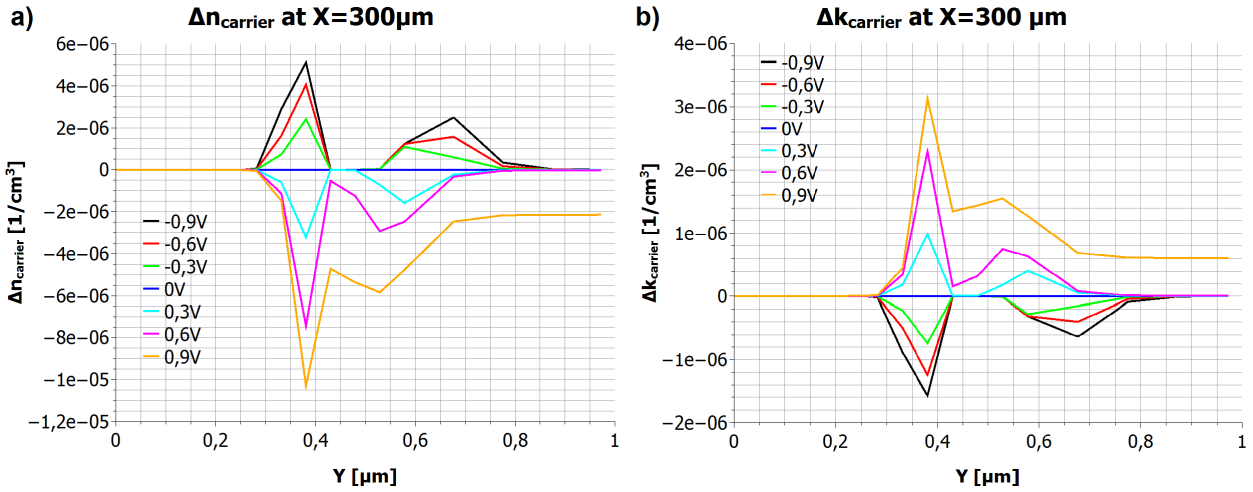

Figure 144: (a) Comparison of the change of the real part $\Delta n_{carrier}$ of the complex refractive index depending on voltage (negative voltages: reverse bias; positive voltage: forward bias). (b) Comparison of the change of the imaginary part $\Delta k_{carrier}$ of the complex refractive index depending on voltage.

The absolute value of ΔR_{total} in (fig. 145) is proportional to the EOFM signal, which is measurable with Phemos-1000. Generally for negative voltages a square-root-like dependance of ΔR_{total} can be identified, which correlates to the square-root-like dependance of space charge region width on voltage (fig. 146). As for MOSFETs all pn-junction are always in reverse, this is the reason why EOFM signals often have a seemingly linear signal-with-voltage characteristic, even when only drain is pulsed and the linear capacitance contribution of the MOSFET channel is inactive. A closer look on the situation reveals that the dependance of EOFM signals on voltage for dominant space charge region modulation are truely square-root-shapes, which can be approximated well with linear functions.

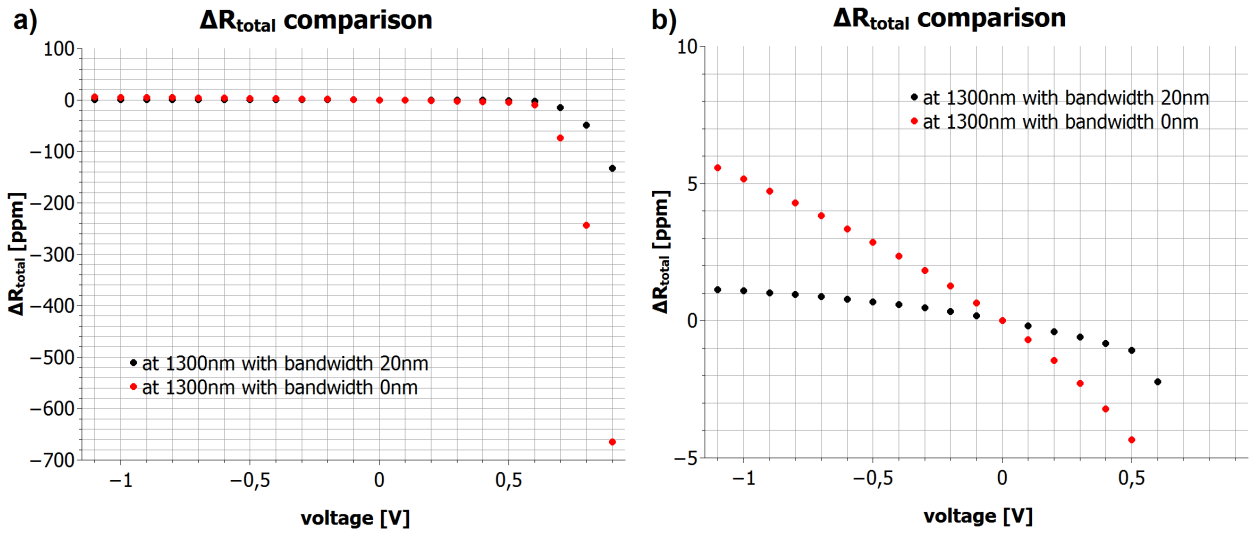

Figure 145: (a) ΔR_{total}/-/EOFM-signal over voltage obtained in the simulations. (b) Identical, but with smaller y-axis interval.

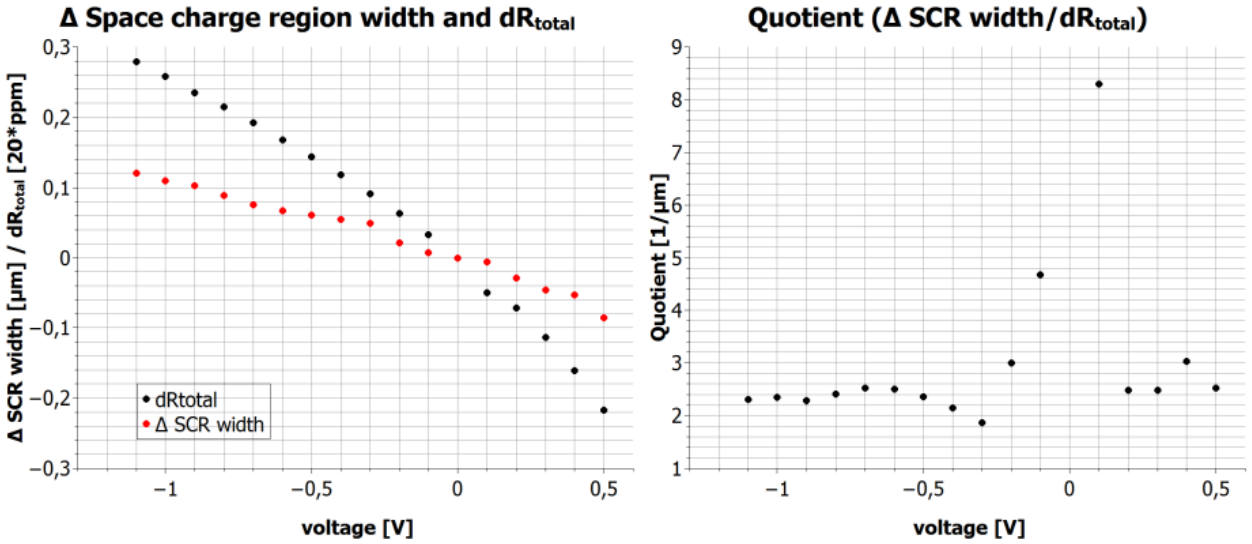

Figure 146: Comparison of space charge region width change and EOFM signal over voltage (left). The image on the right proves the direct proportionality of both entities as their quotient is almost constant within a small numerical failure interval of $\approx 10\%$. Higher failure intervals for very small voltages can be attributed to higher numerical inaccuracy of the simulation. A small failure interval generally has to be expected because of the discrepancy between continuous space charge courses across the whole pn-structure and the rigid definition of space charge region width at a predetermined value.

The change of ΔR_{total} (= total reflectance change) with voltage correlates closely to the change of the integrated absorbed photon density in fig. 147. Table 12 shows that especially for voltages between $-1,1V$ and $0,3V$ the change of ΔR_{total} is almost completely due to increasing or decreasing photon absorption by free charge carriers in the space charge region. Above a forward bias of 0,6 V effects deeply within the substrate start to influence the change of the EOFM signal (orange curve in fig. 143 for $Y > 0,8\mu m$).

The positive sign of the EOFM-signal (ΔR_{total}) for reverse bias matches the negative sign of the imaginary part of the refractive index ($\Delta k_{carrier}$). If this imaginary part is negative, the laser light becomes less absorbed causing a slight increase of the reflected light (i.e. EOFM-signal is positive). The decreasing absorption for reverse bias can be directly observed by the negative sign of the absorbed photon density in fig. 143. For forward voltages the explanation is analog, but with switched signs.

6.5.1.5 Discussion of the simulation results The parameters of the device and optics simulations in this section were identical except for a variation of either bulk temperature, frontside or backside doping level of the diode. The evaluation of EOFM signals was done for two different light source profiles - HSL and HIL. Mostly the qualitative square-root-like signal dependence on voltage for reverse bias and the strong exponential-like increase for forward bias remain the same for all temperatures. But quantitatively, the results with respect to temperature variation in figures 148 to 153 show an EOFM signal rise with increasing device temperature, both for reverse and forward bias. The only exception from that is the analysis of signals caused by the real part of the refractive index for HIL, where a signal decrease by $\approx 30\%$ due to varied interference can be seen. For HSL and reverse bias the signal rises by $\approx 20\%$ for a temperature increase of $100K$ and

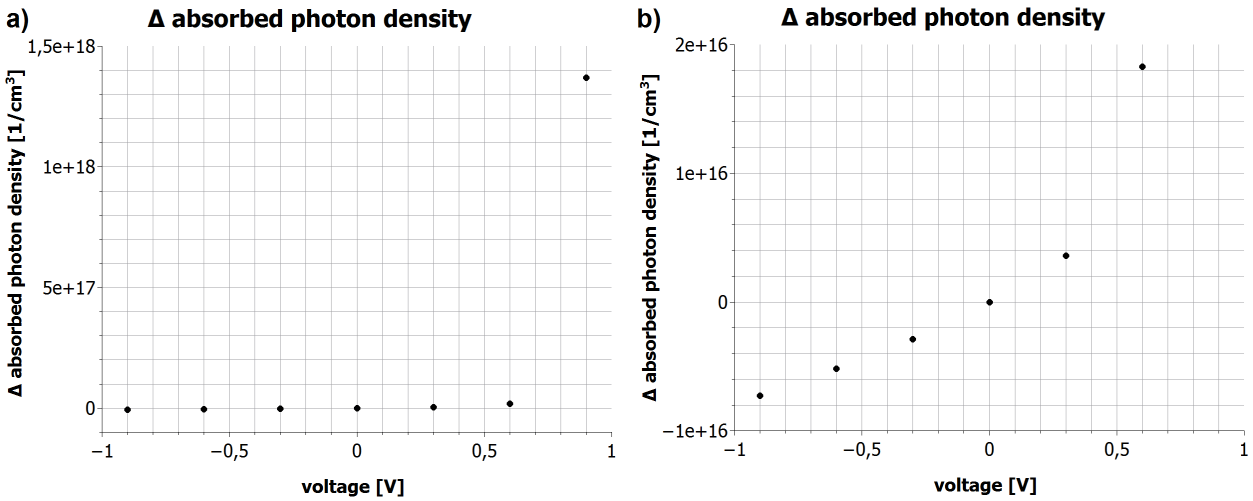

Figure 147: (a) Absorbed photon density change integrated from $Y = 0\mu m$ to $Y = 100\mu m$ (front to backside). (b) Identical, but with smaller y-axis interval.

Voltage [V]	EOFM [a.u.]	Int. abs. photon density [a.u.]	Quotient [a.u.]
-0,9	4,73	-7,29	-0,65
-0,6	3,35	-5,19	-0,65
-0,3	1,83	-2,90	-0,63
0	0	0	
0,3	-2,29	3,62	-0,63
0,6	-10	18,3	-0,55
0,9	-665	1370	-0,49

Table 12: Comparison of simulated EOFM-signal (ΔR_{total}), integrated absorbed photon density (integrated at $X = 300\mu m$ from $Y = 0\mu m$ to $Y = 100\mu m$) and their quotient.

the overall signal range is much lower ($< 1ppm$) than for forward bias (some $1000ppm$ at $0.7V$). For forward bias the relative signal increase from lower to higher temperature is also much higher ($\approx 1000\%$ for $100K$ increase). For HIL and reverse bias the signal change is much lower ($< 5\%$) for the full complex refractive index, as changes of real and imaginary part (in the range of 10 to 50%) cancel each other out. Signals for HIL laser profile are roughly a factor of 2 to 4 smaller than for HSL and sometimes have an alternating sign, both depending strongly on the substrate thickness effecting the interference pattern especially for HSL. The temperature results correspond well with results reached with similar simulations but a less extensive layer structure for the transfer matrix model [82, 89, 101, 104].

Interestingly, the EOT signal contribution due to the real part of the complex refractive index is about 4 to 5 times higher in absolute value than the contribution of the imaginary part for the HSL light source, both for reverse and forward bias. For HIL the situation is different: Here the contribution of the imaginary part is dominant by factors of 3 up to 150. Same signal behavior for the two light sources can also be seen for all simulations regarding different substrate doping concentrations and different frontside doping concentrations, indicating that this effect is not caused by variation of simulation parameters, but is due to bandwidth and position of center wavelength of the respective laser. Another observation concerning the two different light sources can be made with respect to signals caused by imaginary and real part of the refractive index: While for the imaginary part the sign for the EOFM signal is identical for HIL and HSL light sources, it is always opposite for the real part. The reason is obvious: increasing/decreasing absorption (imaginary part) effects both lasers in the same way, whereas the effect for variation of the optical path length (real part) strongly depends on the individual laser profile and can have opposite signs.

Concerning different doping concentrations of substrate (figures 154 to 159) and frontside (figures 160 to 165), both have a much stronger relative effect for reverse bias than for forward bias. A signal increase by a factor of $10 - 20$ can be achieved for reverse bias by changing the substrate doping concentration from $4 \cdot 10^{13}/cm^3$ to $1 \cdot 10^{16}/cm^3$, while it is only a factor of ≈ 2 for forward bias. Concerning frontside doping concentration, a change from $1 \cdot 10^{19}/cm^3$ to $1 \cdot 10^{21}/cm^3$, signal increase by a factor of $3-4$ can be achieved for reverse bias, but only $10-20\%$ for forward bias. The obtained EOFM simulation results correspond qualitatively to other data presented in [82, 101], but quantitatively show ≈ 50 times smaller absolute signal values. This is not surprising as those results were obtained for a n^+p-pn-junction of a MOSFET with much higher well doping concentration ($\approx 3 \cdot 10^{17}/cm^3$) and slightly different geometrical doping profile, also for the drain and source diffusions. Interpolating the data in figure 154 for a substrate doping concentration of$3 \cdot 10^{17}/cm^3$ gives roughly a signal increase factor of 20-40, so that in this case the results match previous data also quantitatively.

As a summary, the spectral laser profile (large/narrow bandwidth) as well as the center wavelength and coherence/incoherence of the light source play a major role for the absolute EOFM value. For EOFM measurements in the lab a wide choice of different light sources differing in the aforementioned parameters is recommended. While different doping concentrations can have a large effect on the evolution of electro-optical signals, they cannot be changed during the measurement and are therefore of less importance. The chip temperature can be changed with thermal chucks though, but the signal increase of $\approx 20\%$ caused by $100K$ temperature increase for reverse bias (which

is the standard case in all integrated circuits) is probably too low to consider this as a regular improvement technique for signals.

Simulation results regarding temperature

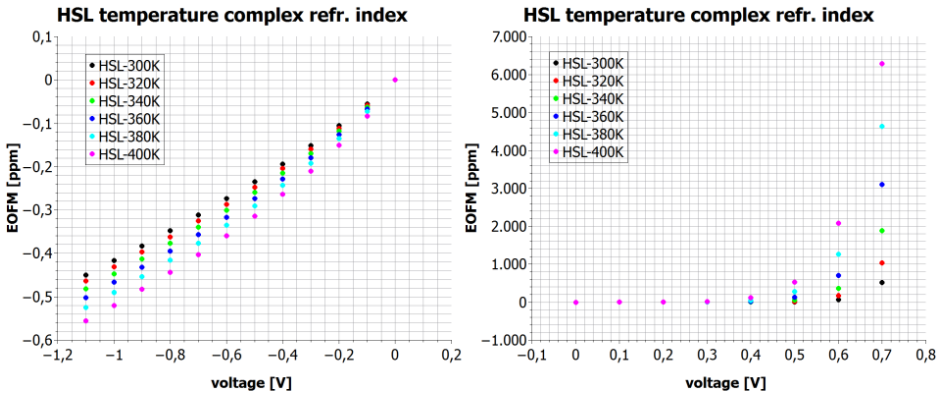

Figure 148: Simulated EOFM signal curve over reverse (left) and forward bias (right) for different bulk temperatures and HSL light source. The full complex refractive index (real + imaginary part) was used for simulation.

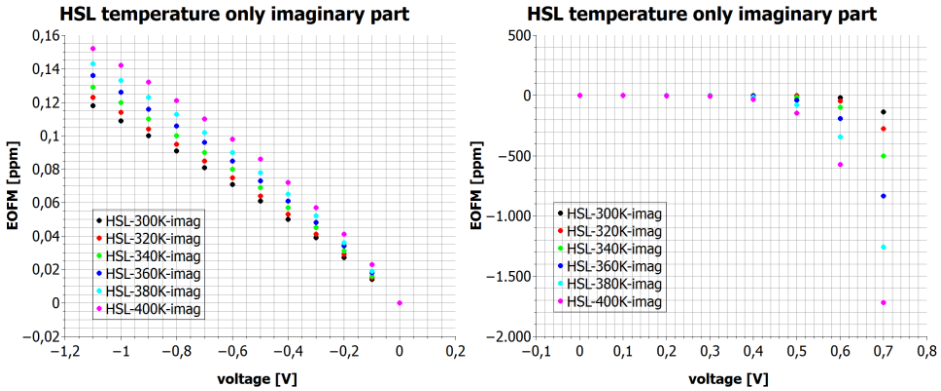

Figure 149: Simulated EOFM signal curve over reverse (left) and forward bias (right) for different bulk temperatures and HSL light source. Only the imaginary part of the refractive index was used for simulation.

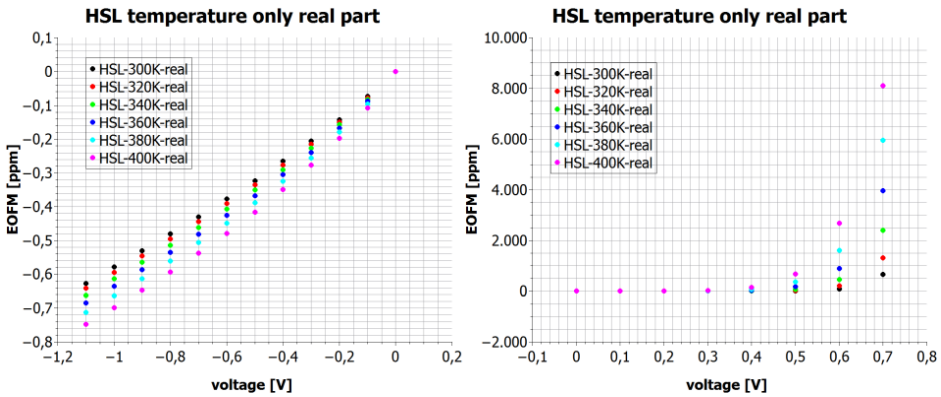

Figure 150: Simulated EOFM signal curve over reverse (left) and forward bias (right) for different bulk temperatures and HSL light source. Only the real part of the refractive index was used for simulation.

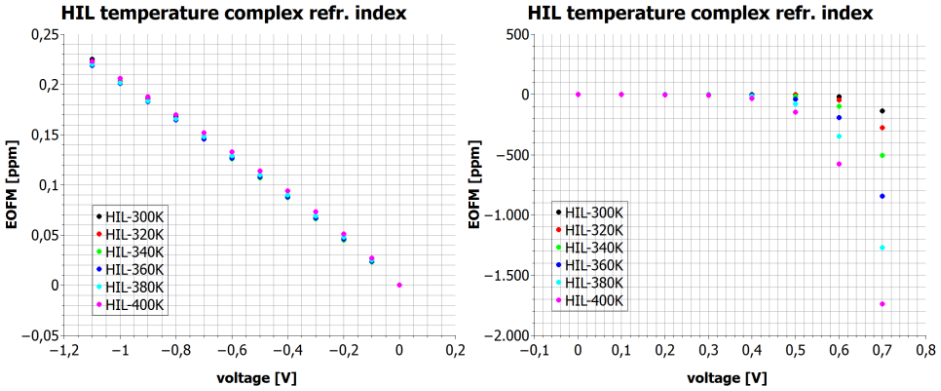

Figure 151: Simulated EOFM signal curve over reverse (left) and forward bias (right) for different bulk temperatures and HIL light source. The full complex refractive index (real + imaginary part) was used for simulation.

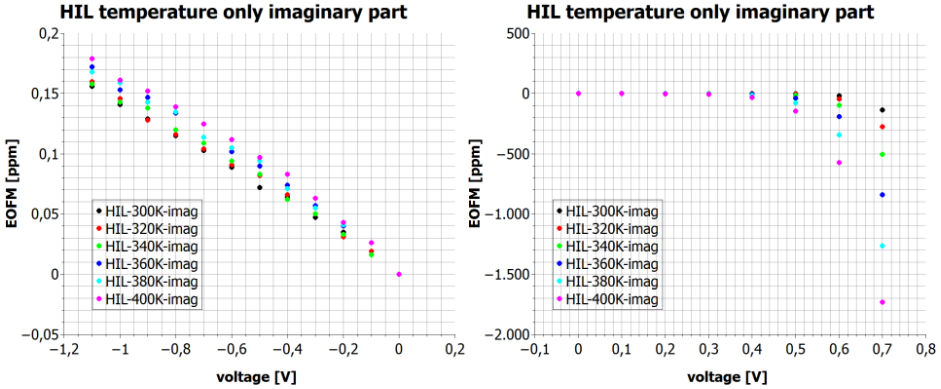

Figure 152: Simulated EOFM signal curve over reverse (left) and forward bias (right) for different bulk temperatures and HIL light source. Only the imaginary part of the refractive index was used for simulation.

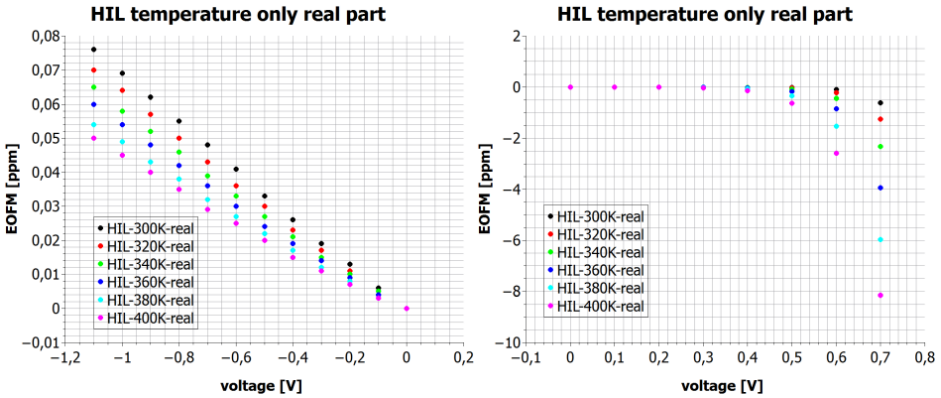

Figure 153: Simulated EOFM signal curve over reverse (left) and forward bias (right) for different bulk temperatures and HIL light source. Only the real part of the refractive index was used for simulation.

Simulation results investigating the effect of the substrate doping

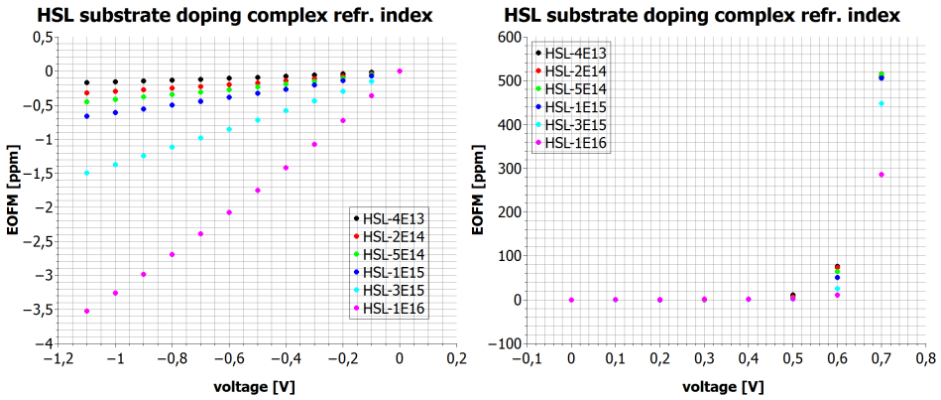

Figure 154: Simulated EOFM signal curve over reverse (left) and forward bias (right) for different substrate doping concentrations and HSL light source. The full complex refractive index was used for simulation.

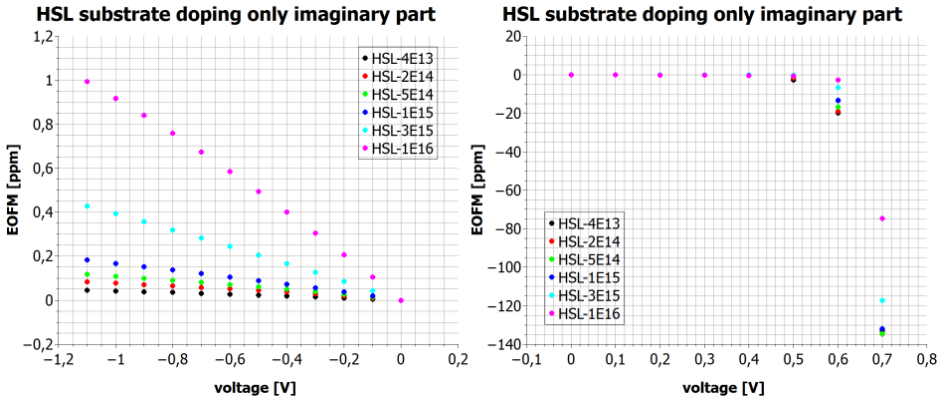

Figure 155: Simulated EOFM signal curve over reverse (left) and forward bias (right) for different substrate doping concentrations and HSL light source. Only the imaginary part of the refractive index was used for simulation.

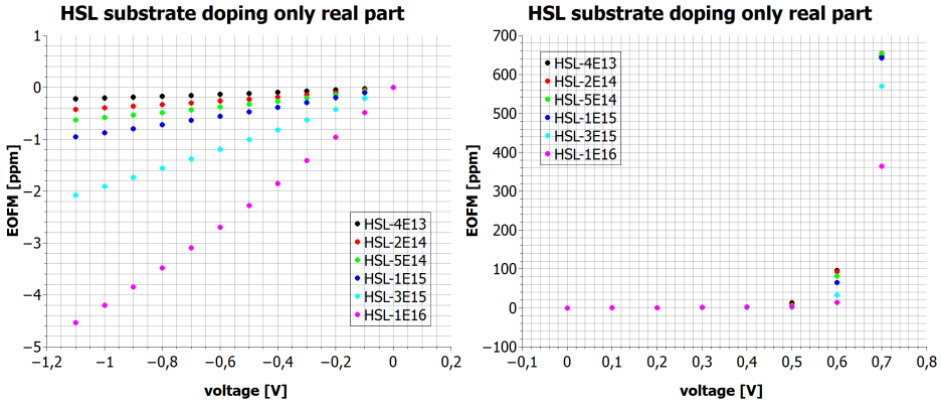

Figure 156: Simulated EOFM signal curve over reverse (left) and forward bias (right) for different substrate doping concentrations and HSL light source. Only the real part of the refractive index was used for simulation.

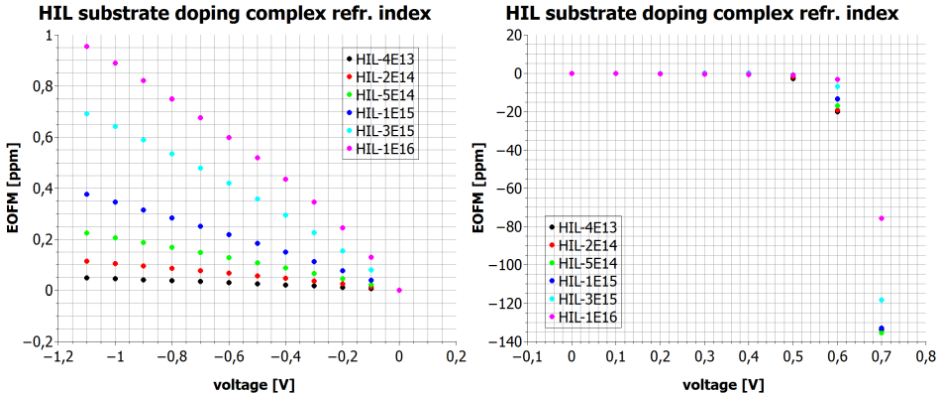

Figure 157: Simulated EOFM signal curve over reverse (left) and forward bias (right) for different substrate doping concentrations and HIL light source. The full complex refractive index (real + imaginary part) was used for simulation.

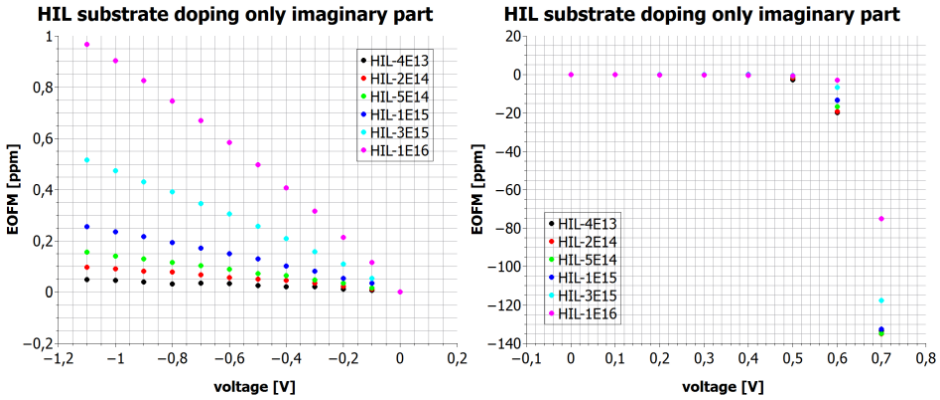

Figure 158: Simulated EOFM signal curve over reverse (left) and forward bias (right) for different substrate doping concentrations and HIL light source. Only the imaginary part of the refractive index was used for simulation.

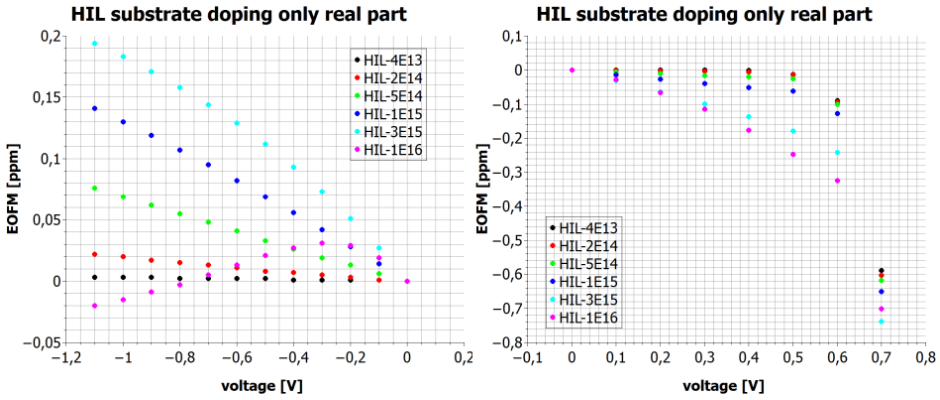

Figure 159: Simulated EOFM signal curve over reverse (left) and forward bias (right) for different substrate doping concentrations and HIL light source. Only the real part of the refractive index was used for simulation.

Simulation results investigating the effect of the front doping

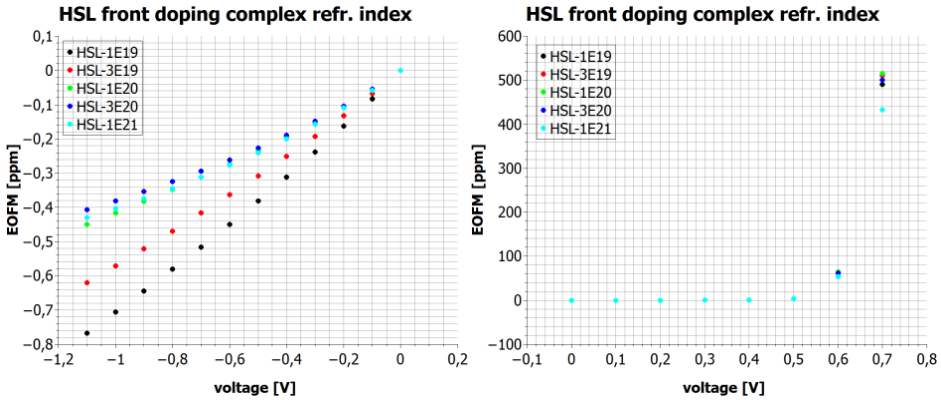

Figure 160: Simulated EOFM signal curve over reverse (left) and forward bias (right) for different front doping concentrations and HSL light source. The full complex refractive index was used for simulation.

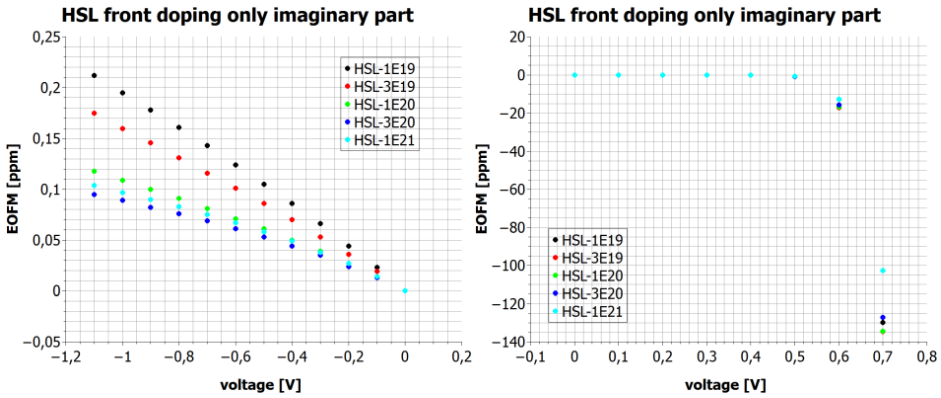

Figure 161: Simulated EOFM signal curve over reverse (left) and forward bias (right) for different front doping concentrations and HSL light source. Only the imaginary part of the refractive index was used for simulation.

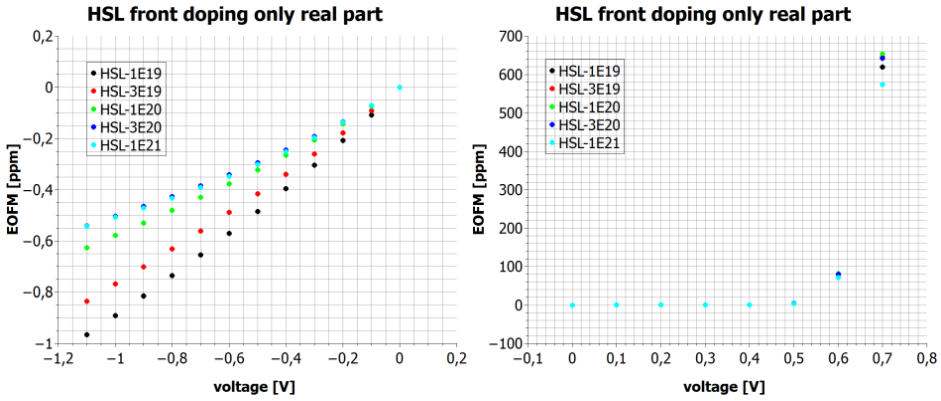

Figure 162: Simulated EOFM signal curve over reverse (left) and forward bias (right) for different front doping concentrations and HSL light source. Only the real part of the refractive index was used for simulation.

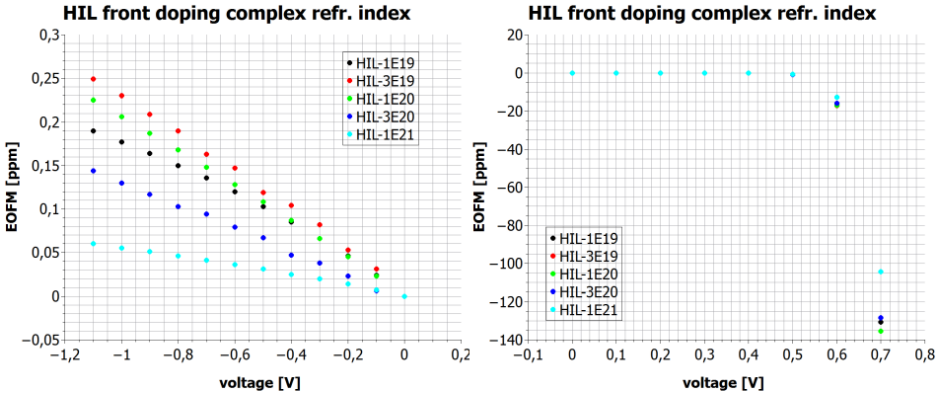

Figure 163: Simulated EOFM signal curve over reverse (left) and forward bias (right) for different front doping concentrations and HIL light source. The full complex refractive index (real + imaginary part) was used for simulation.

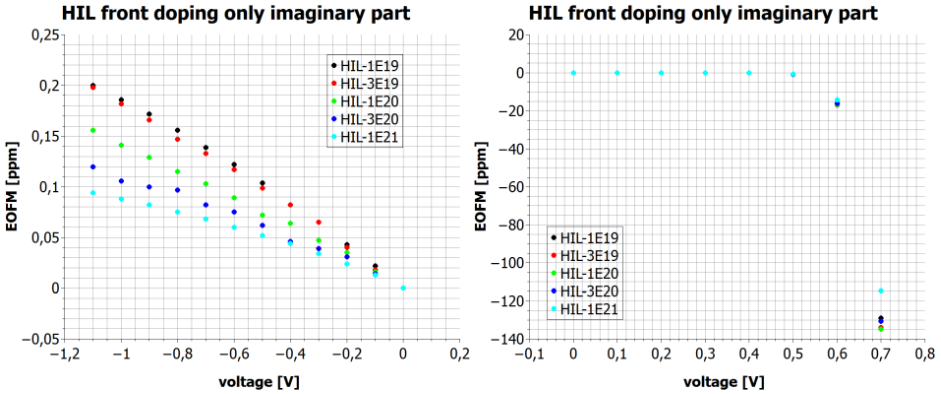

Figure 164: Simulated EOFM signal curve over reverse (left) and forward bias (right) for different front doping concentrations and HIL light source. Only the imaginary part of the refractive index was used for simulation.

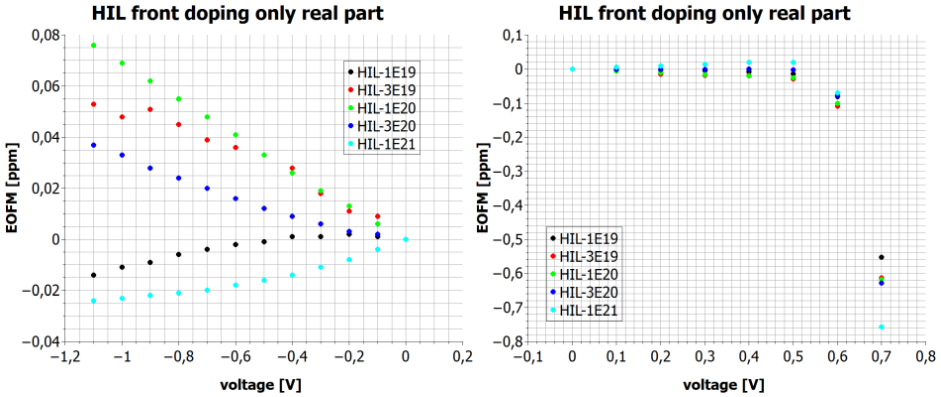

Figure 165: Simulated EOFM signal curve over reverse (left) and forward bias (right) for different front doping concentrations and HIL light source. Only the real part of the refractive index was used for simulation.

6.5.2 EOFM measurements

To verify the results for the EOFM simulations experiments were carried out on the pn junction of a real diode on a test chip from IHP Germany. Nominal voltage for the $250nm$ technology was $2.5V$. For all EOFM experiments presented here the Hamamatsu HIL light source was used at 100% power. Pulse frequency was $1MHz$ with a duty cycle of 50% and different high level voltages (low level voltage was always kept at $0V$). The samples were bonded, thinned to $\approx 100\mu m$ remaining silicon bulk thickness and polished for backside access. A pattern image of the test structure along with several EOFM images can be seen in figures 166 and 167.

For forward bias a strong, exponential rise of EOFM signal can be observed (fig. 168) due to the increasing current across the junction. Once the diffusion voltage is roughly compensated by forward bias ($\approx 0.8V$) the junction enters high injection, which causes a free carrier flooding of neighboring areas and substrate. This results in very strong EOFM signals and vast expansion of the signal area as visible in fig. 167 right. This effect is similar to a parasitic thyristor, which thereby can also be identified via the use of EOFM.

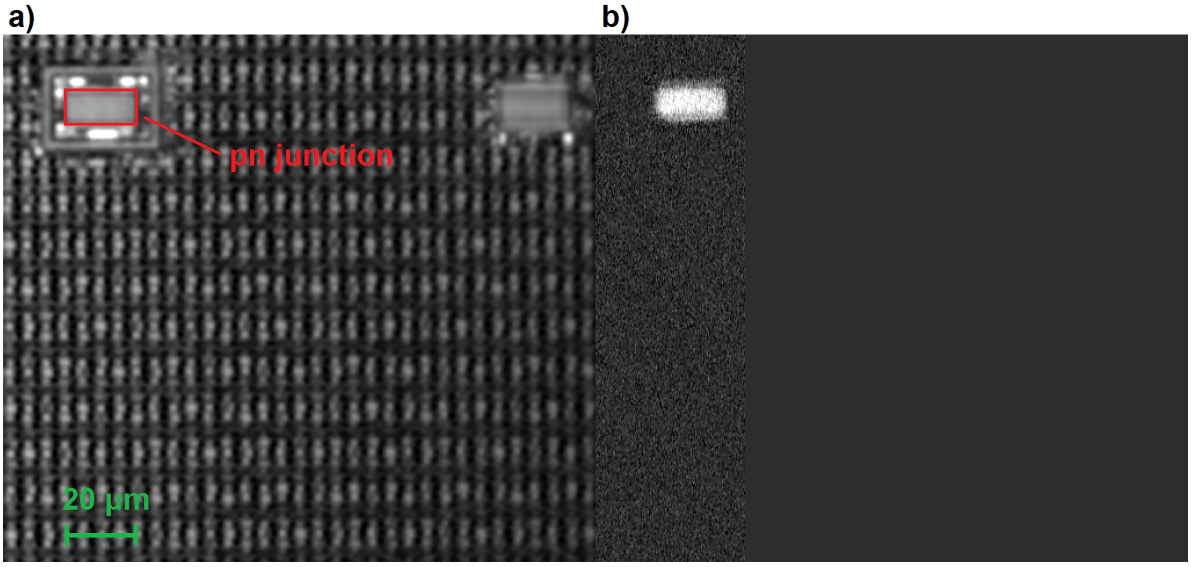

Figure 166: Pattern image of the pn junction test structure (a) and EOFM signal of the pn junction pulsed at $-2.5V$ reverse bias (b). In the image on the left typical interference patterns due to different layers of metal fill etc. can be identified throughout the image. Data acquired with HIL light source at 100% light power and 50x lens with 1x optical zoom without Nanolens.

The EOFM signal shows a slow square root-like rise with voltage in reverse bias (see figure 168) due to the square root-like dependence of space charge region thickness on reverse bias. Here, the optical modulation (i.e. EOFM signal) is generated by the decreasing absorption due to the increasing space charge layer with reverse voltage. The course of the experimentally obtained EOFM signal curves in forward and reverse bias match our simulation results presented in figure 145, when taking into account that negative originally negative EOFM values in forward bias are converted to positive values by the Phemos-1000 software. The software calculates the absolute value of the EOFM signal given as the square root of the sum of squares of EOFM x- and y-component (for further explanation see 3.7).

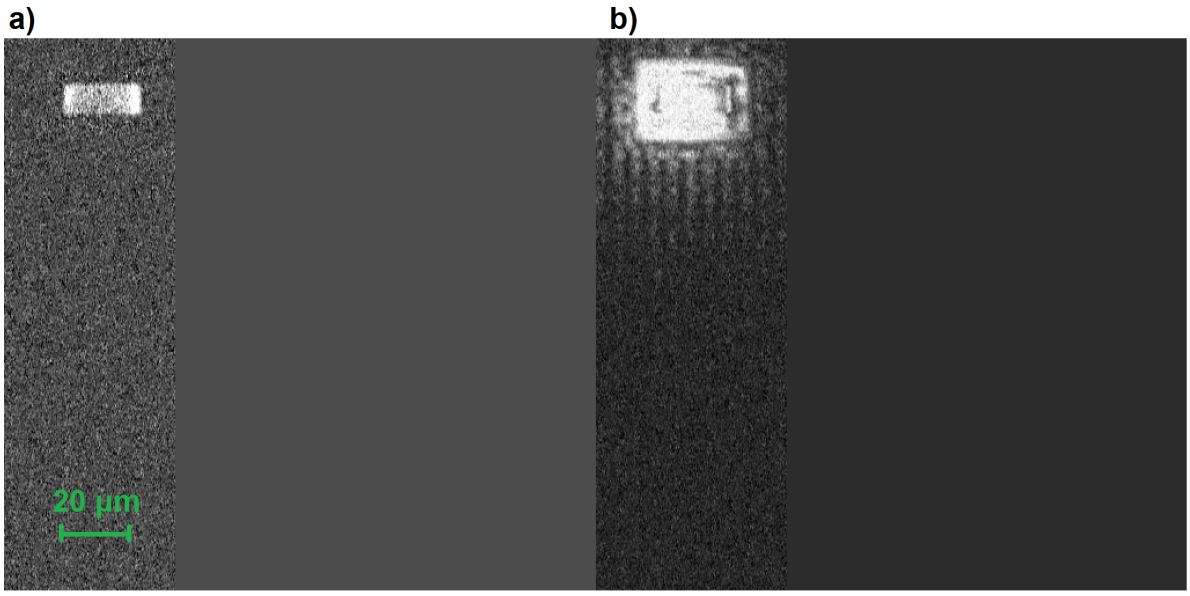

Figure 167: EOFM signal of the pn junction pulsed at $0.7V$ (a) and $0.8V$ (b) forward bias. The step from $0.7V$ to $0.8V$ marks the transition from normal to high injection. On the right it is clearly visible that the region and substrate in neighboring areas of the pn junction are flooded with charge carriers, which is not the case for voltages of $0.7V$ and lower. Data acquired with HIL light source at 100% light power and 50x lens with 1x optical zoom without Nanolens.

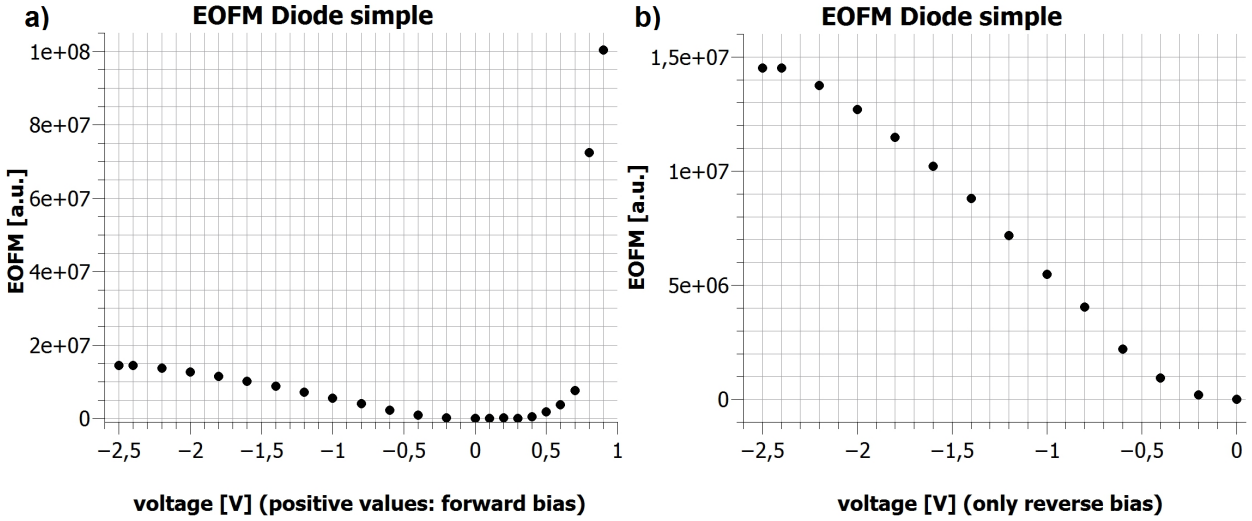

Figure 168: EOFM signal of the diode / pn junction in reverse and forward bias (a). For reverse voltages (b) a square-root-shape of the signal course is visible, corresponding to the square-root-like dependence of the space charge region thickness on voltage. Data acquired with HIL light source at 100% light power and 50x lens with 1x optical zoom without Nanolens.

7 Conclusion and Outlook

Regarding photon emission microscopy, in this thesis it was proven that PEM analysis is still well possible even for state-of-the-art $14 - 40nm$ FinFET devices with voltages well below $1V$ down to less than $0.5V$ with optimal equipment and deeper infrared detectors. The author does not share the common believe that PE as a technique for FA of ICs and characterization is dying out. As long as charge carriers in MOSFETs or FinFETs are supplied with energy (via drain voltage) and have to pass a high electric field close to pinch-off, they will always emit light due to the scattering processes, which are necessarily involved. Of course, the spectral intensity distribution will be shifted continuously towards higher wavelengths for decreasing supply voltage, thus even deeper infrared detectors have to be developed / applied to detect emission. The spectral emission results of this thesis strongly suggest, that red-shift of intensities is not proportional to device voltage decrease, but clearly slows out with decreasing technology parameter and with hot carrier gas temperature.

The argument that deeper infrared emissions will interfere or even be surpassed by black-body radiation of surrounding areas is only semi-true: Yes, there will be such interference, but as the temperature of the hot carrier gas in the channel will always be higher than the temperature of surrounding areas (chip, package, objective lens, optical path etc.), photon emission will still set itself apart from these black-body radiation sources. When the temperature difference between hot carrier gas and surrounding areas gets lower and is therefore harder to detect, one might also think of the use of dynamic photon emission techniques (similar to EOFM pulsing) for spectra acquisition, which would surely enhance signal-to-noise ratios here.

Furthermore, this thesis has opened up several new areas of application for spectral photon emission microscopy in the semiconductor industry. For the first time a systematic spectral analysis of device functionality and failure mechanisms for modern FinFETs was carried out with a meticulous camera and system calibration. Photon emission spectra can now be used as a standard failure analysis method to categorize active devices. Furthermore, PE spectra can be used to obtain valuable device parameters such as charge carrier energy distributions, free mean path lengths within the active region, electric field strengths and more. These parameters can not only be used as experimental verifications of device modeling and optimization processes but also for reliability research of individual transistors. For spectral analysis of complex emission patterns and to further increase resolution and signal-to-noise-ratio for photon emission techniques a new 2d-tomography-like method was developed including mathematical, physical, experimental and numerical treatment as well as a proof-of-concept on a ring oscillator structure. The method can be adopted for industrial use and thus contribute it's share to further PE technique enhancement.

In the end photon emission will always contain much more information about the concrete physical device characteristics compared to EOFM. EOFM is a good technique to see, where (but not necessarily *what*) processes happen at a certain frequency, as reflected laser light can be modulated by a lot of major and minor sources. Also the linear voltage dependence of EOFM/EOP is a big advantage here. The electro-optical techniques don't suffer from anything comparable to a red-shift, too. But when it comes to understanding what exactly is happening physically at device level, photon emission is and will be by far the superior technique as was shown in this thesis. Photon emission is also non-invasive (in contrast to electro-optical techniques) and therefore only

contains information about the untainted device operation. Furthermore photon emission doesn't suffer from interference like electro-optical techniques as the emitted light is generally incoherent.

The next step for SPEM analysis of state-of-the-art devices will be to build up a library with spectral data of more transistors than investigated in this thesis. The library could be segmented into several parts regarding e.g. SPEM results for device parameter extraction on the one hand and correlation of failure mechanisms and respective spectra on the other hand. This will be a sensible and fruitful task especially with the use of better equipment (e.g. MCT or Emmi-X cameras). This together with the development of a new/expanded theoretical approach for the sub-400K hot carrier gas regime would form a very good PhD topic for an interested and physically-minded student. A cooperation with the TRE-research group at IBM New York could be very fruitful for anything related to the development of a dynamic SPEM technique.

The presented results for EOFM simulations on a pn-structure have deepened the understanding of electro-optical signal composition with respect to many physical parameters such as temperature, doping levels, laser wavelength and bandwidth, remaining substrate thickness after thinning and others. Also several long existing questions e.g. about the (seemingly) contrast between *linear* rise of EOFM signals with voltage due to *square-root-like* space charge region modulations could be clarified. The simulational results were confirmed with EOFM measurements on a real diode test structure with similar device parameters compared to the simulations. All simulation results were explained on physical level or matched previously existing assumptions and theories. However there is vast potential of getting more physical insight into electro-optical signal generation with simulations: The simulations presented here can be expanded towards laser sources with wavelengths smaller than the silicon bandgap ($\leq 1110nm$) or even visible light to study the influence of free carrier generation by the laser on device activity and EOFM signal. This will be particularly useful for new techniques like visible light probing (Vis-EOFM), but also conventional failure analysis techniques such as photoelectric laser stimulation (PLS) will profit from these investigations. Another promising expansion for the simulations would be the investigation of DIBL and GIDL effects with EOFM, which are important for modern FinFET device performance. A project in this direction is currently planned at TU Berlin. Further possibilities include extension of the EOFM simulations towards modern FinFET devices or more complex logic structures (e.g. NANDs, inverter etc.) in order to understand more about the fascinating light-matter interaction happening in small-size devices.

This thesis provided many new insights into photon emission and electro-optical techniques for complex logic structures and analog devices. This path should be continued to match the upcoming demand of FA techniques for analog and mixed-signal circuits. PEM and EOFM research of 3d-devices will also be of general scientific interest, as this is a major trend for modern and future chip performance enhancement. Finally and last but not least (S)PEM and EOFM are still good for many kinds of failure detection analysis on modern devices. Many new FA case studies were presented within this work, which will hopefully inspire a lot of new and innovative FA approaches to new arising problems.

Appendix

A Commented Scilab scripts for tomography

```
PART A: PROGRAM FOR PREPROCESSING EXPERIMENTAL DATA FROM IMAGES

clear

// "Np" is the number of pixels in x-/y-direction minus 1.
Np=511;

// Parameters for pixel binning (if used):
blocksize=round(512/Np);
numberofblocks=round(512/blocksize);
counter=1

// The 0°-image without prism is processed first,
// serving as total intensity normalization for all other images:
    image_in=msprintf('%s%d%s',"..\512pixels\",0,"wp.png");
    I = double(imread(image_in));
    disp('Original size of image: '+string(size(I)))
    I(:,:,3)=[]
    I(:,:,2)=[]
    disp('Correct size of image: '+string(size(I)))
    // The smaller matrix C after binning is filled with the mean value of each block:
    if Np==511 then
        C=zeros(Np+1,Np+1)
        else
        C=zeros(Np,Np)
    end
    if Np<511 then
        for a=0:1:(numberofblocks-1)
            for b=0:1:(numberofblocks-1)
                for k=0:1:(blocksize-1)
                    for j=0:1:(blocksize-1)
                        C(1+a,1+b)=C(1+a,1+b) + I((1+blocksize*a+k),(1+blocksize*b+j));
                    end
                end
            end
        end
        ;
    else
        C=I;
    end

    // Statistical image processing of the experimental data
    // by deletion of emission values at noise level:
    meanvalue=mean(C)
    disp("Mean value for 0°-image: "+string(meanvalue))
    C=C-meanvalue
    maximum=max(C)
    disp('Maximum value:')
    disp(maximum)
    for m=1:numberofblocks
        for n=1:numberofblocks
            if C(m,n)<=(maximum/10) then
               C(m,n)=0;
            end
        end
    end
    if Np<511 then
    C=C/(blocksize*blocksize);
    end
    totalintensity0wp=sum(C)
    disp("Total intensity in 0°-image without prism: "+string(totalintensity0wp))
    image_out=msprintf('%s%d%s',"..\512pixels\",0,"wp.txt")
    disp(image_out)
    write(image_out,C)

// Processing of all images with prism for all rotations:
for x=-90:3:90
    disp("Angle in radian measure: "+string(counter))
    tic
    image_in=msprintf('%s%d%s',"..\512pixels\",x,"deg.png");
    I = double(imread(image_in));
    disp('Original size of the image: '+string(size(I)))
    I(:,:,3)=[]
```

```
0074      I(:,:,2)=[]
0075      disp('Correct size of the image: '+string(size(I)))
0076      // The smaller matrix C after binning is filled with the mean value of each block:
0077      if Np==511 then
0078      C=zeros(Np+1,Np+1)
0079      else
0080      C=zeros(Np,Np)
0081      end
0082      if Np<511 then
0083          for a=0:1:(numberofblocks-1)
0084              for b=0:1:(numberofblocks-1)
0085                  for k=0:1:(blocksize-1)
0086                      for j=0:1:(blocksize-1)
0087                          C(1+a,1+b)=C(1+a,1+b) + I((1+blocksize*a+k),(1+blocksize*b+j));
0088                      end
0089                  end
0090              end
0091          end
0092          ;
0093      else
0094          C=I;
0095      end
0096
0097      // Statistical image processing of the experimental data
0098      // by deletion of emission values at noise level:
0099      meanvalue=mean(C)
0100      C=C-meanvalue
0101      maximum=max(C)
0102      for m=1:numberofblocks
0103          for n=1:numberofblocks
0104              if C(m,n)<=(maximum/10) then
0105                 C(m,n)=0;
0106              end
0107          end
0108      end
0109      if Np<511 then
0110      C=C/(blocksize*blocksize);
0111      end
0112
0113      // Simple normalization of total emission intensity using the total emission intensity
0114      // of the 0°-image without prism multiplied by 0.8 (optical transmission of the prism,
0115      // almost constant for all wavelengths))
0116      intensity=sum(C)
0117      disp("Mean emission value for this angle "+string(counter))
0118      disp(meanvalue/(blocksize*blocksize))
0119      disp("Total intensity for this angle: "+string(intensity))
0120      if totalintensity0wp~=intensity then
0121          C=C*0.8*totalintensity0wp/intensity;
0122      end
0123
0124      // Saving processed image to harddrive:
0125      image_out=msprintf('%s%d%s',"..\512pixels\",x,".txt")
0126      write(image_out,C)
0127      disp(string(counter)+" images processed.")
0128      counter=counter+1
0129      disp("Corrected intensity for this angle: "+string(sum(C)))
0130      time=toc()
0131      disp("Time per image: "+string(time/60)+ "minutes.")
0132  end
0133
0134  disp('All images processed.')
```

```
PART B: MAIN TOMOGRAPHY PROGRAM WITH EQUATION SOLVER AND RESULT VISUALIZATION

clear

// Timer starts here to observe general time consupmtion of the entire program.
timer()

// "Np" is the number of image pixels in x- or y-direction.
Np=512;

// "weightfactor" enhances / decreases the weight that the additional normalizing equations
// from the 0°-image have compared to the existing lines of the U-matrix. Default value=1.
weightfactor=1;

// "rotation" is a vector including all angles for 61 rotations from -90° to 90° in steps of 3°.
// The angle of rotation is given in radian measure and clockwise.
rotation= [0;3/360*2*%pi;6/360*2*%pi;9/360*2*%pi;12/360*2*%pi;15/360*2*%pi;18/360*2*%pi;21/360*2*%pi;
24/360*2*%pi;27/360*2*%pi;30/360*2*%pi;33/360*2*%pi;36/360*2*%pi;39/360*2*%pi;42/360*2*%pi;
45/360*2*%pi;48/360*2*%pi;51/360*2*%pi;54/360*2*%pi;57/360*2*%pi;60/360*2*%pi;63/360*2*%pi;
66/360*2*%pi;69/360*2*%pi;72/360*2*%pi;75/360*2*%pi;78/360*2*%pi;81/360*2*%pi;84/360*2*%pi;
87/360*2*%pi;90/360*2*%pi;-3/360*2*%pi;-6/360*2*%pi;-9/360*2*%pi;-12/360*2*%pi;-15/360*2*%pi;
-18/360*2*%pi;-21/360*2*%pi;-24/360*2*%pi;-27/360*2*%pi;-30/360*2*%pi;-33/360*2*%pi;-36/360*2*%pi;
-39/360*2*%pi;-42/360*2*%pi;-45/360*2*%pi;-48/360*2*%pi;-51/360*2*%pi;-54/360*2*%pi;-57/360*2*%pi;
-60/360*2*%pi;-63/360*2*%pi;-66/360*2*%pi;-69/360*2*%pi;-72/360*2*%pi;-75/360*2*%pi;-78/360*2*%pi;
-81/360*2*%pi;-84/360*2*%pi;-87/360*2*%pi;-90/360*2*%pi];

// "wavelength" contains all wavelengths in nanometers, which have been chosen for the calculation.
wavelengths=  [730,755,780,805,830,855,880,905,930,950,1000,1025,1050];

// "transmittance" contains the product of light absorption factor (first value) for respective bulk
// thickness and transmission coefficient of the whole optical system (second value)
// for each wavelength in the order the wavelengths are given in "wavelength").
transmittance= [0.0098*0.943226448,0.02*0.87,0.048*0.787084076,0.085*0.68,0.144*0.579545838,
0.217*0.47,0.317*0.369456854,0.421*0.276,0.5325*0.198033315,0.624*0.146528702,0.825*0.062434469,
0.900*0.037,0.952*0.011897963];

// "pixelshift" contains the number of pixels that each wavelength is shifted to the right
// by dispersion when inserting the prism into the optical path in backside analysis mode.
// The order of values corresponds to the order of wavelengths in "wavelength".
pixelshift=  ([66,69.5,73,76,79,81.5,84,86.5,89,90,94,95.5,97])/(512/(Np));

// Here the preprocessed 0°-image without prism ("wp")) is read in and transformed
// into the vector "wpvector".
wp=read('..\images\0wp.txt',Np,Np);
wpvector=matrix(wp,Np*Np,1);
wpvector_transponed=matrix(wp',Np*Np,1);

// Minor parameter definitions and transformations:
N_phi=size(rotation,1);
nrot=N_phi;
rotationhrbrgl=rotation'
rotangle=vec2list(rotationhrbrgl,ones(N_phi,2))
N_l=size(wavelengths,"c");
nlambda=N_l;
wavelengthshrgbrgl=wavelengths'
lambdalist=vec2list(wavelengthshrgbrgl,ones(N_l,2))

//Maximum linear array size for temporary storage.
maxsize=5E7

// Input values from above are printed for control purposes:
disp("weightfactor for normalizing eqution: "+string(weightfactor))
disp("wavelengths: ")
disp(wavelengths)
disp('pixelshift: ')
disp(pixelshift)
disp('transmittance: ')
disp(round(transmittance*100)/100)
disp("Number of angles: "+string(N_phi))
disp("Number of wavelengths: "+string(N_l))
disp('Image size: '+string(Np) +"x" +string(Np))

// Definition of the function "createfullsensordata" which creates the vector
```

```
0074 // "I_total" containing all measurement data from all images for all rotations:
0001 function I_total=createfullsensordata(Np, N_phi)
0002    counter=1
0003    for phi=0//(-90):(180/(N_phi-1)):90
0004        filename=msprintf('%s%d%s',"..\512pixels\",phi,".txt");
0005        A=read(filename,Np,Np);
0006        Avector=matrix(A,Np*Np,1);
0007        if counter==1 then
0008        I_total=Avector
0009        else
0010        I_total=[I_total;Avector];
0011        end
0012        counter=counter+1
0013    end
0014 endfunction
0089
0090 // Definition of the function "vectortomatrix", which converts the final tomography result
0091 // vector "I_0" into single matrices for each wavelength
0092 // for result evaluation/display with "heatmap":
0001 function I_wl_matrix=vectortomatrix(I_0, N_l, wavelengths, Np, wp)
0002     m=size(I_0);
0003     n=nnz(wp);
0004     for lambda=1:(N_l+1)
0005         if lambda == N_l+1 then
0006         C=sumofzeros
0007         else
0008         C=wp
0009         if (n~=(m/N_l)) then
0010             disp('Warning: Number of entries in I_0 and wp-matrix do not match. Error in Code.');
0011         end
0012         counter = 0;
0013         for i=1:Np*Np
0014             if C(i)~=0 then
0015                C(i) = I_0(lambda+N_l*counter);
0016                counter = counter +1 ;
0017             end
0018         end
0019         end
0020         I_wl=C;
0021         I_wl=round(I_wl);
0022         I_wl_matrix=(matrix(I_wl,Np,Np))';
0023         I_wl_matrix=I_wl_matrix'
0024         I_wl_matrix=full(I_wl_matrix);
0025         if lambda==N_l+1 then
0026         disp("Sum of all wavelengths:")
0027         // "heatmap" displays result for each wavelength as a 2d colour plot.
0028         heatmap(I_wl_matrix,111,Np);
0029         else
0030         disp("Wavelength"+string(wavelengths(lambda)));
0031         heatmap(I_wl_matrix,wavelengths(lambda),Np);
0032         end
0033     end
0034 endfunction
0127
0128 // Definition of parameters for the "colormap"-result evaluation function:
0001 function heatmap(A, wl, Np)
0002     scf();
0003     for i=1:Np
0004         for j=1:Np
0005             if A(i,j)<0 then A(i,j)=-A(i,j); end
0006         end
0007     end
0008     // Color scale adjustments:
0009     if wl<450 then xset('colormap',coolcolormap(round(max(A))));
0010     elseif wl<520 then xset('colormap',oceancolormap(round(max(A))));
0011     elseif wl<560 then xset('colormap',summercolormap(round(max(A))));
0012     elseif wl<620 then xset('colormap',autumncolormap(round(max(A))));
0013     else xset('colormap',hotcolormap(round(max(A))));
0014     end
0015     xtitle("Heatmap Wellenlänge "+string(wl)+"nm","p","q");
0016     colorbar(0,max(A));
0017     Matplot(A);
0018 endfunction
```

```
0147
0148  // Algorithm for the creation of the point spread matrix "U":
0149  disp('Creation of U is running...')
0150  primcoord=zeros(2,Np*Np)
0151  row=[1:Np]
0152  for i=1:1:Np
0153      primcoord(:,(i-1)*Np+1:i*Np)=[row ; i*ones(1:Np)]
0154  end
0155  // Deletion of useless lines in "U" (every line where "I_0" is zero):
0156  H=find(wpvector==0)
0157  uselesscoordinates=length(H)
0158  primcoord(:,H)=[]
0159  N_s=size(primcoord,"c")
0160  if (Np*Np-N_s)~=uselesscoordinates then
0161      disp("Warning: Deletion of useless lines in U failed.")
0162  end
0163  disp("Number of useless coordinates deleted = " + string(Np*Np-N_s) + " of "
0164  + string(Np*Np)+". " +string(N_s) + " total coordinates left.")
0165  // "transvec" is a vector with periodic values of "transmission".
0166  transvec=matrix(transmittance(1:nlambda)'*ones(1:N_s),1,nlambda*N_s)
0167  U=spzeros(Np*Np*nrot,N_s*nlambda)
0168  stacksize('max')
0169  chunksize=floor(maxsize/(Np*Np))*(Np*Np)
0170  if chunksize > Np^2*N_s*nlambda then
0171      chunksize = Np^2*N_s*nlambda
0172  elseif chunksize == 0
0173      disp("0")
0174      chunksize=Np^2*N_s*nlambda
0175  end
0176  disp('Chunksize: ' + string(chunksize))
0177
0178  // The new coordinates after rotation for each pixel for each entry of "rotation" are calculated:
0179  tic
0180  nphi=1
0181  for angle=(-90):(180/(N_phi-1)):90
0182      if angle == 0 then
0183          v=primcoord;
0184      else
0185          v=rotate(primcoord,angle/360*2*%pi,[(Np+1)/2,(Np+1)/2])
0186      end
0187      disp("Angle: " +string(nphi))
0188      // Now the pixelshift induced by the prims dispersion is added to the x-coordinate:
0189
  newcoord=round([[matrix(pixelshift(1:nlambda)'*ones(1:N_s)+ones(1:nlambda)'*v(1,:),1,nlambda*N_s)];
0190      matrix(ones(1:nlambda)'*v(2,:),1,N_s*nlambda)])
0191      //Coordinates outside Np*Np image size are deleted:
0192
  outlier=[find(newcoord(1,:)>Np) find(newcoord(2,:)>Np) find(newcoord(1,:)<1) find(newcoord(2,:)<1)]
0193      outlier=gsort(unique(outlier))
0194      newcoord(:,outlier)=[1 1]'*ones(1:length(outlier))
0195      transvec(outlier)=0
0196      indall=sub2ind([Np*Np nlambda*N_s], sub2ind([Np Np],newcoord(2,:),newcoord(1,:)),[1:nlambda*N_s])
0197      chunk=find(indall<=chunksize)
0198      for i=0:1:(floor(Np^2*N_s*nlambda/chunksize)-1)
0199          Utemp=zeros(Np*Np,chunksize/(Np*Np))
0200          Utemp(indall(chunk)-chunksize*i)=transvec(chunk)
0201          U((nphi-1)*Np*Np+1:nphi*Np*Np,i*chunksize/(Np*Np)+1:(i+1)*chunksize/(Np*Np))=Utemp
0202          i=i+1
0203          chunk=find((indall > i*chunksize)&(indall <= (i+1)*chunksize))
0204      end
0205      if chunk($) ~= [] then
0206              Utemp=zeros(Np*Np,N_s*nlambda-i*chunksize/(Np*Np))
0207              Utemp(indall(chunk)-chunksize*i)=transvec(chunk)
0208              U((nphi-1)*Np*Np+1:nphi*Np*Np,i*chunksize/(Np*Np)+1:$)=Utemp
0209       else
0210              disp("[]")
0211      end
0212      nphi=nphi+1
0213  end
0214  clear Utemp
0215  time=toc()
0216  mprintf("Point spred matrix U was completed in: " + string (time/60) + " minutes")
0217
```

```
// Here the vector of all experimental data I_total is created:
tic()
disp('Creating I_total ...')
I_total=createfullsensordata(Np, N_phi)
P=toc()
disp('I_total completed in ' + string(P/60)  + " minutes")

// Deletion of all lines of "U" and "I_total", which contain only zeros:
tic
zeroline=spzeros(1,N_s*N_l)
disp("Size of U: "+string(size(U)))
H=vectorfind(U,zeroline,'r')
counter=length(H)
I_total(H)=[]
U(H,:)=[]
time=toc()
disp(string(counter)+' Useless lines of U and I_total deleted in ' +string(time/60) +' minutes.')

disp("Size of U after deletion of all lines containing only zeros:")
disp(size(U))

// Adding additional normalizing lines to U,
// which originate from the additional information of the 0°-degree image without prism:
tic
disp('Adding additional normalizing lines to U ...')
contributing_coordinates=nnz(wpvector)
U_additional=spzeros(contributing_coordinates,N_s*N_l)
a=1
zeilen_I_total=size(I_total,"r")
    for i=1:Np*Np
        if wpvector(i)~=0 then
        counter=1
        for j=((a-1)*N_l+1):(a*N_l)
            U_additional(a,j)=weightfactor*transmittance(counter);
            counter=counter+1
        end
        I_total(zeilen_I_total+a)=weightfactor*wpvector(i);
        a=a+1
        end
    end
m=size(U,"r")
U=[U;U_additional]

time=toc()
disp('Additional ' + string(contributing_coordinates) +' lines added in ' + string(time/60) + "
 minutes.")
// Saving new "U"-matrix and determining new size of "U":
mmwrite('..\512pixels\U-Matrix_512.mm',U)
disp("U matrix saved.")
disp("New size of U:")
disp(size(U))
disp("Number of non-zero entries in U: "+string(nnz(U)))

// Numerical solution of the overdetermined system of equations "I_0 = U\I_total"
// by least mean square algorithm:
tic()
disp('Solving system of equations with least mean square ...')
disp("Size of I_total = " + string(size(I_total)))
disp("Size of U = " + string(size(U)))
I_0 = U\I_total
A=toc()
disp('System of equations solved within '+string(A/60)+' minutes')
// Result "I_0" is saved to harddrive:
mmwrite('..\512pixels\ErgebnisI0_512.mm',I_0)
I_0=full(I_0)

// For evaluation of final result accuracy the deviation of the result data
// from the total emission intensities in the 0°-image is calculated:
    m=size(I_0);
    n=nnz(wp);
    sumofzeros=zeros(Np,Np)
    for lambda=1:N_l
        C=wp
```

```
0290          counter = 0;
0291          for i=1:Np*Np
0292              if C(i)~=0 then
0293                 C(i) = I_0(lambda+N_l*counter);
0294                 counter = counter +1 ;
0295              end
0296          end
0297          sumofzeros=sumofzeros+C
0298      end
0299      Diff=sumofzeros-wp
0300      Diff=sparse(Diff)
0301      intermediatesum=0
0302      counter=1
0303      for i=1:Np
0304          for j=1:Np
0305              if wp(i,j)~=0 then
0306                 Diff(i,j)=(Diff(i,j))^2
0307                 intermediatesum=intermediatesum + Diff(i,j)
0308                 counter=counter+1
0309              end
0310          end
0311      end
0312      deviation=sqrt(intermediatesum)
0313      Diff=round(Diff)
0314      disp("Total deviation:")
0315      disp(deviation)
0316      disp("Average deviation per entry:")
0317      disp(deviation/counter)
0318
0319  // Creating colormaps to display spectral results:
0320  disp('Creating color maps...')
0321  vectortomatrix (I_0,N_l,wavelengths,Np)
0322  time=toc()
0323  disp('All color maps finished in ' + string(time) + ' seconds')
0324
0325  Nullspalte=spzeros(size(U,"r"),1)
0326  disp("Größe von U: "+string(size(U)))
0327  H=vectorfind(U,Nullspalte,'c')
0328  counter=length(H)
0329  disp(string(counter)+' nach Koordinatenstreichung übrig gebliebene Nullspalten')
0330
0331  // Alternative solution of the system of equations with start value I_0 from calculation above:
0332  disp("Alternative solution:")
0333  disp('Solving system of equations with Scilab leastsq-function...')
0334  disp("Size of I_total = " + string(size(I_total)))
0335  disp("Size of U = " + string(size(U)))
0336  tic()
0337  I_0=abs(I_0)
0338  x0=I_0
0339  function y=f(I_0, U, I_total)
0001      y= U*I_0 - I_total
0002  endfunction
0003  binf=zeros(N_s*N_l,1)
0343  bsup=max(wpvector)*ones(N_s*N_l,1)
0344  disp("Solving system of equations with Scilab leastsq-method...")
0345  [fopt,I_0]=leastsq(list(f,U,I_total),'b',binf,bsup,x0)
0346  I_0=full(I_0)
0347  zeit4=toc()
0348  disp('System of equations solved in '+string(zeit4/60)+' minutes')
0349  mmwrite('..\512pixels\ErgebnisI0_512_leastsq.mm',I_0)
0350  if size(I_0,"r")~= N_l*nnz(wp) then
0351      disp("Warning: Image processing / read-in not working properly!");
0352  end
0353  if size(I_0)~=N_l*N_s then
0354      disp("Warning: I_0 has wrong size!");
0355  end
0356
0357  // For evaluation of final result accuracy the deviation of the result data
0358  // from the total emission intensities in the 0°-image is calculated as above:
0359      m=size(I_0);
0360      n=nnz(wp);
0361      sumofzeros=zeros(Np,Np)
0362      for lambda=1:N_l
```

```
0363          C=wp
0364          counter = 0;
0365          for i=1:Np*Np
0366              if C(i)~=0 then
0367                 C(i) = I_0(lambda+N_l*counter);
0368                 counter = counter +1 ;
0369              end
0370          end
0371          sumofzeros=sumofzeros+C
0372      end
0373      Diff=sumofzeros-wp
0374      Diff=sparse(Diff)
0375      intermediatesum=0
0376      counter=1
0377      for i=1:Np
0378          for j=1:Np
0379              if wp(i,j)~=0 then
0380                 Diff(i,j)=(Diff(i,j))^2
0381                 intermediatesum=intermediatesum + Diff(i,j)
0382                 counter=counter+1
0383              end
0384          end
0385      end
0386      deviation=sqrt(intermediatesum)
0387      Diff=round(Diff)
0388      disp("Total deviation:")
0389      disp(deviation)
0390      disp("Average deviation per entry:")
0391      disp(deviation/counter)
0392
0393  // Creating colormaps to display spectral results for Scilab leastsq-method:
0394  tic
0395  disp('Creating colormaps')
0396  vectortomatrix (I_0,N_l,wavelengths,Np)
0397  time=toc()
0398  disp('Colormaps finished in ' + string(time) + ' seconds.')
0399
0400  totaltime=timer()
0401  disp('Total time consumption of program: ' + string(totaltime/3600) + ' hours.')
```

B TCAD Diode scripts for EOFM simulations

C TCAD MOSFET scripts for EOFM simulations

D Acronyms

FA	failure analysis
FET	field effect transistor
MOSFET	metal-oxide-semiconductor field effect transistor
CMOS	complementary metal-oxide-semiconductor
SOI	silicon on insulator
DUT	device under test
IC	integrated circuit
PE	photon emission
PEM	photon emission microscopy
TRE	time resolved emission
PICA	picosecond imaging circuit analysis
SPEM	spectral photon emission microscopy
EOFM	electro-optical frequency mapping
EOP	electro-optical probing
LVI	laser voltage imaging (very similar to EOFM)
LVP	laser voltage probing (very similar to EOP)
SCR	space charge region
FCA	free carrier absorption
SIL	solid immersion lens
NL	Nanolens (Hamamatsu SIL)
SNR	signal-to-noise ratio
NDA	non-disclosure-agreement
FEOL	front-end-of-line (semiconductor device level design/architecture of IC)
BEOL	back-end-of-line (mainly interconnect level architecture of IC)
ppm	parts per million
FIB	focused ion beam
PCB	printed circuit boards
FPGA	field programmable gate array
NA	numerical aperture
CCD	charge-coupled device
TMM	transfer matrix model
HSL	high stable light source
HIL	high power incoherent light source
SLD	super-luminescence diode
LED	light-emitting diode
LD	laser diode
FKE	Franz-Keldysh effect
NA	numerical aperture
OBIRCH	optical beam induced resistance change technique
TLS	thermal laser stimulation technique

E Physical constants

ϵ_0	$8,85 \cdot 10^{-12} F/m$	electric field constant
k_B	$1,38 \cdot 10^{-23} J/K$	Boltzmann constant
e	$1,602 \cdot 10^{-19} C$	elementary charge

References

PE basics and theory

[1] S. Tam, C. Hu: *Hot-Electron-Induced Photon and Photocarrier Generation in Silicon MOSFET's*, IEEE Transactions on Electron Devices, Vol. ED-31, No.9, p. 1264-1273, 1984. 41, 42

[2] M. V. Fischetti, S. E. Laux, D. J. Dimaria: *The physics of Hot-Electron Degradation of Si MOSFET's - Can we understand it?*, Applied Surface Science 39, p. 578-596, 1989. 41

[3] J. Bude, N. Sano, A. Yoshii: *Hot-carrier luminescence*, Physical Review B, Vol. 45, No. 11, p. 5848-5856, 1992. 30, 41

[4] S. Villa, A. L. Lacaita, A. Pacelli: *Photon emission from hot electrons in silicon*, Physical Review B, Vol. 52, No. 15, p. 10993-10999, 1995. 30, 41

[5] M. V. Fischetti, S. E. Laux: *Long-range Coulomb interactions in small Si devices. Part I: Performance and reliability*, Journal of Applied Physics 89, p. 1205-1231, 2001. 41

[6] M. V. Fischetti: *Long-range Coulomb interactions in small Si devices. Part II: Effective electron mobility in thin-oxide structures*, Journal of Applied Physics 89, p. 1232-1250, 2001. 41

[7] C. Boit: *Fundamentals of Photon emission (PEM) in Silicon - Electroluminescence for Analysis of Electronic Circuit and Device Functionality*, Microelectronics Failure Analysis, EDFAS Desk Reference Fifth Edition, ASM International, Ohio, USA, p. 356-367, 2004. 30, 40, 69

[8] G. Shade: *Photon Emission Microscopy*, Microelectronics Failure Analysis, EDFAS Desk Reference Fifth Edition, ASM International, Ohio, USA, p. 347-355, 2004. 30

[9] C. Boit: *Photon Emission: A Technique Supposed to Fade Is Dying Really Hard.*, Electronic Device Failure Analysis, 46-47, 2012. 52

[10] G. Faggion, P. Sardin, S. Dudit, M. Vallet, H. Deslandes, J.-P. Roux, H. Koike, T. Kuki *Effect of IC Geometry Shrink on Photon Emission Spectrum*, LSI Testing Symposium (LSITS), Osaka, 2007. 52

[11] I. Vogt, C. Boit: *Low Power and Fault Isolation: Spectral Aspects of Photon Emission*, will be published in proceedings of IPFA 2018. 99

PE case studies

[12] H.-S. Wong: *Experimental Verification of the Mechanism of Hot-Carrier-Induced Photon Emission in N-MOSFETs with a CCD Gate Structure*, Electron Devices Meeting, IEDM 1991, Technical Digest, IEEE, p. 549-552, 1991. 30

[13] J.-S. Seo, S.-S. Lee, C.-S. Choe, K.-D. Hong, S. Daniel, C. K. Yoon: *Intelligent Defect Localization Methodology through the use of Photoemission Spectral Analysis*, Proceedings from the 5th IEEE International Symposium on the Physical and Failure Analysis of Integrated Circuits (IPFA 1995), Singapore, p. 49-54, 1995. 52

[14] M. Rasras, I. De Wolf, G. Groeseneken, J. Chen, K. Bock, H. E. Maes: *Temperature profile measurement and failure characterization of ESD protection devices using spectroscopic photon emission microscopy and Raman spectroscopy*, Conference Proceedings from the 25th International Symposium for Testing and Failure Analysis (ISTFA 1999), ASM International, p. 69-76, 1999. 35, 40

[15] M. Rasras, I. De Wolf, G. Groeseneken, B. Kaczer, R. Degraeve, H. E. Maes: *Photo-carrier generation as the origin of Fowler-Nordheim-induced substrate hole current in thin oxides*, IEEE Transactions on Electron Devices, 48(2), p. 231-238, 2001. 35, 40

[16] M. Rasras, I. De Wolf, G. Groeseneken, H. E. Maes: *Spectroscopic identification of light emitted from defects in silicon devices*, Journal of Applied Physics, Vol. 89 (1), p. 249-258, 2001. 35, 40

[17] I. De Wolf, M. Rasras: *Spectroscopic photon emission microscopy: a unique tool for failure analysis of microelectronics devices*, invited paper, Microelectronics Reliability, Vol. 41 (8), p. 1161-1169, 2001. 35

[18] M. Funada, T. Matsuda, T. Ohzone, S. Odanaka, K. Yamashita, N. Koike, K.-I. Tatsuuma: *A New Test Structure to Measure Precise Location of Hot-Carrier-Induced Photoemission Peak from Gate Center of Subquarter-Micron n-MOSFETs* Proceedings of IEEE Int. Conference on Microelectronic Test Structures, Vol. 14, p. 223-228, 2001. 31, 42

[19] A. Tosi, F. Stellari, F. Zappa, S. Cova: *Backside Flip-Chip testing by means of high-bandwidth luminescence detection*, Microelectronics Reliability 43, p. 1669-1674, 2003. 30

[20] A. Tosi, F. Stellari, F. Zappa, S. Cova: *Hot-carrier luminescence: comparison of different CMOS technologies*, 33rd Conference on European Solid-State Device Research (ESSDERC 2003), IEEE, p. 351-354, 2003. 30

[21] I. De Wolf: *From photon emission microscopy to Raman spectroscopy: Failure analysis in microelectronics*, invited paper at DRIP conference, The European Physical Journal-Applied Physics, Vol. 27 (1-3), 59-65, 2004. 35

[22] A. Tosi, F. Stellari, A. Pigozzi, G. Marchesi, F. Zappa: *Hot-Carrier Photoemission in scaled CMOS Technologies: A Challenge for Emission Based Testing and Diagnostics*, 44th Annual Reliability Physics Symposium Proceedings (IRPS 2006), IEEE International, 2006. 30, 33, 51, 52, 57, 102, 103

[23] F. Stellari, A. Tosi, F. Zappa, S. Cova: *CMOS Circuit Testing via Time-Resolved Luminescence Measurements and Simulations*, IEEE Transactions on instrumentation and measurement, Vol. 53, No. 1, IEEE International, 2004. 51

[24] T. Parrassin, S. Dudit, M. Vallet, A. Reverdy, H. Deslandes: *Introduction of spectral mapping through transmission grating, derivative technique of photon emission*, Proceedings from the 40th International Symposium for Testing and Failure Analysis (ISTFA 2014), USA, 2014. 69

[25] F. Stellari, K. A. Jenkins, A. J. Weger, B. Linder, P. Song: *Self-Heating Characterization of FinFET SOI Devices using 2d Time Resolved Emission Measurements*, 53rd Annual Reliability Physics Symposium Proceedings (IRPS 2015), IEEE International, 2015. 40, 113

[26] A. B. Shehata, A. J. Weger, F. Stellari, P. Song, H. Deslandes, T. Lundquist, E. Ramsay: *Time-Integrated Photon Emission as a Function of Temperature in 32 nm CMOS*, 53rd Annual Reliability Physics Symposium Proceedings (IRPS 2015), IEEE International, 2015. 31, 40, 113

[27] F. Stellari, A. Ruggeri, A. B. Shehata, H. Ainspan, P. Song: *Spontaneous photon emission from 32 nm and 14 nm SOI FETs*, 54th Annual Reliability Physics Symposium Proceedings (IRPS 2016), IEEE International, 2016. 31, 40

[28] M. Gurfinkel, M. Borenshtein, A. Margulis, S. Sade, Y. Fefer, Y. Weizman, Y. Shapira: *Study of hot-carrier-induced photon emission from 90 nm Si MOSFETs*, Applied Surface Science 248, Elsevier, p. 62-65, 2015. 31, 51

[29] F. Stellari, P. Song, J. C. Tsang, M. K. McManus, M. B. Ketchen: *Testing and Diagnostics of CMOS Circuits Using Light Emission from Off-State Leakage Current*, IEEE Transactions on Electron Devices, Vol. 51, No. 9, IEEE International, 2004. 31, 52

[30] J. Fine, C. D. Young, C. Hobbs, G. Bersuker, T. Lundquist, C.-C. Tsao: *Optical Probing of FinFETs*, Proceedings from the 19th IEEE International Symposium on the Physical and Failure Analysis of Integrated Circuits (IPFA 2012), IEEE International, p.28-31, 2013. 110

[31] S. Polonsky, M. Bhushan, A. Gattiker, A. Weger, P. Song: *Photon Emission Microscopy of inter/intra Chip Device Performance Variations*, Microelectronics Reliability, Vol. 45, p. 1471-1475, 2005.

[32] S. Polonsky, A. Weger: *Off-state luminescence in metal-oxide-semiconductor field-effect transistors and its use as on-chip voltage probe*, Applied Physics Letters, Vol. 85, No. 12, p. 2390-2392, 2004. 31

[33] D. V. Isakov, B. W. M. Tan, J. C. H. Phang, Y. C. Yeo, A. A. B. Tio, Y. Zhang, T. Geinzer, L. J. Balk: *Applications of Scanning Near-field Photon Emission Microscopy*, Proceedings from the 16th IEEE International Symposium on the Physical and Failure Analysis of Integrated Circuits (IPFA 2009), IEEE International, 2009.

[34] F. Stellari, F. Zappa, S. Cova, L. Vendrame: *Tools for Non-Invasive Optical Characterization of CMOS Circuits*, Electron Devices Meeting, IEDM 1999, Technical Digest, IEEE, p. 487-490, 1999.

[35] A. J. Weger, F. Stellari, P. Song: *Device Channel Temperature Measurement Using NIR Emission*, Conference Proceedings from the 43rd International Symposium for Testing and Failure Analysis (ISTFA 2017), ASM International, 2017. TRE 40, 113

[36] A. Tosi, A. Dalla Mora, F. Pozzi, F. Zappa: *Modeling and Probing Hot-Carrier Luminescence from MOSFETs*, IEEE Electron Device Letters, Vol. 29, No. 4, p. 350-352, 2008.

[37] I. Vogt, A. Glowacki, U. Kerst, P. Perdu, T. Nakamura, C. Boit: *New Method for enhancing Photon Emission Measurements similar to 2d-Tomography*, will be published in proceedings of IPFA 2018. 69

PE spectra

[38] M. Koyanagi, H. Kurino, T. Hashimoto, H. Mori, K. Hata, Y. Hiruma, T. Fujimori, I.-W. Wu, A. G. Lewis: *Relation between Hot-Carrier Light Emission and Kink Effect in Poly-Si Thin Film Transistors*, Technical Digest of Electron Devices Meeting IEDM 1991, p. 571-574, 1991. 30, 44

[39] A. L. Lacaita, F. Zappa, S. Bigliardi, M. Manfredi: *On the Bremsstrahlung Origin of Hot-Carrier-Induced Photons in Silicon Devices*, IEEE Transactions on Electron Devices, IEEE, Vol. 40, No. 3, p. 577-582, 1993. 30, 44

[40] Y. Y. Liu, J. M. Tao, D. S. H. Chan, J. C. H. Phang and W. K. Chim: *A new Spectroscopic Photon Emission Microscope System for Semiconductor Analysis*, Proceedings of the 5th IEEE International Symposium on the Physical and Failure Analysis of Integrated Circuits (IPFA 1995), IEEE, Singapore, p. 60-65, 1995. 44

[41] J. M. Tao, D. S. H. Chan, W. K. Chim: *Spectroscopic observations of photon emissions in n-MOSFETs in the saturation region*, Journal of Physics D: Applied Physics 29.5, p. 1380-1385, 1996. 30, 44

[42] D. L. Barton, P. Tangyunyong, J. M. Soden, A. Y. Liang, F. J. Low, A. N. Zaplatin, K. Shivanandan, G. Donohoe: *Infrared light emission from semiconductor devices*, No. SAND–96-2218C, CONF-961180–4, Sandia National Labs., USA. 44

[43] L. Selmi, M. Mastrapasqua, D. M. Boulin, J. D. Bude, M. Pavesi, E. Sangiorgi, M. R. Pinto: *Verification of Electron Distributions in Silicon by Means of Hot Carrier Luminescence Measurements*, IEEE Transactions on Electron Devices, IEEE, Vol. 45, No.4, p.802-808, 1998. 42, 44

[44] J. C. H. Phang, D. S. H. Chan, S. L. Tan, W. B. Len, K. H. Yim, L. S. Koh, C. M. Chua, L. J. Balk: *A Review of Near Infrared Photon Emission Microscopy and Spectroscopy*, Proceedings of the 12th IEEE International Symposium on the Physical and Failure Analysis of Integrated Circuits (IPFA 2005), IEEE, Singapore, p. 275-281, 2005. 44

[45] S. L. Tan, J. K. J. Teo, K. H. Toh, D. Iskaov, D. S. H. Chan, L. S. Koh, C. M. Chua, J. C. H. Phang: *Near-Infrared Spectroscopic Photon Emission Microscopy of 0.13 um Silicon nMOSFETs and pMOSFETs*, Proceedings of the 15th IEEE International Symposium on the Physical and Failure Analysis of Integrated Circuits (IPFA 2008), IEEE, Singapore, p. 275-281, 2008. 44

[46] A. Beyreuther, I. Vogt, T. Nakamura, G. G. Fischer, B. Motamedi, C. Boit: *Characterization of bandgap engineering on operative transistor devices by spectral photon emission*, submitted to IPFA 2018. 30

[47] S. Rusu, S. Seidel, G. Woods, D. Grannes, H. Muljono, J. Rowlette, K. Petrovsky: *Backside Infrared Probing for Static Voltage Drop and Dynamic Timing Measurements*, Solid-State Circuits Conference, Digest of Technical Papers, ISSCC, IEEE International, 2001. 44

[48] U. Kindereit, A. J. Weger, F. Stellari, P. Song, H. Deslandes, T. Lundquist, P. Sabbineni: *Near-Infrared Photon Emission Spectroscopy of a 45 nm SOI Ring Oscillator*, 50th Annual Reliability Physics Symposium Proceedings (IRPS 2012), IEEE International, 2D.2.1 - 2D.2.7, 2012. 31, 40, 44, 47, 99

PE spectra with electron temperatures

[49] A. Toriumi, M. Yoshimi, M. Iwase, K. Taniguchi: *Experimental Determination of Hot-Carrier Energy Distribution and Minority Carrier Generation Mechanism Due to Hot-Carrier Effects*, IEEE Electron Devices Meeting, p. 56-59, 1985. 44

[50] A. Toriumi, M. Yoshimi, M. Iwase, Y. Akiyama, K. Taniguchi: *A Study of Photon Emission from n-Channel MOSFET's*, IEEE Transactions on Electron Devices, Vol. ED-34, No. 7, p. 1501-1508, 1987. 31, 32, 33, 41, 42, 43, 44, 49, 100, 101, 102

[51] A. Toriumi: *Experimental Study of Hot Carriers in Small Size Si-MOSFETs*, Solid-State Electronics Vol. 32, No. 12, p. 1519-1525, 1989. 30, 44

[52] M. Lanzoni, M. Manfredi, L. Selmi, E. Sangiorgi, R. Capelletti, B. Ricco: *Hot-Electron-Induced Photon Energies in n-Channel MOSFET's Operating at 77 and 300 K*, IEEE Electron Device Letters, Vol. 10, No. 5, p. 173-176, 1989. 44

[53] M. Lanzoni, E. Sangiorgi, C. Fiegna, M. Manfredi, B. Ricco: *Extended (1.1-2.9 eV) Hot-Carrier Induced Photon Emission in n-Channel MOSFETS*, Electron Devices Meeting IEDM 1990, Technical Digest, IEEE, p.69-72, 1990. 30, 44

[54] M. Lanzoni, E. Sangiorgi, C. Fiegna, M. Manfredi, B. Ricco: *Extended (1.1-2.9 eV) Hot-Carrier Induced Photon Emission in n-Channel Si MOSFET's*, Electron Device Letters, IEEE, Vol. 12, No. 6, p. 341-343, 1991. 42

[55] Y. Uraoka, N. Tsutsu, Y. Nakata, S. Akiyama: *Evaluation Technology of VLSI Reliability Using Hot Carrier Luminescence*, IEEE Transactions on Semiconductor Manufacturing, Vol. 4, No. 3, p. 183-192, 1991. 44

[56] J. Koelzer, C. Boit, A. Dallmann, G. Deboy, J. Otto, D. Weinmann: *Quantitative Emission Microscopy*, Journal of Applied Physics 71, No. 11, p. R32-R41, 1992. 40, 42, 44

[57] E. Bano, C. Banc, T. Ouisse, S. Scharnholz: *Hot carrier-induced photon emission in 6H and 4H-SiC MOSFETs*, Solid-State Electronics 44, p. 63-69, 2000 . 44

[58] T. Matsuda, T. Ohzone, S. Odanaka, K. Yamashita, N. Koike, K.-I. Tatsuuma: *A Test Structure for Spectrum Analysis of Hot-Carrier-Induced Photoemission from Subquarter-Micron CMOSFETs*, Proceedings IEEE 2002 International Conference on Microelectronic Test Structures, Vol. 15, p. 95-99, 2002. 44

[59] T. Matsuda, T. Ohzone, S. Odanaka, K. Yamashita, N. Koike, K.-I. Tatsuuma: *A Test Structure for Spectrum Analysis of Hot-Carrier-Induced Photoemission from MOSFETs*, IEEE Transactions on Semiconductor Manufacturing, Vol. 16, No. 2, p. 233-238, 2003. 44

[60] T. Matsuda, T. Maezawa, H. Iwata, S. Odanaka: *A Test Structure for Spectrum Analysis of Hot-Carrier-Induced Photoemission from Scaled MOSFETs under DC and AC Operation*, IEEE International Conference on Microelectronic Test Structures (ICMTS 2009), p. 71-74, 2009. 44

[61] A. Glowacki, C. Boit, P. Perdu and Y. Iwaki: *Backside spectroscopic photon emission microscopy using intensified silicon CCD*, Microelectronics Reliability, Volume 54, No. 9-10, p. 2105-2108, 2014. 44, 70, 82, 92, 100, 101, 102

[62] M. Herzog, M. Schels, F. Koch, C. Moglestue, J. Rosenzweig: *Electromagnetic Radiation from Hot Carriers in FET-Devices*, Solid-State Electronics Vol. 32, No. 12, p. 1765-1769, 1989. 44

[63] A. Glowacki, C. Pagano, C. Boit, Y. Yokoyama, A. Jankowski, P. Perdu: *Photon Emission Spectra Through Silicon of Various Thicknesses*, Conference Proceedings from the 37th International Symposium for Testing and Failure Analysis (ISTFA 2011), ASM International, p.164-169, 2011. 16, 44

[64] C. Boit, A. Glowacki, C. Pagano, U. Kerst, Y. Yokoyama: *Quantitative Aspects of Optical IC Debug using State-of-the-Art Backside Preparation*, Proceedings from the 19th IEEE International Symposium on the Physical and Failure Analysis of Integrated Circuits (IPFA 2012), p. 1-6, 2012. 44, 129

[65] A. Glowacki, Y. Yokoyama, P. Perdu, C. Boit: *Photon Emission Spectra of FETS as obtained by InGaAs detector*, Proceedings from the 38th International Symposium for Testing and Failure Analysis (ISTFA 2012), ASM International, p.123-127, 2012. 42, 44

[66] A. Glowacki, C. Boit, P. Perdu, Y. Yokoyama: *Electron Temperature - the parameter to be extracted from backside spectral photon emission*, 51st Annual Reliability Physics Symposium Proceedings (IRPS 2013), IEEE International, 2013. 16, 44

[67] I. Vogt, T. Nakamura, C. Boit: *Optical Interaction in Active Analog Circuit Elements*, Microelectronics Reliability 76, p. 233-237, 2017. 44, 94, 115

[68] I. Vogt, T. Nakamura, B. Motamendi, C. Boit: *Optical Investigations on Temperature Effects in 14/16nm FinFETs*, Proceedings from the 43rd International Symposium for Testing and Failure Analysis (ISTFA 2017), ASM International, 2017. 35, 44, 52, 112

[69] I. Vogt, T. Nakamura, B. Motamedi, C. Boit: *Device Characterization of 16/14nm FinFETs for Reliability Assessment with Infrared Emission Spectra*, accepted at ESREF 2018, will be published in Microelectronics Reliability, 2018. 44

[70] I. Vogt, T. Nakamura, I. De Wolf, C. Boit: *Detection of Failure Mechanisms in 24-40nm FinFETs with (Spectral) Photon Emission Techniques using InGaAs Camera*, accepted at ESREF 2018, will be published in Microelectronics Reliability, 2018. 52

[71] J. A. Rowlette, E. B. Varner, S. Seidel, M. Ballon: *Hot Carrier Emission from 50 nm n- and p-Channel MOSFET Devices*, The 16th Annual Meeting of the Lasers and Electro-Optics Society (LEOS 2003), Vol. 2, IEEE, p.740-741, 2003. 44

EOT basics

[72] M. Bruce, G. Dabney, S. McBride, J. Mulig, V. Bruce, C. Bachand, S. Kasapi, J. A. Block: *Waveform Acquisition from the Backside of Silicon Using Electro-Optic Probing*, Proceedings from the 25th International Symposium for Testing and Failure Analysis (ISTFA), 19, 1999. 1

[73] J. A. Block, W. K. Lo, C. Shaw: *Benefits of Phase Interference Detection to IC Waveform Probing*, IEEE Proceedings of 10th Asian Test Symposium, p. 185-190, 2001. 105

[74] W. Lo, S. Kasapi, K. Wilsher: *Comparison of Laser and Emission Based Optical Probe Techniques*, Proceedings from the 24th International Symposium for Testing and Failure Analysis (ISTFA 2001), p. 33-42, USA, 2001. 105

[75] W. Lo, N. Nataraj, N. Boiadjieva, P. Vedegarbha, K. Wilsher: *Polarization Difference Probing: A New Phase Detection Scheme for Laser Voltage Probing*, Proceedings from the 30th International Symposium for Testing and Failure Analysis (ISTFA 2004), Worcester, Massachusetts, USA, 2004. 105

[76] S. Kolachina: *Introduction to Laser Voltage Probing (LVP) of Integrated Circuits*, Microelectronics Failure Analysis, EDFAS Desk Reference Fifth Edition, ASM International, Ohio, USA, p. 426-430, 2004. 105

[77] Y. S. Ng, T. Lundquist, D. Skvortsov, J. Liao, S. Kasapi, H. Marks: *Laser Voltage Imaging: A new Perspective of Laser Voltage Probing*, Proceedings from the 36th International Symposium for Testing and Failure Analysis (ISTFA 2010), Addison, Texas, USA, 2010. 25, 105, 117

[78] U. Kindereit: *Fundamentals and Future Applications of Laser Voltage Probing*, Reliability Physics Symposium (IRPS), IEEE International, p. 3F.1.1-3F.1.11., 2014. 105

[79] U. Ganesh: *Laser Voltage Probing (LVP)*, Microelectronics Reliability 64, p. 294-298, 2016. 105

[80] I. Vogt, R. Leihkauf, T. Nakamura, C. Boit: *New Laser Voltage Signal Insights from EOFM Simulations and Measurements on different pn-junctions*, will be published in proceedings of IPFA 2018. 129

EOT case studies and new developments

[81] T. Eiles, G. Woods, V. Rao: *Optical Probing of Flip-Chip-Packaged Microprocessors*, Solid-State Circuits Conference (ISSCC 2000), Digest of Technical Papers, IEEE International, p. 220-221, 2000. 110

[82] U. Kindereit, G. Woods, J. Tian, U. Kerst, R. Leihkauf, C. Boit: *Quantitative Investigation of Laser Beam Modulation in Electrically Active Devices as Used in Laser Voltage Probing*, IEEE Transactions on Device and Materials Reliability, Vol. 7, No. 1, p. 19-30, 2007. 137

[83] J. Beutler, J. J. Clement, M. A. Miller, J. Stevens and E. I. Cole Jr.: *Visible Light LVP on Ultra-Thinned Substrates*, Proceedings from the 40th International Symposium for Testing and Failure Analysis (ISTFA 2014), Houston, Texas, USA, p. 110-114, 2014. 16, 105

[84] H. Lohrke, P. Scholz, A. Beyreuther, U. Ganesh, E. Uhlmann, S. Kühne, M. Jagodzinski, Y. Iwaki, R. Chivas, S. Silverman, C. Boit: *Contactless Fault Isolation for FinFET Technologies with Visible Light and GaP SIL*, Proceedings from the 42th International Symposium for Testing and Failure Analysis (ISTFA 2016), Fort Worth, Texas, USA, 2016. 16, 105

[85] G. Celi, S. Dudit, T. Parrasin, P. Perdu, A. Reverdy, D. Lewis, M. Vallet: *Thermal Frequency Imaging: A new application of Laser Voltage Imaging applied on 40nm technology*, Proceedings from the 37th International Symposium for Testing and Failure Analysis (ISTFA 2011), San Jose, California, USA, p. 18-23, 2011. 105, 112, 113

[86] G. Celi, S. Dudit, T. Parrasin, P. Perdu, A. Reverdy, D. Lewis, M. Vallet: *LVI detection on passive structure in advance CMOS technology. New opportunities for device analysis*, Microelectronics Reliability 51, p. 1662-1667, 2011. 105

[87] T. Parrassin, G. Celi, S. Dudit, M. Vallet, A. Reverdy, P. Perdu, D. Lewis: *Laser Voltage Imaging and its derivatives, efficient techniques to address defect on 28nm technology*, Proceedings from the 39th International Symposium for Testing and Failure Analysis (ISTFA 2013), San Jose, California, USA, p. 306-312, 2013. 105

[88] M. M. Rebaï, F. Darracq, D. Lewis, P. Perdu, K. Sanchez: *How to interpret the reflected laser probe signal of multiple elementary substructures in very deep submicron technologies*, Proceedings from the 39th International Symposium for Testing and Failure Analysis (ISTFA 2013), San Jose, California, USA, p. 471-481, 2013. 118, 129

[89] M. M. Rebaï, F. Darracq, J.-P. Guillet, D. Lewis, P. Perdu, K. Sanchez: *Temperature Effect on Reflected Laser Probing Signal of Multiple Elementary Substructures*, Proceedings of the 21st IEEE International Symposium on the Physical and Failure Analysis of Integrated Circuits (IPFA 2014), IEEE, p. 374-378, 2014. 129, 137

[90] M. M. Rebaï, F. Darracq, J.-P. Guillet, E. Bernou, K. Sanchez, P. Perdu, D. Lewis: *A comprehensive study of the application of the EOP techniques on bipolar devices*, Microelectronics Reliability 54, p. 2088-2092, 2014. 105

[91] Y. S. Ng, H. Marks, C. Nemirov, C.-C. Tsao, J. Vickers: *Scan-Shift Debug using LVI Phase Mapping*, Proceedings from the 39th International Symposium for Testing and Failure Analysis (ISTFA 2013), San Jose, California, USA, p. 322-328, 2013. 110

[92] K. Sanchez, P. Perdu, K. Melendez, T. Nakamura: *Comparison of C. W. Electro Optical Probing and light emission techniques*, Proceedings from the 39th International Symposium for Testing and Failure Analysis (ISTFA 2013), San Jose, California, USA, p. 329-335, 2013. 105

[93] S. H. Goh, B. L. Yeoh, G. F. You, W. H. Hung, J. Lam: *Advanced CMOS device fault isolation using frequency mapping on passive structures*, Proceedings from the 39th International Symposium for Testing and Failure Analysis (ISTFA 2013), San Jose, California, USA, p. 420-423, 2013. 110

[94] V.-K. Ravikumar, A. Phoa, P. Sabbineni, D. Skvortsov, T. Lundquist: *Continuous-wave 1064nm laser for Laser Voltage Imaging and Probing Applications*, Proceedings from the 40th International Symposium for Testing and Failure Analysis (ISTFA 2014), USA, p. 344-348, 2014. 110

[95] K. Melendez, A. Desmoulin, K. Sanchez, P. Perdu, D. Lewis: *A way to implement the electro-optical technique to inertial MEMS*, Microelectronics Reliability 55, p. 1916-1919, 2015. 105

[96] K. Melendez, K. Sanchez, P. Perdu, D. Lewis: *Fast 3D Electro-Optical Frequency Mapping and probing in frequency domain*, Reliability Physics Symposium (IRPS), IEEE International, p. FA-2-1-FA-2-5, 2016. 105

[97] A. Boscaro, S. Jacquir, K. Sanchez, H. Terada, P. Perdu, S. Binczak: *Automatic processing scheme for low laser invasiveness electro optical frequency mapping mode*, Proceedings of the 23rd IEEE International Symposium on the Physical and Failure Analysis of Integrated Circuits (IPFA 2016), IEEE, p. 94-99, 2016. 105

[98] W. Lua, G. Ranganathan, V. R. Ravikumar, A. Phoa: *Combinational Logic Analysis Case Studies Using Laser Voltage Probing*, Proceedings of the 23rd IEEE International Symposium on the Physical and Failure Analysis of Integrated Circuits (IPFA 2016), IEEE, p. 51-54, 2016. 118

[99] I. Vogt, T. Nakamura, C. Boit: *Optical probing on digital circuit elements (NANDs)*, Proceedings of the 24th IEEE International Symposium on the Physical and Failure Analysis of Integrated Circuits (IPFA 2017), IEEE, Chengdu, China, p. 1-6, 2017. 118

PhD Theses on related topics

[100] M. Rasras: PhD-thesis, IMEC, Belgium, 2000. 35, 40

[101] U. Kindereit: *Investigation of laser-beam modulations induced by the operation of electronic devices*, PhD-thesis, Berlin University of Technology, Berlin, Germany, 2008. 9, 23, 105, 129, 137

[102] G. Celi: *Etude, applications et amélioratıons de la technique LVI sur les défauts rencontrés dans les technologies CMOS avancées 45nm et inferieur*, PhD thesis, Université de Bordeaux, Bordeaux, 2013. 113

[103] C. Pagano: *Electro-Optical Frequency Modulation on Silicon Integrated Circuits with 1300nm and 1064nm Laser Sources*, PhD-thesis, Berlin University of Technology, Berlin, 2014. 9, 23, 24, 105, 124, 129

[104] M. Rebaï: *Analyse des circuits intégrés par laser en mode sonde*, PhD thesis, Université de Bordeaux, Bordeaux, 2014. 129, 137

Student Theses supervised by the author

[105] H. Ray: *Entwicklung eines numerischen Verfahrens zur oertlichen Rekonstruktion eines Photonemissionsspektrums von elektronischen Bauelementen mittels Tomographie (english translation: Development of a numerical method for the spatial reconstruction of a photon emission spectrum via tomography)*, bachelor thesis, Berlin University of Technology, Berlin, 2014. 71

Miscellaneous

[106] M. Bina, S. Tyaginov, J. Franco, K. Rupp, Y. Wimmer, D. Osintsev, B. Kaczer, T. Grasser: *Predictive Hot-Carrier Modeling of n-Channel MOSFETs*, IEEE Transactions on electron devices, Vol. 61, No. 9, 2014. 30, 46

[107] S. Tajik, H. Lohrke, J.-P. Seifert, C. Boit: *On the Power of Optical Contactless Probing: Attacking Bitstream Encryption of FPGAs*, Proceedings of the 2017 Conference on Computer and Communications Security, ACM SIGSAC, p. 1661-1674. 2017. 20, 117

[108] M. Chester, P. H. Wendland: *Electroabsorption spectrum in silicon*, Physical Review Letters, Vol. 13, No. 6, p. 193-195, 1964. 14

[109] M. Chester, P. H. Wendland: *Electric field effects on indirect optical transitions in silicon*, Phys. Rev., 140(4A), p. 1384-1390, 1965. 14

[110] D. A. B. Miller, D.S. Chemla and S. Schmitt-Rink: *Electroabsorption of highly confined systems: Theory of the quantum-confined Franz-Keldysh effect in semiconductor quantum wires and dots*, Appl. Phys. Letters 52, American Institute of Physics, p. 2154-2156, 1988. 14

[111] *The Dynamic Franz-Keldysh Effect*, http://www.ece.rice.edu/ irlabs/dfke.htm, Junichiro Kono Labatory, Texas, USA (Version of 2014) 14

[112] R. A. Soref, B. A. Bennett: *Electrooptical effects in silicon*, IEEE journal of quantum electronics, QE-23, 1987. 11, 12, 13

[113] B. J. Frey, D. B. Leviton, T. J. Madison: *Temperature-dependent refractive index of silicon and germanium*, Optomechanical Technologies for Astronomy, Vol. 6273, p. 62732J, International Society for Optics and Photonics, 2006. 13

[114] P. Scholz: *Focused Ion Beam created refractive and diffractive lens techniques for the improvement of optical imaging through silicon*, PhD-thesis, Berlin University of Technology, Berlin, Germany, 2012. 18, 19

[115] C. Hamaguchi: *Basic Semiconductor Physics*, Springer 2010, ISBN:978-3-642-03302-5, 2010. 4

[116] Phemos-1000 product catalog from hamamatsu.com (downloaded March 3rd, 2018) 1, 29, 36

[117] iPhemos-MP product catalog from hamamatsu.com (downloaded March 29th, 2018) 1

[118] https://www.ihp-microelectronics.com/de/services/mpw-prototyping/sigec-bicmos-technologies.html (viewed on April 3rd, 2018) 28

[119] https://en.wikipedia.org/wiki/P-n_junction (viewed on April 6th, 2018) 5

[120] https://en.wikipedia.org/wiki/MOSFET (viewed on April 6th, 2018) 7

[121] https://en.wikipedia.org/wiki/FinFET (viewed on April 6th, 2018) 8

[122] https://en.wikipedia.org/wiki/Inverter_(logic_gate) (viewed on April 6th, 2018) 8

[123] https://en.wikipedia.org/wiki/NAND_gate (viewed on April 6th, 2018) 9

[124] https://en.wikipedia.org/wiki/Wave_interference (viewed on April 11th, 2018) 11